UNIVERSITY OF SOUTHAMPTON

Faculty of Engineering and Physical Sciences
Optoelectronics Research Centre

Laser-based Direct-write Technique for Enabling Newer Functionalities in Paper-based Devices

by

Panagiotis Galanis

ORCiD: 0000-0002-2028-5803

A thesis for the degree of
Doctor of Philosophy

23rd November 2021

University of Southampton

Abstract

Faculty of Engineering and Physical Sciences
Optoelectronics Research Centre

Doctor of Philosophy

by Panagiotis Galanis

The demand for low-cost diagnostic devices that are user-friendly and deliver results rapidly to the patients is a universally accepted goal that has led to extensive development of paper-based microfuidic devices (µPADs). Despite the progress in the field of µPADs, there are still some important requirements yet to be addressed to improve their performance and enable their widespread use as a commercial product.

In this thesis, we focus on the use of a laser-based direct-write (LDW) technique for enabling newer functionalities in paper-based devices for improved sensitivity of diagnostic tests as well as the quantitative detection of either a single or multiple analytes. The LDW method we are using for paper patterning is based on the local deposition of a photo-polymer on top of a porous substrate followed by the exposure with a laser light source to create solid polymeric structures.

In our first demonstration, we are using the LDW method to create in-line filters on a porous nitrocellulose membrane that are capable of separating particles based on their size. These in-line filters act as barriers to delay the flow of samples and increase the sensitivity for the detection of an analyte. The LDW method is later used to create porous flow-through filters on cellulose paper that again have the ability for the size-exclusive separation of particles. When these flow-through filters are combined with a lateral flow assay they can act as a diagnostic tool for the detection of a single analyte over a wide concentration range. Additionally, the LDW can be extended for the fabrication of platforms that are able to detect multiple analytes within the same device. For that, we report the fabrication of multilayer 3D-µPADs used for the simultaneous detection of three analytes spiked in artificial urine as well as the pH of the tested sample. Finally, we report the use of light-activated materials (hydrogels) on paper-based devices to create optically triggered gates that are able to control the flow of samples, and therefore provide an alternative pathway to increase the sensitivity for the detection of analytes.

Adding these newer functionalities to paper-based devices is highly desirable, as this will allow their extensive use as a diagnostic sensor at the point-of-care.

Contents

List of Figures

List of Tables

Abbreviations

µPAD Microfluidic paper-based analytical devices.

3D Three dimensional.

Anti-D Rh0(D) immune globulin.

Au NPs Gold nanoparticles.

BSA Bovine serum albumin.

CFU Colony-forming unit.

CRP C-reactive protein.

CW Continuous wave.

DI Distilled.

E. coli Escherichia coli.

EGDMA Ethylene glycol dimethacrylate.

ELISA Enzyme-linked immunosorbent assay.

IgG Immunoglobulin G.

IPA Isopropyl alcohol.

LDW Laser direct writing.

LED Light-emitting diode.

LFA Lateral flow assay.

LOD Limit of detection.

MBIS N,N′-Methylenebisacrylamide.

NC Nitrocellulose.

NIPAM N-isopropylacrylamide.

OEGMA Oligoethylene glycol.

PBS Phosphate buffer saline.

pH Power of hydrogen.

POC Point of care.

RBCs Red blood cells.

RhD Rhesus D.

TBPB Tetrabromophenol blue.

UV Ultraviolet.

WHO World Health Organization.

Declaration Of Authorship

Print name: **Panagiotis Galanis**

Title of Thesis: **Laser-based Direct-write Technique for Enabling Newer Functionalities in Paper-based Devices**

I declare that this thesis and the work presented in it is my own and has been generated by me as the result of my own original research.

I confirm that:

1. This work was done wholly or mainly while in candidature for a research degree at this University;
2. Where any part of this thesis has previously been submitted for a degree or any other qualification at this University or any other institution, this has been clearly stated;
3. Where I have consulted the published work of others, this is always clearly attributed;
4. Where I have quoted from the work of others, the source is always given. With the exception of such quotations, this thesis is entirely my own work;
5. I have acknowledged all main sources of help;
6. Where the thesis is based on work done by myself jointly with others, I have made clear exactly what was done by others and what I have contributed myself;
7. Parts of this work have been published as:

Journal Papers

1. **P. Galanis**, I. N. Katis, P. J. He, A. H. Iles, A. K. John, R. W. Eason, and C. L. Sones,"Laser-patterned paper-based flow-through filters and lateral flow immunoassays to enable the detection of C-reactive protein," *Talanta*, vol. 238, p. 123056, 2021. [Online]. Available: https://doi.org/10.1016/j.talanta.2021.123056

2. A. H. Iles, P. J. He, I. N. Katis, **P. Galanis**, A. K. John, P. Elkington, R. W. Eason, and C. L. Sones, "Semi-quantitative detection of inflammatory biomarkers using a laser-patterned multiplexed lateral flow device," *Talanta*, vol. 237, p. 122944, 2021. [Online]. Available: https://doi.org/10.1016/j.talanta.2021.122944

3. A. K. John, P. J. He, I. N. Katis, **P. Galanis**, A. H. Iles, R. W. Eason, and C. L. Sones, "Capillary-based reverse transcriptase loop-mediated isothermal amplification for cost-effective and rapid point-of-care covid-19 testing," *Analytica Chimica Acta*, p. 339002, 2021. [Online]. Available: https://doi.org/10.1016/j.aca.2021.339002

4. **P. Galanis**, P. He, I. Katis, A. Iles, A.K. John, R. Eason, and C. Sones, "Local photopolymer deposition-assisted fabrication of multilayer paper-based devices," *Sensors and Actuators B: Chemical*, vol. 322, p. 128574, 2020. [Online]. Available: https://doi.org/10.1016/j.snb.2020.128574

Conference Contributions

1. (Invited) C. Sones, P. He, I. Katis, A. John, **P. Galanis**, A. Iles, and R. Eason, "Fabrication of paper-based microfluidic devices using laser direct-writing," presented at *The 82nd JSAP Autumn Meeting 2021*, Online, September 2021.

2. (Poster) **P. Galanis**, P. J. W. He, I. N. Katis, A. H. Iles, A. K. John, R. W. Eason, and C. L. Sones, "Flow-through filter-based lateral flow assays," presented at *Biosensors 2020*, Busan, South Korea, July 2021.

3. (Poster) **P. Galanis**, P. J. W. He, I. N. Katis, A. H. Iles, A. K. John, R. W. Eason, and C. L. Sones, "Laser patterning method for the fabrication of multilayer paper -based devices," presented at *Biosensors 2020*, Busan, South Korea, July 2021.

4. (Oral) **P. Galanis**, P. J. W. He, I. N. Katis, A. H. Iles, A. J. Kumar, R. W. Eason, and C. L. Sones, "Laser patterned flow-through filters for paper-based immunoassays," in *14th Pacific Rim Conference on Lasers and Electro-Optics (CLEO PR 2020)*. Optical Society of America, Sidney, Australia, August 2020, p. C11D_2. [Online]. Available: https://doi.org/10.1364/CLEOPR.2020.C11D_2

5. (Oral) **P. Galanis**, P. He, I. Katis, M. Thomas, Y. Xianyu, M. Stevens, R. Eason, and C. Sones, "Laser-direct-writing to enable filtration in paper-based devices," in *Proc. SPIE 10875, Microfluidics, BioMEMS, and Medical Microsystems XVII*, San Francisco, USA, February 2019. [Online]. Available: https://doi.org/10.1117/12.2508753

6. (Oral) P. He, I. Katis, **P. Galanis**, J. Teeling, C. Holmes, R. Eason, and C. Sones,Multiplexed detection of CRP-SAA1 using laser direct-write-fabricated multiple flow-path

lateral flow devices," in *Proc. SPIE 10875, Microfluidics, BioMEMS, and Medical Microsystems XVII*, San Francisco, USA, February 2019. [Online]. Available: https://doi.org/10.1117/12.2506771

7. (Oral) C. Sones, P. He, I. Katis, **P. Galanis**, and R. Eason, "Fabrication of paper-based microfluidic devices using laser direct-writing," in *Photonics 2018*, New Dehli, India, December 2018.

8. (Poster) **P. Galanis**, P. He, I. Katis, M. Thomas, Y. Xianyu, M. Stevens, R. Eason, and C. Sones, "In-line filtration for lateral flow devices by laser direct write technique," presented at *the Twenty Second International Conference on Miniaturized Systems for Chemistry and Life Sciences, MicroTAS 2018*, Taiwan, November 2018.

9. (Poster) I. Katis, P. He, **P. Galanis**, R. Eason, and C. Sones, "A novel manufacturing technique and design for improved CRP lateral flow devices," presented at *the Twenty Second International Conference on Miniaturized Systems for Chemistry and Life Sciences, MicroTAS 2018*, Taiwan, November 2018.

10. (Oral) C. Sones, P. J. W. He, I. N. Katis, **P. Galanis**, and R. W. Eason,"Performance improvement and add-on functionalities to conventional lateral-flow devices using a laser direct-write patterning technique," presented at *CLEO Pacific Rim Conference 2018*. Optical Society of America, Hong Kong, China, August 2018, p. W1E.4. [Online]. Available: https://doi.org/10.1364/CLEOPR.2018.W1E.4

11. (Poster) **P. Galanis**, P. He, I. Katis, M. Thomas, Y. Xianyu, M. Stevens, R. Eason, and C. Sones, "Introduction of in-line filtration in paper diagnostic device via a laser direct-write technique," presented at *Biosensors 2018*, Miami, USA, June 2018.

12. (Poster) P. He, I. Katis, **P. Galanis**, R. Eason, and C. Sones, "Laser direct-write technique for rapid multiplexed detection on lateral-flow devices," presented at *Biosensors 2018*, Miami, USA, June 2018.

13. (Poster) I. Katis, P. He, **P. Galanis**, R. Eason, and C. Sones, "Enhancing lateral flow devices using spatial constrictions," presented at *Biosensors 2018*, Miami, USA, June 2018.

14. (Poster) C. Sones, P. He, I. Katis, **P. Galanis**, and R. Eason, "Local deposition assisted laser direct-write technique for fabrication of paper-based microfluidic devices," presented at *Biosensors 2018*, Miami, USA, June 2018.

15. (Invited) R. Eason, I. Katis, P. He, **P. Galanis**, and C. Sones, "Laser direct-write of microfluidic flow channels via additive manufacturing for paper-based rapid diagnostics," presented at *Laser Precision Microfabrication, LPM 2018*, Edinburgh, United Kingdom, June 2018.

Signed: _____

Date: 23/11/2021

Acknowledgements

First and foremost, I would like to thank my supervisors Prof. Rob Eason and Dr. Collin Sones for their invaluable support and the guidance they provided all these years during my PhD. We had a wonderful collaboration and I would also like to give them special thanks for their patience with me and the fact that they trusted and gave me the opportunity to study in the group. I would also like to express my gratitude to the two postdocs working in the group, Dr. Ioannis Katis and Dr. Peijun He, for their constant support and help. They were always there for me whenever I needed assistance either in the lab or discussing about work. Without them this project would have been harder. I would also like to acknowledge Dr. Anto Jesuraj Uday Kumar John for his assistance especially in the "optically controlled fluid flow" work. Further, I would also like to thank Ms Alice Iles for helping me understand, develop and optimize the biological assays presented throughout this thesis.

The "optically controlled fluid flow" work presented in this thesis was performed in collaboration with the University of Birmingham, department of Chemistry. I would like to express my sincere gratitude to the leader of the group, Prof. Rachel O'Reilly, as with her guidance she helped me gain a deep understanding of the hydrogel materials. Additionally, I would like to thank Dr. Turgay Yildirim and Dr. Yujie Xie for the synthesis and optimization of the hydrogel materials and the important help they provided to succeed in this work.

Finally, I would like to thank Thalia Dominguez Bucio for her invaluable support and the help she provided me in technical issues during the writing process of this thesis. Most importantly, I would like to thank and express my love to my family that gave me the chance to study abroad. They were always next to me in good and bad moments. Without them I would not be the person that I am now.

To my family, whom motivates me to become a better person

Chapter 1

Introduction

Public health is of universal importance and to that end, there is a constant research effort to create novel diagnostic tools world-wide. This need led to the development of point-of-care (POC) diagnostic sensors that have been widely used for more than a decade and are intended for near patient diagnostic testing for detection of various conditions and diseases [1]. These diagnostic tests, which can be of vital importance especially in resource-limited settings, are simple to use and can be easily performed by untrained personnel giving results within 30 minutes [2, 3]. Any POC diagnostic sensor designed for use in resource-limited settings would need to comply with the ASSURED criteria set by the World Health Organization (WHO) which addresses the need to be Affordable, Sensitive, Specific for analyte detection, User friendly, Robust while providing the results rapidly to the patients, Equipment-free and Deliverable to those who need it [4].

Paper has been shown to be an attractive platform for the development of POC sensors that would comply with all the WHO-specified requirements. Among the different substrates, such as silicon, polymer or glass which have been used to manufacture diagnostic sensors, paper is a promising alternative due to its inherent characteristics. Paper is a cost-effective material composed of a network of hydrophilic cellulose fibres, and has a porous structure that allows the passive transport of liquids through capillary action. The concept of paper-based devices was first proposed by the Whiteside's group in 2007 and has been used extensively for the detection of pathogens [5, 6]. Such devices have the ability to obtain, control and process small volumes of complex fluids with efficiency and speed. Furthermore, the miniaturization of the devices reduces the detection time and the volumes of the reagents that are used. Paper and porous nitrocellulose (NC) membranes are the flow media that are at the heart of every flow-based diagnostic device. Commercially available porous NC membranes are routinely used in the fabrication of paper-based devices as these offer distinct advantages such as their smooth surface, uniform pore size and high protein-binding capability which has led to

their almost universal adoption as the substrate of choice within a typical POC lateral flow assay (LFA).

1.1 Motivation

Despite of the advantages of paper-based devices previously mentioned, some important requirements yet to be addressed for their commercial deployment have also been identified. These include improvement in the sensitivity of these device, quantitative measurements of either a single or multiple analytes, detection of multiple analytes within a single device and finally, simplification of the sample preparation step. If addressed, this would allow for paper to become a platform for diagnostic devices on a wider scale. It is therefore of immediate benefit to add these functionalities to such a platform-medium for improved performance and to enable its use as stand-alone infield testing tools.

The need to address these requirements is the inspiration of this research project which focuses on the use of a laser-based direct-write (LDW) technique for the creation of novel paper-based devices with newer functionalities. The proprietary technique involves the local deposition of a photo-polymer onto a porous substrate at pre-defined locations, and its subsequent polymerization by exposure to a laser source to form polymeric structures that define and demarcate the flow path and, therefore, the fluidic device in the porous substrate. The focus of this project is to further explore the potential of this LDW technique in improving the performance of laser-patterned microfluidic devices through the incorporation of additional functionalities that can allow the use of such devices in real world POC scenarios. This includes the use of filtration which is a highly desirable feature as it will enable the segregation and analysis of complex liquid samples through the separation of different particles based on their size. This functionality provides a promising route to minimise or even eliminate complicated instrumental-based sample preparation steps, which are currently a critical impediment to the use of such low-cost devices by unskilled patients at the POC. Additionally, the filtration can also be used as a tool to develop novel assays that would improve the performance of existing paper-based devices used for the detection of analytes over a broad concentration range. Furthermore, we have explored the use of the LDW technique to develop three dimensional (3D) paper-based platforms that enable the simultaneous detection of multiple analytes within the same device.

Finally in this thesis we address the next steps towards the fluid control in paper-based devices. While paper-based fluidic devices that rely on their current passive self-wicking process can address some basic functionalities, enabling triggerable on-demand fluid flow using photo-responsive polymers will provide a hugely significant step towards the improvement of their performance. This will allow the incubation

of fluidic samples with a desired biochemical reagent within a channel to maximize the sensitivity and the limit of detection (LOD) of the diagnostic assays. Also a timed on/off gating will allow dispensing of pre-determined sample volumes to a specific site of the paper-based device for semi-quantitative detection of analytes. Our aim is to use our LDW technique to develop a paper platform where liquid flow can be controllably switched on and off via non-contact illumination of photo-responsive polymers using low power optical addressing. Such a capability will massively transform the current passive paper-based devices into true lab-on-chip type multi-functional testbeds bringing immediate and quantifiable impact within the medical diagnostic and healthcare sectors.

1.2 Outline of this thesis

Chapter 7.3 of this thesis presents an introduction to microfluidic paper-based analytical devices (μPADs) and highlights the advantages of using paper as a material for the development of POC sensors. After explaining the principle of operation of a standard LFA, we describe the techniques used to pattern paper to make μPADs and we focus on the LDW method. Next, we present the method of the light-induced photopolymerization, which is the main principle applied during LDW modification and then we describe our developed local photo-polymer deposition method that we use for paper patterning. Lastly, we introduce hydrogels and we emphasize the way that photo-responsive hydrogels interact with light that induces change in their mechanical properties, specifically their volume.

Chapter 7.3 presents the use of the local photo-polymer deposition method to fabricate in-line filters on an NC membrane for the separation of particles based on their size. First, this chapter presents the testing using different types of particles namely gold nanoparticles (Au NPs) and latex microbeads to define the parameters in which in-line filters transition from being impermeable to porous to the flow of these particles of varying sizes. Afterwards, we demonstrate the simultaneous filtering of two different sized particles when flowing within the same fluidic device and the application of the same method for the separation of plasma from red blood cells (RBCs). Lastly, the in-line filters were used as delay barriers in an LFA to increase the sensitivity of the detection of the common inflammatory marker C-reactive protein (CRP).

In chapter 7.3 we report the use of the same paper patterning approach to make flow-through filters that when combined with an LFA provide an alternative pathway for the detection of analytes over a wide concentration range. Similar to the work in chapter 7.3, we define again the parameters to create flow-through filters that are able to block or enable the flow of different sized latex microbeads into an LFA. Next, we use the flow-through filters as a tool for analyte detection and there after describe the principle

of operation of our developed filter-based assay that we use it for the quantitative detection of CRP. Finally, a flow-through filtration method is reported for two applications namely the separation of plasma from RBCs as well as the purification of a water-based sample containing the bacteria Escherichia coli (E. coli).

The local photo-polymer deposition method is further explored in chapter 7.3 to stack several layers of porous materials and create 3D-µPADs. We demonstrate the usefulness of the developed multilayer 3D-µPADs for the simultaneous and quantitative detection of three analytes spiked in artificial urine as well as the power of hydrogen (pH) of the tested urine sample.

Chapter 7.3 reports the use of our developed LDW technique to deposit light-activated hydrogels on paper-based devices, and the use of their light-induced volume change to control the flow of samples. We demonstrate the use of different hydrogels that are exposed to light of different wavelengths namely 365 nm and 470 nm in order to either shrink or swell respectively. We also present the results of patterning various types of paper in different designs and structures for use to optically control the flow of samples and increase the sensitivity for the detection of both CRP and the COVID-19 virus.

Finally in chapter 7.3 we summarize the work presented in this research thesis which is focused on the use of a LDW technique to enable newer functionalities in paper-based devices. We also present our ideas for future work on how to further explore this method in order to use paper-based devices as POC sensors on a wider scale.

Chapter 2

Background

2.1 Microfluidic paper-based analytical devices

The demand for low-cost diagnostic devices that are user-friendly and deliver the results rapidly to the patients, is a universally accepted goal that has led to extensive development of paper-based devices as POC sensors. Paper is an attractive medium for use, for the fabrication of POC diagnostic devices due to its attributes. Paper is a hydrophilic porous medium, which is abundant and can be found in different forms with different properties such as pore size, porosity and thickness. The most common types of paper which are used for the development of POC paper-based devices are cellulose paper, NC membrane and microglass fibre and figure 2.1 shows their internal structure. Paper is a low cost material so a simple paper-based device can be fabricated for less than $ 0.01 which is a factor that contributes to their mass production [1]. One of the most important characteristics of paper is the ability to wick fluids through capillary action and its use in diagnostic devices negates the need to use pumps and valves in order to guide the flow of samples. Additional attributes of paper include its flexibility, the ease of transportation, the biocompatibility and disposability via incineration if needed. Finally, paper can be chemically modified and has been used for decades in clinical diagnostics for colorimetric assays as its white colour provides a strong contrast against a coloured substrate.

The field of paper-based devices was first proposed by the Whiteside's group who developed and reported a range of analytical assays for the detection of glucose and protein [2, 3]. These devices are called µPADs because they can be designed to obtain, control and process small volumes (microliters) of complex fluids with efficiency and speed [4]. These characteristics can lead to the use of lower sample or reagent volumes required, compared with using other diagnostic platform substrates including polymer, silica and glass, which in many cases are expensive and they have the possibility to reduce the detection times due to the robust structure and the miniaturization of the

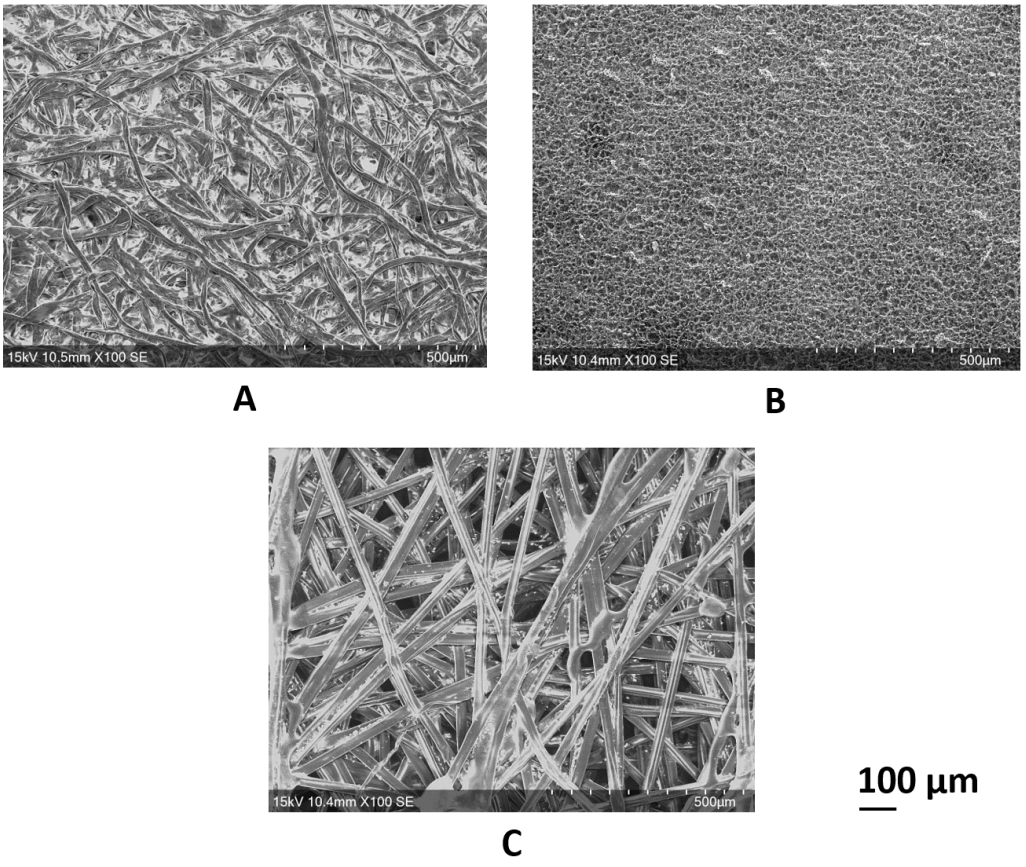

FIGURE 2.1: Scanning electron microscope images showing the internal structure of (A) cellulose paper, (B) NC membrane and (C) microglass fibre.

devices [5]. For the aforementioned reasons, µPADs are a promising alternative to conventional devices, made of silicon and glass, and many research groups have focused their attention towards their study.

LFAs are a specific category of µPADs that have been used for the detection and quantification of analytes within biological fluids such as urine [7], blood [8] and saliva [9]. LFAs are made up of four different constituents namely the sample pad, the conjugate pad, the membrane (detection pad) and the adsorbent pad, with each overlapping and are stacked on a backing card as shown in the schematic of figure 2.2. The principle of operation of an LFA is based on the interaction and binding of the target analyte with antibodies. The sample, which contains the analyte, is introduced via the sample pad and after travelling laterally in the porous paper, it first encounters the conjugate pad where immobilized antibodies (detection antibodies) tagged with a coloured label such as Au NPs bind with the analyte to form a complex. The sample and this complex then flow to the membrane (used as a detection pad) where capture antibodies specific to the analyte and the conjugate (detection antibodies tagged with Au NPs) are immobilized at the test and the control line respectively producing a visual signal. These lines are important for the operation of an assay as the appearance of a test lines indicates the

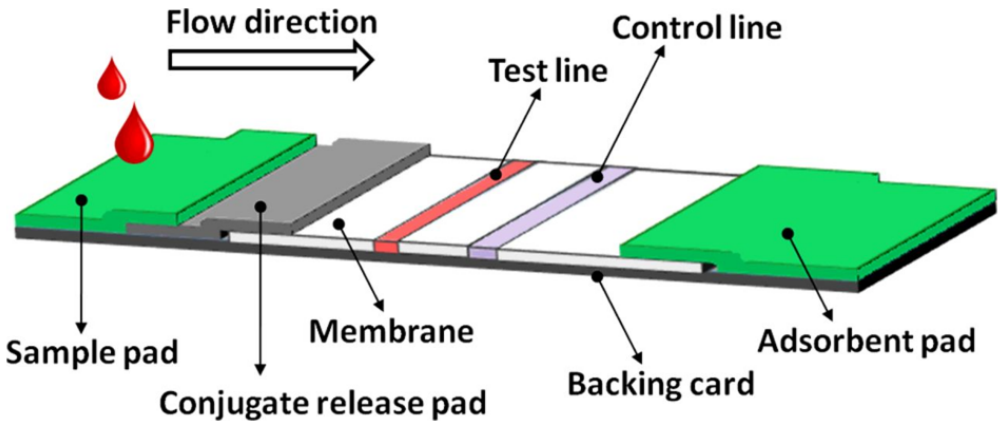

FIGURE 2.2: Schematic of a typical configuration of porous materials in an LFA [6].

presence of the analyte in the sample, whereas the appearance of a control line, which is not related to the presence of the analyte in the sample, shows the correct operation of the assay, i.e. a proper flow of the sample along the membrane. In this thesis, we use a BioDot dispensing system to dispense the test and the control lines and details for its operation can be seen in appendix A. The excess amount of sample is finally absorbed in a pad located at the end of the LFA [6].

Each of the components previously mentioned has a different role in the operation of the assay, and for that reason the choice of the appropriate material is essential for the correct operation of a test. The sample pad is responsible for evenly distributing the sample and guiding it to the conjugate pad. It is normally treated with blocking agents (e.g. Bovine serum albumin (BSA)) to reduce the non-specific binding of the conjugate which otherwise would result in a reduced signal intensity on the test line. The most commonly used material is cellulose paper due to the fact that it can be loaded with the blocking agents. The role of the conjugate pad is to preserve the dry conjugate and upon rehydration from the sample allow its travel to the membrane, therefore as a material of choice microglass fibre pads known to effectively release liquids are used. Next, for the membrane (detection pad) the material of choice is NC due to its high antibody binding capability, whereas for the adsorbent pad cellulose filter paper is used again because it can hold large volumes of liquids. In the latter case, special consideration must be given to parameters such as the paper thickness and porosity in order for the adsorbent pad to be able to hold volumes larger than the volume of the liquid flowing in the strip of the LFA.

To date, there are several approaches used to pattern paper and make µPADs and the most popular ones include the use of photolithography [10], wax printing [11] and inkjet printing [12]. All the existing paper patterning methods rely on the formation

of hydrophobic patterns on paper substrates in order to define the regions that allow the transport of fluids. Despite the fact that the aforementioned methods are widely used, there are certain disadvantages during their operation. The photolithography technique although cost-effective, requires multiple steps for the fabrication of µPADs, which might be a critical parameter when using this method for mass production. Furthermore, the wax printing method is environmentally sensitive as the ambient conditions such as the temperature and the humidity affect the viscosity, and hence possible melting of wax, and this adds an additional constraint for the more general adoption of this method. Lastly, the inkjet printing method requires the use of solvents as well as multiple printing steps.

Finally, as previously mentioned µPADs are used for the detection of analytes and common methods include electrochemical [13], chemiluminescent [14], fluorescent [15] and colorimetric detection [16]. Additionally, the detection of analytes is accomplished via the use of different labels such as colloidal particles like Au NPs and latex beads, enzymes such as horseradish peroxidase [17] and fluorescent particles (e.g. quantum dots) [18]. As will be described in the following subsections and throughout this thesis, we are using a LDW technique to pattern paper which is based on the local deposition of a photo-polymer on top of porous substrates. We are also using a colorimetric method for the detection of analytes using Au NPs as coloured labels.

2.2 Laser direct-write techniques

Direct-writing is a technique that is used to pattern substrates such as polymers by altering the chemistry or by depositing, removing and dispensing various materials in a pre-determined pattern [19]. Compared with other patterning methods, in direct-writing the structures are built directly on the substrate without any physical contact between the system and the substrate and with no use of masks and this allows for rapid prototyping. The resolution of the lines patterned with direct-writing can be as low as a few micrometers with speeds greater than 200 mm/s [20].

LDW is a specific category of the direct-writing technique, in which materials are being processed using a laser beam. A LDW system consists of three main parts namely the laser source, the beam delivery system and the substrate. Common examples of laser sources that are used in LDW are ultrafast lasers, femtosecond-pulsed lasers and continuous wave (CW) lasers that use laser media such as solid-state, gas, fibre or semiconductors [21]. The laser source that is used depends on the application, where laser parameters should be considered such as the wavelength, the pulse duration, the beam divergence and the laser power which define the energy absorption and the material response. The beam delivery can be adjusted using mirrors, lenses, optical fibres and galvo scanners, and the choice depends again on the application where critical

parameters include the working distance, the spot size and the energy required which should be properly selected during the fabrication work [22].

The wide range of existing LDW techniques has led to their classification into three main groups namely: LDW subtraction, addition and modification. In the first category, methods are reported using lasers such as excimer [23] and CO_2 to remove material and create channels on paper substrates with minimum widths of 128 µm [24] and 150 µm [25]. As for the second category of LDW addition, this is based on the deposition of material from a thin film directly to the substrate, and a method is reported [26] that this approach is able to achieve line resolution below 10 µm. Our reported method belongs to the third category of LDW modification, in which we deposit a photo-polymer on a porous substrate and after its exposure to light, it changes its physical properties due to light-induced photo-polymerization.

2.2.1 Light-induced photo-polymerization

By the term light-induced photo-polymerization we describe the process in which light initiates a chain reaction leading to a cross-linked network and the formation of a polymer [27]. The most commonly used light-curable materials are acrylate-based resins, due to the high reactivity of the acrylate monomers [28]. Such a pre-polymer system consists of various components namely monomers, oligomers and photo-initiators and the polymerization reaction takes place after light irradiation as shown in figure 2.3. Most of the light-curable materials are exposed to the ultraviolet (UV) light to initiate the photo-polymerization process, however it is reported that exposure to visible light can also lead to a cross-linked network [29].

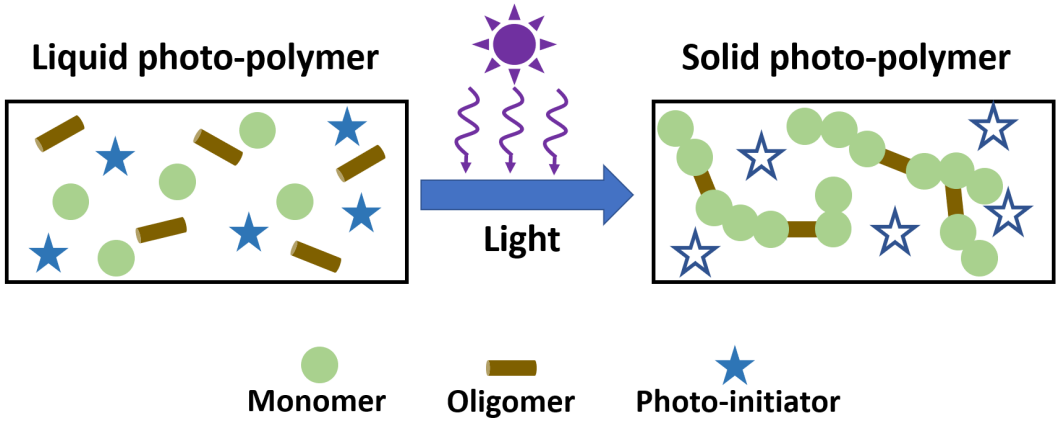

FIGURE 2.3: Schematic showing the process of light-induced photo-polymerization. The liquid pre-polymer which consists of a monomer, an oligomer and a photo-initiator transforms into a solid photo-polymer after being exposed to UV light.

The photo-polymerization process is divided into three major groups: anionic, cationic and free-radical, and based on the type, different photo-initiators are used. In the anionic photo-polymerization, the chain reaction is initiated by photo-generated anions such as ferrocenes [30], whereas in cationic photo-polymerization the cross-linking is accomplished with a photolysis reaction which produces acids [31]. The photo-polymer that we use in our experimental work undergoes a polymerization process which belongs to the third group of free-radical. This reaction begins with the fragmentation of the photo-initiator, upon exposure to light, producing radicals. Next, the radicals combine with the molecules of monomers and oligomers which they link together to form a long chain. This causes a chain reaction which propagates as every time a monomer and/or an oligomer link together, an additional radical will be generated and will help with the bonding of further molecules resulting in the formation of a cross-linked network [32]. The chain reaction finally terminates and the reason for that could be the formation of a highly dense cross-linked network where free-radicals are trapped inside and are unable to combine with other molecules. Another reason for the termination of the reaction is the radical-radical recombination which leads to the formation of non-reactive products or chain transfer, a reaction that increases the mobility of the radicals, reducing their lifetime, hence the rate of polymerization [33]. The result of the photo-polymerization process is depicted in figure 2.3 where the liquid photo-polymer which contains monomers, oligomers and the photo-initiator, becomes solid after the exposure to light.

It is worth mentioning here that apart from light, the polymerization process can be initiated by other stimuli such as voltage [34] and mechanical force [35]. However, using lasers to polymerize materials has some unique advantages over the other methods, such as the high energy output of the lasers and the fast curing speed; two factors that both contribute to significantly reduce the time to cross-link a material to only a few seconds.

2.2.2 Local photo-polymer deposition method

In order to pattern porous substrates such as cellulose paper and NC membrane to create paper-based devices, we used the LDW technique of the local photo-polymer deposition. The key components of this patterning approach are the dispensing system which delivers the photo-polymer on top of the porous substrate and the laser source which is used to polymerize the photo-polymer. We used a PICO® Pμlse™ dispensing system from Nordson EFD, UK which is designed to deposit micro-droplets of 0.5 nL through an orifice with 100 μm diameter at a frequency of 100 Hz. The laser source which is used to polymerize the photo-polymer is a fibre-coupled CW diode laser (Cobolt MLD, Cobolt AB, Sweeden) operating at a wavelength at 405 nm with an output power of 70 mW. Additionally, the numerical aperture of the laser has a value of 0.075,

the beam divergence (full angle, mrad) is <1.1 and the beam quality (M^2) is <1.2. Also, the beam has circular symmetry (>0.9:1) and is non-collimated as we do not use any focusing lens or mirror, therefore the laser beam propagates in free space.

Lastly, as a light-curable material we used an acrylate-based negative photo-polymer namely Desolite® 3471-3-14 from DSM Desotech, Inc., USA. The Desolite photo-polymer is a liquid material with viscosity of 10.000 mPa · s (at 25 °C) and composed of 10-25% multifunctional acrylate, 10-25% glycol ether acrylate, 1-5% photo-initiators, <1% additive and <1% monomer. Additionally, the photo-polymer has a density of 1110 kg · m^{-3}, refractive index of 1.5 and surface tension of 25 dynes · cm^{-1} when measured at a temperature of 23 °C. The Desolite is stored in an opaque (black colour) tube to avoid exposure to ambient light and kept in room temperature and under these conditions has self life of 18 months from the date of manufacture.

Figure 2.4 illustrates a schematic of the local photo-polymer deposition method. First the photo-polymer is locally deposited on top of the porous substrate at locations pre-defined by a computer design. Next, and after leaving sufficient time for the photo-polymer to spread throughout the entire thickness of the porous substrate, the tip of the fibre-coupled laser follows the same pattern over which the photo-polymer has

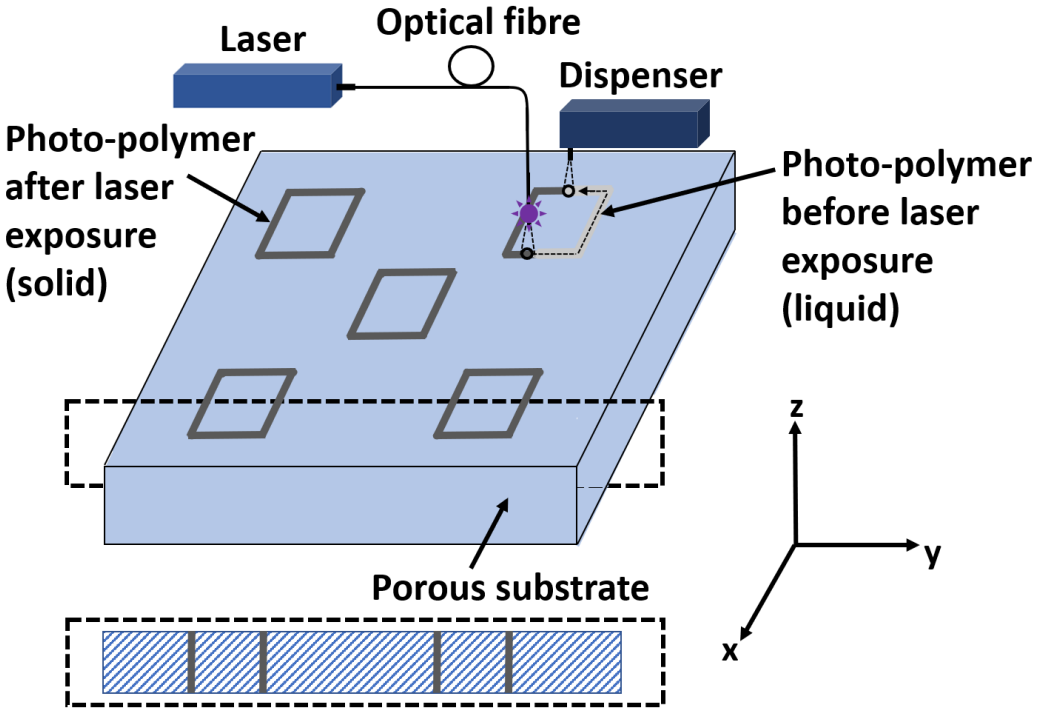

FIGURE 2.4: Schematic of the local photo-polymer deposition setup. The photo-polymer is locally deposited on top of a porous substrate and subsequently exposed to a CW laser source operating at 405 nm to create solid polymeric structures. In the dashed line box, we represent a cross-sectional image of the porous substrate in which the polymerized photo-polymer has extended throughout its thickness.

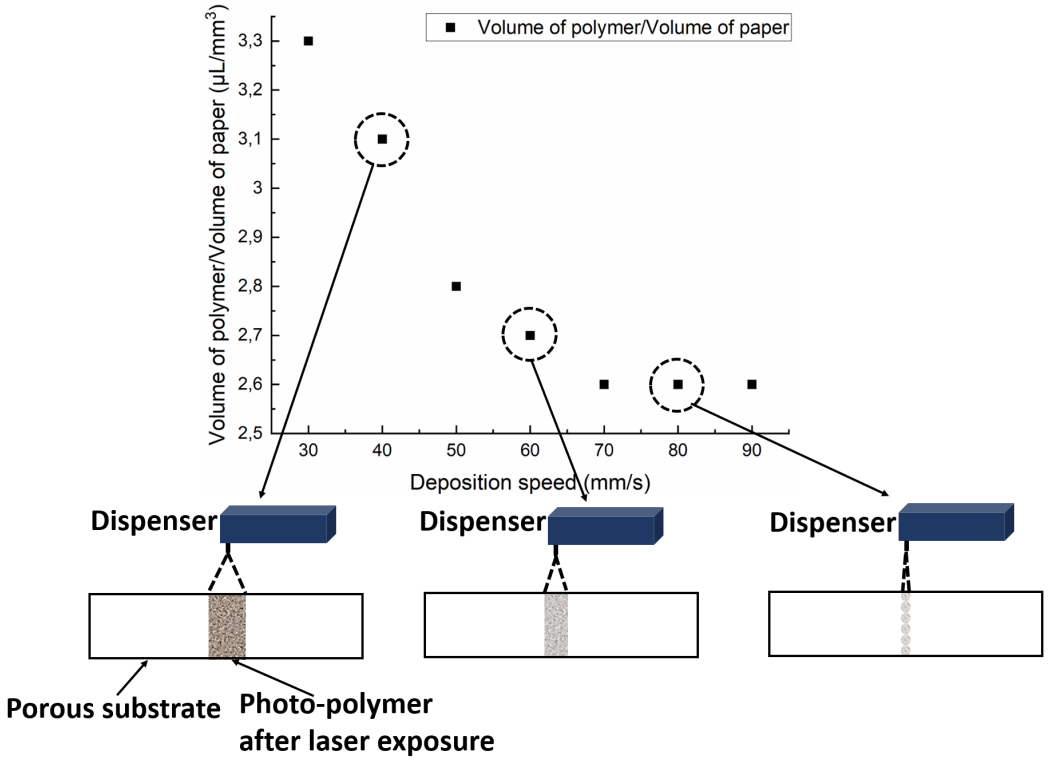

FIGURE 2.5: Schematic showing the volume of the photo-polymer per volume of the paper substrate as a function of the photo-polymer deposition speed. For different photo-polymer deposition speeds (e.g. 40 mm/s, 60 mm/s, 80 mm/s) we present a drawing of the cross-section of the paper impregnated with the photo-polymer following the exposure to the laser source.

been previously deposited. By exposing the photo-polymer to light we induce photo-polymerization leading to the creation of solid polymeric structures. The flexibility of this paper patterning approach allows us to change and adjust accordingly parameters such as the speed in which the dispenser is moving, or similarly the speed in which the photo-polymer is deposited, the speed in which the tip of the laser is moving (laser scanning speed) and also the distance between the laser tip and the substrate. It is important to mention here that the speed in which the dispenser is moving and delivers the photo-polymer on top of the porous substrate dictates the volume of the photo-polymer that is deposited. Figure 2.5 illustrates a schematic of the volume of the photo-polymer per volume of the paper substrate for the different deposition speeds in the range between 30–90 mm/s. In the same figure we also present a drawing of the cross-section of the paper that is impregnated with the photo-polymer when deposited with different speeds following by exposure to the laser source. Details for the calculation of the volume of the photo-polymer per volume of the paper substrate as a function of the deposition speed can be seen in the appendix B.

For the fabrication of paper-based devices, it is very important for the photo-polymer

to penetrate throughout the entire thickness of the porous substrate before its full polymerization (leaving no unpolymerized material) after the laser exposure. This will lead to the creation of solid polymeric structures that extend throughout the paper and are able to guide the flow of liquids. A critical parameter for that is the time required for the photo-polymer to penetrate throughout the thickness of the porous substrate. For that we defined as a time delay the difference in time between the photo-polymer deposition and the laser exposure. It is important to note here that the use of another photo-polymer with a different viscosity and chemical properties or the use of a porous substrate with different thickness, inner structure and fluid flow properties would require a different amount of time to penetrate throughout the porous substrate and consequently a different time delay for its laser exposure.

The spatial resolution of the fabricated devices is defined by the spreading of the photo-polymer. The viscosity of the photo-polymer, the pore size, as well as the porosity of the porous substrate are factors that determine the spreading of the photo-polymer and therefore the minimum producible feature size. Furthermore, the achievable feature size of the devices is also determined by the time delay and most importantly the laser fluence.

Another important parameter for the fabrication of the devices is the laser fluence that we use to expose the photo-polymer in order to fully polymerize it (for its calculation see appendix C). For the calculation of the threshold value of the laser fluence, we created square patterns on an NC membrane. Later and for each square pattern, we polymerized the polymeric lines using different fluences before we deposit 10 µL of a red dye. Although we do not present the results in this thesis, we visually assessed the ability of the square patterns to contain the flow of the sample. It worth mentioning here, that in the case there was unpolymerized material left inside the polymeric lines, we would see a leakage of the sample outside of the square pattern. With this method we determined the least amount of laser fluence required for the photo-polymer to fully polymerize and this has a value of 63 mJ/cm^2. Based on that, we defined a value of the laser fluence of 0.3 J/cm^2, which is higher than the threshold value, in order to ensure fully polymerization of the photo-polymer. Once we defined this value, the laser fluence remained unaltered during the device fabrication work and hence the laser power, the laser scanning speed and the distance between the laser tip and the substrate. Any change in the values of these parameters would lead to an alteration of the incident fluence that defines the photo-polymerization process.

In order to ensure that the fabrication parameters of the photo-polymer deposition speed, the laser scanning speed and the time delay are sufficient to produce solid polymeric structures, we patterned cellulose paper and NC membrane and we assessed the performance of the structures based on their ability to contain the flow of sample. In figure 2.6 we present the results after patterning cellulose paper and NC membrane. We created six square polymeric structures on a single sheet of cellulose paper using

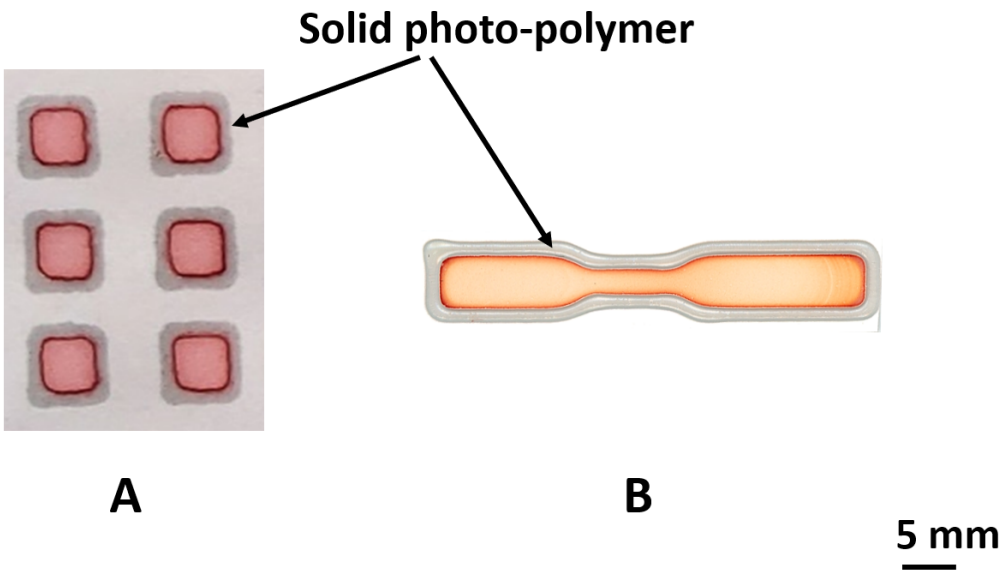

FIGURE 2.6: (A) Six square polymeric structures all fabricated with the same patterning conditions and each with a dimension of 25 mm^2 are created on a single sheet of cellulose paper. (B) Channel fabricated on an NC membrane. Each of the square structures and the channel were tested with 10 µL of a red chemical dye.

the same fabrication parameters for each of them and with dimensions of 25 mm^2 (figure 2.6A). Additionally, we created a channel on an NC membrane (figure 2.6B). The fabrication parameters used for both the patterning of cellulose paper and NC membrane are presented in table 2.1. We used these values to produce lines in both cellulose paper and NC membrane with the same width which was measured at 1 mm. For that the parameters of the photo-polymer deposition speed, the laser scanning speed and the laser fluence have the same value, and we only changed the time delay. As previously mentioned, this is due to the different porosity, thickness and inner structure of the NC membrane compared with those of the cellulose paper.

We tested each of the square structures and the channel with 10 µL of a red chemical dye and we visually evaluated whether there is any leakage of the sample outside of the polymeric structures. As we can clearly see in figure 2.6, the chosen values of the photo-polymer deposition speed, the laser scanning speed, the laser fluence and the time delay are sufficient to fully polymerize the photo-polymer, therefore leaving no unpolymerized material. It is important to mention here that the values presented in table 2.1 are not the minimum values required for the creation of solid polymeric structures on cellulose paper and NC membrane. We did not conduct a detailed study to define those minimum values as this would be out of the scope of this thesis. However, we know that using the presented values, we are able to create solid polymeric structures able to guide the flow of liquids and these fabrication parameters remained unaltered throughout the experimental work presented here.

TABLE 2.1: Parameters used for patterning cellulose paper and NC membrane.

Substrate	Photo-polymer deposition speed (mm/s)	Laser scanning speed (mm/s)	Laser fluence (J/cm^2)	Time delay (s)
Cellulose paper	20	20	0.3	180
NC membrane	20	20	0.3	30

The method of the local photo-polymer deposition is used in our group and reported for applications such as the detection of a single analyte (e.g. Leishmaniasis) [36], but also in multiplexed detection of analytes [37] as well as for bacterial infection testing [38].

2.3 Hydrogels

Hydrogels are water-soluble polymeric materials, which have a 3D structure and an elastic nature (gel-like form) [39]. Due to the presence of hydrophilic groups in their structure, such as hydroxyl OH^-, hydrogels have the ability to absorb large amounts of water or body fluids and this makes them attractive for use in biomedical applications (e.g. tissue engineering and release of proteins and drugs) [40].

Hydrogels can be synthesized by two different methods namely, physical and chemical cross-linking [41]. In physical cross-linking, the formation of a hydrogel does not require the use of a cross-linker, instead the polymer network is formed by using H-bonding [42], by crystallization [43], by ionic interactions [44] and by protein interaction such as the interaction between an antibody (used as the cross-linking agent) and an antigen [45]. On the other hand, the synthesis of chemically cross-linked hydrogels involves methods such as the use of chemical reactions to create linkages between polymer chains that have complementary groups [46], the irradiation with high energy sources such as gamma rays [47] and electron beams [48], the use of enzymes [49] and finally by free radical polymerization.

Compared with other types of biomaterials, hydrogels have some unique mechanical properties such as strength and stability as well as biological properties such as biocompatibility and biodegradability [50]. However, the most important characteristic of hydrogels is the ability to change their volume (swelling) as a response to an external stimulation [51]. There are many factors that affect the swelling of hydrogels and one of them is the cross-linking ratio. In that case, an increased amount of cross-linker added in the hydrogel results in an increase in the cross-linking ratio, thus the structure of the hydrogel becomes tighter and the swelling ratio decreases. Another factor that influences the swelling of hydrogels is the chemical structure of the polymer and specifically the presence of hydrophilic groups in their structures which leads to an

increase in the swelling ratio as compared with hydrogels that contain hydrophobic groups. Lastly, hydrogels can swell as a response to an environmental stimulation such as a change in the temperature or the pH [52].

Among the different stimuli, light is particularly interesting, due to the fact that it can activate and change the properties of the hydrogels in a controllable way as light can be guided and delivered at the location of choice at a desired time. For that reason, photo-responsive hydrogels are used extensively, especially in the biomedical field [53] for applications such as the release of proteins [54]. The light-induced reaction of photo-responsive hydrogels is divided into three categories namely: photocleavage, photodimerization and photoisomerization. The method of photocleavage is based on the break of the polymer network and the change in the chemical properties of interacting molecules [55], whereas the method of photodimerization includes dimers (oligomers consisting of two monomers) such as coumarin which are used as cross-linkers [56]. The photo reaction of the hydrogels that we report in chapter 7.3 is based on the third category of photoisomerization, where polymers can be synthesized with different functional groups such as azo-benzene [57], stilbene [58] and spiropyran [59]. The most important characteristic of this type of reaction, is that upon exposure to UV light, these functional groups undergo a chemical process in which they change into a different form with the same composition but different structure. The photoisomerization process is both reversible, which means that after exposing these functional groups to visible light they transform back to their initial form and also repeatable as this process can happen multiple times.

2.3.1 Photo-responsive hydrogels

In order to synthesize polymeric materials (hydrogels) with photo-responsive moieties which show a reversible volume change when exposed to light of a specific wavelength, we used azo-benzene and spiropyran functional polymers. These polymers show isomerization [60] when they are exposed to light and this results in a change in their physical properties such as their hydrophobicity. The spiropyran [61] is an organic compound known for its photochromic properties since 1952 [62], and this is associated with its reversible transformation between two different forms namely an opened-ring isomer and a closed-ring isomer after irradiation by light. In figure 2.7A the structural formula of the closed-ring isomer of spiropyran is represented as SP. After irradiation of the spiropyran to the UV light (365 nm), the closed-ring isomer transforms into the open ring isomer merocyanine, which is labelled as MC in the schematic of figure 2.7A. The merocyanine to spiropyran reverse isomerization usually occurs spontaneously, but it can be accelerated after visible light illumination, which in our case is a light-emitting

diode (LED) blue light source operating at 470 nm. Spiropyran and merocyanine isomers have very different physiochemical properties with the most important one being that merocyanine is hydrophilic, whereas spiropyran is hydrophobic.

The reversible isomerization of spiropyran can also be triggered by several other independent stimuli such as temperature, pH, solvent polarity, metal ions and even mechanical force [63]. For example, treating spiropyran with acids (e.g. acrylic acid) can induce ring opening (represented as MCH^+ in figure 2.7B) even in the absence of any UV irradiation because of the high affinity of the open-ring form to H^+. Under acidic conditions, spiropyran represents the metastable state, which can exist only if the system is exposed to visible light. This property is referred to as negative photochromism and is very important for the hydrogel-based materials, which exhibit volume shrinkage under the exposure to the blue light source (470 nm) as shown in figure 2.7C).

This property of spiropyran has been extensively studied [64, 65, 66] with the use of cross-linked spiropyran incorporated N-isopropylacrylamide (NIPAM) hydrogels as materials of light actuated microvalves for microfluidic devices. For example, a method

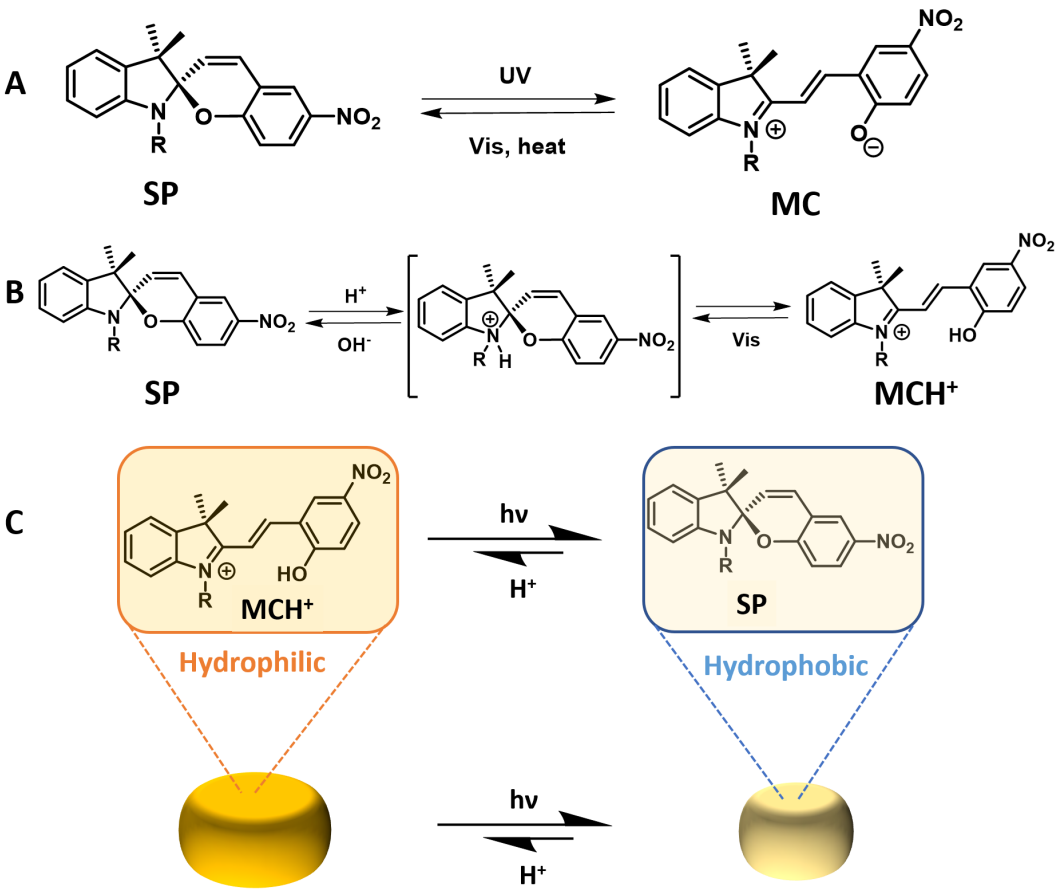

FIGURE 2.7: Schematics showing (A) the photo-isomerization and (B) the acid-isomerization of spiropyran. (C) Schematic representation of the volume shrinkage of spiropyran-based hydrogels after exposure to the blue light source (470 nm).

is reported [67] for the fabrication of nanogels by photo-polymerization at the desired positions in a microchannel. The illumination of the hydorgels with blue light (440 nm) induced their shrinkage and resulted in the opening of the microvalves. In this system, they needed to expose the hydrogels to an acidic aqueous solution to generate the swollen gel (i.e. conversion of the SP to MCH^+ form). Blue light irradiation triggered the closure of the ring and caused dehydration of the gels (shrinkage) because of the change of the properties of the hydrogel from hydrophilic to hydrophobic. However, the need for an acidic environment is a drawback since neutral pH is frequently required in biological applications.

A pioneering work was later reported [68] that solved the previously mentioned problem by incorporating acrylic acid into the structure of a hydrogel, to provide an internal source of protons (H^+). In order to synthesize the hydrogel, they used NIPAM (a water soluble monomer) which was mixed with N,N'-methylenebisacrylamide (MBIS) (cross-linker), spiropyran and acrylic acid. In this study it is reported that the acidity constant (pK_a) values of MCH^+ is between 6-7, of spiropyran at 2.3 and that of acrylic acid at 4.2. When NIPAM hydrogel incorporates spiropyran in the polymer backbone and considering these values and the fact that the lower the pK_a value, the stronger the acid therefore the greater its ability to donate protons, we conclude that, in the absence of light, acrylic acid will spontaneously protonate merocyanine to MCH^+. Hence the hydrogel will increase its hydrophilicity and begin to swell due to water intake. Conversely, when the hydrogel is exposed to a white light source the MCH^+ is deprotonated and the protons travel back to the acrylic acid, thus the spiropyran transforms to its closed-ring form. As a result, the hydrogel becomes hydrophobic and the water is expelled leading to its shrinkage. The significance of this work stems from the fact that the protonation and deprotonation occurs internally within the hydrogel and there is no need for an external source of protons. Furthermore, the shrinkage-swelling cycles of this hydrogel in distilled (DI) water is repeatable, as protonation throughout the gel does not rely on movement of protons from an external acidic solution into the hydrogel.

The previously described work has been adopted by many research groups which used acrylic acid incorporated spiropyran contained NIPAM hydrogels as photo-responsive valves in microfluidic devices [69, 70, 71, 72]. When these hydrogels are used as valves in microfuidic devices, they observed that there is no flow when there is no light, whereas when the valve was locally illuminated using a blue LED light source, flow was observed in the channel within a few seconds. When the light was turned off, the flow of the sample was reduced and then stopped. The promising results of the previously reported methods that used hydorgels as photo-responsive valves in microfluidic devices, inspired us to adapt acrylic acid and spiropyran incorporated NIPAM hydrogel systems in our paper-based devices to control the flow of samples. The synthesis of this hydrogel system has a number of advantages such as the fact that all the materials

(except the spiropyran) are commercially available, just 1% of the spiropyran moiety in the hydrogel is enough to obtain light responsive behaviour and also there is no need to use any toxic organic solvent during the process of synthesis.

Chapter 3

In-line filtration process in paper-based devices

3.1 Introduction

To date, there have been many reported techniques for the filtration of nanoparticles [1]. These methods take advantage of the intrinsic properties of the particles such as their size, density [2], their electric [3] as well as magnetic properties [4]. Common filtration approaches are centrifugation, where particles are separated based on their size [5], and gel electrophoresis where particles are separated based on their size, shape and charge [6]. However, these methods are expensive and require special equipment and multiple steps to operate which is an impediment for the implementation of these techniques for sample preparation. For that reason, the research community widely uses microfluidics for nanoparticle separation. The size of these devices offers the capability to reduce the sample volume and provide real-time control of the separation by changing parameters such as buffer solution and external field. Most importantly, it is a low cost approach that allows the segregation of nanoparticles where it can be used in clinical diagnostics.

In the field of microfluidics, the methods for the separation of particles are divided into two major groups, namely active and passive separation. In the first group, the separation of particles depends on an external field and typical examples are optical manipulation [7], magnetophoresis [8] and acoustophoresis [9]. On the other hand, passive separation of particles does not require any external forces and the mechanism of separation relies solely on the properties of the microfluidic device such as the hydrodynamic and the surface forces. An indicative example of this method includes deterministic lateral displacement where structures of pillars and arrays filter particles creating a flow streamline with application in the separation of blood cells [10] and bacteria [11]. Another method is the filtration technique using nanosized porous membranes to separate particles based on their size. In this approach [12], they have developed a method for

the separation of polystyrene beads using a porous polymer monolith membrane with pressure driven flow. The fabrication of a sized-based three-dimensional filter is another suggested method, where micrometre-sized pores are used for the separation of 3 µm beads from rhodamine in a commercial microfluidic chip [13].

Our proposed filtration method belongs to the second group of passive separation and is based on the local deposition of a photo-polymer on top of a porous paper substrate before its exposure to a laser source. By changing the speed at which the photo-polymer is delivered on the porous substrate, we are able to create porous in-line barriers able to either block or enable the flow of particles based on their size. This size-exclusive filtration method was tested for the separation of the various constituents of a complex sample within a flow-path and also for the separation of plasma from whole human blood. The role of plasma is very important and is used in clinical tests for the detection of diseases such as cancer [14], Alzheimer [15] and sepsis [16]. However it needs to be separated from the red blood cells (RBCs) due to the fact that cell inclusion and lysis interfere with readouts for colorimetric assays disrupting the detection of biomarkers [17]. Common filtration methods used for the separation of plasma from whole blood include the use of a centrifuge, electrochemical paper-based devices [18] or even the use of a pipette [19]. However these methods can be either expensive or require the use of external equipment to operate, which are factors that prohibit the use of such devices for mass manufacture and use in point-of-care (POC).

Last, but not least, our reported fabrication method can be used to increase the sensitivity of lateral flow assays (LFAs). Enhancing the signal of LFAs is a highly desired feature which improves their performance and enables their extensive use as diagnostic tools. There are many reported methods used to increase the sensitivity in LFAs such as the use of a silver enhancement technique [20], magnetic nanoparticles [21] or the modification in the structure of the LFAs. In the last category there are methods to increase the sensitivity of assays either by changing the size of the sample and the conjugate pads [22], by applying constrictions in the channel of an LFA [23] or by using a wax printing technique [24]. In the latter case, hydrophobic pillars, which are used as barriers, are located in the channel of a nitrocellulose (NC) membrane and delay the flow of the sample, therefore increase the incubation time between the analyte and the conjugate resulting in an increase in the intensity of the signal on the test line. Similar to that method we are using in-line barriers as porous filters to delay the flow of the sample at the area of the test line and increase the sensitivity in the detection of a common inflammation marker namely C-reactive protein (CRP).

3.2 Experimental section

3.2.1 Experimental setup and materials

The material used to make in-line filters was a Unisart CN 95 NC membrane acquired from Sartorius Stedim Biotech GmbH, Germany with thickness 140–170 µm, pore size of 15 µm and capillary flow speed of 90–135 s/40mm. An absorbent pad (Whatman^{TM} CF4) acquired from GE Healthcare with thickness of 480 µm was placed at the end of the LFAs to absorb the excess sample that reaches the end of the flow channel.

For the characterization of the in-line filters we used three different samples namely, a water-based solution of different coloured dyes as well as water-based suspensions of different sized gold nanoparticles (Au NPs) and latex microbeads. In order to study the flow properties of the in-line barriers, we used three dyes, each one with a different colour, namely allura red AC (red colour), tartrazine (yellow colour) and fast green FCF (green colour). The dyes were acquired from Sigma-Aldrich and each one was diluted in distilled (DI) water to have a concentration of 0.5 mg/mL. We later used different sized Au NPs and latex microbeads to study the filtration properties of the variable-porosity in-line barriers. The Au NPs were obtained from BBI Solutions, UK and have sizes of 40 nm (density 9.0×10^{10} particles/mL), 100 nm (density 5.6×10^{9} particles/mL) and 200 nm (density 7.0×10^{8} particles/mL). Two different sized latex microbeads, acquired from Polysciences, Inc., USA, were tested and have sizes of 200 nm (density 5.7×10^{11} particles/mL) and 1000 nm (density 4.5×10^{9} particles/mL).

To highlight the applicability of the in-line filters we tested them for two different applications: the separation of plasma from whole blood and the increase in the sensitivity of an assay designed for the detection of the common inflammation marker CRP. In our first demonstration we used human blood as a sample which was acquired from a healthy patient at the Southampton General Hospital and belongs to the blood group A with RhD positive (A+). The donated blood was stored in a green-top tube which contains sodium heparin as an anticoagulant to prevent the blood from clotting. The tube was inverted several times immediately after the collection of the blood, and all the experiments were conducted within 2 hours after the time of collection to prevent blood coagulation.

In our next experiment, we tested the in-line filters with human CRP (used as the analyte) acquired from Sigma-Aldrich with stock concentration of 1 mg/mL and diluted in PBS to have a concentration of 50 ng/mL. For the preparation of the conjugate we mixed in 1:2 ratio mouse CRP biotinylated antibodies (with stock concentration of 50 µg/mL) diluted in 1:10 ratio in PBS and 40 nm streptavidin Au NPs (optical density 10) diluted in 1:15 ratio in PBS. Last but not least, in the channels of the LFAs we dispensed and immobilized at the test line CRP capture antibodies with stock concentration of 1 mg/mL and at the control line a mouse IgG antibody with stock concentration

of 500 µg/mL. After the printing of the test and the control lines, the LFAs were left overnight to dry before testing of the sample.

3.2.2 Fabrication method and procedure

For the fabrication of the fluidic devices within the porous NC membrane we formed solid polymeric structures (walls) that extend through the entire thickness of the porous substrate and demarcate the boundaries of the fluidic device. The values of the photo-polymer deposition speed, the laser scanning speed, the laser fluence as well as the time delay used for the fabrication of the solid walls are shown in table 2.1. The same patterning method was used for the fabrication of the variable porosity in-line barriers used for the filtration of different size particles which are positioned at 90° to the direction of the sample flow. Figure 3.1 shows a schematic of a flow channel on an NC membrane with an incorporated porous in-line barrier. The time delay for the fabrication of solid walls was set at 30 s. This waiting time is sufficient for the photo-polymer to spread throughout the entire thickness of the NC membrane and this is evident by the fact that the polymer has spread laterally to have a width of 1 mm. This value is larger than the thickness of the NC membrane and because of that we are certain that the photo-polymer has completely penetrated throughout the entire thickness of the substrate. Additionally, in all the performed experiments, we did not observe any side leakage of the sample outside of the solid walls which would have been the case if the photo-polymer had not extended throughout the entire thickness of the NC membrane.

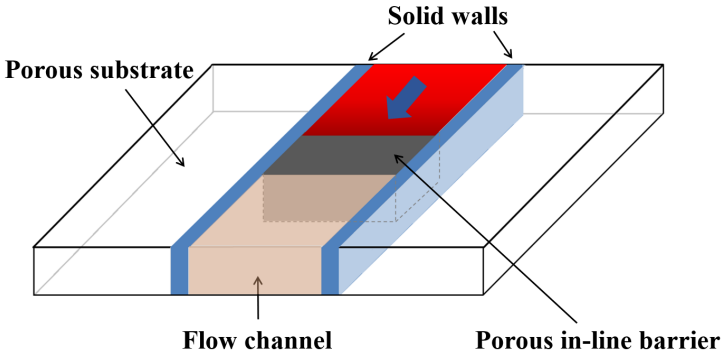

FIGURE 3.1: Schematic of a flow channel with solid walls fabricated on a porous NC membrane with an in-line porous barrier positioned 90° to the direction of the fluid flow.

For the fabrication of the porous in-line barriers we set the value for the time delay again at 30 s to ensure that the photo-polymer has extended throughout the entire thickness of the NC membrane. If that was not the case and the photo-polymer had not extended entirely throughout the substrate, then the sample would have flowed under the barrier and this would negate the functionality of the in-line barrier for the purpose of this experiment.

In order to create in-line barriers in an NC membrane, we used our LDW method where by controlling the local deposition speed of the photo-polymer we are able to fabricate polymeric structures with variable levels of porosity. Any change in the deposition speed of the photo-polymer translates into a change in the volume of the photo-polymer that is deposited per unit volume of the paper, hence by controlling the volume we are able to create in-line barriers with different levels of permeability. With this method we are able to create both solid walls and barriers porous to any fluid flow by simply changing the photo-polymer deposition speed. For a porous in-line barrier the volume of the photo-polymer is not sufficient to completely block the pores of the NC membrane. Instead, it partially fills the pores of the substrate and acts as a porous mesh reducing the pore size of the NC membrane and therefore acts as a filter for the fluids passing through it. On the other hand, for the denser walls of the channel, the volume of the photo-polymer is sufficient to completely block the pores of the substrate which become impermeable to the flow of liquids, therefore preventing any leakage outside of the boundary walls of the fluidic device.

We patterned the variable porosity in-line barrier by changing the deposition speed of the photo-polymer within the range between 30 mm/s and 60 mm/s. As mentioned earlier, a change in the deposition speed of the photo-polymer is associated with a change in the volume of the photo-polymer that is being deposited. For the deposition speeds that we use to pattern the in-line barrier, the volume of the dispensed photo-polymer per volume of paper ranges between 2.7–3.3 $\mu L/mm^3$ (see appendix B). In both the fabrication of the solid walls of the channel and the variable porosity in-line barrier, the laser fluence was always sufficient to completely polymerize all the deposited photo-polymer.

3.3 Results and discussion

3.3.1 Characteristic study of in-line barriers in NC membrane

In our first demonstration, we studied the effect that the in-line barriers have in the flow of a water-based sample. For the purpose of this experiment, we tested fluidic devices with an incorporated in-line barrier, with three different coloured dyes in order to find the exact photo-polymer deposition conditions that would allow the in-line barrier to

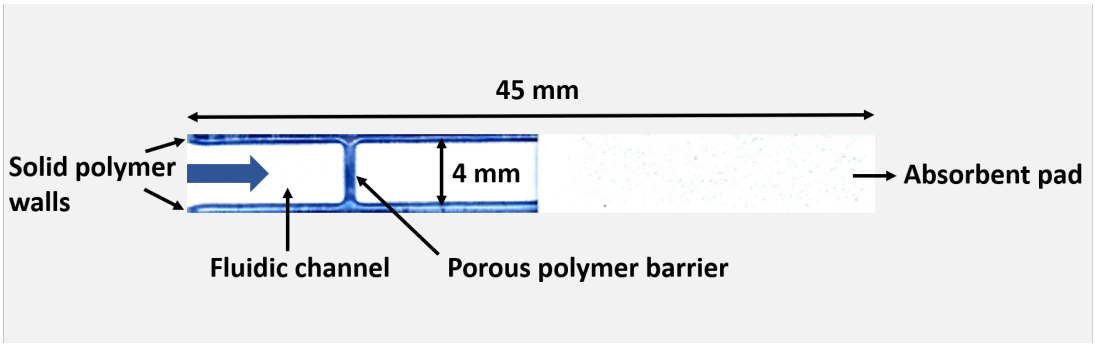

FIGURE 3.2: Image of a laser-patterned fluidic device used to study the filtering capabilities of a porous in-line polymer barrier. The blue arrow in the image indicates the direction of the sample flow from the inlet point and towards the position of the in-line barrier. The part of the sample that moves past the porous barrier accumulates in the absorbent pad located at the end of the fluidic channel.

transfer from being completely impermeable to being porous to the flow of the sample. We therefore fabricated a set of five devices each of which with a single in-line barrier located at the same position. The solid polymer walls of the fluidic channels were fabricated under the same patterning conditions whereas, for the in-line barriers we used different deposition line-speeds. Figure 3.2 shows an image of a fluidic device designed to have a width of 4 mm, which is the size commonly used in standard LFAs. The length of the fluidic channel was set at 23 mm and the in-line barrier is positioned at a distance of 10 mm from the inlet (bottom end) of the fluidic channel, where the sample is introduced. An absorbent pad is placed at the end of the fluidic channel to remove the excess liquid that moves past the in-line barrier. During the experimental process, we dipped each of the devices in the sample and only removed them after the end of the test to take photos of the devices. Our choice to use a coloured dye stems from the fact that it not only provides an aid to visualize the progression of the aqueous solution along the fluidic channel, but also assists to identify whether the barrier is porous or not to the flow of the sample.

Figure 3.3 illustrates the results after testing 20 µL of sample on fluidic devices with an in-line barrier fabricated with volumes of photo-polymer per volumes of paper in the range between 3.26–2.83 $\mu L/mm^3$. As we can clearly see, for volumes of photo-polymer per volumes of paper of 3.18 $\mu L/mm^3$ and below the in-line barrier is impermeable to the flow of the green dye solution, hence there is no flow of the sample beyond the position of the barrier. However, for volumes of photo-polymer per volumes of paper greater than 3.18 $\mu L/mm^3$ the barrier becomes porous and therefore permits the flow of the sample through it and towards the absorbent pad. Apart from using the green dye, we also tested two more aqueous solutions namely a yellow and a red dye, to study the porosity of the in-line barriers with different samples. For this experiment we used again the same volume of sample (20 µL) and the results are depicted in figure 3.4. We observe that for the flow of different samples the in-line barrier becomes porous at different volumes of photo-polymer per volumes of paper due to the different size of

particles that constitute the dyes. Specifically, an in-line barrier printed with volume of photo-polymer per volume of paper at 3.00 µL/mm^3 is only porous to the flow of a red dye, whereas the yellow dye can flow through in-line barriers fabricated with volume of photo-polymer per volume of paper at 2.88 µL/mm^3 and above.

In table 3.1, we present all the results after fabricating a set of five fluidic devices with

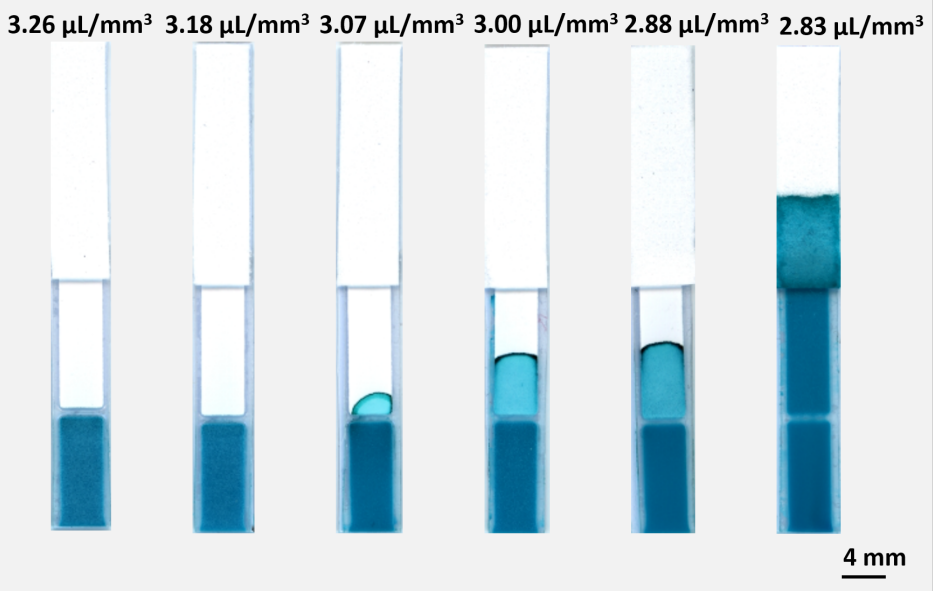

FIGURE 3.3: Images of fluidic devices showing the flow of a green dye through a fluidic channel with an incorporated in-line barrier created with various volumes of photo-polymer per volumes of paper in the range between 3.26–2.83 µL/mm^3. The in-line barrier can be designed to either completely block or enable the flow of the sample through it.

TABLE 3.1: Table of results after fabricating a set of five fluidic devices with an incorporated in-line barrier and testing with three different coloured dyes. The in-line barriers were fabricated with volumes of photo-polymer per volumes of paper in the range between 3.34–2.88 µL/mm^3. We have marked with red the range for the volume of photo-polymer per volume of paper in which the in-line barriers transition from being completely impermeable to being porous to the flow of samples.

Volume photo-polymer per volume paper (uL/mm^3)	Green dye	Yellow dye	Red dye
3.34	1/5	0/5	0/5
3.33	0/5	0/5	0/5
3.26	**0/5**	0/5	0/5
3.19	**1/5**	0/5	0/5
3.18	**2/5**	0/5	0/5
3.11	**5/5**	0/5	0/5
3.07	5/5	1/5	0/5
3.03	5/5	0/5	**0/5**
3.00	5/5	**0/5**	**5/5**
2.94	5/5	**1/5**	5/5
2.88	5/5	**5/5**	5/5

an incorporated in-line barrier printed with volume of photo-polymer per volume of paper in the range between 2.88–3.34 $\mu L/mm^3$ and tested with different coloured dyes. Looking at these results we observe that there is a range marked in red in which the in-line barriers transition from being completely impermeable to being porous to the flow of the different samples. This transitional range could be the result of minor variabilities in the pore size in different regions of the NC membrane and between batches, variations in the composition of the membrane (e.g. surfactant coverage) or the levels of humidity which affect the penetration and the wetting of the photo-polymer. Additionally, the variability in the photo-polymer deposition and most importantly the size of the particles constituting the chemical dyes are two factors that contribute to the transition range.

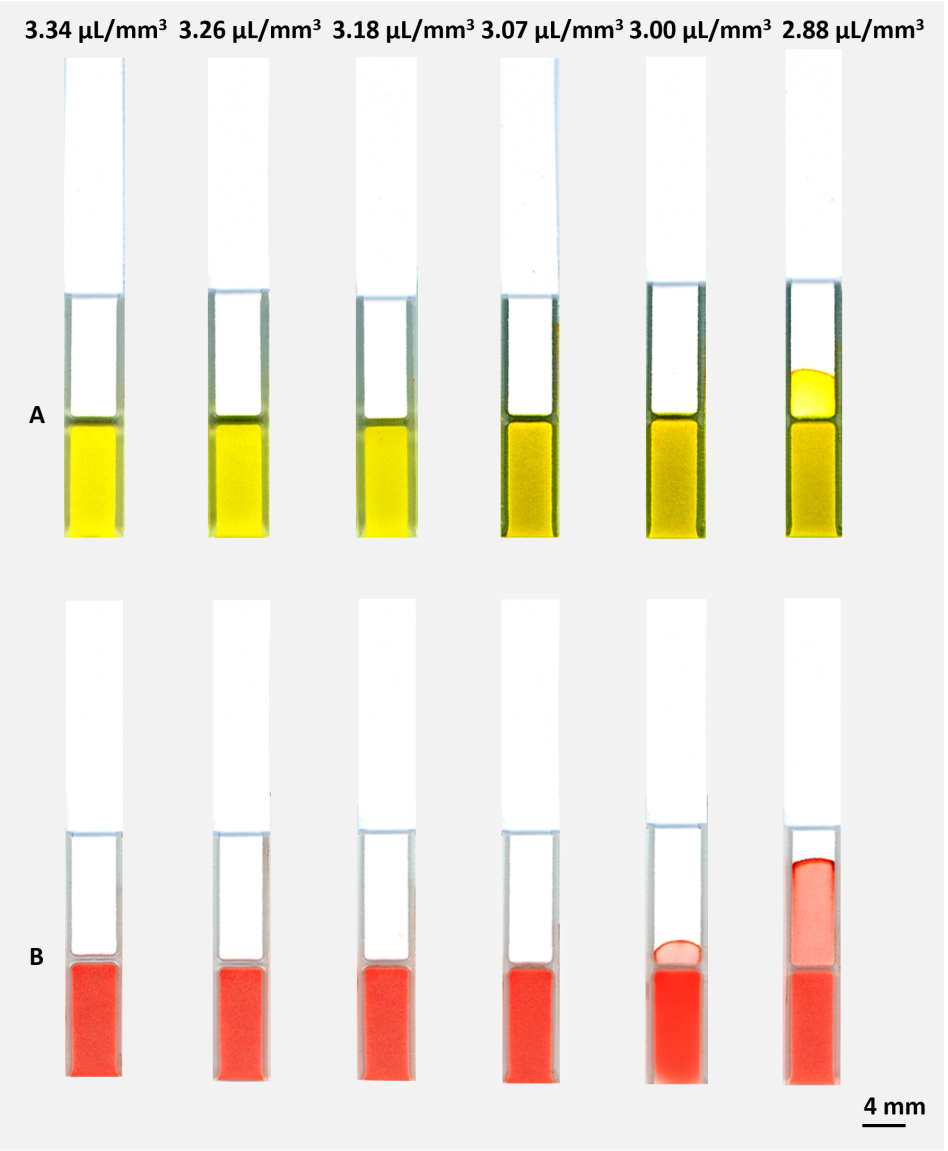

FIGURE 3.4: Images of fluidic devices tested with (A) a yellow and (B) a red chemical dye. Numbers indicate the volumes of the photo-polymer per volumes of the NC membrane to form in-line barriers with variable porosities.

This experimental work was successful in finding that the in-line barriers can be porous to the flow of different samples and that the porosity of the in-line barriers can change according to the deposition speed of the photo-polymer. However, the undefined particle size of the water-based solutions of the chemical dyes that we tested, prevent us from the characterization of the porosity of the in-line barriers. For that reason, in the following subsection we tested the fluidic devices with two different samples namely Au NPs and latex microbeads, both with well defined particle sizes with minimal variations.

3.3.2 Filtering of different sized Au NPs

In this subsection we tested fluidic devices with in-line barriers of different porosities using a water-based suspension of Au NPs with sizes of 40 nm, 100 nm and 200 nm. Our choice to use Au NPs is based on their extensive use as coloured labels that tag detection antibodies to the test line of a lateral flow test. Au NPs have the potential for biomolecule adsorption on surfaces, and due to the strong absorbance of light and the presence of a plasmon absorption band, they provide a bright coloured contrast (when collected on the test line) against the white paper substrate, which makes them ideal for use in diagnostic assays for the colorimetric detection of biomarkers. Apart from the significance of using Au NPs to the operation of diagnostic assays, these particles have well defined size with 8% coefficient of variance (CV). This value corresponds to the variation in the size of particles and is given by equation 3.1, where (SD) corresponds to the standard deviation and (d) corresponds to the diameter of the particles. The small variation in the size of Au NPs provides a pathway for the precise characterization of the different porosity in-line barriers.

$$\mathrm{CV}\ (\%) = \left(\frac{\mathrm{SD}}{\mathrm{d}}\right) \times 100 \tag{3.1}$$

After studying the photo-polymer deposition speed that allows for the creation of porous barriers, we then used these as a starting point for exploring the deposition parameters that would produce in-line barriers able to completely block or allow the flow of different size Au NPs. In this experimental work we fabricated a set of five fluidic devices, with the same geometry as previously presented in figure 3.2 and an incorporated in-line barrier deposited with volumes of photo-polymer per volumes of paper in the range between 3.34–2.77 $\mu L/mm^3$. Each of the devices was dipped in 20 µL of the Au NPs solution (stock density) and was only removed after the end of the experiment to take photos as presented in figure 3.5. For each of the different photo-polymer deposition speeds that we used to fabricate the in-line barriers, we calculated the parameters of the volume of the photo-polymer, the area over which the photo-polymer is

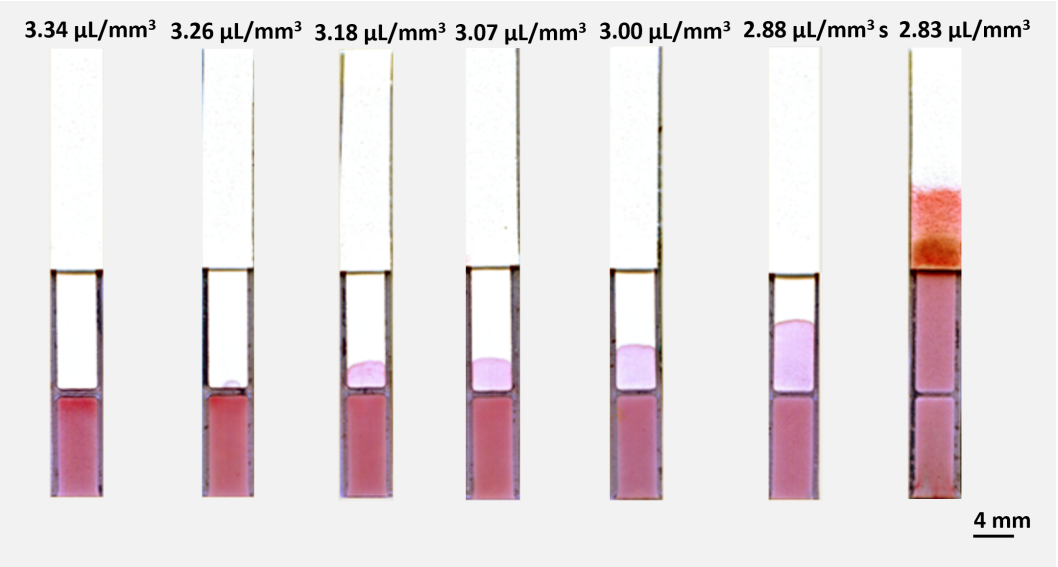

FIGURE 3.5: Images showing the flow of 40 nm Au NPs through fluidic devices each of which had an in-line barrier fabricated with volume of photo-polymer per volume of paper in the range between 3.34–2.83 µL/mm^3. The different porosity in-line barriers are able to either complete block or enable the flow of particles of a specific size.

deposited as well as the volume of the photo-polymer per volume of the paper (D) and the results are presented in table 3.2.

From the results of figure 3.5 we can see that the in-line barrier becomes porous to the flow of 40 nm Au NPs only at volumes of photo-polymer per volumes of paper

TABLE 3.2: Table of results presenting the volume of the photo-polymer, the area over which the photo-polymer is deposited as well as the volume of the photo-polymer per volume of the paper (D) for the different photo-polymer deposition speeds in the range between 30–60 mm/s.

Deposition line-speed (mm/s)	Photo-polymer volume (uL)	Area (mm^2)	D (uL/mm^3)
30	24.4	70.0	3.34
32	23.0	65.7	3.33
34	21.6	62.8	3.26
36	20.4	60.9	3.19
38	19.4	58.1	3.18
40	18.4	56.2	3.11
42	17.5	54.3	3.07
44	16.7	52.4	3.03
46	15.9	50.4	3.00
48	15.3	49.5	2.94
50	14.7	48.5	2.88
52	14.1	46.6	2.87
54	13.6	45.7	2.83
56	13.1	43.8	2.80
60	12.2	41.9	2.77

greater than 3.26 µL/mm^3. For volumes lower than the value of 3.26 µL/mm^3 the in-line barrier is impermeable and therefore blocks the flow of particles of that size. This can be easily understood by looking the results in table 3.2 in which a decrease in the deposition speed of the photo-polymer results to an increase in the volume of the photo-polymer that is being deposited per volume of the paper. As a result, for deposition speeds lower than 34 mm/s the volume of the photo-polymer is sufficient to completely block the pores of the paper, therefore create an in-line barrier capable of preventing the flow of particles with size of 40 nm. For a comparative analysis of the collected data, we have defined a threshold volume of photo-polymer per volume of paper that permits the flow of a particle of a specific size. In table 3.3 we present the results when devices with an incorporated in-line barrier fabricated with volume of photo-polymer per volume of paper in the range between 3.34–2.77 µL/mm^3 were repeated five times and tested with Au NPs of size at 40 nm, 100 nm and 200 nm.

Similar to the devices tested with the chemical dyes, there is a volume per volume range, marked with red in table 3.3, for which the in-line barriers transition from being impermeable to being partially permeable and then completely porous to the flow of the different sized Au NPs. For each of the different Au NPs we defined a threshold volume per volume as presented in table 3.4, at which more than 60% (3/5) of the in-line barriers are porous to the flow of particles of that size. Taking both table 3.3 and 3.4

TABLE 3.3: Table of results of the different size Au NPs tested in fluidic devices with in-line barriers fabricated with volumes of photo-polymer per volumes of paper in the range between 3.34–2.77 µL/mm^3. For each of the different porosity barriers, a set of five devices were tested and numbers indicate the devices in which the in-line barriers are porous to the flow of sample. In red we have marked the volume per volume range at which a barrier transitions from being impermeable to being partially permeable and then porous to the flow of sample.

Volume photo-polymer per volume paper (uL/mm^3)	40 nm	100 nm	200 nm
3.34	0/5	0/5	0/5
3.33	**0/5**	**0/5**	0/5
3.26	**3/5**	**2/5**	0/5
3.19	**5/5**	**5/5**	**0/5**
3.18	5/5	5/5	**2/5**
3.11	5/5	5/5	**0/5**
3.07	5/5	5/5	**5/5**
3.03	5/5	5/5	5/5
3.00	5/5	5/5	5/5
2.94	5/5	5/5	5/5
2.88	5/5	5/5	5/5
2.87	5/5	5/5	5/5
2.83	5/5	5/5	4/5
2.80	5/5	5/5	5/5
2.77	5/5	5/5	5/5

TABLE 3.4: Threshold volume of photo-polymer per volume of paper for the creation of in-line barriers that allow the flow of different size Au NPs.

Au NPs size (nm)	Threshold volume photo-polymer per volume paper (uL/mm^3)
40	3.26
100	3.19
200	3.07

into consideration, we observe that despite the overlap in the volume per volume range there is a decreasing trend in terms of the threshold volume per volume that allows the flow of particles increasing in size. This trend is easily understood by the fact that a lower volume of photo-polymer per volume of paper results in a more porous in-line barrier as the deposited photo-polymer, per unit of length, will leave larger unfilled voids in the porous mesh, hence allowing the flow of larger size particles.

There are numerous factors affecting the threshold volume per volume such as the pore size, the porosity of the NC membrane and its uniformity. Those parameters as well as the nature of the porous materials are critical and affect the way that the photo-polymer penetrates the substrate and creates the porous in-line barriers. Additionally, the inner structure of the porous material and variations from batch to batch are two important factors influencing the threshold speed either to higher or lower values.

Despite the fact that the in-line barriers can be designed to become porous to the flow of different size particles, for volumes of photo-polymer per volumes of paper in the range between 3.26–2.87 $\mu L/mm^3$ only a certain percentage of the sample is able to flow through the barrier whereas the rest accumulates just before it. This is the result of the finite porosity of the in-line barriers which delay the penetration of the sample through it and consequently the DI water evaporates over time and prevent any further flow of the sample through the in-line barrier. In order to assess the performance of the different porosity in-line barriers, we measured the particle filtration efficiency (PFE) which is a measure of the amount (%) of the Au NPs that move past the barrier. In graph 3.6 we present the results after testing different size Au NPs (40 nm, 100 nm and 200 nm). We observe that for the in-line barriers a decrease in the volume of the photo-polymer that is being deposited per unit volume of the paper translates into an increase in the amount of the sample that flows through it, and this is explained by the fact that the porosity of the barrier has increased.

In order to analyse the collected data and extract the values for the particle filtration efficiency, we used the RGB channel in the histogram function of Adobe Photoshop. Using this program we measured the mean intensity value of the pixels of the area into which the sample has spread, both above and below the position of the in-line barriers. These values were subtracted from 255, which corresponds to the pixel intensity of the background (white), in order to obtain the actual colour intensity values. Additionally, we measured the total number of pixels, of the area covered by the sample, both below

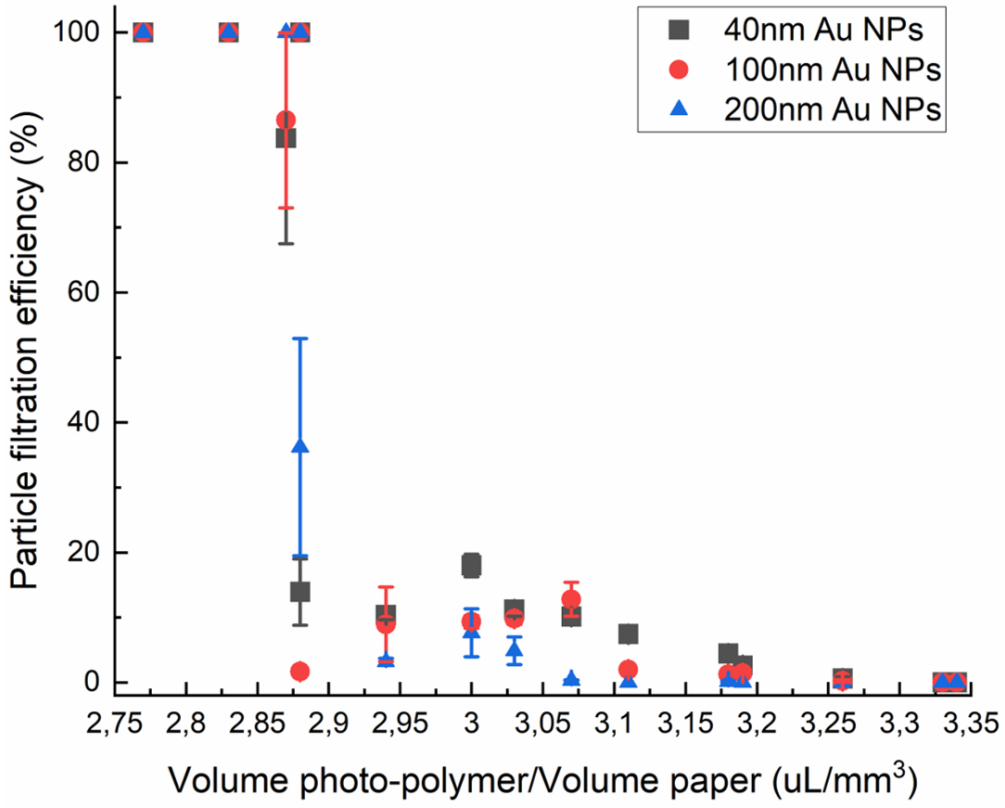

FIGURE 3.6: Particle filtration efficiency of the in-line barriers fabricated after depositing different volumes of the photo-polymer per unit volume of the paper. The in-line filters were tested with Au NPs of sizes: 40 nm, 100 nm and 200 nm.

(d_{below}) and above (d_{above}) the position of the in-line barrier and using equation 3.2 we were able to measure the sample quantity that flows through the in-line barriers.

$$\text{PFE (\%)} = \left(\frac{255 - \text{Colour intensity above the barrier}}{255 - \text{Colour intensity below the barrier}}\right) \times \left(\frac{d_{above}}{d_{below}}\right) \times 100 \qquad (3.2)$$

3.3.3 Filtering of different sized latex microbeads

In order to further explore the capability of the in-line barriers to either block or allow the flow of particles of a specific size, this time we tested a water-based suspension of latex microbeads with sizes of 200 nm and 1000 nm. We tested 20 µL of sample on fluidic devices with the same geometry as the one presented in figure 3.2 and an incorporated in-line barrier fabricated at volumes of photo-polymer per volumes of paper

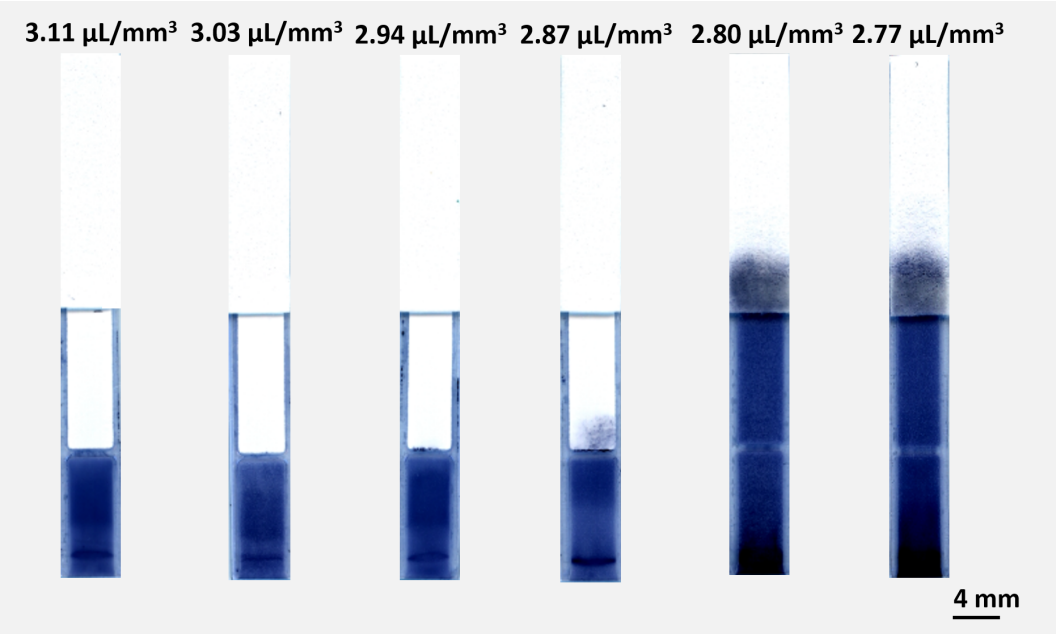

FIGURE 3.7: Images showing the results after testing a water-based suspension of latex microbeads with size of 1000 nm. The sample flowed through devices each of which with an in-line barrier fabricated with volume of photo-polymer per volume of paper in the range between 3.11–2.77 µL/mm^3.

in the range between 3.34–2.77 µL/mm^3. The devices were only removed after the testing process to capture photos as presented in figure 3.7 where we depict devices after testing latex microbeads with size of 1000 nm.

As we can clearly see, an in-line barrier fabricated with volumes of photo-polymer per volumes of paper greater than the threshold of 2.87 µL/mm^3 is porous to the flow of 1000 nm latex microbeads which are collected from the absorbent pad located at the end of the fluidic devices. On the other hand, an in-line barrier fabricated with volume of photo-polymer per volume of paper at 2.94 µL/mm^3 and below is impermeable to the flow of particles of that size hence accumulates at the bottom of the barrier.

In table 3.5, we present the results after testing a set of five devices each one with an in-line barrier fabricated at volume of photo-polymer per volume of paper in the range between 3.34–2.77 µL/mm^3. Each of the fluidic devices was tested with 20 µL of sample containing different size latex microbeads and table 3.6 shows the respective threshold line-speed values. Similar to the results for the case of testing the Au NPs, there is again a decreasing trend in terms of the volume of the photo-polymer per volume of paper and the ability of the barriers to allow the flow of particles increasing in size. It is worth mentioning here that the Au NPs and the latex microbeads with the same particle size (200 nm) have different volume per volume thresholds and specifically these are higher in the case of the latex microbeads. We believe that this is the result of the different nature and the surface properties of the latex microbeads (chemically modified for stability) compared with the Au NPs. It is reported in literature [25, 26]

TABLE 3.5: Table of results of the different size latex microbeads tested with devices with a variable porosity in-line barrier fabricated with volumes of photo-polymer per volumes of paper in the range between 3.34–2.77 µL/mm^3. For each volume per volume, we fabricated a set of five devices and tested with 20 µL of sample. Numbers indicate the devices in which the barriers are porous to the flow of sample and in red we have marked the volume per volume range at which a barrier transitions from being impermeable to being partially permeable and then porous to the flow of sample.

Volume of photo-polymer per volume of paper (uL/mm^3)	200 nm	1000 nm
3.34	0/5	0/5
3.33	0/5	0/5
3.26	0/5	0/5
3.19	0/5	0/5
3.18	0/5	0/5
3.11	0/5	0/5
3.07	0/5	0/5
3.03	0/5	0/5
3.00	**0/5**	0/5
2.94	**3/5**	0/5
2.88	**5/5**	**0/5**
2.87	5/5	**5/5**
2.83	5/5	5/5
2.80	5/5	5/5
2.77	5/5	5/5

that in the case of flow of the latex microbeads with a size of hundred nanometers, the shear rate created in the fluid flow has a significant impact in the aggregation process of these particles. In the case where the sample flows through the pores of the in-line barriers, the shear stress on the latex particles is increasing and this leads to their aggregation and the formation of clusters. For that reason a higher porosity in-line barrier (a volume per volume of 2.94 µL/mm^3) is needed for the latex microbeads to flow through, as opposed to that of the Au NPs of the same particle size (volume per volume of 3.07 µL/mm^3).

TABLE 3.6: Threshold volume of photo-polymer per volume of paper for the creation of in-line barriers that allow the flow of different size latex microbeads.

Latex microbeads size (nm)	Threshold volume of photo-polymer per volume of paper (uL/mm^3)
200	2.94
1000	2.87

Finally, we measured the particle filtration efficiency using the same method that we previously reported and equation 3.2 and the results are depicted in figure 3.8. It is also important to note here that during the testing process, in none of the cases from using the Au NPs and the latex microbeads did we observe any separation of the particles

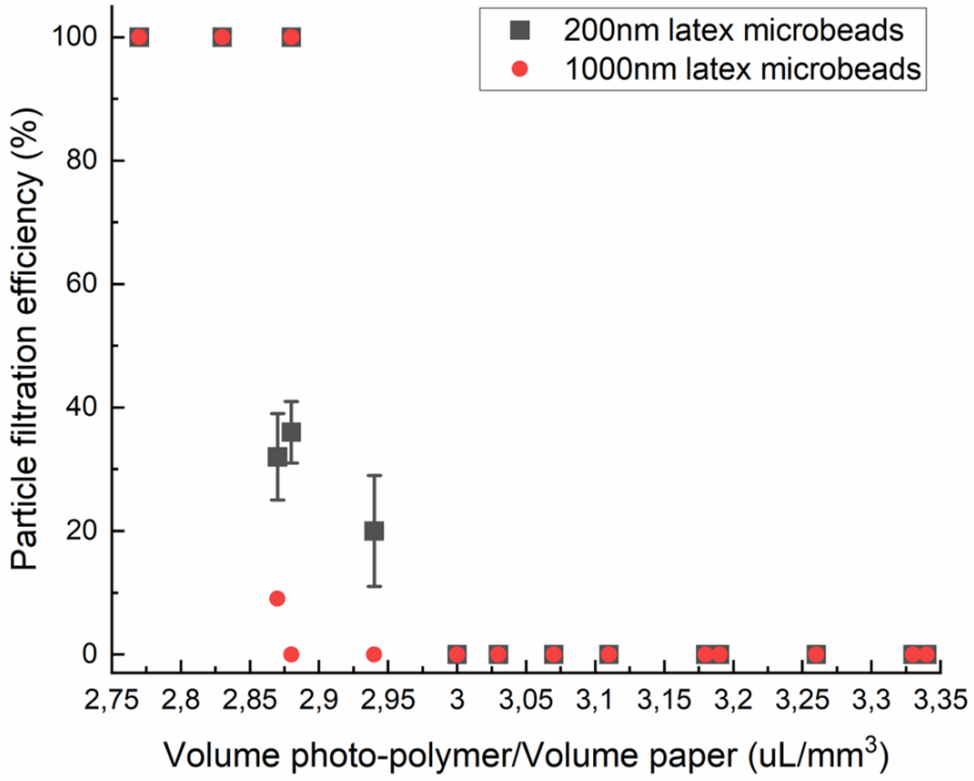

FIGURE 3.8: Particle filtration efficiency of the in-line barriers fabricated after depositing different volumes of the photo-polymer per unit volume of the paper. The in-line barriers were tested with latex microbeads of different sizes namely 200 nm and 1000 nm.

from the water-based solution in which they are suspended. We believe that this is due to the fact that in both cases and for certain volume per volume (below 3.26 µL/mm^3 for Au NPs and below 2.94 µL/mm^3 for latex microbeads) the pores of the barriers are getting blocked from the particles therefore the water-based solution can not flow through.

3.3.4 Simultaneous filtering of different sized Au NPs and latex microbeads within the same fluidic device

In our next experiment we studied the ability of the in-line barriers to separate two particles of different sizes namely 40 nm Au NPs and 1000 nm latex microbeads flowing in the same channel. For this measurement we mixed in 1:1 ratio 40 nm Au NPs (stock density) and 1000 nm latex microbeads (diluted in ratio 1:50 in DI water) and we used 20 µL of that sample. In our first approach we used a fluidic device with an incorporated in-line barrier fabricated with a volume of photo-polymer per volume of paper

of 2.88 µL/mm^3, which we know (see table 3.3 and table 3.5) to be porous enough to allow the flow of particles with size of 40 nm and at the same time is able to block the flow of particles with a size of 1000 nm. Our choice to test the sample with a fluidic device with an in-line barrier fabricated at a volume per volume of 2.88 µL/mm^3 stems from the fact that this value is just below the threshold value for the flow of latex microbeads with size of 1000 nm. We believe that under this condition we can achieve the maximum quantity of Au NPs to flow through the barrier and at the same time prevent the flow of the latex particles.

In figure 3.9A we present the results after testing the sample where photos of the same fluidic device have been taken at different times spanning from 5 minutes to 16 minutes starting from the time that the sample was introduced in the channel. As we can see, the Au NPs flow along the channel and penetrate the in-line barrier after a period of 7 minutes. However, the latex microbeads which have a larger size remain at the bottom-end of the device and are unable to flow in the channel and we believe that this is the result of the hydrophobic nature of that particles. Although the Au NPs were able to flow through the barrier, we cannot consider this experiment successful due to the fact that the latex microbeads did not flow towards the position of the barrier and in such a case we cannot highlight the usefulness of our filtration method. In order to solve

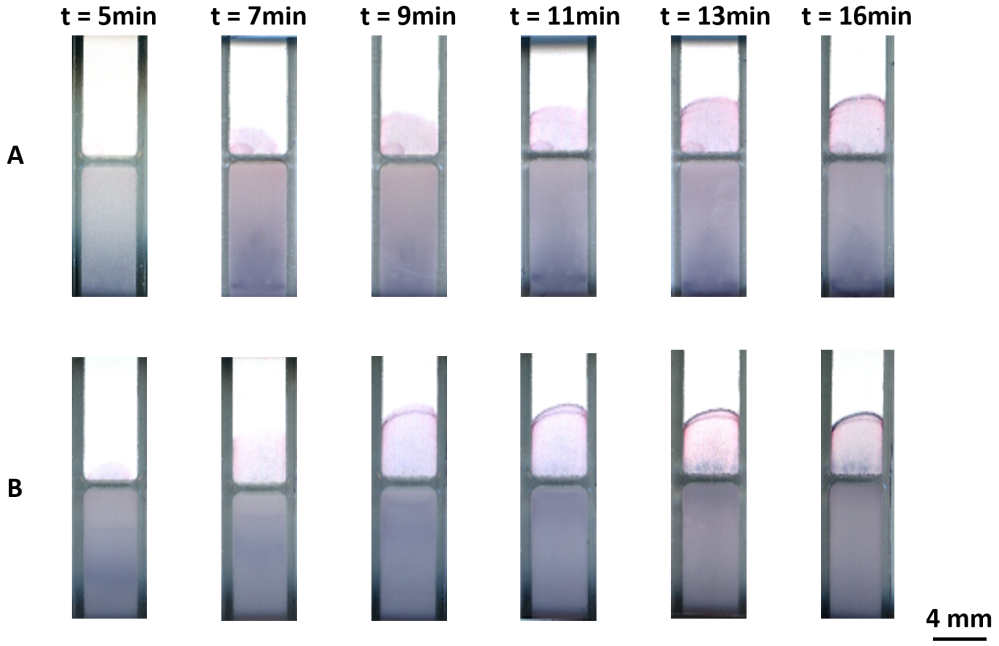

FIGURE 3.9: Sequential images showing the testing of a sample (A) without and (B) after mixing with 1% of Tween20 in PBS. The sample consists of 40 nm Au NPs and 1000 nm latex microbeads mixed in ratio a 1:1 and 20 µL of that sample was tested within the same fluidic device with an incorporated in-line barrier fabricated at volume of photo-polymer per volume of paper of 2.88 µL/mm^3. Photos of the fluidic devices were taken at different periods between 5 and 16 minutes after flowing the sample.

this problem and enable the flow of the latex microbeads along the fluidic channel, we added in the sample 1% of Tween20 (diluted in a 1:10 ratio in PBS). Tween20 is a nonionic detergent with an amphiphilic nature due to the ethylene oxide subunits which are responsible for the hydrophilic nature of this surfactant and the hydrocarbon chains which provide the hydrophobic environment. This surfactant is adsorbed on the hydrophobic surface of the latex microbeads and acts as a cover around these particles resulting in a change to their morphology [27] to make them hydrophilic. Adding Tween20 in our sample will result in a good mixing of the latex microbeads in water and this will enable their flow in the fluidic channel along with the Au NPs.

Figure 3.9B depicts the results after adding 1% of Tween20 into our sample and taking photos of the same fluidic device over a period of time. We observe that this time both the Au NPs and the latex microbeads can flow along the fluidic channel and towards the position of the in-line barrier which is fabricated under the same volume per volume as before i.e. $2.88\,\mu L/mm^3$. Despite the fact that the in-line barrier has been designed to retain particles with a size of 1000 nm, the latex microbeads of that size are able to flow through the barrier after a period of 13 minutes. We believe that this is due to the fact that we chose to test an in-line barrier fabricated with a volume per volume close to the threshold value for the flow of particles with a size of 1000 nm. Additionally, any inconsistency in either the deposition of the photo-polymer, the size of the particles or the paper inner structure might result in a small change of that threshold volume per volume either to higher or lower values and this we believe could be the reason that some of the latex microbeads penetrate through the barrier.

In our next experiment, we prepared the same sample (in a 1:1 ratio of 40 nm Au NPs and 1000 nm latex microbeads) and we mixed with 1% of Tween20 (diluted in a ratio 1:10 in PBS), however, this time we tested with in-line barriers of lower porosity. Specifically, we fabricated a barrier with a volume of photo-polymer per volume of paper of $3.03\,\mu L/mm^3$ which is close to the mean volume per volume value between the thresholds for the flow of 40 nm Au NPs ($3.26\,\mu L/mm^3$) and the flow of 1000 nm latex microbeads ($2.87\,\mu L/mm^3$). We tested 20 µL of sample and photos of the tested device are taken at different times (between 5 and 20 minutes after the start of the experiment) and depicted in 3.10A. Unlike what we expected to see, we observe that the in-line barrier not only prevents the flow of the larger size latex microbeads but also retains the smaller Au NPs from flowing through, although the barrier's volume per volume value is above the threshold value for the flow of 40 nm Au NPs. This is due to the low porosity of the in-line barrier and the fact that some of the latex microbeads might have reached the position of the barrier and consequently blocked the pores, preventing the flow through of the Au NPs.

Lastly, we tested 20 µL of the same sample that we previously used but this time on a fluidic device with an in-line barrier fabricated with a volume per volume of $3.00\,\mu L/mm^3$. Similar to our previous experiment, photos of the same fluidic device

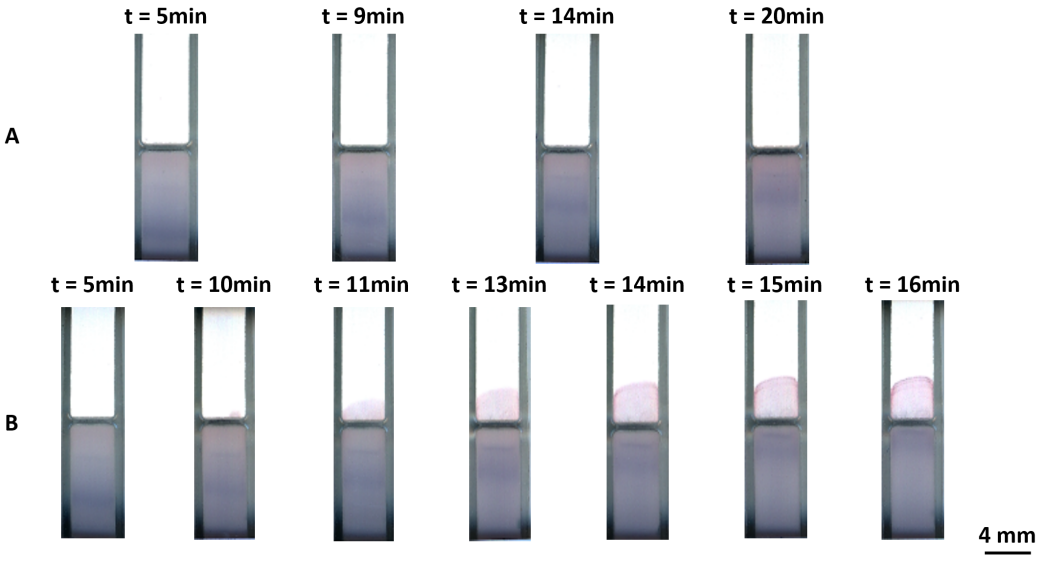

FIGURE 3.10: Sequential images showing the testing of a sample containing a 1:1 ratio of 40 nm Au NPs and 1000 nm latex microbeads. The sample is mixed with 1% of tween20 diluted in PBS in a 1:10 ratio and 20 µL of that sample was tested within the same fluidic device. The sample was tested on a fluidic device with an in-line barrier fabricated at a volume of photo-polymer per volume of paper of (A) 3.03 µL/mm^3 and (B) 3.00 µL/mm^3 and photos of the same device were taken at different times.

were taken at different times between 5 minutes and 16 minutes after starting of the testing process and the results are depicted in figure 3.10B. As we can see, after a period of 10 minutes the Au NPs start to flow through the in-line barrier while the latex microbeads are unable to flow through and progressively accumulate in the fluidic channel just before the position of the barrier. This demonstration is our first successful attempt using our developed in-line filtration method for the separation of two different sized constituents of a mixed sample when flowing in the same fluidic channel. In the next subsections we aim to further explore this filtration method on real applications to highlight its functionality as a POC sensor.

3.3.5 In-line filtration method for the separation of plasma from whole blood

Our developed in-line filtration method is not limited to only the separation of Au NPs from latex microbeads, but it can also be extended for use with samples commonly used for diagnostics such as blood. In this subsection we demonstrate the use of the in-line filters for the separation of plasma from the RBCs.

In our first experiment we tested fluidic devices with the same geometry as the ones presented in the previous subsections and an incorporated in-line barrier fabricated

with volume of photo-polymer per volume of paper in the range between 2.94–2.71 µL/mm^3. Our choice to fabricate barriers at this line-speed range stems from the fact that the RBCs have a size of approximately 6–9 µm and are able to squeeze through capillaries less than half their size [28]. From our previous set of results presented in table 3.5 we believe that making an in-line barrier capable of retaining (or delaying) the flow of particles with size at 1 µm will be sufficient for the separation of plasma from the RBCs.

Each of the fluidic devices was tested with 20 µL of the blood sample and photos were taken and presented in figure 3.11. As a reference we tested a fluidic device which does not have an in-line barrier and from the results we see that the blood sample is able to flow uniformly (equal flow velocity per unit of area) on the NC membrane and this can be easily visualized by the formation of a convex meniscus in the liquid's flow-front. Unlike what we expected to see, an in-line barrier fabricated with volume

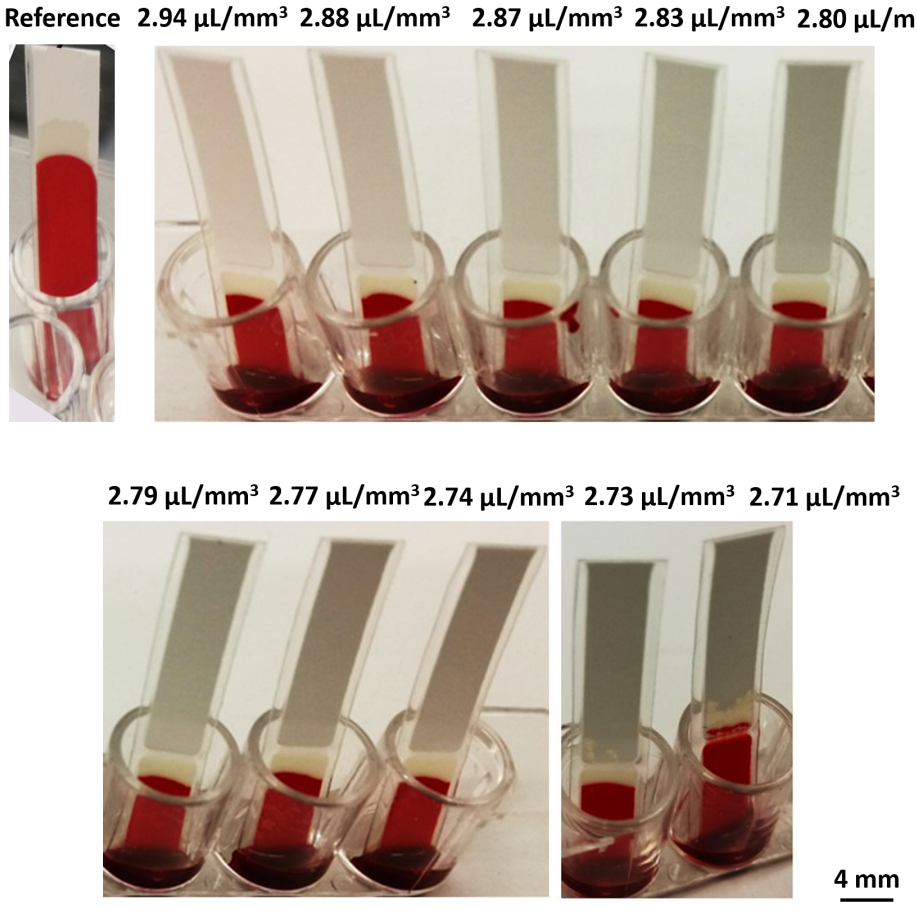

FIGURE 3.11: Fluidic devices with an incorporated in-line barrier fabricated with volume of photo-polymer per volume of paper in the range between 2.94–2.71 µL/mm^3 and each one tested with 20 µL of blood sample. For reference we fabricated and tested with the same volume of sample a fluidic device which does not have an in-line barrier.

of photo-polymer per volume of paper of 2.74 µL/mm^3 and below is impermeable to the flow of blood and we do not observe any separation of the plasma from the RBCs. This is the result of the nature of the blood and its constituents such as white blood cells (based on the type the size ranges between 7–30 µm) and platelets (size between 2–3 µm) which we believe that they reach the position of the barrier and block the open pores of the filter preventing the extraction of plasma. An increase in the barrier's volume per volume to 2.73 µL/mm^3 and 2.71 µL/mm^3 results in the extraction of a small amount of plasma, which is not sufficient to flow along the channel, hence this method cannot be used to perform a diagnostic assay. Given the fact that for volume of photo-polymer per volume of paper of 2.71 µL/mm^3 a small amount of RBCs flow through the barrier, we did not test in-line barriers beyond this threshold point as we believe that in such a case the amount of the RBCs flowing through the barrier will be increased and this will oppose the purpose of this experiment.

In our next experiment the intention was to increase the plasma extraction efficiency and for that we treated the sample with Anti-D solution. Our choice is based on the fact that the blood is RhD positive and that means that the RBCs have on their surface a protein known as D antigen. The Anti-D is a polyclonal IgG antibody which is prepared after purification from the plasma of human donors immunized to the D antigen and is extensively used to prevent hemolytic diseases of newborns [29]. When an Anti-D solution is mixed with a RhD positive blood, the Anti-D antibodies eliminate the RBCs [30] after binding to the surface of the RBCs leading to their agglutination [31]. We believe that the aggregation will lead the RBCs to form a big complex which will get blocked from the in-line barrier allowing only the plasma to flow through.

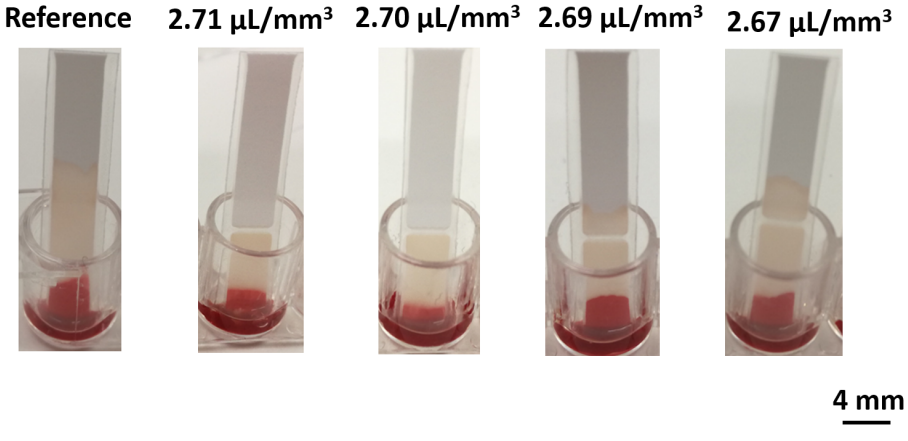

FIGURE 3.12: Fluidic devices with in-line barriers fabricated at photo-polymer volume per volume of the paper in the range between 2.71–2.67 µL/mm^3 were tested with 20 µL of sample. The sample (whole blood) was treated with Anti-D solution in a 1:4 ratio and a reference fluidic device was also tested.

In this experiment we mixed 20 µL of blood with 5 µL of Anti-D solution (in a 1:4 in ratio) and 20 µL of that sample was tested with fluidic devices with an in-line barrier fabricated with volume of photo-polymer per volume of paper in the range between 2.71–2.67 µL/mm^3. The results are depicted in figure 3.12 from which we can see that the aggregated RBCs are unable to flow along the fluidic channel, whereas the plasma is flowing in the channel. Despite the fact that the plasma separates from the RBCs, the fact that the aggregated red cells are unable to flow in the channel negates the purpose of having an in-line filter incorporated in our device, therefore the approach of pre-treating the blood with an Anti-D solution will not be further tested.

In our next demonstration, we aim to prevent the flow of the RBCs through the in-line barrier by increasing the area of the filter. In order to do that, we fabricated two in-line barriers in the same fluidic device at a distance of 0.5 mm from each other and at volume of photo-polymer per volume of paper of 2.88 µL/mm^3 and 2.81 µL/mm^3. We then repeated the same process, however we reduced the distance between the in-line barriers to 0.1 mm followed by an increase of the volume of photo-polymer per volume of paper from 2.77 µL/mm^3 to 2.65 µL/mm^3. We believe that by increasing the area of the filter we will achieve a progressive delay and eventually block the flow of the RBCs, therefore the plasma will be able to penetrate through the filter before the red cells block its pores. The results after testing 20 µL of sample are illustrated in figure 3.13. As we can clearly see, in none of the cases did we observe any separation of plasma from the RBCs. This is due to the fact that printing two polymer lines at a close

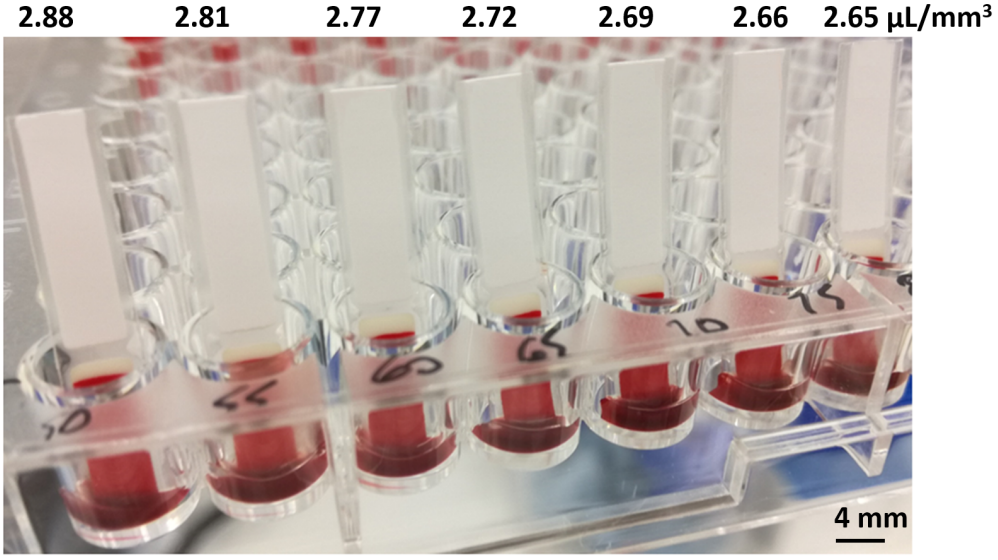

FIGURE 3.13: Fluidic devices with two in-line barriers at a distance of 0.5 mm from each other fabricated with volume per volume of 2.88 µL/mm^3 and 2.81 µL/mm^3 and tested with 20 µL of sample. The same volume of sample was also tested with fluidic devices which have two in-line barriers each one fabricated with volume per volume in the range between 2.77–2.65 µL/mm^3 with a separation of 0.1 mm.

separation (0.1 mm or 0.5 mm) will result into merging of these lines and consequently block the pores of the NC, hence preventing the flow of plasma which accumulates just before the position of the filter.

In our next approach, we fabricated fluidic devices with multiple in-line barriers across the channel. Our aim is again to progressively delay the flow of the RBCs, while allowing the plasma to flow through the barriers and separate from the blood. In our first demonstration of this method, we fabricated five in-line barriers with the same porosity and volume of photo-polymer per volume of paper in the range between 2.72–2.65 µL/mm^3 and each barrier had a distance of 2 mm from the next one. Each of the devices was tested with 20 µL of sample and the results are depicted in figure 3.14A. As we can clearly see, in none of the tested devices the in-line barriers were capable of blocking the RBCs, which manage to squeeze through the pores of the filters and flow along the channel. Despite the fact that the plasma separates from the blood, this method can not be studied further for any diagnostic assay as the flow of the red cells would be detrimental to the performance of the test interfering with the results.

In our last demonstration of testing blood we followed the same approach of fabricating multiple in-line barriers across the channel to progressively delay the flow of the RBCs. However, unlike our previous method this time we fabricated 10 in-line barriers across the same fluidic device each one with a different porosity and distance of 0.5 mm between each. In each of the channels the porosity of the in-line barriers does

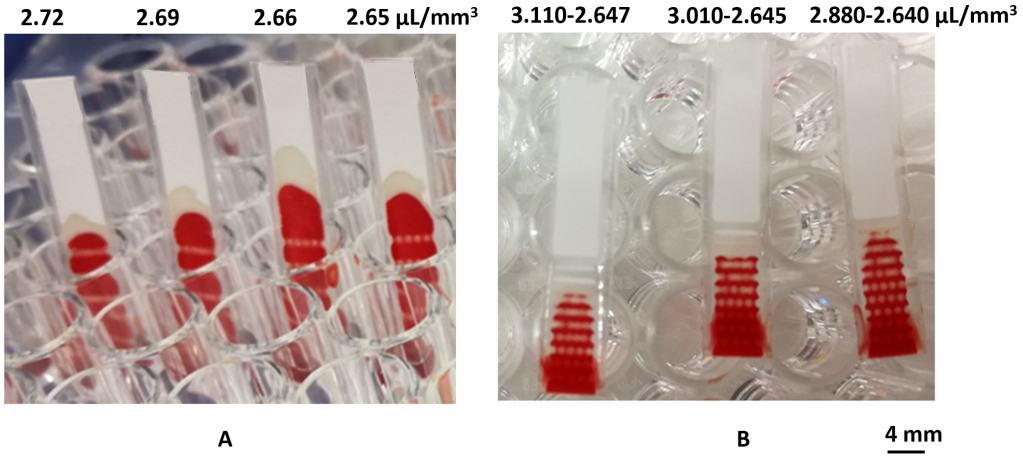

FIGURE 3.14: Fluidic devices each one tested with 20 µL of sample. (A) The devices have five incorporated in-line barriers of the same porosity fabricated with volume of photo-polymer per volume of paper in the range between 2.72–2.65 µL/mm^3 and distance of 2 mm from each other. (B) The devices have ten in-line barriers fabricated with varying values of volume per volume in the ranges between 3.110–2.647 µL/mm^3, 3.010–2.645 µL/mm^3 and 2.880–2.640 µL/mm^3. The porosity of the in-line barriers across the same channel varies starting from low porosity for the barriers located at the bottom-end of the channel to high porosity as we follow the direction of the sample flow.

not remain the same but changes progressively starting from very porous barriers at the bottom-end of the devices to less porous barriers following the direction of the sample flow along the channel. In order to progressively change the pore size of the in-line barriers we printed the photo-polymer at low volume of photo-polymer per volume of paper (e.g. 2.647 µL/mm^3, 2.645 µL/mm^3 and 2.640 µL/mm^3 for the three devices in figure 3.14B) and for every additional barrier we increased the value of the volume per volume until we get barriers with low porosity (e.g. 3.110 µL/mm^3, 3.010 µL/mm^3 and 2.880 µL/mm^3 as in figure 3.14B). We tested the fluidic devices again with 20 µL of sample and by looking the results in figure 3.14B, we do not see any separation of the plasma from the RBCs. we believe that is due to the fact that other components found in blood such as the platelets and the leukocytes block the pores of the filter preventing the flow of plasma.

3.3.6 In-line filtration method for increasing the sensitivity in LFAs

In our last demonstration we used the in-line filtration method on an LFA to increase its sensitivity for the detection of a pre-determined analyte namely CRP with concentration of 50 ng/mL. Unlike the previously mentioned methods, in this approach we do not use the in-line filters as a tool to block the flow of the sample but as a means to delay its flow along the channel. Our aim is, by delaying the flow of the sample, to increase the interaction (incubation) time between the analyte and the capture antibodies located at the test line of the LFA resulting in an increase in the colour intensity of the test line.

In our first experiment we fabricated fluidic devices with a channel width at length of 4 mm and an incorporated in-line barrier fabricated with a volume of photo-polymer per volume of paper of 2.66 µL/mm^3. In order to find the position of the in-line barrier that gives the maximum colour intensity on the test line, we placed the barrier in different positions spanning from 6 mm to 19 mm from the bottom-end of the devices. Also, in the channel of the fluidic devices, we have dispensed and immobilized antibodies in the test and the control lines at positions of 15 mm and 17 mm respectively. Each one of the devices was tested with 28 µL of sample which is prepared after mixing 20 µL of CRP with 8 µL of the conjugate antibody and the results after the testing process are illustrated in figure 3.15. As a control we have fabricated and tested a fluidic device with no barrier.

Looking at the results of the figure we observe that fabricating an in-line barrier at a distance of 6 mm from the bottom-end of the device does not have a significant impact in the delay of the sample at the position of the test line, therefore the colour intensity of the test line remains similar to the one of the control device. However, when the in-line barrier approaches the position of the test line, then there is a delay in the flow of the sample at the position of the test line and consequently there is an enhancement of its

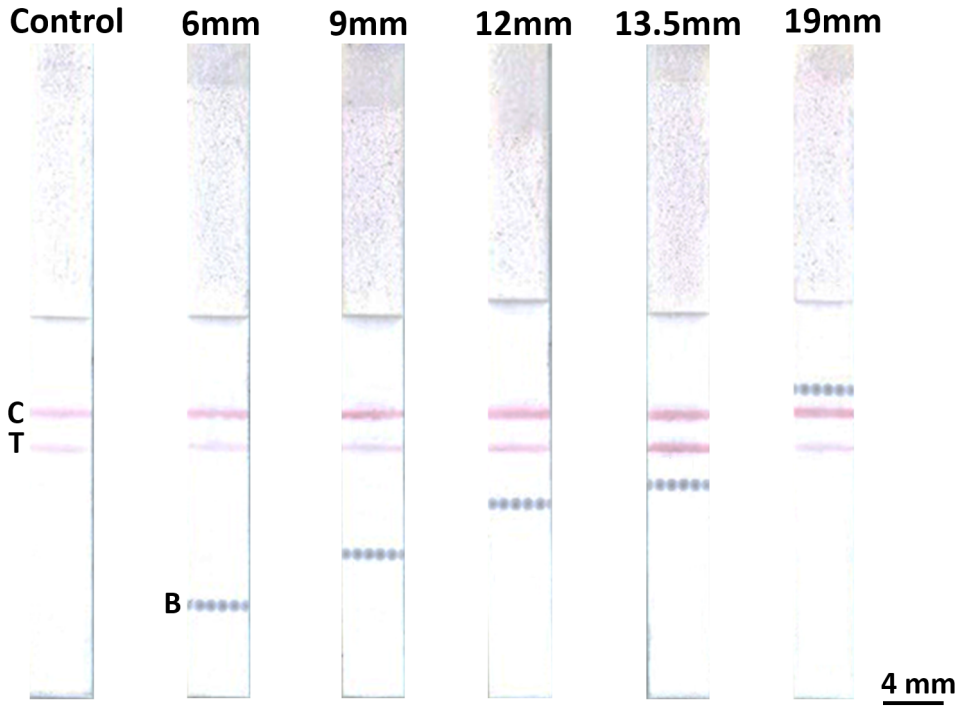

FIGURE 3.15: Fluidic devices with an incorporated in-line barrier fabricated at a volume of photo-polymer per volume of paper of 2.66 µL/mm^3. In the channel, we have dispensed a test (T) and a control (C) line and the position of the barrier (B) varies from 6 mm to 19 mm from the bottom-end of the device. Each of the devices was tested with 28 µL of sample and a control device which does not contain an in-line barrier was also tested as a reference.

signal intensity. We observe that the peak value for the colour intensity of the test line derives after printing the in-line barrier at a distance of 13.5 mm from the bottom-end of the device, whereas a further increase in the distance, beyond the position of the test line, results in a decrease in the signal intensity. Figure 3.16 shows a graph of the colour intensity on the test line for the various positions of the in-line barrier and each data point represents the mean value from the total of three devices.

In order to measure the colour intensity of the test lines of the LFAs we used the RGB channel in the histogram function of Adobe Photoshop. Then we used equation 3.3 to calculate the average intensity value of the test line of the three devices and we subtracted this value from the pixel value of the background (which corresponds to a pixel intensity of 255) to obtain the actual colour intensity.

$$\text{Colour intensity (a.u.)} = 255 - \text{Average intensity value on the test line} \tag{3.3}$$

In the next experiment we studied the effect of different porosity in-line barriers in the increase of the sensitivity of a CRP assay. For this experiment we chose the parameter of the position of the in-line barrier that gives the maximum signal enhancement and

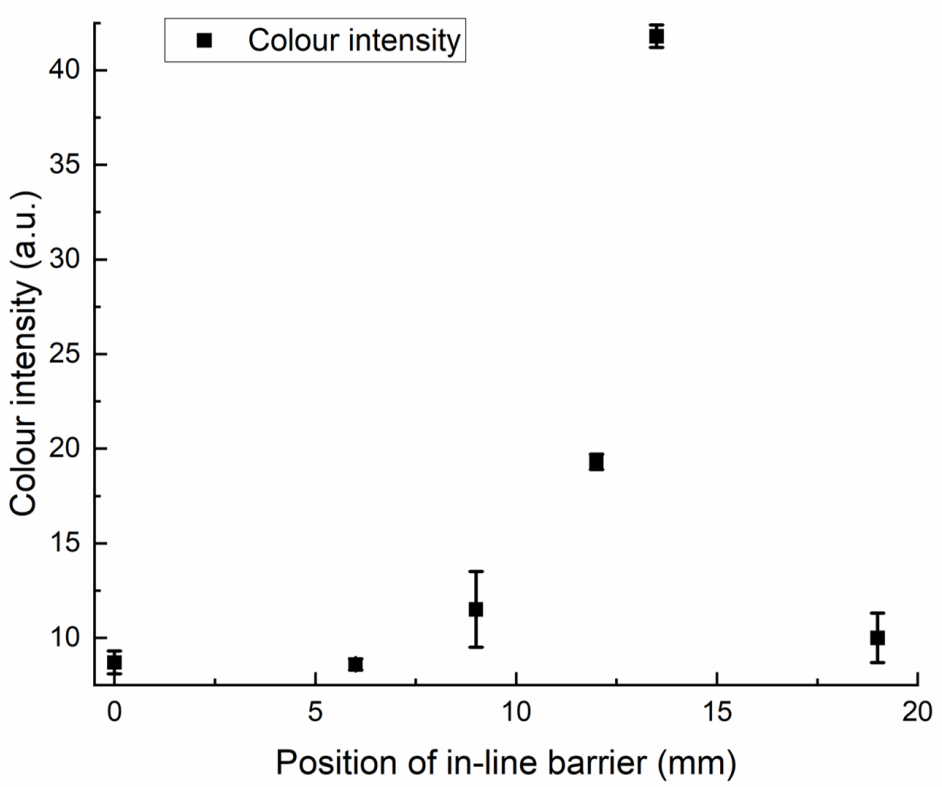

FIGURE 3.16: Colour intensity on the test line of LFAs for the different positions of an in-line barrier fabricated with a volume of photo-polymer per volume of paper of 2.66 µL/mm^3. Each data point represents the mean value of the total of three devices. The data point at position of 0 mm corresponds to the one of the control device.

based on the previous results this value was set at 13.5 mm. Having fixed the position of the in-line barrier throughout the entire experimental process, we changed the volume per volume of the barriers from 2.69 µL/mm^3 to 2.64 µL/mm^3 and we tested each of the devices with 28 µL of sample. The results after the testing process are depicted in figure 3.17 and figure 3.18 shows the respective graph in which each data point is the mean value from the total of three devices. As we can clearly see, there is a peak value for the colour intensity on the test line and that is for the in-line barrier printed with deposition speed of 2.66 µL/mm^3. For the lower porosity in-line barriers (e.g. 2.69 µL/mm^3) we believe that a small part of the sample is getting blocked from the filter and does not reach the position of the test line, hence the colour intensity is decreased. On the other hand, for higher porosity in-line barriers (e.g. 2.65 µL/mm^3 or 2.64 µL/mm^3) we assume that the filters do not delay the flow of the sample sufficiently, thus the signal intensity on the test line is again decreased as compared with the signal in the case of the barrier printed at 2.66 µL/mm^3.

In order to calculate the colour intensity in the test line of the LFAs we followed the method that we previously described and equation 3.3. From the previous results we can see that the maximum signal enhancement on the test line of the LFAs comes when

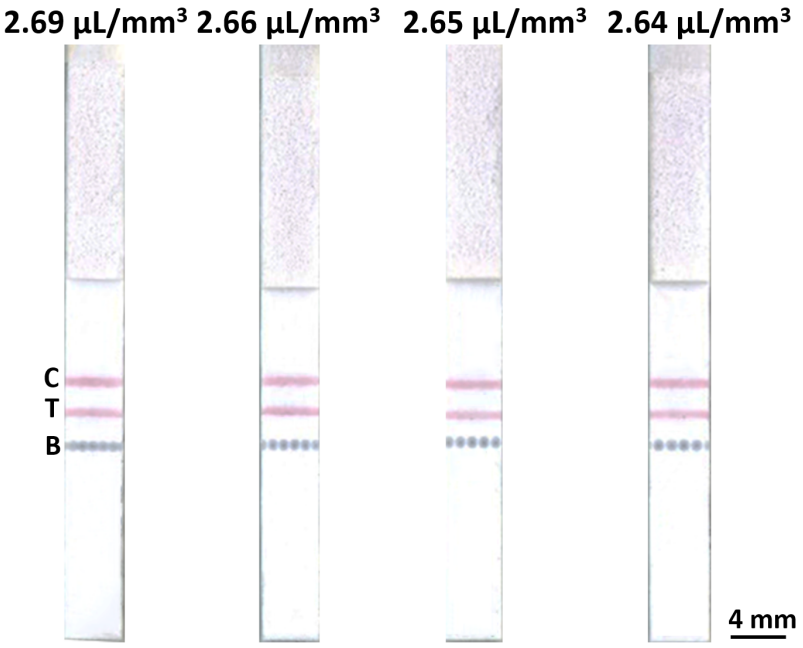

FIGURE 3.17: Fluidic devices with an incorporated in-line barrier (B) at a position of 13.5 mm from the bottom-end of the channel fabricated with different volume of photo-polymer per volume of paper in the range between 2.69–2.64 µL/mm^3. Each one of the devices was tested with 28 µL of sample containing the CRP. With T and C we indicate the test and the control lines respectively.

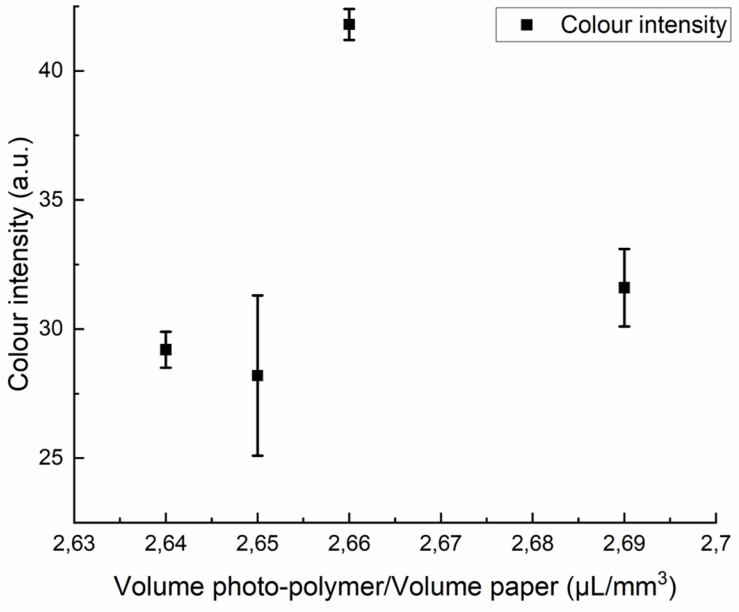

FIGURE 3.18: Colour intensity on the test line of LFAs for the various porosities of the in-line barriers fabricated with volume of photo-polymer per volume of paper in the range between 2.69–2.64 µL/mm^3. Each data point represents the mean value of the total of three devices.

we fabricate an in-line barrier with a volume per volume of 2.66 µL/mm^3 at a position of 13.5 mm. Using equation 3.4 we calculate the respective improvement in the sensitivity and this has increased by 3.8-fold where I_m corresponds to the maximum signal intensity and I_c corresponds to the signal intensity of the control device.

$$\text{Increase of the sensitivity} = \left(\frac{I_m - I_c}{I_c}\right) \tag{3.4}$$

Since there is no further increase in the sensitivity of the CRP assay for the in-line barriers fabricated above and below value of volume per volume of 2.66 µL/mm^3, in our next experiment, we fabricated two in-line barriers within the same fluidic channel. Specifically, we chose to print two barriers with the same porosity at distance of 13.5 mm and 16.5 mm from the bottom-end of the device and with volume of photo-polymer per volume of paper in the range between 2.690–2.640 µL/mm^3. We believe that printing a second barrier just above the test line (15 mm) will further increase the delay of the sample at the position of the test line, and therefore we will observe a signal enhancement.

Each of the devices was tested with 28 µL of the sample and the results are illustrated in figure 3.19A and the respective colour intensity graph in figure 3.19B. From the results we observe that printing a second in-line barrier just above the position of the test line with volume per volume in the range between 2.690–2.640 µL/mm^3, contributes significantly to an additional delay in the flow of the sample, thus the signal intensity is further increased as compared with the case of having a single barrier. This effect is more evident in the case of the more porous barriers (e.g. 2.647 µL/mm^3) where the signal had increased by 40.8% whereas for the case of the barriers with lower porosity (e.g. 2.690 µL/mm^3) the signal has only enhanced by 24.1%. In terms of the sensitivity of the assay, we observe a 4.6-fold increase after testing a fluidic device with two in-line barriers fabricated at a speed of 2.647 µL/mm^3.

3.4 Summary

In conclusion, in this chapter we presented a laser-based local photo-polymer deposition method which is used for the fabrication of in-line barriers on an NC membrane, positioned at 90° to the direction of the sample flow and within the solid walls of a fluidic channel. With this technique we are able to control the volume that we deliver the photo-polymer per volume of the porous substrate, and create porous in-line barriers able to separate particles based only on their size.

In our first demonstration, we tested the in-line barriers with a water-based suspension of coloured dyes to study the effect of the different porosity barriers on the flow of the

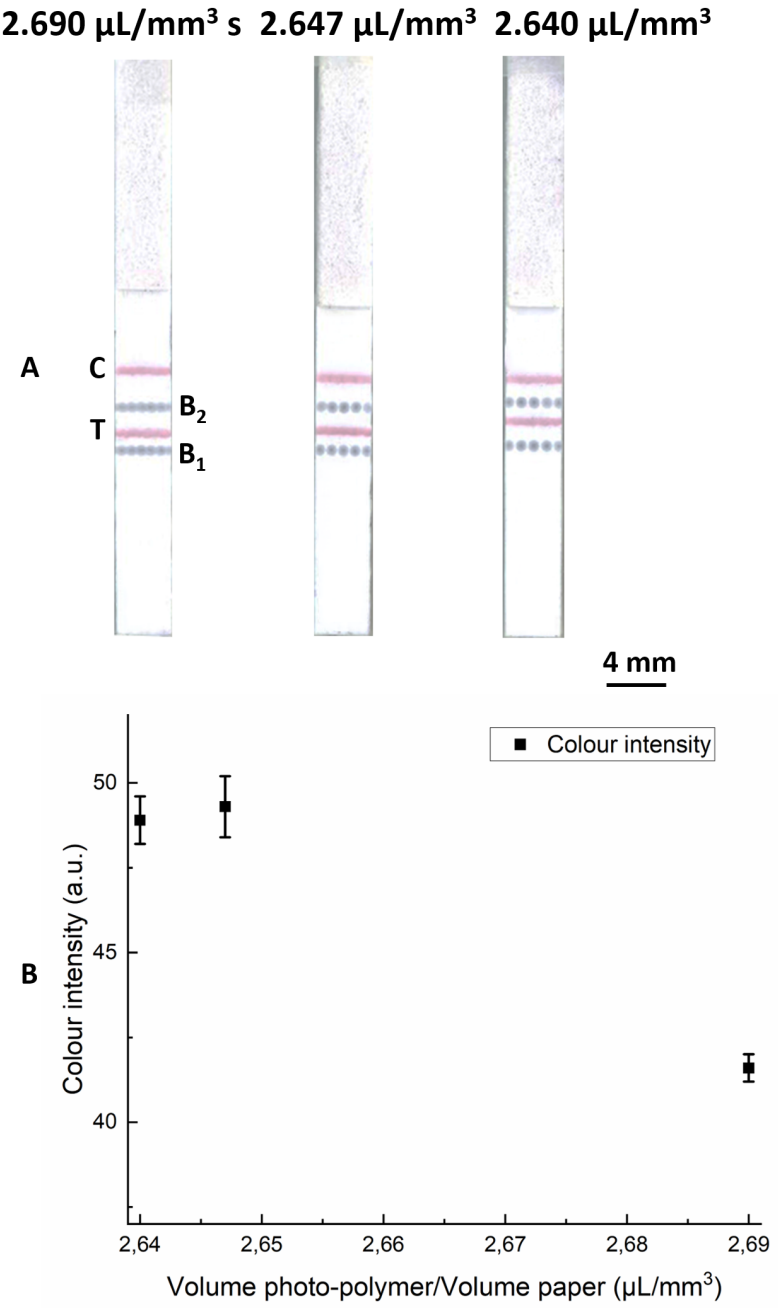

FIGURE 3.19: (A) Fluidic devices each with two in-line barriers (B_1 and B_2) fabricated with the same porosity and volume of photo-polymer per volume of paper in the range between 2.690–2.640 µL/mm^3. In the channel we have dispensed a test (T) and a control (C) line and each of the devices was tested with 28 µL of sample. (B) Graph presenting the colour intensity for the different volumes of photo-polymer per volumes of paper of the two barriers. Each data point is the mean value of the total of three devices.

sample. From our results we saw that barriers fabricated with higher volumes of photo-polymer per volumes of paper, are more porous as compared with barriers printed with lower values of volume per volume, hence allowing the flow of greater volume of

sample through the barrier. The utility of a controllable change in the porosity of the in-line barriers was later studied more systematically by testing a water-based solution of different size Au NPs (40 nm, 100 nm, 200 nm) and latex microbeads (200 nm, 1000 nm). Our result show that by controlling the volume of the photo-polymer per volume of paper of the in-line barriers we were able to either completely block or enable the flow of the different size particles.

The ability of the in-line filters to separate particles based on their size was later tested with a complex sample containing 40 nm Au NPs and 1000 nm latex microbeads. After fabricating and testing fluidic devices with in-line barriers printed at different values of volume per volume, we successfully found the parameters to create a filter capable of stopping the flow of the larger sized latex microbeads while simultaneously allowing the flow of the smaller sized Au NPs through the in-line barrier.

We later tested the in-line filtration method with a blood sample for the separation of plasma from the RBCs. In our first approach we fabricated a single barrier in a fluidic channel and this approach proved to be unsuccessful as the amount of the extracted plasma was not sufficient to perform an assay. Next we presented the results after pre-treating the blood with Anti-D solution, a method that allowed the separation of plasma from the RBCs but negated the purpose of having a filter as the aggregated red blood cells were not able to flow along the fluidic channel. Finally, we tried to incorporate additional in-line barriers within the same fluidic channel in order to delay the flow of the RBCs and allow the plasma to flow through the filters however, from our results we observed that the sample is either completely blocked or the RBCs can flow together with the plasma through the in-line barriers.

In our last application using this method, we used the in-line barriers as a tool to increase the sensitivity in an LFA designed for the detection of CRP. After studying the effect of the different positions of the in-line barrier as well as the different porosities of them, we found a signal increase of the test line of 3.8-fold. Furthermore, we tested the effect of having two in-line barriers within the same fluidic device and the result show a further signal enhancement of the test line which reached the value of 4.6-fold.

Chapter 4

Flow-through filtration method in lateral flow immunoassays

4.1 Introduction

In the last few decades, LFAs have been widely studied for use as POC sensors for the detection of pathogens [1]. There is a wide range of applications [2] where LFAs can be used and indicative examples include the use in agriculture for sensing of pesticides [3], the detection of infectious diseases such as hepatitis and malaria [4, 5] as well as the detection of food-borne pathogens such as E. coli [6]. The operation of LFAs is based on processing different types of samples such as water-based samples, biological fluids such as urine [7], blood [8] and saliva [9] as well as food samples (e.g. diary products) for the detection and quantification of biomarkers.

Compared with other diagnostic sensors, LFAs possess some unique characteristics such as the absence of need for maintenance (e.g. refrigeration) following manufacture which makes them ideal for use in remote settings and developing countries. Additionally, the testing process is simple, fast and produces results which can then be interpreted visually by the patients within a few minutes [10, 11]. However, there are certain limitations [12] of LFAs arising primarily from the detection methods that are used (e.g. assay design, chemistries), and this can limit the range of concentrations in which the analytes can be detected. In addition, in the case of semi-quantitative analysis, visual inspection by human eye is sometimes not reliable or definitive, therefore cameras, readers or even use of multiple lines as capture sites in the detection pad are used [13].

One of the biggest disadvantages of using LFAs is the hook effect which is the result of testing samples containing high analyte concentration [14]. In that case, a large

amount of unlabelled analytes bind to the test line preventing the capture of the labelled analytes on the same site. Due to the hook effect, there is a high threshold value for the analyte concentration which depends on the assay design as well as the detected biomarker, above which the colour intensity of the test line decreases with increasing concentration [15]. As a direct consequence, there is a false interpretation of the results due to the fact that the patients can not distinguish between a very low and a very high analyte concentration as in both cases there is low or no signal on the test line. In order to overcome this limitation and increase the dynamic range in which the analyte can be detected, there are reported methods that either use an additional line formed of the antigen and positioned between the test and the control lines [16] or use of multiple lines in the detection pad [17]. Despite the fact that using the aforementioned techniques can successfully increase the dynamic range in which the analyte can be detected, the methods require the use of a conjugate pad and subsequently the incubation and drying of the reagents for several minutes which increases the time for the fabrication of the device.

In this chapter, we report an alternative to the previously mentioned in-line filtration method for the size-exclusive separation of particles using a porous flow-through filter. Using the local photo-polymer deposition method we fabricated porous flow-through filters on cellulose paper with controllable levels of porosity. The flow-through filters can be designed to retain particles larger than a specific size and simultaneously allow smaller particles to flow through the filter. Following the fabrication process, we used the porous filters as a tool for different applications such as the detection of analytes over a broad concentration range, the separation of plasma from the RBCs as well as the purification of a water-based sample containing the bacteria E. coli.

In our first demonstration, we used the porous flow-through filters to counter the hook effect and detect the common inflammation marker CRP [18] over a broad concentration ranging from 10 ng/mL to 50.000 ng/mL. The detection of CRP is clinically significant [19] and although this protein is present in our body, elevated levels of it are associated with diseases such as chronic inflammation as well as type 2 diabetes mellitus [20]. It is important to measure CRP over a wide concentration range as the levels of this protein are associated with different risk levels for cardiovascular disease [21] and specifically concentrations $<$1000 ng/mL and $>$3000 ng/mL are an indication of low and high risk respectively.

For the detection of CRP, we positioned the flow-through filter on top of the front end of an LFA where capture antibodies are immobilized at the test line. The novelty of this method is based on the fact that we used the same materials that are commonly used in standard LFAs, however we did not make use of the sample pad and the conjugate pad simplifying the device design and the fabrication protocol. The detection mechanism is based on the interaction and binding between the target analyte with two antibodies, each tagged with a different sized label, namely 40 nm Au NPs and 3 µm latex beads.

Similar to a competitive type assay, the presence of the analyte in the sample leads to the binding of the analyte with the two antibodies leading to the formation of a complex with size bigger than the effective pore size of the filter, hence the complex is blocked and the Au NPs cannot be captured at the test line (no signal). However, if the analyte is not present in the sample, then the complex is not formed then the unbound Au NPs can flow through the filter and get captured in the test line of the device producing a red-coloured line. In the case that the analyte is present in the sample in different concentrations, some of the Au NPs will be captured to form the complex and only the unbound ones will flow through the filter and get captured in the test line. In that case a coloured signal of variable intensity will be produced in the test line, indicating the presence of the analyte in the sample.

In our next demonstration, we used the porous flow-through filters for the same application that we previously reported in subsection 3.3.5 which is the separation of plasma from whole blood. In this subsection, we report different designs using the porous filters which again are located on the top of the front end of an LFA in order to achieve a maximum yield in the extraction of plasma.

Lastly, the porous flow-through filters were tested on a water-based sample containig E. coli bacteria. E. coli is a rod-shaped bacteria with length of 2000 nm and diameter of 250–1000 nm and its monitoring and analysis is of utmost importance due to the fact that it can easily contaminate food as well as drinking water [22]. Human infection with E. coli can result in diseases such as hemorrhagic diarrhoea, hemolytic uremic syndrome [23] and thrombocytopenic thrombotic purpura [24]. There are reported methods that make use of colorimetric [25] and bioluminescence [26] techniques for the detection of E. coli and although we do not report a novel detection method herein, we use the porous flow-through filters as a tool for the purification of a water-based sample containing E. coli.

4.2 Experimental section

4.2.1 Experimental setup and materials

The substrate of choice to make the porous flow-through filters is cellulose paper (Whatman^{TM} grade 1 qualitative filter paper) from GE Healthcare, with a thickness of 180 µm and pore size of 11 µm. In order to make the LFAs, which are used for the immunoassays, the material we used was Unisart CN 95 NC membrane acquired from Sartorius Stedim Biotech GmbH, Germany, with thickness of 140–170 µm and pore size of 15 µm. An absorbent pad (Whatman^{TM} CF4) acquired from GE Healthcare with thickness of 480 µm was placed at the end of the LFAs to absorb the excess sample that flows over the test line.

For the fabrication of the porous flow-through filters, we dissolved the photo-polymer in isopropyl alcohol (IPA) (Sigma Aldrich) following different concentrations and later we added 5% of Tween®20 (Sigma Aldrich) in DI water to make the filter hydrophilic. For the characterization of the different porosity flow-through filters we tested black-dyed polystyrene microspheres of different diameters, namely 200 nm with density 5.68×10^{12} particles/mL, 500 nm with density 3.64×10^{11} particles/mL, 1000 nm with density 4.55×10^{10} particles/mL and 3000 nm with density 1.68×10^{9} particles/mL. The polystyrene microspheres were all suspended in DI water at a concentration of 25 mg/mL.

In order to demonstrate the mechanism of the flow-through filters for the detection of analytes, we used an assay with anti-mouse antibodies (acquired from BBI solutions with stock concentration of 500 µm/mL) labelled with 40 nm Au NPs (BBI solutions, optical density 20) used as a detection antibody, 3 µm latex beads (white-dyed acquired from Spherotech) labelled with streptavidin with stock concentration of 500 µm/mL used as a filtration antibody and a mouse biotinylated IgG antibody (acquired from BBI solutions) with stock concentration of 500 µm/mL used as the analyte. All these constituents were mixed in a 1:1:1 ratio to form the sample for testing. A mouse IgG antibody (BBI solutions with stock concentration of 500 µm/mL) was dispensed and immobilized on the test line of the LFA and used as a capture antibody. The performance of the flow-through filtration method was tested on an assay for the detection of a common inflammation marker namely CRP. In this assay we tested a sample which contained in a 1:1:1 ratio of a human CRP (acquired from BBI solutions) used as the analyte with stock concentration of 1 mg/mL, a mouse anti-human CRP (BBI solutions) with stock concentration of 500 µm/mL labelled with 40 nm Au NPs used as the detection antibody and a mouse anti-human CRP biotinylated IgG antibody (BBI solutions with stock concentration of 50 µm/mL) tagged with 3 µm latex beads (white-dyed acquired from Spherotech) labelled with streptavidin used as the filtration antibody. A goat anti-mouse IgG antibody (BBI solutions) with stock concentration of 500 µm/mL was dispensed on the LFA and used as a test line to capture the detection antibody.

Lastly, the flow-through filtration method was tested with a water-based solution containing E. coli. The E. coli strain is stored in a vial using a porous bead under $-20\,^{\circ}\mathrm{C}$ in the freezer. To make the bacteria solution, the vial was removed from the freezer and moved to an aseptic environment. Under aseptic conditions, the bead was removed using a sterile loop. This was followed by inoculation of the bead into a broth medium (Tryptic Soy Broth). To help mixing the microorganisms into the medium, the tube was inverted a few times. The bead was removed from the broth medium and the tube was incubated at $37\,^{\circ}\mathrm{C}$ for 24 hours. The bacteria suspension was then ready to use. In order to determine the bacteria concentration we diluted E. coli in PBS with a dilution factor of 10^5 on the agar plate and the concentration was determined using the colony counting method.

4.2.2 Fabrication method and procedure

For the creation of the solid polymer walls of the flow-through filters on cellulose paper and the LFAs on an NC membrane, we used the patterning method of the local photo-polymer deposition and the fabrication parameters are listed in table 2.1.

In figure 4.1 we have an illustration of the different stages involved in the fabrication of a porous flow-through filter as well as the position of the filter at the front end of an LFA. After the creation of the solid boundary walls on cellulose paper (stage 1), we used the same photo-polymer again (Desolite) but this time we diluted it in IPA in different concentrations to create filters with controllable levels of porosity. The porosity of the flow-through filters is defined by the volume concentration of the deposited photo-polymer solution in IPA and by changing the v/v% concentration, we were able to create filters with different porosities. The use of IPA is essential for the creation of the porous filters as the photo-polymer is a viscous liquid with density $1110\,\mathrm{kg/m^3}$ at 23 °C and viscosity $10.000\,\mathrm{mPa \cdot s}$ at 25 °C which makes the spreading of the photo-polymer difficult in the entire volume of the paper. However, the solubility and compatibility of the photo-polymer in IPA assists with its dilution and helps with the homogeneous spreading of the photo-polymer, which after penetrating throughout the cellulose paper, acts as a coating around its fibrous structure.

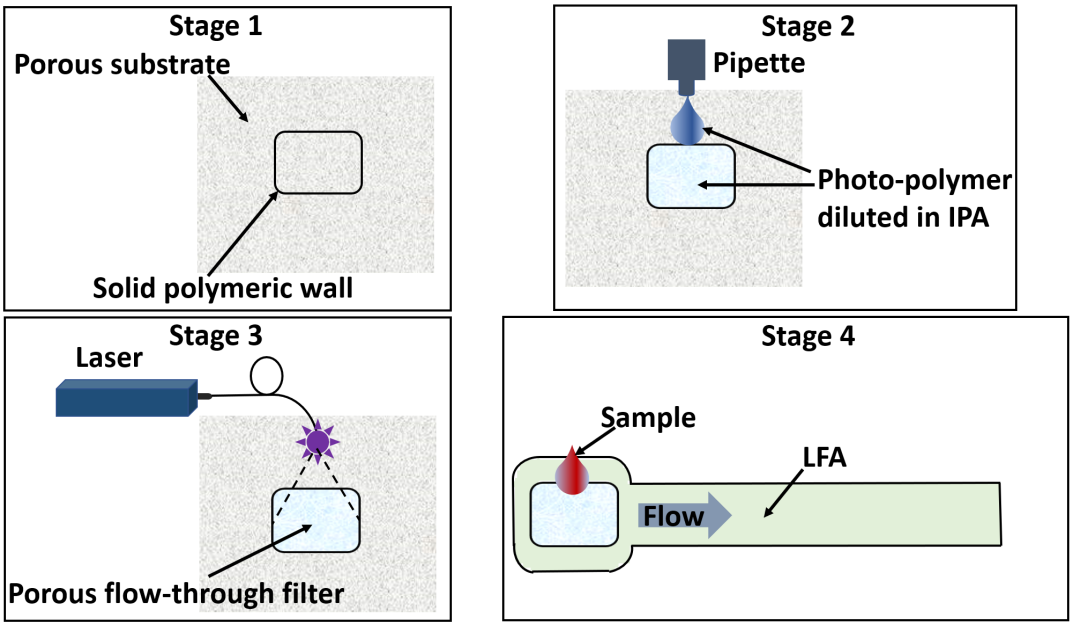

FIGURE 4.1: Schematics showing the various steps involved in the fabrication and use of a porous flow-through filter with an LFA. Stage 1 represents the creation of a solid polymeric wall on cellulose paper, in stage 2 we deposit 10 µL of the diluted in IPA photo-polymer inside the solid polymeric wall. Stage 3 involves the laser exposure of the diluted photo-polymer to create the porous flow-through filter and stage 4 illustrates the position of the same filter at the front end of an LFA.

From the results presented in figure 2.6A we know that a sample volume of 10 µL is sufficient to penetrate throughout the whole thickness of a square filter with dimensions of 25 mm^2 and for that we are using the same volume of the photo-polymer and we pipette it inside the solid polymeric wall (stage 2). A time delay of 60 s between the photo-polymer deposition and the laser curing was used and the entire area of the square filter was exposed to light with a fluence of 0.3 J/cm^2 to induce photo-polymerization and create the porous flow-through filter (stage 3). As we can clearly see, the time delay we used during the process of making the porous filter was different compared to the time delay that we used for making the solid square polymeric wall of the filter (180 s). This stems from the fact that diluting the photo-polymer in IPA would result in a reduced viscosity allowing the faster penetration of the photo-polymer throughout the cellulose paper (within 60 s). As for the fluence, we chose the same value of 0.3 J/cm^2 that we used to make the solid boundary walls in order to ensure that we do not leave any unpolymerized material which otherwise would be detrimental for the performance of the flow-through filters.

Adding the photo-polymer in different concentrations on cellulose paper and exposing to laser light will result in the creation of porous filters with correspondingly different levels of permeability. Flow-through filters made with higher photo-polymer concentration will be less porous compared with flow-through filters made with lower photo-polymer concentrations as the concentration of the photo-polymer in each case dictates the resultant porosity of the filters. After the formation of the porous filters, we added 10 µL of Tween®20. This surfactant has a hydrophilic nature and provides an aid to the spreading of the sample across the whole area of the filter.

After the fabrication, the flow-through filter is cut around its solid boundary walls and then positioned at the front end of an LFA (stage 4) before the sample is deposited onto the flow-through filter. The flow-through filters with controllable levels of porosity can be designed to retain particles larger than a specific size on top of it and allow smaller particles to flow through and into the LFA and this capability of the filters will be further studied in the following section.

4.3 Results and discussion

4.3.1 Characteristic study of the filtration properties of the flow-through filters

Using the LDW method we were able to create porous flow-through filters and lateral flow devices and images of both are depicted in figure 4.2. The flow-through filters are designed to have a square shape with an area of 25 mm^2 whereas the front end of the LFA has also a square shape with an area of 49 mm^2 and a channel designed to

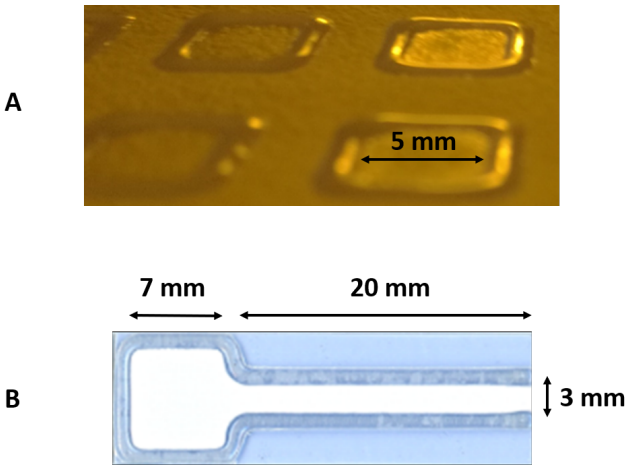

FIGURE 4.2: Images of (A) a porous flow-through filter and (B) an LFA with their respective dimensions. The flow-through filter can be designed to retain particles of a specific size and allow smaller particles to flow through and into the LFA

have a length of 20 mm and width of 3 mm. The area of the flow-through filter was deliberately designed to be smaller than the area of the front end of the LFA so that the porous filter will totally fit inside, allowing the contact between the two substrates. Any gap between the two substrates would have resulted in interrupted flow of the sample from the filter to the device and consequently in poor performance of the assay.

The filtration properties of the flow-through filters were later studied and for that we fabricated identical LFAs and filters with different porosities. In figure 4.3, we present

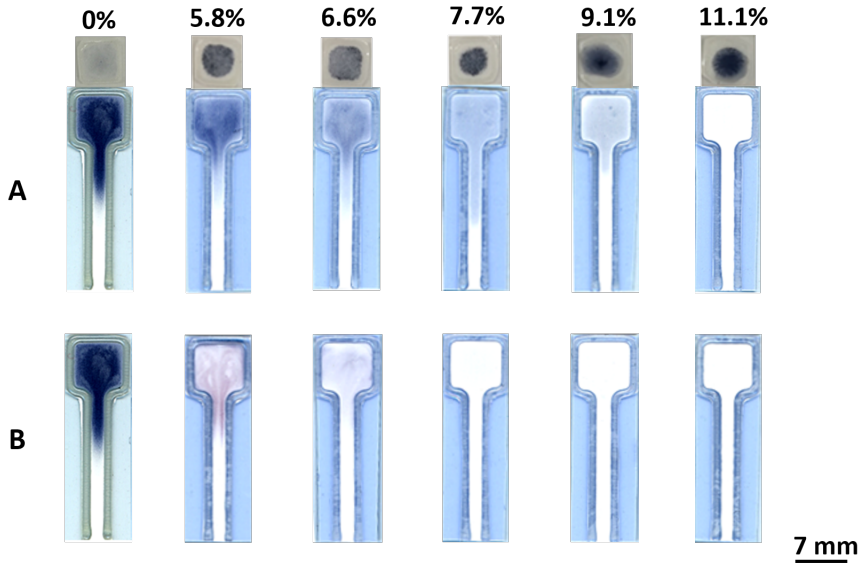

FIGURE 4.3: Flow-through filters tested with 10 µL of sample containing 1000 nm black-dyed polystyrene microspheres suspended in DI water. The LFAs are all identical but the flow-through filters are made with different photo-polymer concentrations ranging from 0% to 11.1%. Images in (A) show the porous filters and the LFAs immediately after the testing process and images in (B) show the same LFAs after the evaporation of the DI water.

the results after testing the flow-through filters with 10 µL of a sample containing black-dyed polystyrene microspheres with a size of 1000 nm. The flow-through filters are all made with different levels of porosity starting from a very porous filter (5.8% photo-polymer in IPA) to a less porous filter (11.1% photo-polymer in IPA). Each of the filters was replicated and tested three times and we also tested a blank filter (0% of photo-polymer in IPA) as a reference in order to show that the cellulose paper itself is incapable of retaining the 1000 nm polystyrene microspheres. The flow-through filters were all positioned at the front end of the LFAs during the testing process as shown in stage 4 of figure 4.1 and were only removed after the completion of the assay to capture photos as presented in figure 4.3. As we can clearly see in figure 4.3A a flow-through filter made with photo-polymer concentration of 11.1% is able to fully retain the 1000 nm polystyrene microspheres preventing their flow into the LFA. However, a more porous flow-through filter made with photo-polymer concentration in the range between 7.7% and 9.1%, is impermeable to the flow of the microspheres but at the same time allows the DI water in which the microspheres are suspended to flow from the filter to the LFA. An even more porous flow-through filter made with photo-polymer concentration below 7.7% is porous to the 1000 nm polystyrene microspheres, enabling the flow of this particle size through the filter and into the channel of the LFA. Looking at the image of figure 4.3A, we observe the formation of a dark region on the surface of the filters after the end of the testing process. This is the result of the porous filters, which delay the flow of the sample and due to electrostatic attractive forces between the polystyrene particles (van der Waals forces), the microspheres aggregate and form a complex bigger than the porosity of the filters, thus are unable to flow through. For the porous filters made with photo-polymer concentration below 9.1%, it is difficult to visually assess, immediately after the testing process, whether the 1000 nm polystyrene microspheres have flowed into the channel of the LFA (figure 4.3A). For that reason, we took photos of the LFAs after the completion of the experiment and when the water had evaporated and these are presented in figure 4.3B in order to assess the ability of the porous filters to block particles larger than a specific size.

Apart from the 1000 nm we also tested polystyrene microspheres of different sizes namely 200 nm, 500 nm and 3000 nm all dispersed in DI water and pictures of them are presented in figure 4.4. We used again the same sample volume of (10 µL) and for each of the different particle sizes and filter porosities we fabricated and tested three identical devices. The results after testing porous flow-through filters made with photo-polymer concentrations in the range between 3.3% and 33.3% with polystyrene microspheres of different sizes are presented in table 4.1. We have defined a transitional range for the photo-polymer concentration (indicated with red in table 4.1) based on the ability of the porous flow-through filters to block particles of different sizes, for which the porous filters transition from being completely impermeable to being porous to particles of a specific size. This transitional range reveals an increasing trend in terms of the v/v% of the photo-polymer concentration and the ability of the filters to block

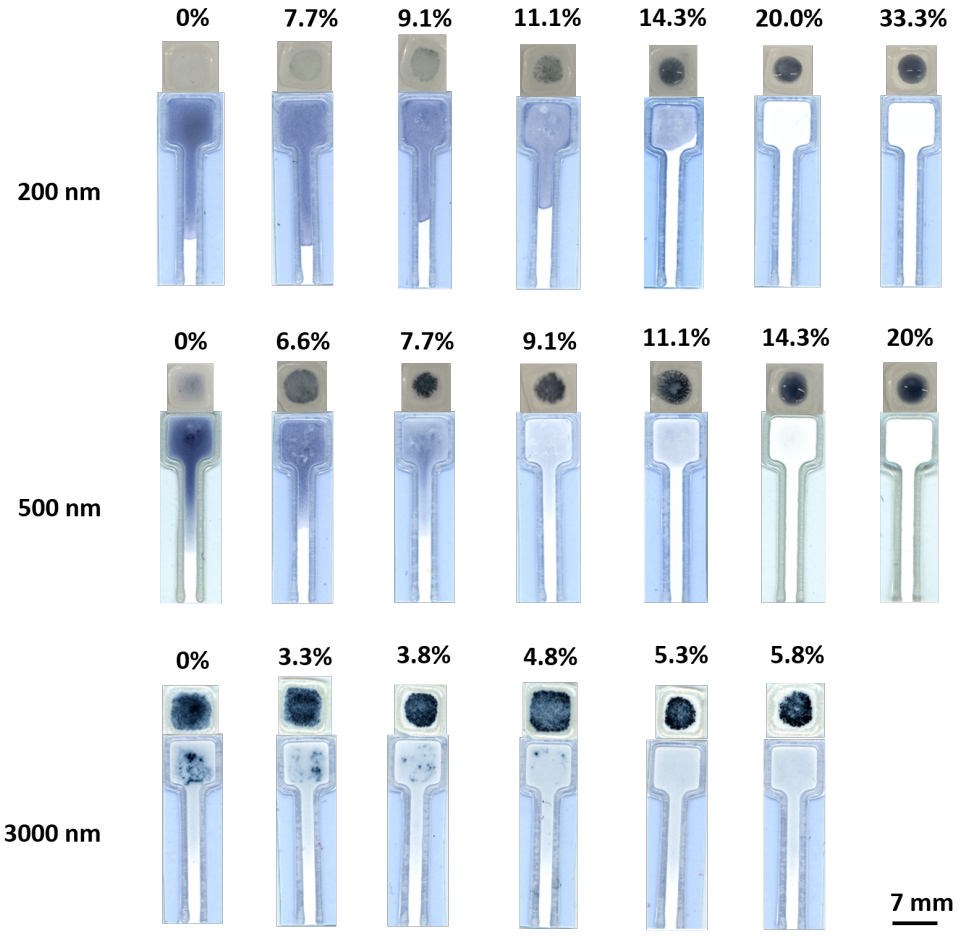

FIGURE 4.4: Flow-through filters made with different photo-polymer concentrations in the range between 3.3% and 33.3%, each one tested with 10 µL of black-dyed polystyrene microspheres of different sizes: 200 nm, 500 nm and 3000 nm. Photos of the flow-through filters and the LFAs are taken immediately after the testing process.

particles decreasing in size. In other words, the smaller the particle size is, the less porous the filter has to be (higher v/v% photo-polymer concentration) in order to be able to prevent the flow through the filter and into the LFA.

The last step in the analysis of the filtration properties of the different porosity flow-through filters is to measure their filtration efficiency when tested with particles varying in size and the results are illustrated in figure 4.5. The particle filtration efficiency is defined as a measure of the performance of the porous flow-through filters when filtering out (retaining on their surface) particles larger than a specific size. The colour analysis of the tested devices to calculate the values for the particle filtration efficiency of the porous flow-through filters was accomplished using Adobe Photoshop. We used the RGB channel in the histogram function of this software and we measured the mean intensity value of the pixels in both the flow-through filters (figure 4.3A) and the LFAs (figure 4.3B). Then we used equation 4.1 to measure the particle's filtration efficiency (%) for the different filter porosities.

TABLE 4.1: Number of flow-through filters with different porosities in which polystyrene microspheres of different sizes will pass through. For each polystyrene microsphere size, we have defined, and marked with red, a transitional range of photo-polymer concentration in which the filters transition from being completely impermeable to being porous.

Photo-polymer concentration (v/v%)	200 nm	500 nm	1000 nm	3000 nm
33.3	0/3	-	-	-
20.0	**0/3**	0/3	-	-
14.3	**3/3**	0/3	-	-
11.1	3/3	0/3	0/3	-
9.1	3/3	**0/3**	0/3	-
7.7	3/3	**3/3**	**0/3**	-
6.6	-	3/3	**3/3**	-
5.8	-	-	3/3	**0/3**
5.3	-	-	-	**1/3**
4.8	-	-	-	**3/3**
3.8	-	-	-	3/3
3.3	-	-	-	3/3

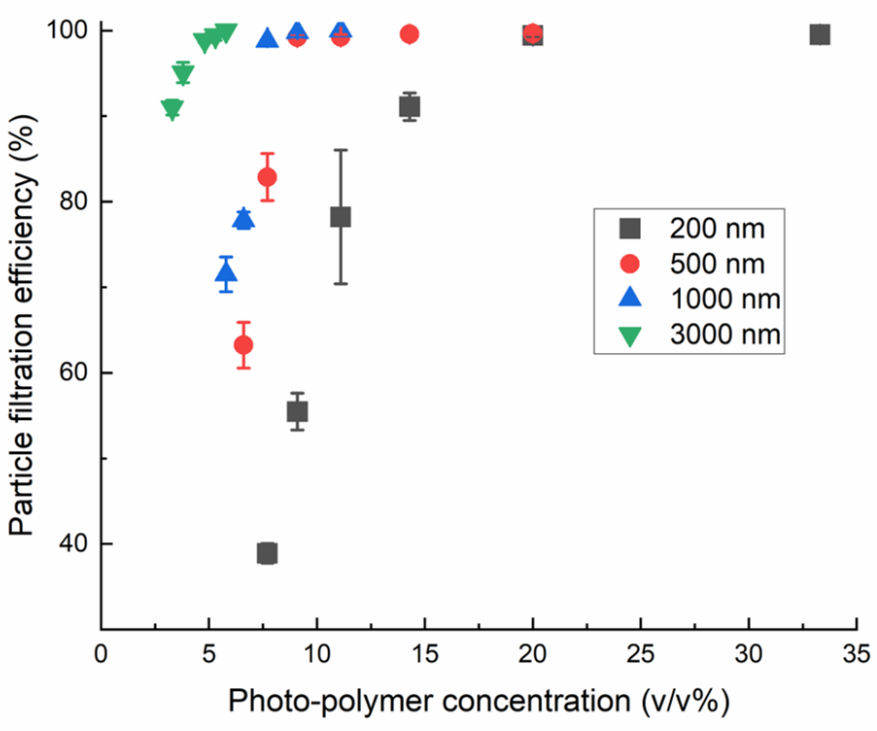

FIGURE 4.5: Particle filtration efficiency of the flow-through filters made with varying photo-polymer concentrations in the range between 3.3% and 33.3% and tested with polystyrene microspheres of different sizes: 200 nm, 500 nm, 1000 nm and 3000 nm.

$$\text{Particle filtration efficiency (\%)} = 1 - \left(\frac{255 - \text{Colour intensity on device}}{255 - \text{Colour intensity on filter}} \right) \times 100 \tag{4.1}$$

The value of 255 corresponds to the pixel intensity of white, which is the background of both the flow-through filter and the LFA before testing of the sample. We calculated the average colour values of the total of three devices for both the flow-through filters and the LFAs and we subtracted these values from 255 to obtain the actual signal intensities.

4.3.2 Flow-through filtration method for analyte detection

The porous flow-through filters that we discussed and analyzed in subsection 4.3.1 can be used in standard LFAs for the detection of analytes using an assay which is based on particle size selection. In this filter-based assay we made the devices using materials that are commonly used in standard LFAs such as cellulose paper (sample pad), nitrocellulose membrane (detection pad) and absorption pad. However, unlike the standard configuration of these materials in an LFA, in our devices we do not make use of a conjugate pad or a sample pad. Instead, these materials were replaced by a porous flow-through filter, which is located at the front end of an LFA as presented in stage 4 of figure 4.1 and can be designed with different porosities.

The detection method is based on the interaction and binding of different-sized Au NPs (40 nm) and latex beads (3 µm) with the same target analyte via antibodies. The flow-through filters were deliberately designed to have a pore size bigger than the size of the Au NPs hence these particles are able to flow through the filter and reach the position of the test line, whereas the latex beads with size bigger than the pore size of the filter are blocked from the filter and are not able to flow into the channel of the LFA. Both the Au NPs and the latex beads capture the analyte and therefore if the analyte is present in the sample (positive test) it will bind to both and form a complex with size of 3 µm and therefore it will be unable to flow through the filter and reach the test line. Only the Au NPs unbound to the analyte which are left in the sample are able to flow through the filter and become captured in the test line of the LFA producing a red coloured line indicating the presence of the analyte in the sample. The principle of operation of this filter-based assay is similar to a competitive-type assay where the absence of the analyte from the sample translates to a strong signal intensity on the test line. On the other hand, when the analyte is present in the sample in different concentrations the signal intensity on the test line varies and the colour ranges from darker for low analyte concentrations to fainter for high analyte concentrations. In the schematic of figure 4.6 we depict the principle of operation of this filter-based assay for the cases of no analyte, low and high analyte concentrations.

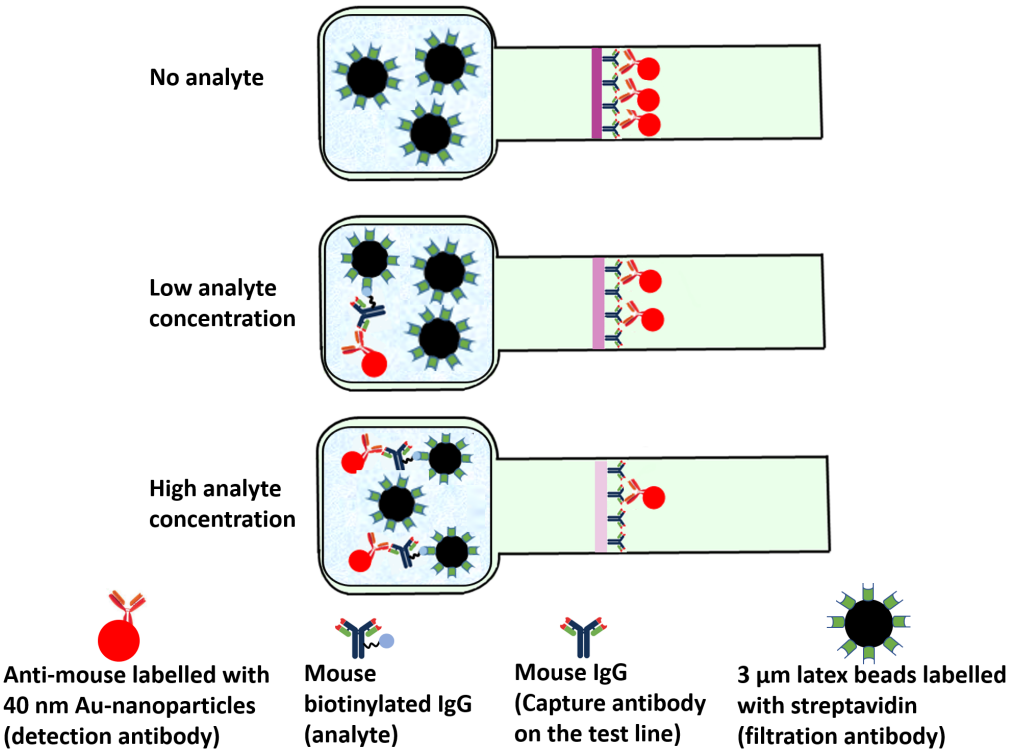

FIGURE 4.6: Schematic showing the detection method in the case of no analyte as well as low and high analyte concentrations. For the case that the analyte is absent from the sample, all the detection antibodies flow through the filter and get captured in the test line producing a strong signal. However, as we increase the concentration of the analyte in the sample, the number of the unbound detection antibodies remaining in the sample decrease and this therefore will result in a decreased signal on the test line.

We tested the performance of this filter-based assay using a porous flow-through filter for the detection of analytes, and for that we prepared a sample containing a 1:1:1 ratio of the following constituents: anti-mouse antibodies labelled with 40 nm Au NPs (used as a detection antibody and diluted in PBS to have a concentration at 100 µg/mL), 3 µm latex beads labelled with streptavidin (stock concentration and used as a filtration antibody) and mouse biotinylated IgG antibody used as the target analyte in concentrations within the range 0–500 µg/mL. In the test line of the LFAs we dispensed and immobilized mouse IgG antibodies (stock concentration) that capture the detection antibodies (figure 4.6).

We tested 20 µL of the sample with flow-through filters made with different photo-polymer concentrations namely 0% (blank filter), 3.8%, 5.3% and 7.7%. In our first demonstration we used a blank filter with 0% photo-polymer concentration and as we can see from the results of figure 4.7 there is no test line appearing on the channel of the LFAs. Instead the detection antibodies accumulated in the bottleneck of the LFAs and are unable to move further along the channel and get captured in the test line. As previously shown in figure 4.4 the cellulose paper itself (0% photo-polymer concentration) is unable to block particles of 3 µm size, hence the latex particles of that size and

consequently the formed complex (detection antibody, filtration antibody and analyte) with similar size, flow through the filter and into the channel of the LFAs. Due to the large amount of latex beads and the formed complex that flow through the filter, the channel is blocked and that prevents the flow of the unbound detection antibodies towards the position of the test line, therefore the test line does not appear. On the other hand, a filter made with 3.8% photo-polymer concentration is porous to the flow of particles with a size of 3 µm and according to the graph presented in figure 4.5 it allows roughly 5% of the particles of that size to flow through. This means that in the

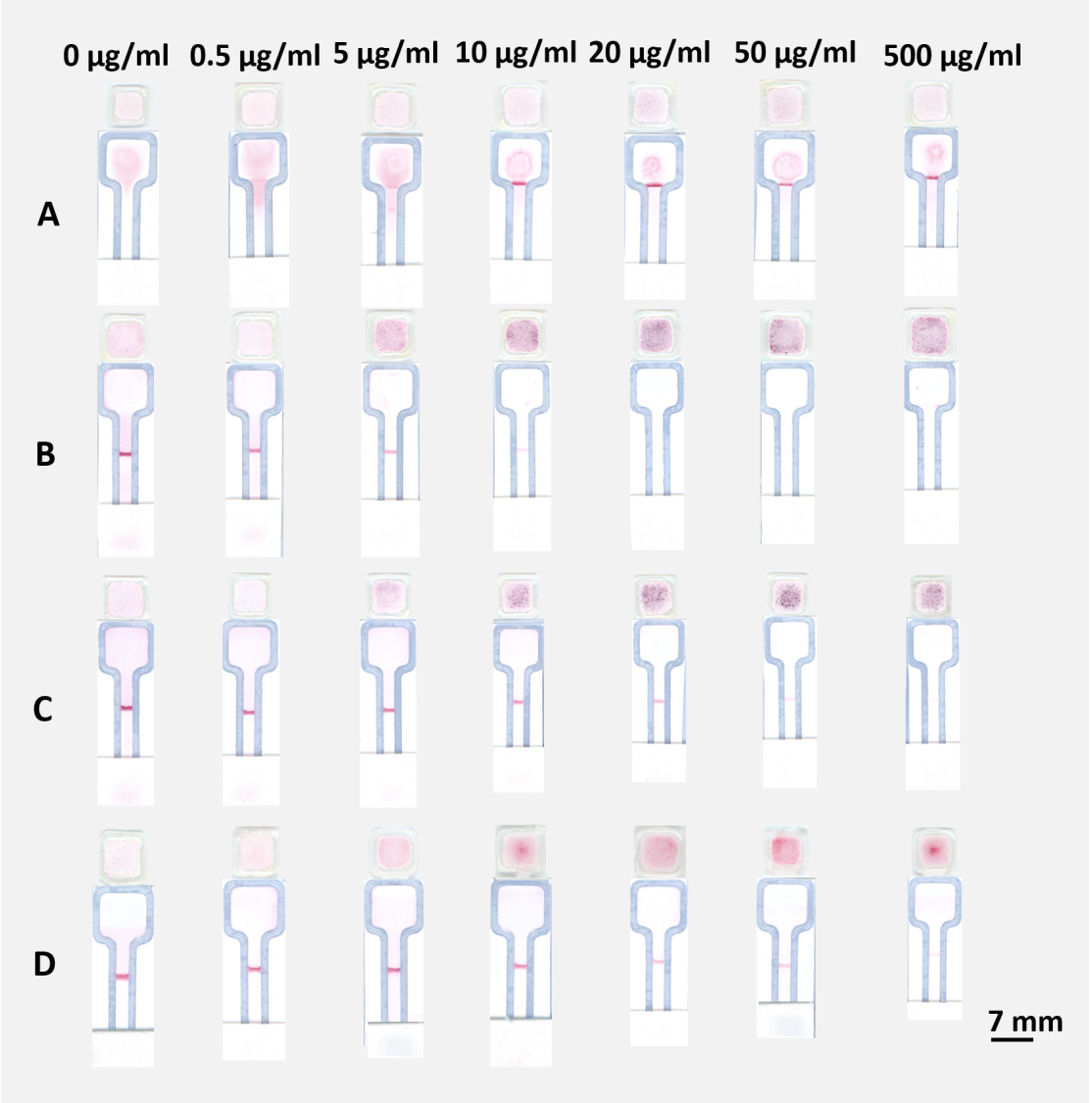

FIGURE 4.7: Flow-through filters made with different photo-polymer concentrations of (A) 0% (B) 3.8% (C) 5.3% and (D) 7.7%. Each of the devices was tested with 20 µL of a sample containing a 1:1:1 ratio of anti-mouse antibodies labelled with 40 nm Au NPs (detection antibody), 3 µm latex beads labelled with streptavidin (filtration antibody) and mouse biotinylated IgG antibody (analyte). The devices were tested for different analyte concentrations in the range between 0 and 500 µg/mL. In the test line of the LFAs we have dispensed and immobilized mouse IgG antibodies which capture the detection antibody.

case that the analyte is present on the sample in high concentrations (above 10 µg/mL) the amount of the formed complex that flows through the filter is sufficient to block the channel and prevent the unbound detection antibodies from getting captured in the test line. In that case we can only visualize a signal within the concentration range 0–10 µg/mL. Lastly, using a porous filter made with photo-polymer concentrations of 5.3% and 7.7% we are able to detect the analyte in the concentration range between 0–500 µg/mL. However, we observe that, using a filter made with 7.7% photo-polymer concentration, we get a stronger signal on the test line as compared with the signal that we visualize when using a filter made with 5.3% photo-polymer concentration. We believe that this happens because a filter made with 5.3% photo-polymer concentration falls within the transitional range in which the filter transitions from being completely impermeable to being porous to particles with size at 3 µm (see table 4.1).

In figure 4.8 we present a graph showing the signal intensity on the test line of the LFAs relative to the concentration of the analyte in the cases that the sample was tested with filters of different levels of porosity. Each data point on this graph represents the mean colour intensity value from the total of three devices. The method that we followed

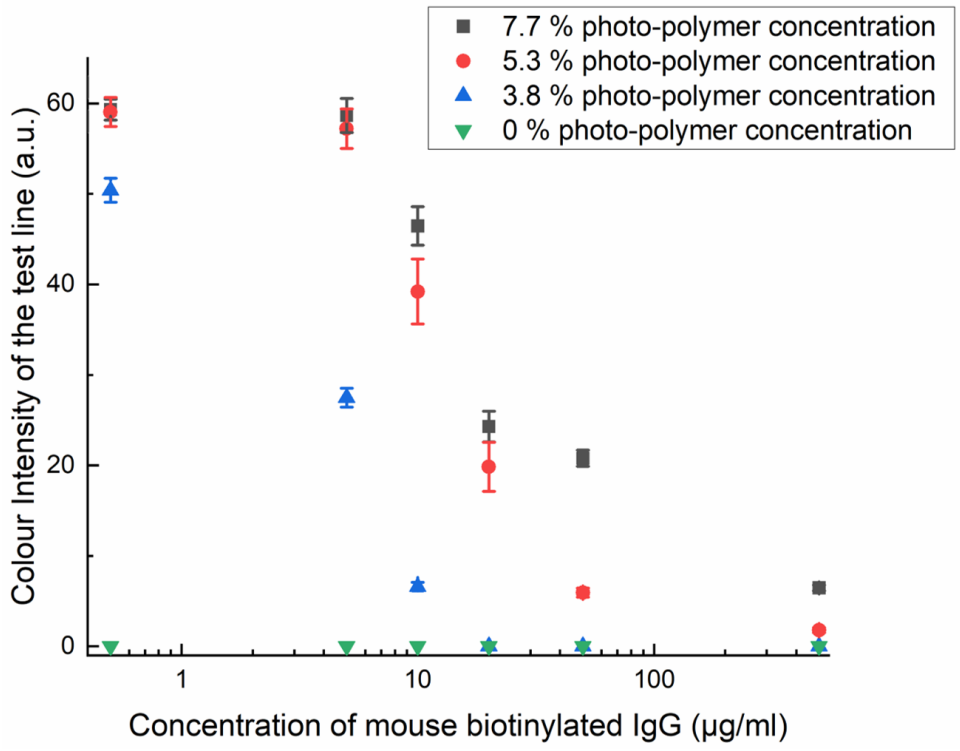

FIGURE 4.8: Colour intensity on the test line of the LFAs relative to the concentration of the mouse biotinylated IgG (analyte) presented in the sample. The analyte was tested in a concentration range between 0 and 500 µg/mL and the flow through filters used for this assay are made with photo-polymer concentrations at 0%, 3.8%, 5.3% and 7.7%.

to calculate the signal intensity on the test line is the same to the one presented in subsection 3.3.6.

4.3.3 Filter-based immunoassay for CRP detection

The performance of the porous flow-through filters was tested on an immunoassay for the detection of the CRP. In this immunoassay we tested a sample containing the following constituents in a 1:1:1 ratio: human CRP (analyte) with concentration in the range between 10 and 100.000 ng/mL, mouse anti-human CRP antibody labelled with 40 nm Au NPs (stock concentration) used as a detection antibody and mouse anti-human CRP biotinylated IgG antibody tagged with 3 µm latex beads labelled with streptavidin (stock concentration) used as a filtration antibody. In the test line of the LFAs we dispensed and immobilized goat anti-mouse IgG antibodies (stock concentration) that capture the unbound detection antibodies. The excess of the sample which flows over the test line, accumulates on an absorbent pad located at the end of the LFAs.

We tested 20 µL of the sample on devices with porous filters made with 7.7% photo-polymer concentration. A filter made with that concentration is not only capable of completely blocking particles with size of 3 µm (see table 4.1) but also able to detect an analyte (e.g. CRP) within 3 minutes in a broad dynamic concentration range as shown in figure 4.7D. Using a less porous filter made with photo-polymer concentration higher than 7.7% will delay (or even block) the flow of the sample through the filter, therefore increase the analyte detection time to several minutes. On the other hand, a filter made with photo-polymer concentration lower than 7.7% and within or above the transitional range for the flow of particles with size at 3 µm will result in a decrease in the concentration range (figure 4.7B) or the intensity of the signal (figure 4.7C) in which the analyte can be detected.

The principle of operation of this assay is the same to the one previously described and figure 4.9 shows a schematic of the assay designed to detect CRP. In the case that the analyte is not present in the sample, the detection antibodies flow through the filter and get captured at the test line producing a strong coloured signal. However, if the analyte is present in the sample, it binds with both the detection antibody and the filtration antibody forming a complex with a size of 3 µm which is unable to flow through the filter. In that case, only the unbound detection antibodies left in the sample are able to flow through the filter and get captured at the test line producing a coloured signal proportional to the concentration of the analyte in the sample.

Figure 4.10 depicts the results when 20 µL of the sample containing the CRP in different concentration between 0–100.000 ng/mL was tested on porous flow-through filters made with 7.7% photo-polymer concentration. The respective colour intensity of the test line for the different analyte concentrations is presented in figure 4.11 and each

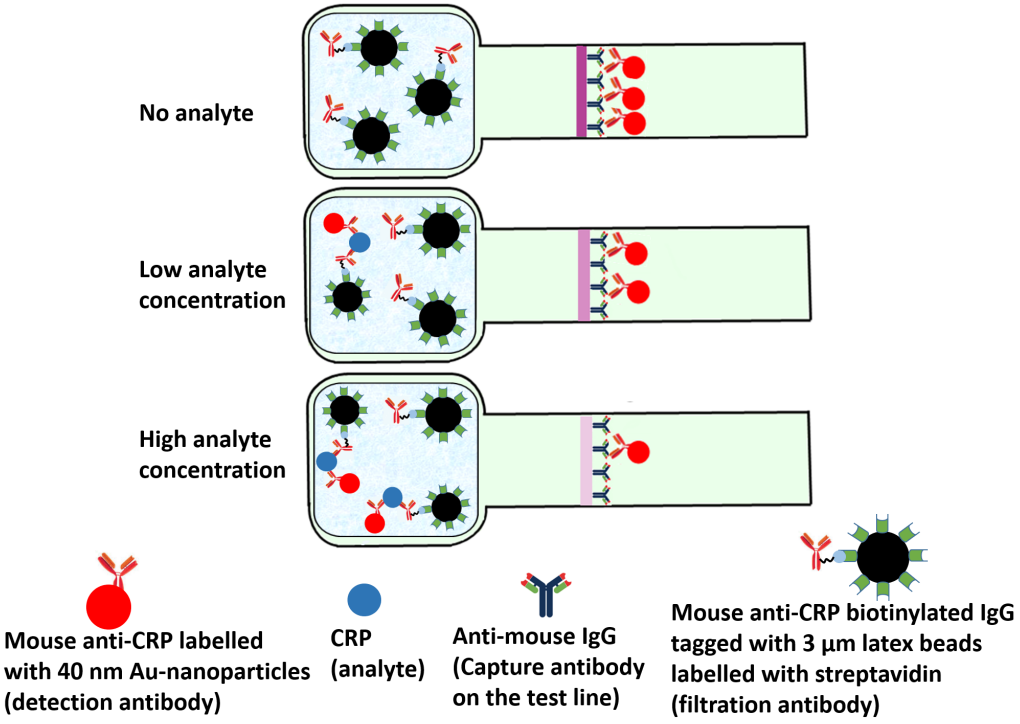

FIGURE 4.9: Schematic showing the method for the detection of the CRP. The target analyte, CRP, binds to two antibodies (detection and filtration antibody) each one tagged with different-sized coloured labels forming a complex which is unable to flow through the filter. Only the unbound detection antibodies flow through the filter and get captured at the test line producing a coloured signal which varies according to the concentration of the CRP in the sample.

data point is the mean value from the total of three tested devices. The mean colour intensity of the control device 0 ng/mL) corresponds to a value of 46.18 a.u. From the previous results, we can see that the colour intensity on the test line is changing relative to the concentration of the analyte in the tested sample. Similar to the previous experiment, an increase in the concentration of the CRP will result in an increase in the number of the complexes (analyte-detection antibody-filtration antibody) that are being formed and therefore, the number of the unbound detection antibodies left in the sample which flow through the filter and get captured on the test line is decreasing. As a result, an increase in the concentration of the analyte will result in a decrease in the intensity of the signal on the test line and in the extreme case of very high analyte concentration (e.g. 100.000 ng/mL) the CRP captures the filtration antibody and all the detection antibodies and as a result there is no test line appearing in the channel of the LFA. Using this filter-based method we are able to detect the CRP in the concentration range between 0–50.000 ng/mL with a LOD found at 13 ng/mL.

The method that we used to measure the colour intensity in the test line of the LFAs is the same as the one that we used in the subsection 4.3.2 where the equation 3.3 was used in order to extract the actual intensity values. In order to calculate the LOD we

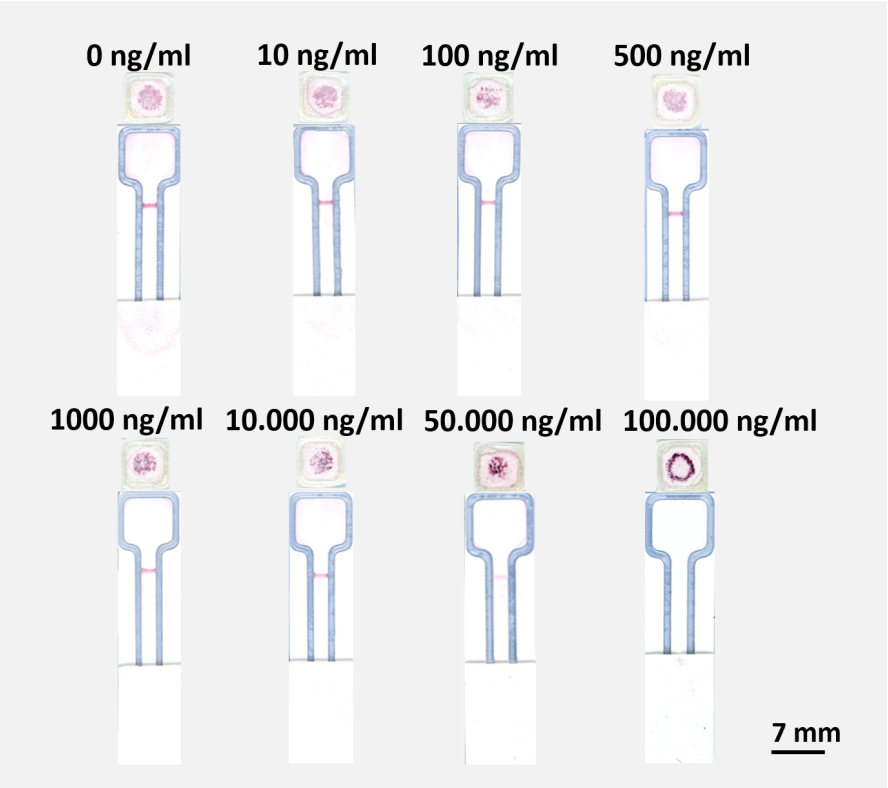

FIGURE 4.10: Flow-through filters made with photo-polymer concentrations of 7.7%. Each one of the filters was tested with 20 µL of a sample containing the CRP (analyte), mouse anti-CRP antibody labelled with 40 nm Au NPs and mouse biotinylated IgG antibody labelled with 3 µm latex beads. Numbers indicate the concentration of the analyte in the tested sample ranged from 0 to 1000 µg/mL. In the test line of the LFA we have dispensed and immobilized anti-mouse IgG antibodies.

used equation 4.2 where σ refers to the standard deviation of the regression line and s refers to the slope of the calibration curve. Both of these parameters were calculated from the graph of figure 4.11 and have values of 4.3 for σ and 1.1 for s.

$$\text{LOD} = 3.3 \times \left(\frac{\sigma}{\text{s}}\right) \tag{4.2}$$

To summarize, we can successfully apply the flow-through filtration method in an assay for the detection of CRP over a broad concentration range which is beyond the threshold value of 500 ng/mL that the hook effect is observed in LFAs [16, 27, 28, 29]. In this study we did not measure the threshold value above which the hook effect is observed as we cannot use the same detection and capture antibodies for a direct comparison. However, since the three repeats (for each of the different analyte concentrations) produce the same answer, we know that our proposed method is able to operate accurately and detect CRP in the range between 10–50.000 ng/mL.

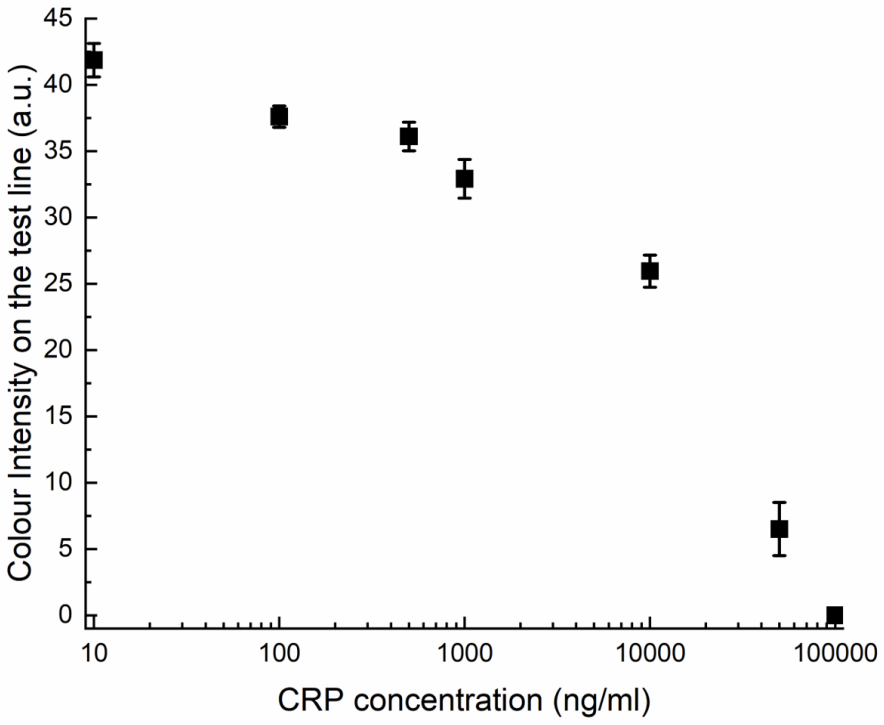

FIGURE 4.11: Colour intensity in the test line of the LFA for various CRP concentrations in the range between 1 ng/mL and 100.000 ng/mL.

4.3.4 Flow-through filters for the separation of plasma from whole blood

The flow-through filtration method was further tested for the separation of plasma from human blood. In this experiment we tested human blood acquired from the same donor that was previously reported in chapter 7.3. The blood sample comes from a healthy patient and belongs to the group A with RhD positive (A+). For the purpose of this experiment, we fabricated flow-through filters with photo-polymer concentration in the range between 3.3% and 6.2% and each one was tested with 10 µL of sample. Our choice to fabricate flow-through filters with photo-polymer concentrations close to the transitional range for the flow of particles with size of 3 µm (see table 4.1), stems from the fact that the RBCs have size approximately 6–9 µm and are able to squeeze through capillaries less than half their size [30]. We believe that a porous filter capable of retaining (or delaying) the flow of particles with a size of 3 µm will be able to separate the plasma from the RBCs. We did not make less porous filters with photo-polymer concentrations higher than 6.2% as this would result in a delay in the flow of the sample through the porous filters and consequently in a condition of low rate of blood flow. We know [31] that under this condition the shear stress of the RBCs is increasing and this leads to their aggregation and formation of clusters which can block the pores of the filter preventing the plasma from flowing into the channel of the LFA.

In figure 4.12 we present the results after testing 10 µL of sample with flow-through filters made with varying photo-polymer concentrations. As we can see, a filter made with 0% photo-polymer concentration (blank filter) is incapable of preventing the flow of the sample into the LFA. However, when the sample is tested with porous flow-through filters made with photo-polymer concentrations in the range between 3.3–6.2 %, we observe that the amount of the blood sample which flows through the filters and into the LFAs is decreasing with a decrease in the filter's porosity and is blocked when tested with a filter made with 6.2% photo-polymer concentration. Unlike what we expected to see, in none of the cases did we observe any separation of the plasma from the RBCs which is the result of the filtration method that we used and the respective porosity of the flow-through filters. A filter made with 6.2% photo-polymer concentration is porous enough to delay the flow of the sample through its pores and as previously mentioned this might result into the aggregation of the RBCs which consequently block the pores of the flow-through filter. Another reason could be that the other components found in blood such as the leukocytes and the platelets blocked the pores of the filter thus preventing the plasma extraction. More porous filters made with photo-polymer concentrations between 3.3% and 5.5% have effective pore sizes bigger than the size of the RBCs which eventually squeeze through the pores of the filters and end up into the channel of the LFAs.

Following on from our previous experiment, this time we fabricated flow-through filters with photo-polymer concentrations in the range between 0% and 5.5% which we know are porous to the flow of the RBCs. We tested each one of the filters with the same blood sample that we previously used but this time pre-treated with Anti-D solution. We believe that the agglutination of the RBCs will lead to the formation of a big complex which will get blocked from the porous filters, allowing only the plasma to flow through and into the LFA. For the purpose of this experiment, we mixed 20 µL of

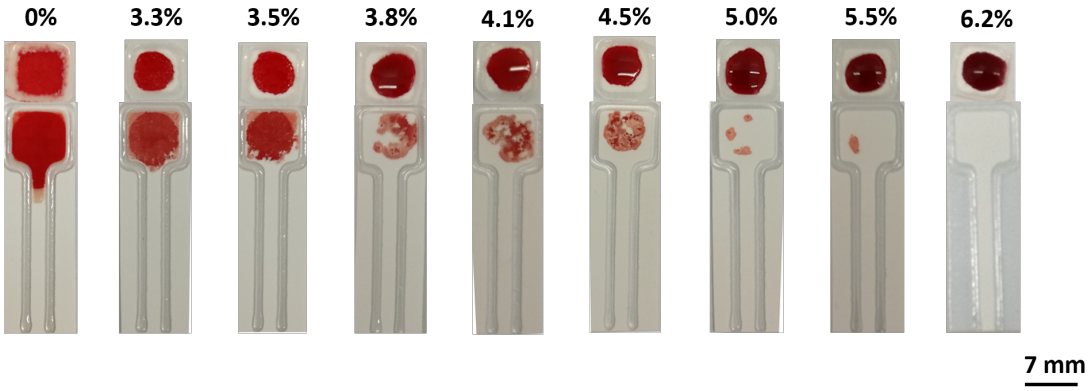

FIGURE 4.12: Flow-through filters fabricated with photo-polymer concentration in the range between 3.3% and 6.2% and tested with 10 µL of human blood. The filters of varying porosities as well as a blank filter made with 0% photo-polymer concentration are incapable of separating the plasma from the RBCs.

blood with 4 µL of Anti-D solution (1:5 *v/v* in ratio) and after leaving the sample for 5 minutes to rest and allow the agglutination of the RBCs we tested 10 µL.

In figure 4.13A we see images of the flow-through filters and the LFAs after the testing process. As we can see, for the filters made with photo-polymer concentrations at 4.5% and higher the aggregated RBCs are getting blocked from the filters and only the plasma flows trough and ends up in the LFA. However, filters made with 4.1% photo-polymer concentrations and below, have pore sizes bigger than the size of the aggregated RBCs and consequently the red cells end up into the LFA and can be seen as red spots located in the front end of the device. Only for the porous flow-through filters which were successful for blocking the RBCs, we calculated the plasma extraction efficiency and the results are shown in table 4.2.

In order to measure the plasma extraction efficiency, we followed a method in which we compared the area to which the extracted plasma has spread on an LFA against the area that a known volume of plasma has spread over an LFA with the same geometry. For that we deposited 5 µL of plasma at the front end of an LFA and then using the RGB channel in the histogram function of Adobe Photoshop, we calculated the number of pixels corresponding to the area that the 5 µL of plasma has spread. Next, we

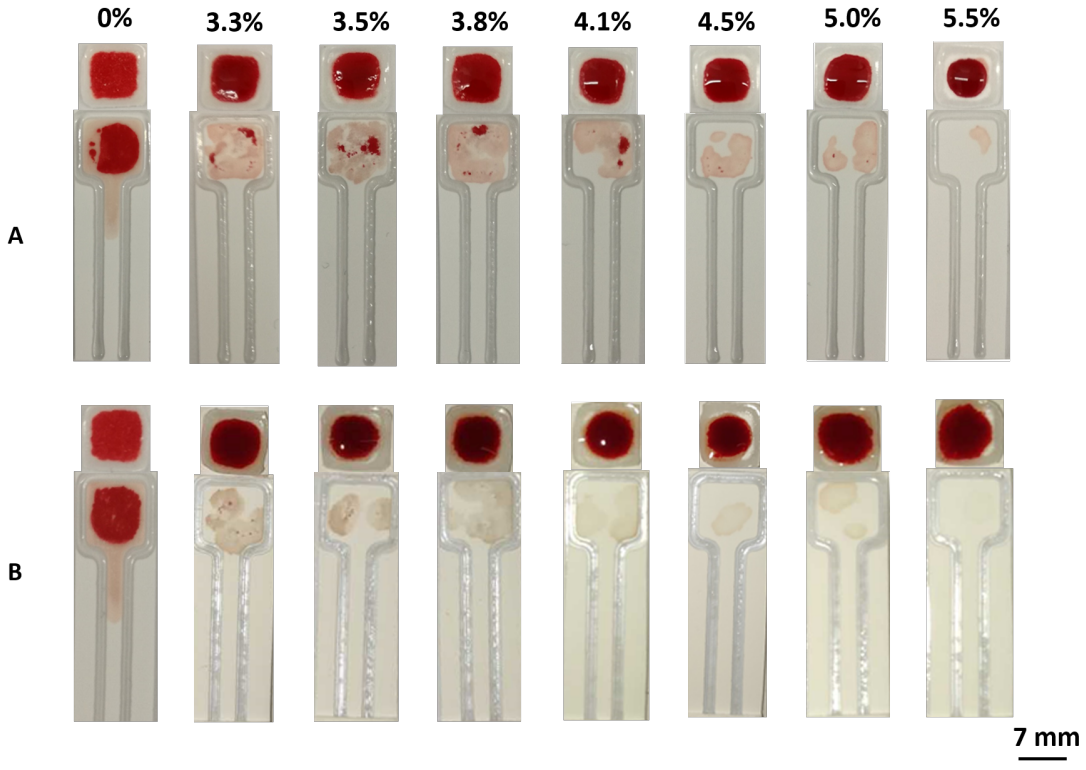

FIGURE 4.13: Flow-through filters fabricated with photo-polymer concentration in the range between 0% and 5.5% are tested with human blood which is pre-treated with Anti-D solution. Images show the results after testing (A) 10 µL of blood sample pre-treated with Anti-D solution in a ratio 1:5 *v/v* and (B) 20 µL of blood pre-treated with Anti-D solution in a ratio 1:4 *v/v*.

repeated the same process this time for the filters tested with human blood in order to calculate the number of pixels corresponding to the area that the unknown volume of the extracted plasma has spread to in the front end of the LFAs. With this method, and by comparing the number of pixels in both cases, we were able to calculate the extracted volume of plasma for filters of different porosities. Given the fact that the plasma constitutes 55% of human blood, we know that in 10 µL of blood sample there is 5.5 µL of plasma and by comparing this value with the volumes of the extracted plasma that we previously calculated, we are able to measure the plasma extraction efficiency (%).

In table 4.2 we present the results of the extracted volume of the plasma and the relative extraction efficiency calculated for the different filter porosities when tested with 10 µL of blood. We observe that the extraction efficiency is low and roughly reaches the 50% level despite the fact that the blood was pre-treated with an Anti-D solution to allow the aggregation of the RBCs. We believe that the low levels of the plasma extraction could be the results of the small volume of the Anti-D solution that we treated the blood sample with. Using a small volume of Anti-D leaves unbound (free) RBCs that block the pores of the porous filters would prevent further plasma extraction.

In the next experiment we increased the volume of the Anti-D solution that we pre-treated the blood sample with in order to increase the amount of aggregation of the RBCs. Furthermore, we increased the volume of the tested sample to 20 µL to increase the plasma extraction efficiency. The protocol that we used for the sample treatment remained the same as before and 20 µL of blood were mixed with 5 µL of Anti-D solution (in ratio 1:4 *v/v*). The sample was left for 5 minutes to rest to allow the aggregation of the RBCs before 20 µL of that sample were tested with filters of different porosities in the range between 0–5.5 %. The results after the testing process are presented in figure 4.13B. At first glance we observe that the amount of the agglutination of the RBCs has increased as compared with the amount of aggregation we had when the blood was pre-treated with Anti-D solution in ratio 1:4 *v/v* (figure 4.13A). The previous statement is evident by the fact that filters made with photo-polymer concentrations in the range between 3.3–4.1 % are now able to completely block the aggregated RBCs (no red spots

TABLE 4.2: Flow-through filters made with different photo-polymer concentrations in the range between 4.5–5.5 % and each one tested with 10 µL of human blood. The blood sample was pre-treated with Anti-D solution in ratio 1:5 *v/v*. The extracted volume of plasma as well as the plasma extraction efficiency were calculated for each one of the different filters.

Photo-Polymer concentration (v/v%)	**Extracted volume (µL)**	**Plasma extraction efficiency** (%)
4.5	2.8	50.6
5.0	2.4	44.6
5.5	0.3	5.1

observed) allowing only the flow of the plasma into the LFAs. It is also worth mentioning here that the colour of the extracted plasma for filters tested with blood pre-treated with Anti-D solution in ratio 1:5 *v/v* (4.13A) tends to be darker as compared with the colour of the extracted plasma of the filters tested with blood pre-treated with Anti-D solution in a ratio 1:4 *v/v* (4.13B). This could be the result of the increased volume of the Anti-D solution which in the latter case leaves a smaller amount of unbound red blood cells which end up in the LFA along with the plasma.

The method that we followed to measure the plasma extraction efficiency is the same as the one that was previously described. The results after the calculation of the extracted volume of plasma as well as the extraction efficiency of the different porosity filters are shown in table 4.3. As we can clearly see, from the total of 20 µL of the tested sample, the extraction efficiency of plasma ranges between 12.5% and 44.7% which is roughly at the same levels as the extraction efficiency we achieved in the previous experiment. The increase in the volume of the Anti-D solution that we used to pre-treat the blood resulted only in the increase in the amount of aggregation of the RBCs. We proved that the increase in the amount of aggregation of the RBCs is not associated with an increase in the extraction efficiency of plasma, as we initially thought it will be, and we believe that this is the result of the aggregated RBCs which block the pores of the porous filters preventing any further plasma extraction. Given the fact that the increase in the volume of the tested sample also did not contribute to an increase in the extraction efficiency of plasma, we conclude that using our developed filter-based method for the separation of plasma from Anti-D solution pre-treated human blood has a 50% maximum plasma yield.

In order to explore different pathways for the increase of the plasma extraction efficiency, in our next demonstration we used a stacking pad method. In this approach two porous flow-through filters are placed on top of each other to form a stacking pad design which is located at the front end of an LFA. With this design we aim to increase

TABLE 4.3: Flow-through filters made with different photo-polymer concentrations and tested with 20 µL of human blood pre-treated with Anti-D solution in a ratio 1:4 *v/v*. The extracted volume of plasma as well as the extraction efficiency of the different porosity filters were calculated and presented in the table.

Photo-Polymer concentration (v/v%)	**Extracted volume (µL)**	**Plasma extraction efficiency** (%)
3.3	4.1	37.6
3.5	2.7	24.5
3.8	4.9	44.7
4.1	3.4	31.3
4.5	1.4	12.5
5.0	1.9	17.9
5.5	1.4	13.0

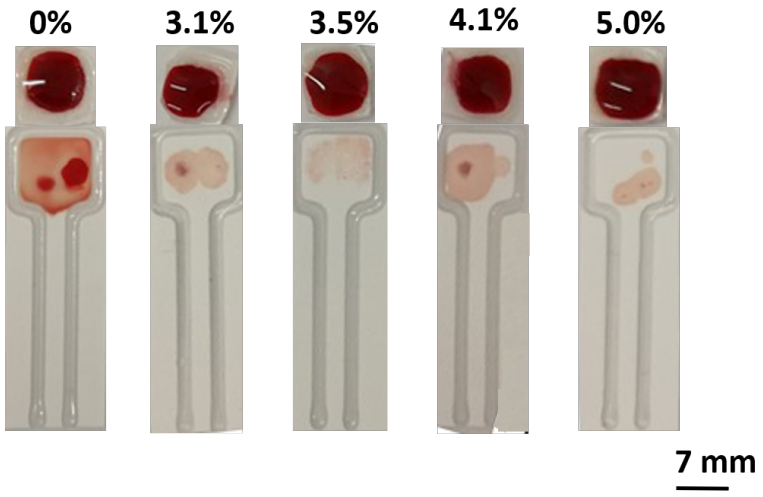

FIGURE 4.14: Stacking pads made with different photo-polymer concentrations in the range between 0–5.0 %. Each stacking pad consists of two porous flow-through filters of the same porosity which are placed on top of each other. Each of the stacking pads was tested with 20 µL of blood pre-treated with Anti-D solution in ratio 1:4 *v/v*.

the thickness of the porous filter and therefore the area through which the sample flows. We believe that with this alternative we will be able to delay the flow of the RBCs through the filter and prevent them from blocking its pores, therefore increasing the plasma extraction efficiency. For the purpose of this experiment we fabricated and stacked two porous filters of the same porosity, each one made with a photo-polymer concentration in the range between 0–5.0 %. Each of the stacking pads was later tested with 20 µL of blood pre-treated with Anti-D solution in a ratio 1:4 *v/v*.

The results after the testing process are depicted in figure 4.14. As we can see, the stacking pad method is successful in filtering out the agglutinated RBCs allowing only the plasma to flow through and into the front end of an LFA. However, looking at the results in table 4.4 where we calculated the volume of the extracted plasma as well as the extraction efficiency of the stacking pads (using the same method that we previously

TABLE 4.4: Plasma extraction efficiency and the respective volume of the extracted plasma using the stacking pad method. The stacking pads are made with different photo-polymer concentrations in the range between 3.1–5.0 % and each one tested with 20 µL of pre-treated with Anti-D solution blood (1:4 *v/v* in ratio).

Photo-Polymer concentration (v/v%)	**Extracted volume (µL)**	**Plasma extraction efficiency** (%)
3.1	2.6	23.5
3.5	3.2	29.0
4.1	3.3	30.3
5.0	1.4	13.2

described) we observe that for the different porosities of the stacking pads the maximum yield does not exceed the threshold of 30.3%. If we compare this value with the maximum yield of the previously reported methods, we conclude that this approach does not offer significant advances in terms of an increase in the extraction of plasma.

In our last demonstration of using the porous flow-through filters to separate the plasma from the RBCs, we used again the previously described stacking pad method but this time we stacked filters with different porosities. In this approach we used a stack of filters each one made with a different photo-polymer concentration and decreasing pore size starting from the top layer which is the more porous and moving to intermediate layer(s) with lower porosity and finally to the bottom layer which is the least porous as presented in figure 4.15 and table 4.5. By gradually changing the porosity of the flow-through filters and creating a stack with an asymmetric inner structure, we aim to delay the flow of the RBCs while allowing the plasma to penetrate throughout the whole thickness of the stacking design and end up in an LFA. In contrast with the previous methods, in this approach we want to gradually delay and prevent the flow of the RBCs and we can achieve that by increasing the area, when adding 3, 4 and 5 layers, through which the blood sample flows. A medium with an asymmetric inner structure, similar to the one presented in this study, already exists as a commercial product in the market (Vivid^{TM} Plasma Separation membrane) and it is used for the separation of plasma from human blood with $\geq$ 80 % plasma yield in less than 2 minutes. There are reported methods in the literature [32], [33] that make use of this plasma separation membrane with a plasma yield of 60% or larger when whole blood is tested. Our end goal is to fabricate a similar device using our developed flow-through filtration method and study the effect of having multiple layers of different

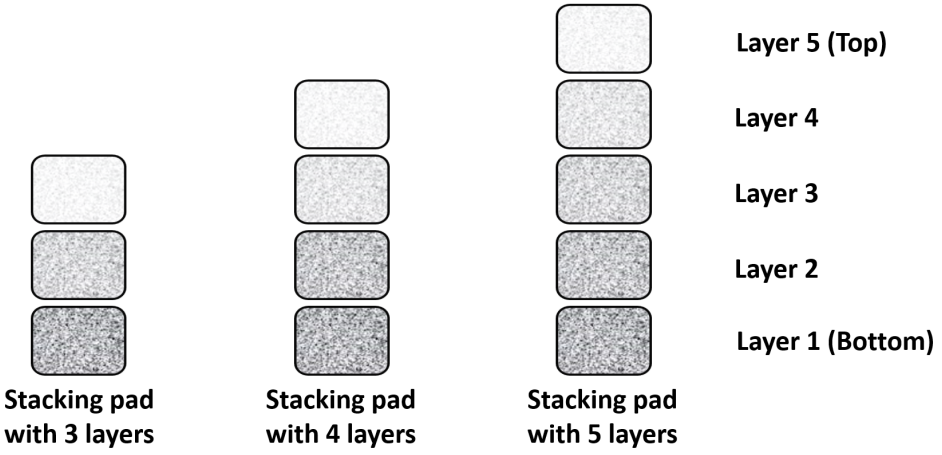

FIGURE 4.15: Stacking pad designs with 3, 4 and 5 layers of cellulose paper. Each one of the porous filters is made with a different photo-polymer concentration and their porosity is decreasing as we move from the top layer (very porous), to the intermediate layer(s) (less porous) and then to the bottom layer (least porous).

TABLE 4.5: Photo-polymer concentration of each layer in a stacking pad design consisting of 3, 4 and 5 layers of cellulose paper respectively.

Layer	Photo-polymer concentration (3 layers)	Photo-polymer concentration (4 layers)	Photo-polymer concentration (5 layers)
Layer 5	3.5%	2.9%	2.9%
Layer 4	-	3.3%	3.1%
Layer 3	4.3%	-	3.3%
Layer 2	-	3.5%	3.5%
Layer 1	5.5%	4.1%	3.8%

porosities in the extraction of plasma.

In figure 4.16 we present the results after the testing process where stacking pads fabricated with 3, 4 and 5 layers were tested with 20 µL of whole blood (figure 4.16A) as well as the same volume of sample as before but this time pre-treated with Anti-D solution in ratio 1:4 (figure 4.16B). From the results we can clearly see that this method is unsuccessful for the separation of plasma from RBCs. Unlike what we expected to see, in none of the cases did we observe any plasma in the front end of the LFAs and this

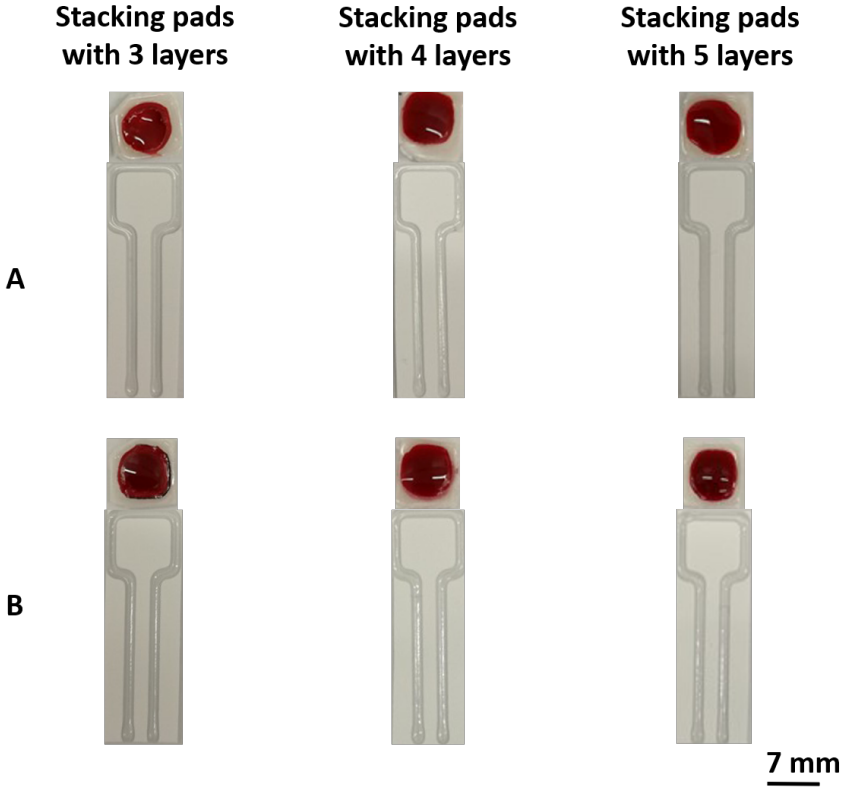

FIGURE 4.16: Stacking pads made with 3, 4 and 5 layers of porous filters each one made with a different photo-polymer concentration. The stacking pads were tested with A) 20 µL of whole blood and B) 20 µL of blood pre-treated with Anti-D solution in ratio 1:4 *v/v*.

could be the result of the reported testing method in which the RBCs and/or the leukocytes and the platelets blocked the pores of the stacking pads preventing the extraction of plasma.

4.3.5 Flow-through filters tested with bacteria

In our last demonstration of using the porous flow-through filters we tested a water-based solution containing E. coli bacteria. The aim of this experiment is to design porous flow-through filters able to retain E. coli while allowing PBS, in which the bacteria are suspended, to flow through and collected into a pad (cellulose paper).

The concentration of the bacteria is defined as a colony-forming unit (CFU), a common method used in microbiology which is based on the number of viable bacteria in a sample. For that we used 10 µL of the bacteria suspension with a dilution factor of 10^5 on an agar plate and we counted 433 colonies (figure 4.17). Then using equation 4.3 we calculated the stock concentration of the bacteria which has a value of 4.33×10^9 CFU/mL.

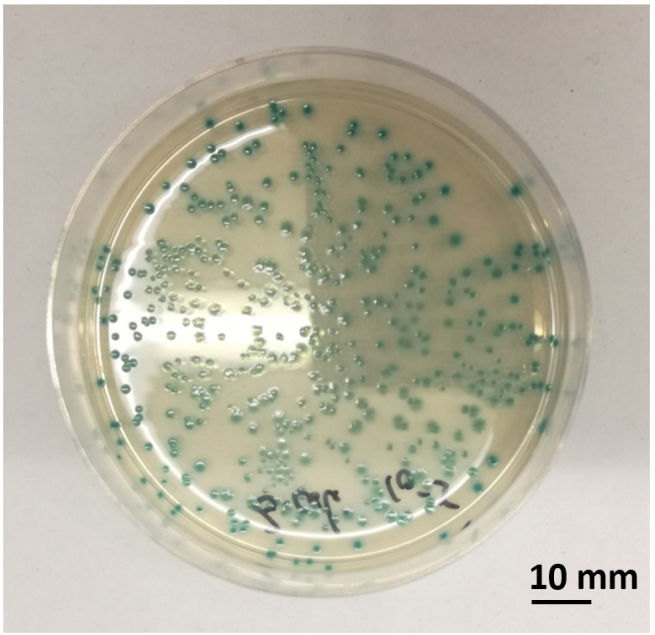

FIGURE 4.17: Image showing the growth of E. coli on an agar plate when diluted in PBS with a dilution factor of 10^5 after an overnight (18 hours) incubation at 37 °C.

$$\text{Bacteria concentration (CFU/mL)} = \frac{\text{CFU counting} \times \text{dilution factor}}{\text{volume of bacterial suspension}} \tag{4.3}$$

During the testing process, 15 µL of the bacteria solution were used with flow-through filters of different porosities. In figure 4.18 we present the results when three identical flow-through filters each one made with the same photo-polymer concentration of 5.8 % were tested with the bacteria solution. During the testing process the porous filters were positioned on top of the collection pads (figure 4.18A) and were only removed after the end of the testing process to capture photos as shown in figure 4.18B. As we can clearly see the PBS has been collected in all the three pads, however we are unable to visualize the growth of bacteria on the paper unless we incubate the collection pads at a certain temperature. For the purpose of this experiment, we placed both the flow-through filters and the collection pads on agar plate and incubated for 18 hours at temperature of 37 °C in order to be able to visualize the bacteria colonies. We repeated the same process with porous filters made with different photo-polymer concentrations (each one replicated three times) in the range between 0–25 % and the results after the incubation are depicted in figure 4.19.

From the results we observe that on top of all the flow-through filters the bacteria has grown, however only those made with photo-polymer concentration at 5.3% and below are porous enough to allow the penetration of E. coli which has grown into the collection pads. Although the porous filters made with photo-polymer concentration at 5.8% and above, allowed the flow of PBS (similar to figure 4.18B), they are impermeable to the flow of the bacteria therefore there is no growth in the collection pads.

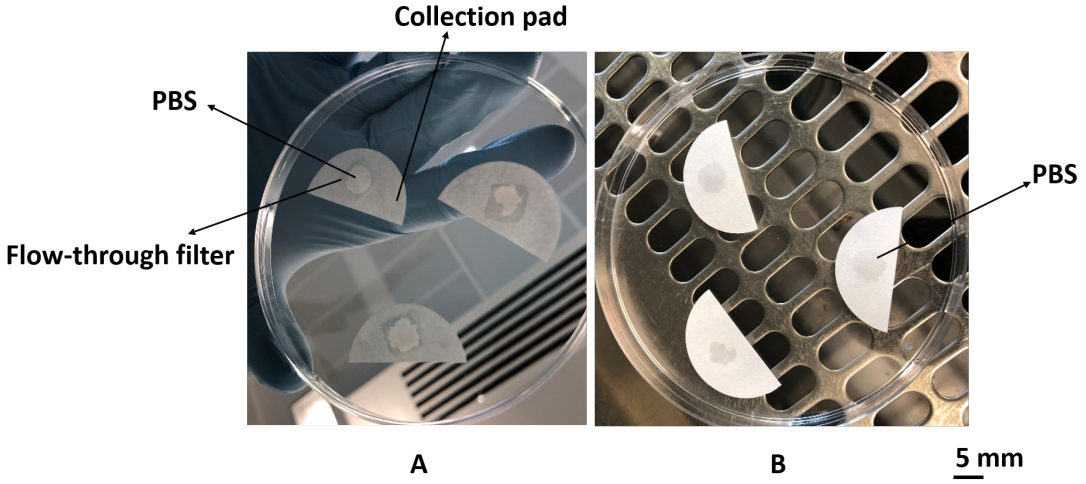

FIGURE 4.18: (A) Three identical flow-through filters each one made with the same photo-polymer concentration of 5.8% and tested with 15 µL of a water-based solution of E. coli. The image is showing the position of the flow-through filters on top of the collection pads during the testing process. (B) Image showing the pads after the testing process where the PBS has been collected.

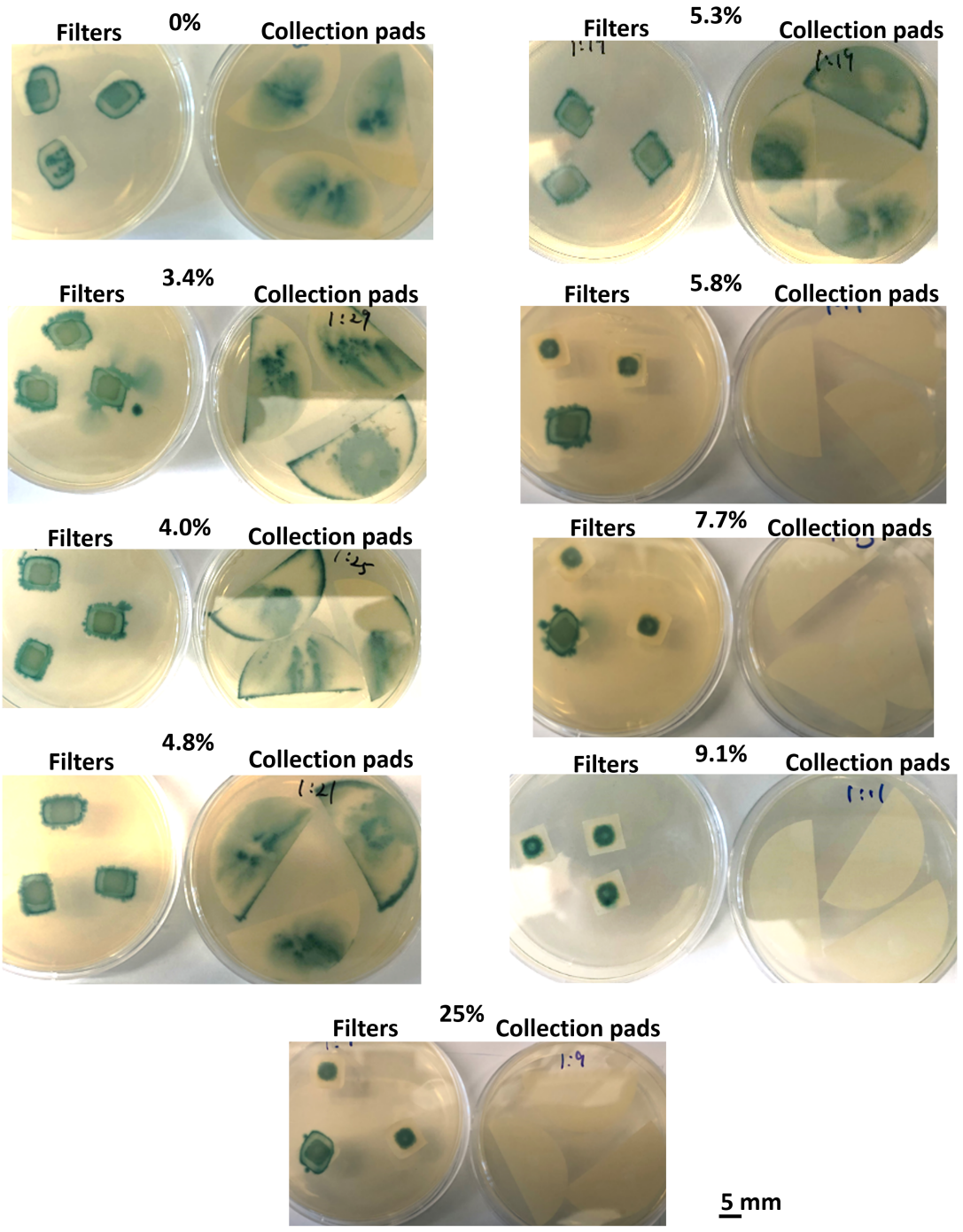

FIGURE 4.19: Flow-through filters made with photo-polymer concentrations in the range between 0–25 % were replicated three times and tested with 15 µL of a water-based solution of E. coli. After the testing process both the porous filters and the collection pads were incubated for 18 hours at temperature of 37 °C to allow the bacterial growth.

The flow-through filtration method proved to be successful for the retention of E. coli on the surface of a filter, which simultaneously allows for the penetration of water that

is collected on a pad. Although we do not present herein an application using the flow-through filtration method with bacteria, we believe that this approach can be used for water purification in the case of contamination with bacteria and this can be included as part of our future work.

4.4 Summary

In this chapter we presented another filtration method using our local photo-polymer deposition technique. This approach is based on the fabrication of porous flow-through filters on cellulose paper made with different porosities that are able to retain particles of a specific size while allowing smaller particles to flow through. During the fabrication process we deposited the photo-polymer, which is diluted in IPA in different concentrations, inside the solid polymeric wall before the exposure to a laser source to form porous flow-through filters. By changing the v/v% concentration of the photo-polymer we were able to create filters with controllable levels of permeability which were placed on the top of the front end of an LFA. We tested the filtration properties of the porous flow-through filters with polystyrene microspheres of different sizes (200 nm, 500 nm, 1000 nm and 3000 nm) and we successfully found the parameters in order to create porous filters able to completely block or allow the flow of these particles. For the filters with different porosities we calculated the particle filtration efficiency which is a measure of their performance when filtering out particles larger than a specific size. The results show that there is an increasing trend in terms of the photo-polymer concentration and the ability of the filters to block particles decreasing in size.

The flow-through filtration method was later used in an assay for the detection of CRP. The detection method is based on the interaction and binding of the target analyte with two antibodies each one tagged with different sized labels namely Au NPs (40 nm) and latex beads (3 µm). The porous filter is designed to retain particles with a size of 3 µm while allowing smaller particles to flow trough the filter and get captured in an LFA where antibodies are immobilized at the test line. Similar to a competitive type assay when the analyte is present in the sample it binds with both the Au NPs and the latex beads forming a complex with size of 3 µm which is unable to flow through the filter. In that case only the unbound detection antibodies can flow through the filter and get captured in the test line producing a signal with varying intensity depending on the concentration of the analyte in the sample. On the other hand, when the analyte is not present in the sample the Au NPs flow through the filter and get captured in the test line producing a strong signal. This filtration method was successfully applied for the detection of CRP over a broader concentration range from 0 ng/mL to 50.000 ng/mL with a LOD found at 13 ng/mL.

In our next demonstration we used the flow-through filtration method in a different application and specifically for the separation of plasma from RBCs. In our first experiment we proved that the porous filters were incapable of extraction of plasma when tested with whole blood. However, when we treated the blood sample with Anti-D solution (1:5 *v/v* in ratio) we achieved the extraction of plasma with a maximum yield of 50.6%. By treating the blood sample with Anti-D solution with a ratio 1:5 *v/v* and increasing the volume of the tested blood to 20 µL we did not see an improvement in the maximum yield as we achieved 44.7% efficiency in the extraction of plasma. In our next approach, we used a stacking pad design where porous filters of either the same or different porosities were placed on top of each other. First we used a two layer stacking design consisting of two filters designed to have the same porosity, however there was no improvement in terms of the plasma extraction efficiency as we achieved a maximum yield of 30.3%. Then we used stacking pads with different number of layers (3,4 and 5) where each one is designed to have different porosity starting from the top layer which is highly porous to layers with decreasing porosity as we move from the intermediate to the bottom layer. This method proved unsuccessful as we did not observe any plasma in the LFAs. Our results show that using our developed flow-through filtration method we have a limit in the plasma extraction as other components found in blood such as the leukocytes and the platelets are blocking the pores of the filters preventing the extraction of plasma beyond the threshold of 50.6%.

Finally, we explored another application of using the porous flow-through filters for the purification of a water-based suspension containing the bacteria E. coli. We successfully developed porous filters able to prevent the flow of the bacteria, allowing only the PBS to flow through and collect in a pad.

Chapter 5

Local photo-polymer deposition method for the fabrication of three dimensional multilayer paper-based devices

5.1 Introduction

Despite the wide use of 2D-μPADs in diagnostics, there are certain disadvantages that prohibit their use as POC sensors. One of the main reasons is the spatial distribution of the fluidic sample, which in the case of 2D-μPADs can only flow in one direction, and this limits the detection of a large number of analytes and also increases the detection time. On the other hand, in 3D-μPADs the sample can flow in both the lateral and vertical directions through multiple stacked layers of porous materials and this allows for the multiple detection of analytes and further also reduces the device footprint due to the fact that additional fluidic channels can be incorporated in the same device [1]. Due to the vertical flow of the sample the analyte detection time as well as the sample volume are reduced [2] and these features are highly desired for POC devices. Additionally, the better distribution of the sample in 3D-μPADs has been reported [3] to result in a better analytical performance (e.g. LOD, analyte detection range) of these devices as compared with the 2D-μPADs.

Another characteristic that μPADs should possess is the ability to control the flow of samples [4, 5] which is important for assays requiring multiple steps during operation (e.g. washing, pre-mixing etc.) [6]. To achieve that in 2D-μPADs, there are reported methods that either using switches that can be activated by mechanical pulling [7] or fabricating multiple flow paths in a single device with varying lengths [8]. Despite

the efficiency of these methods for the sequential delivery of samples, they are either time consuming during operation or laborious in terms of their fabrication process. On the contrary, the use of 3D-µPADs allows performance complex assays, within a few minutes, where mixing of different compounds is needed (e.g. enzyme-linked immunosorbent assay (ELISA)) [9] and we can also avoid any contamination as the sample can be transported within the intermediate paper layers through multiple fluidic channels. Additionally, the use of 3D-µPADs helps prevent any cross-contamination between multiple samples thus enabling simultaneous testing of different assays independently within the same device. Finally, the use of 3D-µPADs allows the reagents to be stored within the middle layers of a device and as the fluid travels within these layers the evaporation of the sample is minimized [10]. This results in a faster wicking rate [11] and also improves the sensitivity of assays as compared with the 2D-µPADs due to the fact that the prevention of the evaporation of the sample allows a bigger volume to reach the detection zone [12].

For the aforementioned reasons, 3D-µPADs are extensively studied and many research groups are working towards the fabrication and optimization of these platforms for use in diagnostic assays. The most common fabrication method for the development of 3D-µPADs includes 3D origami [13, 14], and devices made using this approach are composed of individual pre-patterned tabs such as conjugate pad, detection pad and absorbent pad, that are folded on top of each other to form a 3D structure. Another reported fabrication method is the use of a stack of pre-patterned papers [15, 16] where each layer is patterned individually and then all the layers are stacked together sequentially. Despite the applicability of these methods, there are certain disadvantages arising primarily from their fabrication procedure. The origami-based method while ingenious, require sequential steps for assembly and alignment of the layers of paper, which might be difficult or incorrectly performed by untrained individuals. As for the method that uses and stacks individual layers of pre-patterned paper, the use of additional equipments is required such as double-sided tape [17] and spray adhesive [18] to ensure proper contact between adjoining layers. Alternative methods to stack layers of paper include the use of clamps [19] or holding the device between the thumb and index fingers [20]. As previously mentioned, these methods require external/additional equipment and further fabrication steps, which are two factors that increase the complexity of the design and fabrication. Additionally, the method of stacking layers of pre-patterned paper requires an extra aligning step, which is a critical parameter for the performance of the final device. In addition, an alternative method [21] for the formation of 3D-µPADs reports the formation of 3D structures directly on the paper layer, a method that sorts out any contact issues but lacks simplicity as it requires double-sided wax printing and an extra aligning step during the fabrication process.

In this chapter, we report the use of the local photo-polymer deposition method to

stack several layers of porous materials and create 3D-µPADs. This method is an alternative to the previous method [22] that our group has developed for the fabrication of 3D-µPADs which involved additional fabrication steps such as polymer soaking and solvent-based developing of the paper device. Unlike that method, this technique is simpler, faster in fabrication and most importantly exceeds the maximum number (three) layers that our previous method had. The novelty of this method stems from the fact that it does not require any alignment step between the layers during the fabrication process and simply requires putting layers of paper on top of each other.

We demonstrate the use of this technique to create 3D-µPADs for implementation of single step colorimetric assays for the detection of three analytes, namely BSA, glucose, nitrite as well as the pH of the tested artificial urine sample. Our choice to test the 3D-µPADs for the detection of these analytes stems from the fact that these biomarkers are commonly detected analytes in urine testing assays [23] for monitoring or screening for kidney function, acid-based balance and urinary tract infections. The detection and quantification of proteins in urine [24] is really useful for diagnosis of conditions such as cardiovascular disease and cancer. Herein we test for the detection of BSA which is used instead as the model protein for the human albumin in urine and it is studied extensively because it has similar composition (e.g. molecular weight) to the human protein [25]. Elevated levels of albumin in urine correspond to very low levels in blood and this can be an indication of kidney damage (hypoalbuminemia) [26]. The detection and quantification of glucose in urine [27] is equally important for diagnostics, as elevated levels of it are an indication of underlying health conditions. People having diabetes [28] can develop chronic complications such as kidney problems, and this can lead to the excretion of glucose into the urine (glycosuria). Apart from measuring albumin and glucose levels in urine, the measurement of nitrite is also significant and very common in urinalysis. Nitrates are naturally present in urine and are not harmful. However, the presence of some gram negative bacteria, such as E. coli, have enzymes that covert nitrates into nitrites [29] and the detection of nitrites in urine can be an indication of bacterial infection such as in the urinary tract [30]. If left untreated it can lead to kidney failure or even sepsis and for that colorimetric methods for the detection of this analyte using µPADs are reported [31, 32]. Last but not least, testing the pH of a urine sample reveals how acidic or alkaline a person's urine is. Urine varies from slightly acidic to slightly alkaline with usual values between 6.0 and 7.5 however, abnormal levels are associated with medical conditions such as kidney stones or urinary tract infections.

5.2 Experimental section

5.2.1 Experimental setup and materials

The porous material used to make the multilayer 3D-µPADs is Whatman^{TM} grade 1 qualitative filter paper (cellulose) from GE Healthcare with nominal thickness of 180 µm and pore size of 11 µm. We used glass fibre, from GE Healthcare, with nominal thickness of 355 µm to pre-deposit the reagents used for the assay. In order to evaluate the performance of our method to stack multiple layers of cellulose paper as well as the fabrication of 3D-µPADs, we tested a red chemical dye from Sigma-Aldrich diluted in DI water to have a concentration of 0.5 mg/mL. Next, we tested the performance of the 3D-µPADs by performing a single step colorimetric assay for the detection of BSA, glucose, nitrite and the measurement of the pH. For the BSA assay the reagents used were citrate buffer and tetrabromophenol blue (TBPB) in 95% ethanol solution. The BSA protein which was used as the analyte for the BSA assay was prepared at a concentration of 50 mg/mL. The reagents used for the glucose assay were glucose oxidase/peroxidase solution diluted in DI water and o-Dianisidine dihydrochloride with a concentration of 5 mg/mL in DI water. D-(+)-glucose solution was used as the analyte for the glucose assay with a concentration of 1 mg/mL in 0.1% benzoic acid. Next, for the detection of nitrite, we prepared Griess reagent and used sodium nitrite at a concentration of 0.68 mg/mL as the analyte for testing of this assay. For the pH measurement we used bromothymol blue as an indicator. The protocols for the above mentioned assays as well as the measurement of the pH are listed in the appendix D. Finally, a red chemical dye diluted in DI water at a concentration of 0.5 mg/mL was

TABLE 5.1: List of the reagents used to make the artificial urine medium.

Reagent	**Amount (g/l)**
Urea	10
Sodium chloride	5.2
Sodium sulphate.10H_2O	3.2
Sodium biocarbonate	2.1
Ammonium chloride	1.3
Di-potassium hydrogen phosphate	1.2
Potassium dihydrogen phosphate	1.2
Bacteriological peptone (L37)	1.0
Creatinine	0.8
Magnesium sulphate.7H_2O	0.49
Citric acid	0.4
Calcium chloride.2H_2O	0.37
Lactic acid	0.1
Uric acid	0.07
Yeast extract	0.005
Iron (II) sulphate.7H_2O	0.0012

used to visualize the progression of the sample throughout the layers of the multilayer 3D-µPADs.

The above mentioned analytes were all spiked in an artificial urine sample in different concentrations ranging from 0.3–18.2 mg/mL for BSA, 7.3–363 µg/mL for glucose and 0.6–62.6 µg/mL for nitrite. For the preparation of the artificial urine sample, we used the reagents listed in table 5.1. The reagents were added to 1 L of DI water which then placed on a hotplate at temperature of 50 °C and stirred until all the compounds were completely dissolved. The solution was then sterilised and was filtered through a stericup disposable filter unit and a vacuum pump into sterile bottles.

5.2.2 Methods and procedure

In order to pattern and stack of multiple layers of cellulose paper to make the 3D-µPADs we used the local photo-polymer deposition method and we followed a protocol of sequential fabrication steps. Figure 5.1 shows a schematic of the various steps

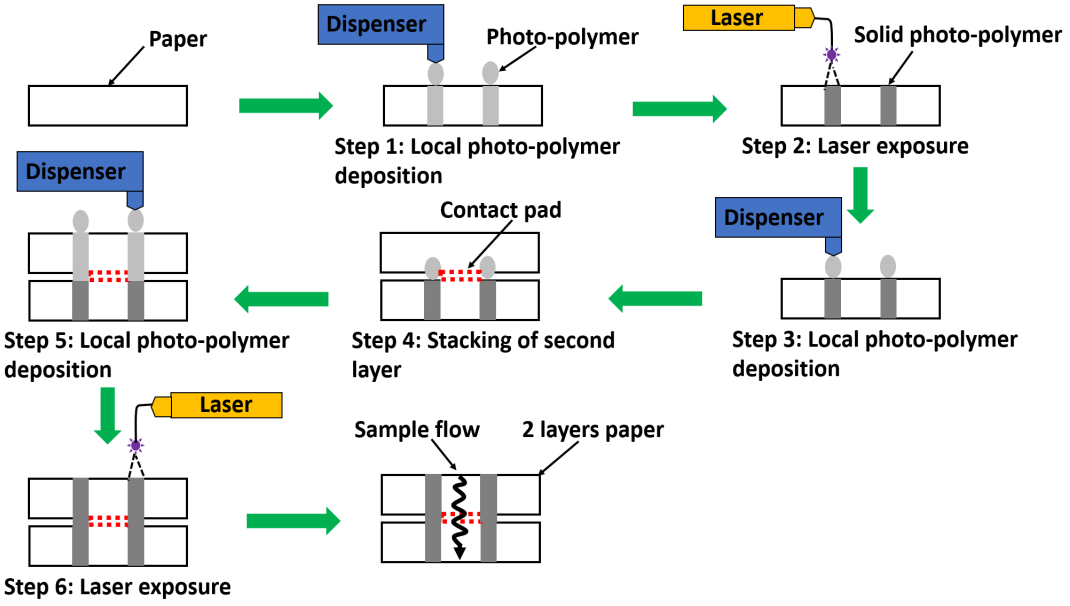

FIGURE 5.1: Schematic of the various steps involved during the fabrication of a 2 layer paper device. The photo-polymer is first deposited on top of the cellulose paper (step 1) and after it has extended throughout the thickness of the paper is exposed to the laser source (step 2). Then the photo-polymer is deposited over the same pattern (step 3) and the next layer is placed on top of it (step 4) before the photo-polymer is deposited again with the same pattern over the top layer. When the photo-polymer penetrates completely through the top layer (step 5) it is exposed again to the laser light (step 6) to create a 2 layer paper device. A contact pad is placed between the layers to ensure proper flow of the sample.

required to pattern and stack 2 layers of cellulose paper. To begin with, the photo-polymer is deposited on top of a porous substrate at locations pre-defined by a computer design, and after it spreads throughout the entire thickness of the paper (stage 1) it is exposed to the laser source (stage 2) to induce photo-polymerization and create a solid polymeric structure. Next, the same photo-polymer is deposited again over the same pattern that was previously printed (stage 3) and immediately after, a second layer of cellulose paper is placed over the top (stage 4). It worth mentioning here that during stage 3 of the fabrication process, the unpolymerized photo-polymer is deposited on top of a solid photo-polymer, therefore it remains on top of the patterned paper. When the next layer of cellulose paper is placed on top of the first as presented in stage 4, then the unpolymerized photo-polymer penetrates only the top layer, thus assisting with the bonding of the two layers. The photo-polymer pattern is added again on top of the second layer (stage 5), followed by exposure from the laser source (stage 6) to create a solid structure and stack the two layers of cellulose paper. With this method we can stack 2 layers of paper and allow for the sample to flow from the top to the bottom layer following the direction of the arrow as presented in the last image of figure 5.1. It is very important to note that in order to ensure complete contact between the two layers and have proper flow of the sample from the top to the bottom layer, a contact pad of the same cellulose material is added in the intersection points between the two paper layers.

The use of a contact pad is critical for the device fabrication as its absence results in leaving a gap between the 2 layers and consequently interrupts the flow of the sample. Furthermore, the addition of the photo-polymer between the layers is equally important to assist with their bonding. Despite the fact that we do not present the results of the tested devices here, we tried another approach to eliminate step 4 of the previously mentioned fabrication process, and we only deposited the photo-polymer on top of the second layer which after extending throughout the whole thickness of the top paper was exposed to the laser irradiation. The result was that we were unable to stack the 2 layers of paper together as the photo-polymer that is deposited from the top can not assist with the bonding of the 2 layers. Lastly, we report the use of an alternative fabrication method that we used to stack together 2 layers of cellulose paper and that involved the position of one layer of paper on top of the other, following by the deposition of the photo-polymer only on the top layer which was later exposed to the laser source. The result was again similar to that of the previous method, which means that we were unable to stack together 2 layers of cellulose paper. We observed that the photo-polymer was only able to penetrate the top layer, however there was no trace of it on the bottom layer and we believe that is the result of the small gaps between the 2 layers which prevented the spreading of the photo-polymer on the bottom layer.

In order to make 3D-μPADs where the sample can flow in both the lateral and vertical directions through multiple stacked layers of cellulose paper, we used the method

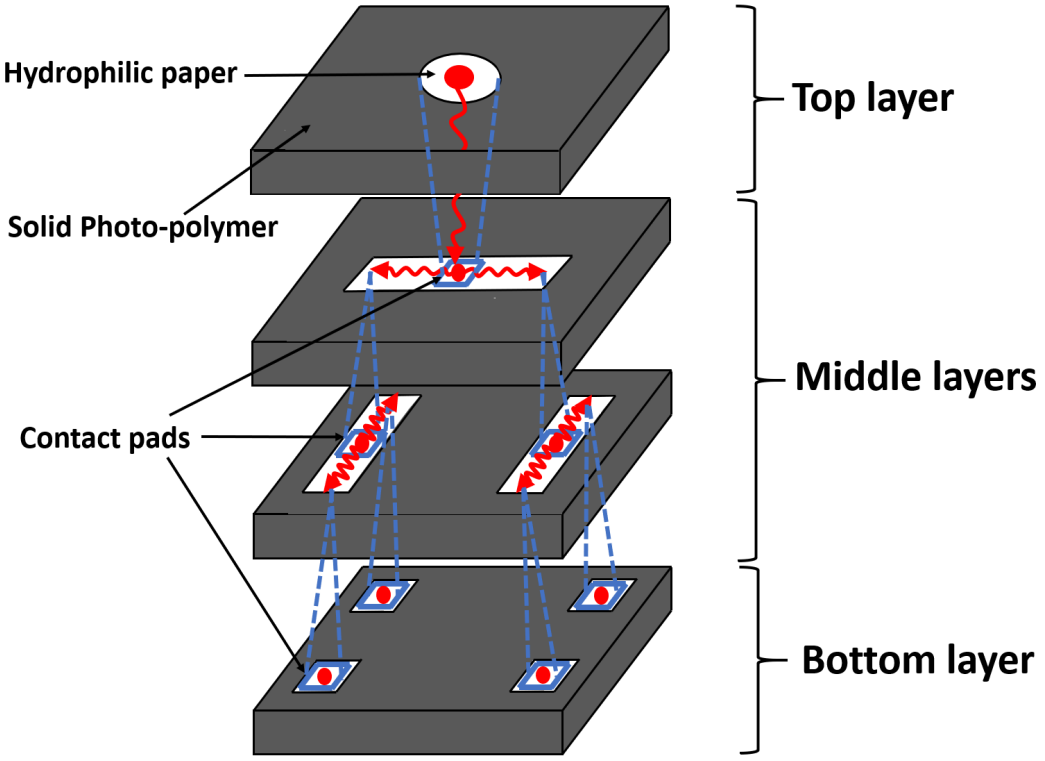

FIGURE 5.2: Schematic showing a 3D multilayer paper-based device used to make the single step colorimetric assays. The device consists of four different layers of patterned cellulose paper stacked together and the sample can only flow to the hydrophilic paper areas demarcated by the solid photo-polymer. In order to ensure proper flow of the sample from the top to the bottom layer, contact pads made of cellulose paper were added to the top three layers, whereas, contact pads made of glass fibre were added between the middle and the bottom layer in the four readout zones which also contain the dry reagents used for the assays.

that described through the schematic in figure 5.1 to produce a multilayer device that implements four independent single-step colorimetric assays. Figure 5.2 illustrates a schematic of a multilayer 3D-µPAD that was fabricated to allow the colorimetric detection of three analytes namely BSA, glucose and nitrite all spiked in artificial urine as well as the pH of the tested sample. The device consists of four different layers of cellulose paper each one patterned and stacked using the method described through the schematic of figure 5.1. In each layer, the sample can only flow in the hydrophilic paper areas, which are demarcated by the solid photo-polymer patterns preventing any leakage of the sample outside of the demarcated hydrophilic areas. As we can see the top layer has an inlet point for introduction of the sample, whereas the bottom layer has four rectangular readout zones designed to visualize the outcome of the colorimetric assays. The two middle layers allow distribution of the sample homogeneously into the four detection areas. To assist with the flow of the sample throughout the device, from the top layer all through to the bottom layer, contact pads (represented as blue square in figure 5.2) of a hydrophilic material were placed at the intersection of the channels

within the adjoining layers. In order to ensure contact between the top three layers, we used cellulose paper as a contact pad, whereas, glass fibre was used as the hydrophilic contact pad material between the third and the bottom layer containing the four detection zones. The glass fibre not only allowed proper flow of the sample between the third and the bottom layer, but also served as pads for storage of the reagents required for each of the different assays. The reagents were pre-deposited and left to dry at room temperature for 20 minutes prior to the addition of the contact/storage pads between the two final layers of our device. Our choice to use glass fibre stems from the fact that this material is able to effectively release the reagents upon rehydration from the incoming flow of a liquid sample. In figure 5.2 we have marked with red arrows the direction of the flow of the sample, starting from the top layer and travelling through the middle layers and finally to the bottom layer where the outcome of the assay can be visualized.

5.3 Results and discussion

5.3.1 Stacking method for the fabrication of multilayer devices

In order to evaluate the performance of our local photo-polymer deposition method to stack multiple layers of a porous material, we fabricated squares in cellulose paper with dimensions of $5 \times 5\,\mathrm{mm}^2$ and tested using a red chemical dye which provided an aid to visualize the progression of the fluid flow through the different layers.

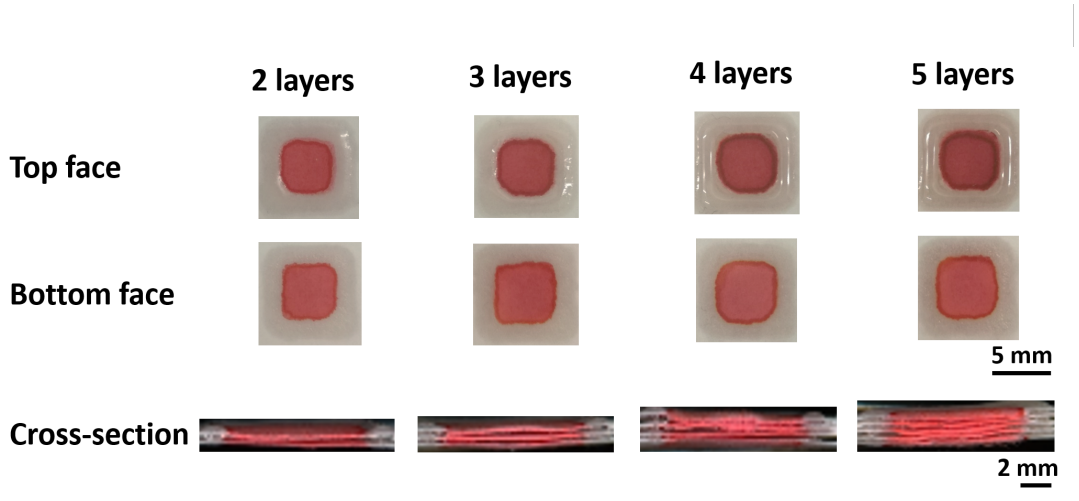

FIGURE 5.3: Photos of multilayer paper devices with two, three, four and five layers respectively; each one was tested with 20 µL of red dye. The sample is introduced from the top face of the devices and after travelling throughout the successive layers it ends up on the bottom face. Photo of the cross-section of the devices is provided to show that the red dye has completely soaked all the layers.

Figure 5.3 depicts the results of different multilayer paper devices for which we have successfully stacked two, three, four and five layers of paper following the same procedure each time (described in detail in the subsection 5.2.2) and tested each one with 20 µL of red dye. The same square pattern was fabricated in each of the different layers and the solid polymer walls that defined those squares had a width of 2 mm. To ensure proper flow of the sample from the top to the bottom layer, a contact pad (cellulose paper) was placed between the layers. We followed the same process to produce six devices for each of the four different multilayer cases, however in figure 5.3 we present indicative images of these four different multilayer devices with either 2-5 layers respectively. The results were consistent for each one of them and as can be clearly seen the red dye which is introduced from the top face of the device, flows through the successive layers of paper and ends up at the bottom face of the device. In order to visualize that the red dye has flowed through each of the different layers of our stack, after the testing process the devices were cut and a cross-sectional image was taken, which shows that in each case the red dye has successfully travelled through all the layers.

5.3.2 Fabrication of 3D paper-based devices

Following the evaluation of the local photo-polymer deposition method used to stack layers of a porous material, we later used this fabrication technique to produce 3D multilayer paper-based devices wherein the sample can flow into channels and distribute homogeneously into four individual detection zones. The fabrication parameters of the photo-polymer deposition speed, the time delay, the laser scanning speed as well as the laser fluence, are listed in table 2.1. Figure 5.4 presents one such 3D device designed according to the schematic of figure 5.2 where four layers of cellulose paper are patterned and stacked together to form a $20 \times 20\,\text{mm}^2$ square device. In order to ensure proper flow of the sample from the top layer, to the middle layers and then into the bottom layer, contacts pads made of cellulose paper were placed at the intersection of the hydrophilic channels within adjoining layers. The dimensions of the flow channels in each layer are listed in table 5.2. The performance of the 3D device was similarly evaluated first using the same red dye and 35 µL were pipetted into the inlet point. The result was observed by looking at the bottom face of the device at the point of the four detection zones and as we can see in figure 5.4 the sample has spread to all of them. The red dye provided an aid to visualize the progression of fluid through the multiple layers of this design and the volume of 35 µL is the smallest sample volume that is needed in order for it to flow through the successive layers, soak completely the middle paper layers, and end up in the bottom face of the device.

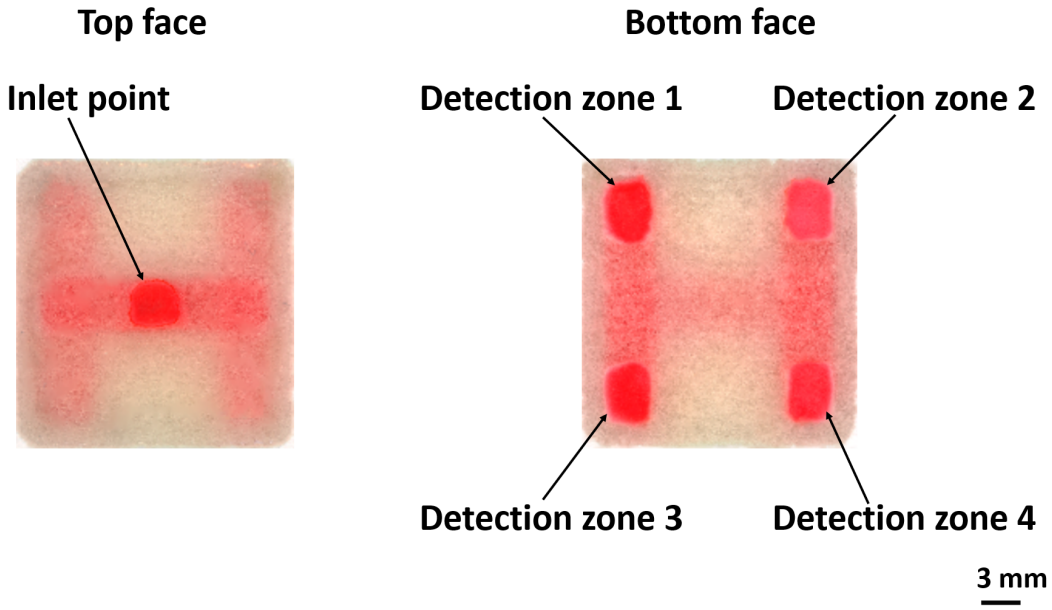

FIGURE 5.4: 3D paper-based device with four layers tested with 35 µL of red dye. Left image: Top face of the device where the red dye is introduced from the inlet point. Right image: Bottom face of the same device where we visualize the outcome of the testing process in the four detection zones.

TABLE 5.2: Dimensions of the channels within each layer of the 3D multilayer device.

Layer	Length (mm)	Width (mm)
Top layer	3	3
Middle with one channel	16	3
Middle with two channels	3	19
Bottom layer	3	4.5

5.3.3 3D paper-based devices used for the colorimetric detection of analytes in an artificial urine sample

We next evaluated the applicability of our methodology by fabricating and testing devices with a design as shown in figure 5.2 and having four layers, for the detection of three common analytes presented in artificial urine. For this testing, artificial urine samples spiked with the three chosen biomarkers, BSA, glucose and nitrite were used, and the detection of each of these was through a colour development in individual detection zones within the bottom layer of the device. The intensity of the colour produced is also an indication of the concentration of that analyte in the artificial urine sample and was therefore used to not only detect, but also quantify the levels of the different analytes in our samples.

For the BSA the colour change within the detection zone should be from yellow to blue. In this assay we use a reagent (dye) called TBPB (yellow colour with maximum light absorption at 595 nm) which under acidic conditions it binds with the albumin through

a combination of electrostatic and hydrophobic interactions. The result of this interaction is the formation of a stable complex (dye-albumin) which has a maximum light absorption at 470 nm (blue colour) [33]. As for the glucose assay, the colour change should be from brown to pink and the color formation is based on glucose oxidase (reagent) which catalyses the oxidation of D-glucose (analyte) to D-gluconic acid with the concurrent release of hydrogen peroxide (H_2O_2). In the presence of peroxidase, the hydrogen peroxide enters into a second reaction involving o-Dianisidine with the formation of a coloured product namely oxidised o-Dianisidine (brown colour) which reacts with sulfuric acid to form a more stable coloured product (pink). The intensity of the pink colour is proportional to the analyte's D-glucose concentration in the sample (all this information is acquired from Sigma-Aldrich technical bulletin). Next, for the nitrite assay the colour change, in the detection zone is from light pink to a red-violet colour. This assay is based on the Griess reaction in which under acidic conditions (created by citric acid) the nitrite reacts with sulfanilamide acid resulting in the formation of diazonium cation which subsequently couples to the aromatic amine N-(1-napthyl)-ethylenediamine dihydrochloride to produce a red-violet coloured product with maximum light absorption at 540 nm [34]. Last but not least, in the case of pH, the

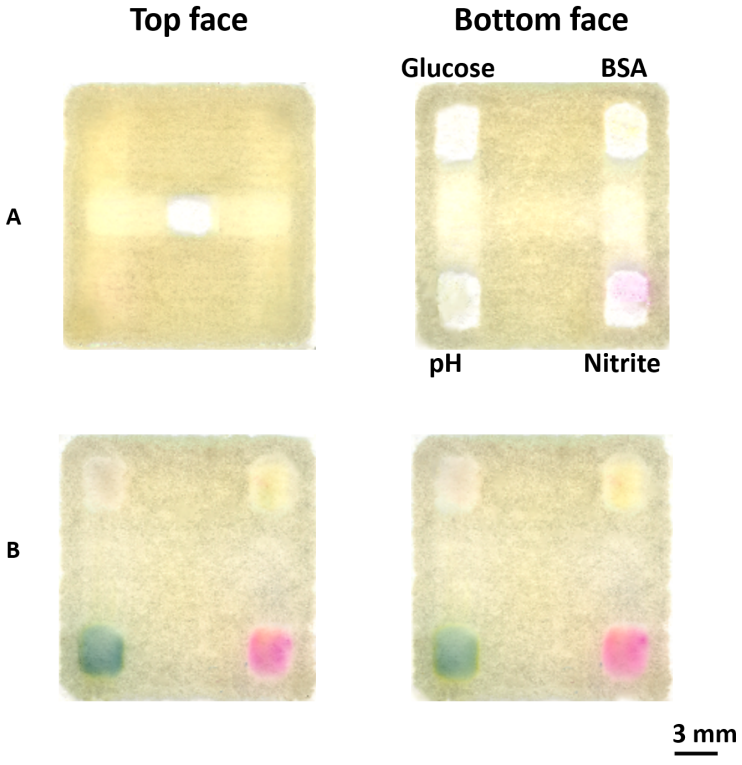

FIGURE 5.5: (A) Top and bottom faces of a 3D paper-based device with four layers designed for the simultaneous detection of three analytes namely BSA, glucose and nitrite, as well as the pH of the tested sample. The image shows the device before the testing process where the reagents for the assays are pre-deposited within the middle and the bottom layer. (B) Bottom face of a control device (no analyte) where photos are taken 1 minute (left device) and 10 minutes (right device) after the assay.

colour changes from yellow (6.0) to green (7.6) for the corresponding pH values. This is because of the bromothymol blue which has a closed-ring form (yellow in colour) and absorbs light between 400–430 nm. This pH indicator acts as a weak acid in solution and under basic conditions (pH values grater than 7.0) it is deprotonated and takes an opened ring form which absorbs light at around 620 nm (blue colour).

As described earlier in subsection 5.2.2, before the testing of a 3D-µPAD we pre-deposited and dried on the glass fibre pad the different reagents for the assays, and these were later positioned between the bottom two layers of the device and figure 5.5A shows the top and bottom face of such a device. The reagents that were used were as follows: for the BSA assay we used 1 µL of TBPB, for the glucose assay we used 2 µL of glucose oxidase/peroxidase solution, for the nitrite assay we used 1 µL of the Griess reagent and for the pH measurement we used 2 µL of bromothymol blue. Before testing the 3D-µPADs with artificial urine sample spiked with the known concentrations and volumes of the analytes, we tested, and used as a control, an artificial urine sample that does not have any of the analytes (negative test). Figure 5.5B depicts the bottom face of the control device where photos are taken 1 minute (left device) and 10 minutes (right device) after the assay.

In figure 5.6 we illustrate the bottom face of a 3D-µPADs at different times namely 1 minute and 10 minutes after 50 µL of an artificial urine sample with analytes, was introduced from the top face of each device. We chose to increase the volume of the sample from 35 µL to 50 µL in order to acquire a better sensitivity during the measurement of the tested analytes. From the results we observe that the volume of 50 µL is not only sufficient for the sample to travel through all the layers of the 3D-µPAD but also does not overload the device to produce any sideways leakage of the sample which would be detrimental for the performance of this detection method. When the sample reaches the in-between glass fibre contact pads, it rehydrates and reacts with the reagents stored within it and then carries on to the detection zones to produce a corresponding colour change within the different detection zones similar to the one described earlier. For this testing, we conducted a detailed study using several devices with known samples concentration across a range of 0.3–18.2 mg/mL for BSA, 7.3–363 µg/mL for glucose and 0.6–62.6 µg/mL for nitrite. As we can clearly see, there is a gradient colour change of the colour intensity for each of the analytes as their concentrations change from a lower to a higher value. The higher the concentration of the analyte in the sample, the greater is the colour intensity in the detection zone.

We later measured the LOD for the three detected analytes using equations 5.1 and 5.2 and were found to be at 0.4 mg/mL for BSA, 14.5 µg/mL for glucose and 2.5 µg/mL for nitrite.

$$\text{LOD} = \text{LOB} + 3 \times \text{Standard deviation}_{\text{Lowest concentration sample}} \tag{5.1}$$

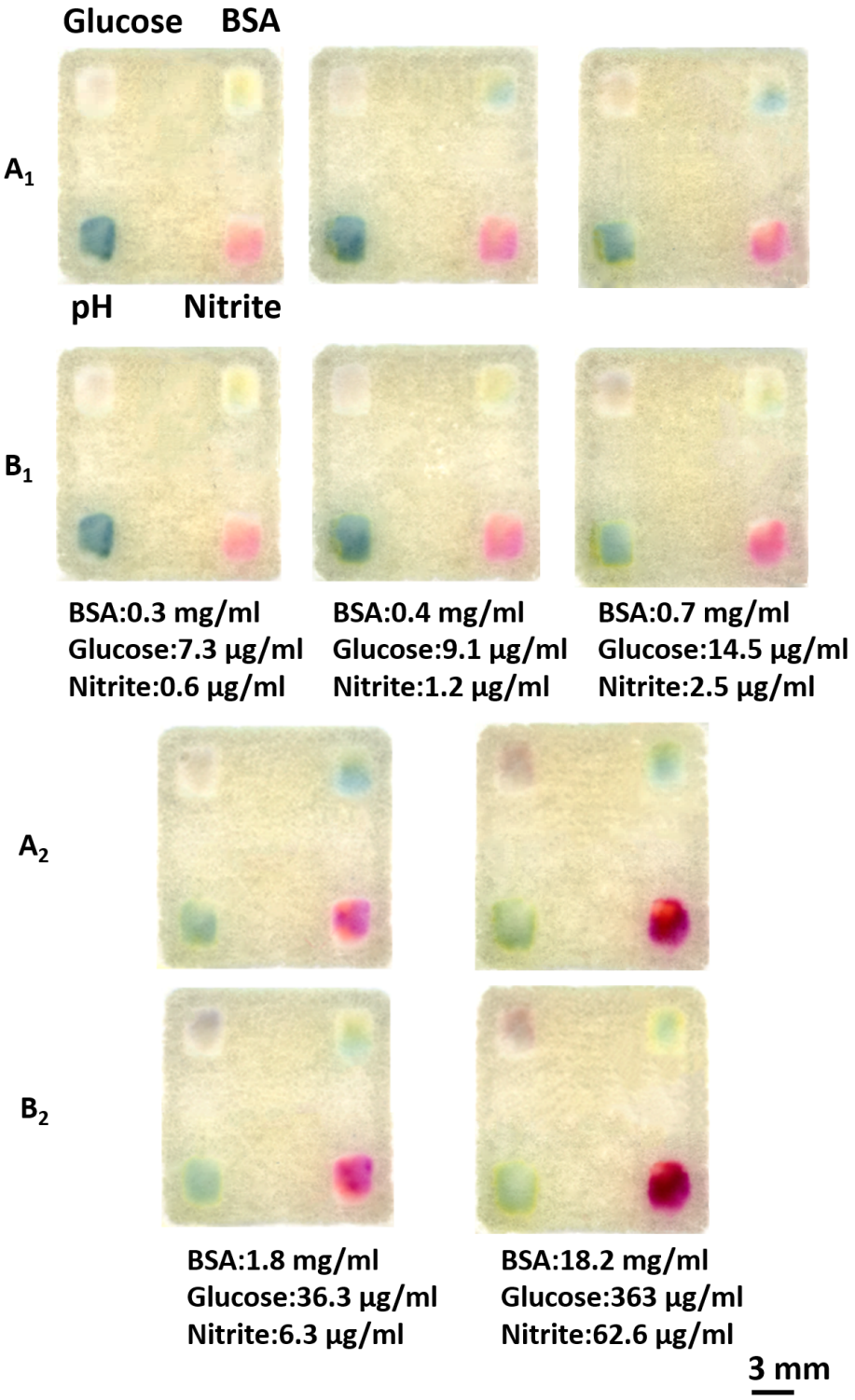

FIGURE 5.6: Images of the bottom face of the four-layered 3D-µPADs when tested with different concentrations of the analytes. Photos of each device were taken (A_1,A_2) 1 minute and (B_1,B_2) 10 minutes after testing 50 µL of the artificial urine sample.

$$\text{LOB} = \langle \text{Blank} \rangle + 1.645 \times \text{Standard deviation}_{\text{Blank}} \tag{5.2}$$

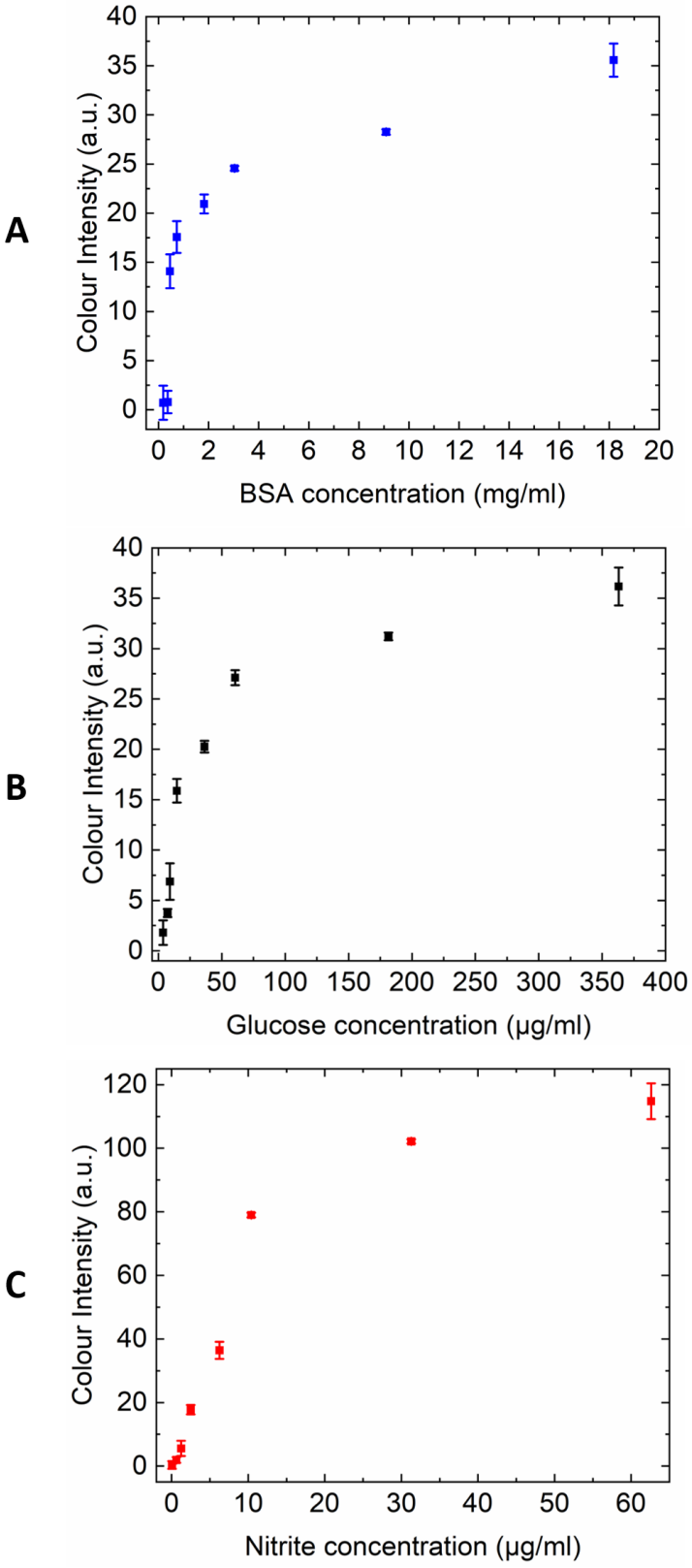

FIGURE 5.7: Calibration curves showing the colour intensity of (A) BSA, (B) glucose and (C) nitrite for their different concentrations in the artificial urine sample.

The significance of our developed analyte detection method for clinical diagnostics is evident from the evaluated LODs. Specifically, in the case of BSA the lowest detected analyte concentration was found at 0.4 mg/mL and this allows the use of such a device for the detection of nephrotic syndrome (protein $>$ 2.3 mg/mL), subnephrotic range proteinuria (0.6 $<$ protein $<$ 2.3 mg/mL) and tubular proteinuria (protein $<$ 0.6 mg/mL). Furthermore, the LOD of 14.5 µg/mL for glucose suggests its usefulness for the practical application of detecting elevated levels of glucose in urine due to the fact that levels $>$ 250 µg/mL is an indication of diabetes. Finally, our reported 3D-µPAD is capable of detecting nitrites in urine as their presence, no matter the concentration, is an indication of urinary tract infection.

The colour intensities on the detection zones for each device were analysed using the RGB channel in the histogram function of the Adobe Photoshop program. After using a scanner to take photos of the tested devices, we measured the mean intensity value of the pixels of each one of the four detection zones and the colour intensity values of the control device (no analyte) were subtracted from the values for the devices tested with the analytes in order to obtain the actual signal intensity. For BSA and nitrite we measured the signal, 1 minute after the assay as presented in figure 5.6A_1,A_2. However, as the glucose assay requires a longer time to complete [35] (10 minutes) the colour was allowed to develop over this period of time, and intensity measured thereafter (as in figure 5.6B_1,B_2). In figure 5.7 we show the calibration curves which are based on the actual colour intensities. We can clearly see for the three detected analytes that as their concentration increases, the corresponding intensity of the colour produced also increases. Also, each measurement was repeated three times to calculate the error.

5.4 Summary

In this chapter we report the use of our developed local photo-polymer deposition method for the fabrication of 3D-µPADs using cellulose paper. This method is simple, fast and inexpensive and unlike other reported patterning techniques for the fabrication of 3D devices, this approach eliminates the need for any sophisticated alignment that may be required between the layers. In addition, this also does not mandate the need for the use of external or additional equipment during the assembly of the device. We tested the performance of this device fabrication method by stacking several layers of cellulose paper and making 3D-µPADs, which were then tested with a red dye that visualize that the sample flowed through the successive layers without blockage or leakage. Lastly, we used the 3D-µPADs with the reagents dried and stored within the layers of the device, to perform single-step colorimetric assays for the detection of three analytes spiked in artificial urine namely BSA, glucose and nitrite, as well as the pH of the tested sample. From the results, we observe an increasing trend between the

concentration of the analytes and their respective colour intensity. Additionally, the devices were shown to be suitable for a quantitative detection of the tested analytes.

Chapter 6

Optically controlled fluid flow in lateral flow devices

6.1 Introduction

It is a global imperative for POC sensors to move beyond a simple binary yes/no result, as happens for a pregnancy test for example, to tests that provide a quantitative or semi-quantitative result. This, together with the demands for greatly enhanced sensitivity and limit of detection are the holy-grail for the diagnostic industry and a multi-testing environment in paper-based devices where fluid flow can be delayed or gated is highly desirable as it will implement these provisions and optimize the outcome of the testing procedure. Towards this goal, there is an extensive research effort in the field of microfluidics and POC sensors to control the fluid flow of samples and perform multistep reactions on paper [1]. The flow control of samples can be divided into two major categories, namely passive and active [2]. In passive fluid control the methods that are used target manipulation of the flow rate of the sample within the paper channel however, they suffer from lack of flexibility in terms of the fluid manipulation. On the other hand, in active fluid control the sample can travel freely within the paper device and be delivered to a desired location at a chosen time, therefore allowing for sequential multi steps assays.

In passive fluid control the reported methods include the modification in the geometry of the fluid channel (e.g. length, width, height or flow path) in order to change the sample's flow speed [3, 4, 5] or the chemical treatment [6, 7] of the flow channel by adding e.g. sucrose or different concentrations or paraffin wax-coated layers in order to change the wicking properties of the paper and delay the flow of the sample. In the case of the active fluid control, there are methods that report the use of a temperature control-operated valve system [8] in which the flow of the sample can be gated by heating the wax or the use of a rotational valve on a paper device [9], a method used to

connect separated paper channels which although it has proved successful to perform multi-step assays, it has the disadvantage of manual operation.

In the category of active fluid flow, many research groups have focused on the use of stimuli responsive materials [10] (polymers) that can change their properties in response to a single or multiple stimuli. Hydrogel [11], is such a material and consists of a three-dimensional cross-linked polymer network with an insoluble but highly hydrophilic structure that is capable of a volume change (swelling or shrinking) reversibly upon triggering from external environmental conditions. There are many factors that can trigger [12, 13] and activate (swell) the hydrogel and some of them include a change in the pH [14, 15], the temperature [16, 17] and the chemicals as a response to the presence of certain molecules such as glucose [18]. Another widely used category of materials is that of the light-responsive hydrogels [19] which can be triggered when exposed to light of a certain wavelength [20, 21]. The advantage of using light-activated hydrogels is the fact that we have more flexibility to trigger the hydrogel as the light can be delivered at a defined area at a desired time and is also a non-invasive method as light can activate the hydrogel remotely. The light-activated hydrogels will be the main material that we will study in this chapter in order to make optical switches. Hydrogels are commonly used as optical switches in microfluidics to control the flow of samples and common methods include their use in silicone microchannels [22], polymer channels [23] and in paper-based devices. In the last category there are reported methods that use thermally responsive hydrogels [24, 25] on paper channels fabricated from cellulose or use of a multilayer paper device functionalyzed with a target (aptamer) responsive hydrogel for the simultaneous detection of analytes [26].

In this chapter we report the use of light-activated hydrogels in paper-based devices to control the flow of samples in order to increase the sensitivity for the detection of analytes. The aim of this work is described through the schematic of figure 6.1. In this example, we use the method of the local photo-polymer deposition to dispense a pre-polymer solution in the form of a porous in-line barrier in an LFA, similar to the method reported in chapter 7.3. Later, the pre-polymer solution is exposed to the 405 nm laser source in order to transform into a hydrogel (optically triggered in-line barrier). The functionality of this porous optically triggered in-line barrier is to control the fluid flow upon exposure to light of different wavelengths. Specifically, when the porous optically triggered in-line barrier is exposed to the 365 nm light source the hydrogel expands and consequently filling the open pores of the paper, therefore preventing the flow of the sample. On the other hand, an exposure of the optically triggered in-line barrier to the 470 nm light source results in the shrinkage of the hydrogel, thus leaving open pores through which the sample can flow. For the purpose of the experiment, we position the optically triggered in-line barrier either after the test and the control lines (figure 6.1A) to increase the incubation time between the sample and the capture antibodies on the test line, or at the conjugate pad (figure 6.1B) to increase the incubation time between

the analyte and the detection antibodies. In either case our intention is to increase the signal intensity on the test line of an LFA, hence the sensitivity of the assay. For that purpose, we conducted a detailed study using different pre-polymer solutions with different compositions, and we explored the light exposure parameters, using a 405 nm laser light source, required for their polymerization and the formation of hydrogels. Next, we used different designs to deposit the hydrogels on paper (e.g. figure 6.1B photo (i)) using our local photo-polymer deposition method and we studied the light exposure parameters to either block the flow of sample (e.g. figure 6.1B photo (ii)) after exposure to the 365 nm light source or enable the flow of sample (e.g. figure 6.1B photo (iii)) after exposure to the 470 nm blue light source. Additionally, we studied an alternative method to activate the hydrogels and block the flow of sample and this

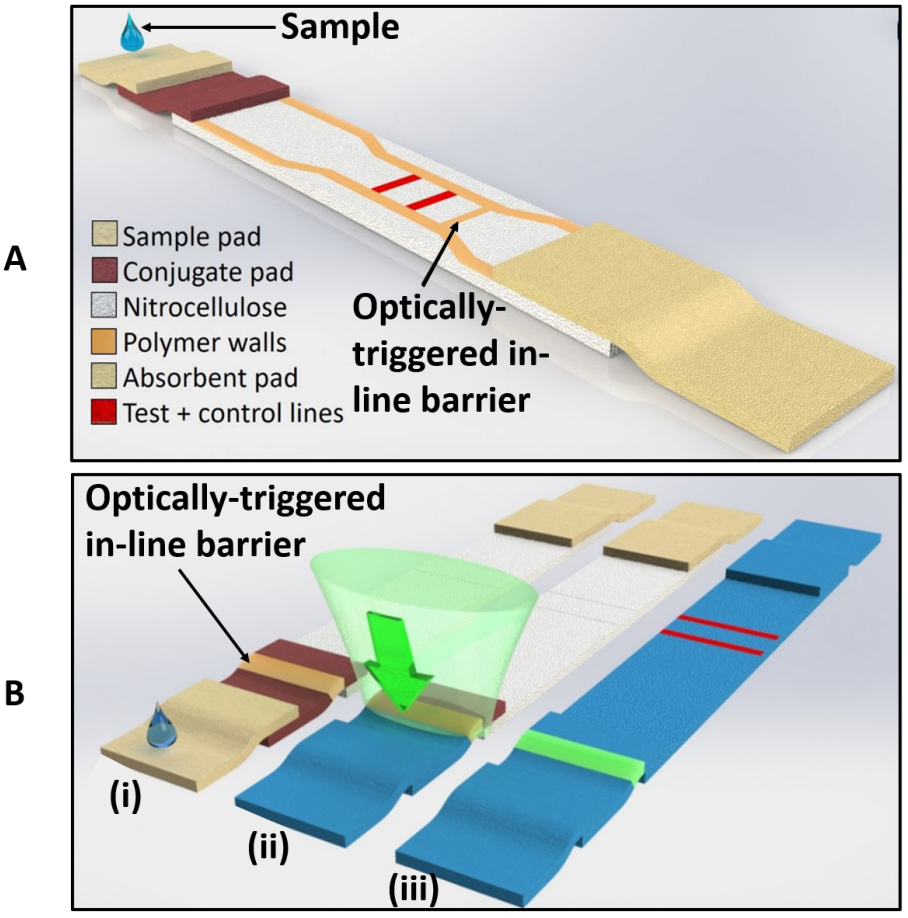

FIGURE 6.1: Schematic showing an LFA with an optically triggered in-line barrier positioned either (A) within the NC membrane after the test and the control lines or (B) at the conjugate pad in order to increase the incubation time between the sample and the capture antibodies on the test line or the analyte with the detection antibodies respectively. (B) After the polymerization of the optically triggered in-line barrier with the 405 nm laser light source (i) it is either exposed to the 365 nm light source to block the flow of sample (ii) or to the 470 nm light source to enable its flow in the NC membrane (iii).

includes the incubation of the hydrogels in water.

Finally, we demonstrate the applicability of using hydrogels in diagnostic assays to increase the sensitivity in the detection of two analytes, namely the COVID-19 virus and CRP.

6.2 Experimental section

6.2.1 Experimental materials

The light source used to polymerize and cross-link the pre-polymer was a fibre-coupled CW diode laser operating at a wavelength at 405 nm with output power of 70 mW. Following the polymerization process and the formation of a hydrogel, we later exposed it to another light source in order to activate the spiropyran and allow the hydrogel to swell. For this we used a UV fibre-coupled LED acquired from Thorlabs operating at a wavelength at 365 nm with output power of 4 mW and intensity of 10.4 mW/cm^2. The fibre used is a multimode fibre with core diameter of 400 µm and distance between the fibre tip and the hydrogel sample measured at 13 mm with a spot size of 7 mm. Finally, we exposed the hydrogel to another source in order to induce its volume shrinkage and that is an LED array light source (Thorlabs) operating at a wavelength of 470 nm (blue light) with a total output power of 85 mW and intensity of 221 mW/cm^2.

We used different pre-polymer solutions which after exposing to light of the correct wavelength (405 nm) led to the formation of hydrogels. Table 6.1 shows the materials and the amount used to prepare four different pre-polymer solutions. Next, we tested other pre-polymer solutions in which oligoethylene glycol (OEGMA) was used as a water soluble monomer and ethylene glycol dimethacrylate (EGDMA) as a cross-linker. The list of the materials mixed to form these pre-polymer solutions are listed in table 6.2. Furthermore, we tested another pre-polymer solution which contained a different, more active, spiropyran and the list of the other components mixed to make the pre-polymer solution are listed in table 6.3. The previously mentioned pre-polymer solutions and the materials used to make them were all prepared and synthesized in the University of Birmingham (School of Chemistry) and upon receiving them, they were covered with aluminium foil to avoid exposure to the ambient light and stored inside the freezer at temperature of $-4\,°C$.

In order to study the pre-polymer solutions we deposited them on different substrates. Specifically, in order to study the effect of the light exposure to polymerize and cross-link the pre-polymer solutions, we deposited them on a glass slide (from Thermo Fisher Scientific) and later we checked whether the exposure conditions led to the formation of a hydrogel. After finding the light exposure parameters (e.g. laser fluence) to form hydrogels, we deposited the pre-polymer solutions on different substrates such as NC

TABLE 6.1: List of materials used for the synthesis of different pre-polymer solutions. Each one contains NIPAM used as the water soluble monomer, acrylic acid used as the proton donor, MBIS used as a cross-linker, spiropyran 1 used as the photo-responsive element and irgacure used as the photo-initiator.

Pre-polymer solution	NIPAM (mg)	Acrylic acid (mg)	MBIS (mg)	Spiropyran 1 (mg)	Irgacure (mg)
1	404	14.4	16	16	5
2	400	14.1	17	18	6
3	402	14.2	19	14	17
4	401	14.3	19	27	17

TABLE 6.2: List of materials used for the synthesis of different pre-polymer solutions. Each one contains $OEGMA_{300}$ or $OEGMA_{900}$+$OEGMA_{300}$ both used as the water soluble monomer, methacrylic acid used as the proton donor, EGDMA used as a cross-linker, spiropyran 1 used as the photo-responsive element and irgacure used as the photo-initiator.

Pre-polymer solution	$OEGMA_{300}$ (mg)	Methacrylic acid(mg)	EGDMA (mg)	Spiropyran 1 (mg)	Irgacure (mg)
5	1000	16	22.1	13	15
6	2000	35.8	168	58.4	30.9
	$OEGMA_{900}$ +$OEGMA_{300}$ (mg)	**Methacrylic acid (mg)**	**EGDMA (mg)**	**Spiropyran 1 (mg)**	**Irgacure (mg)**
7	1825	37.3	165.18	58	30.9

TABLE 6.3: List of materials used for the synthesis of different pre-polymer solutions. Each one contains $OEGMA_{900}$+$OEGMA_{300}$ used as the water soluble monomer, methacrylic acid used as the proton donor, EGDMA used as a cross-linker, spiropyran 2 used as the photo-responsive element and irgacure used as the photo-initiator.

Pre-polymer	$OEGMA_{900}$ +$OEGMA_{300}$ (mg)	Methacrylic acid (mg)	EGDMA (mg)	Spiropyran 2 (mg)	Irgacure (mg)
8	2027	29.1	137.5	47.5	25

membrane (Sartorius Stedim Biotech GmbH, Germany, with thickness at 140–170 µm and pore size at 15 µm), cellulose paper (GE Healthcare with thickness of 180 µm and pore size of 11 µm) and glass fibre (GE Healthcare, with nominal thickness of 355 µm) in order to check the effect of swelling and shrinking on different porous materials.

Afterwords, we mixed both pre-polymer solutions 7 and 8 with a photo-polymer (Desolite) in different ratios in the range between 10–40 % in order to increase the viscosity of the mixed solution and be able to deliver it onto the paper substrate using the local photo-polymer deposition method. In order to mix these two substances together, first we removed the pre-polymer solution from the freezer and we left it at room temperature for 1 hour until it defrosts completely and becomes liquid. Next, we put together the pre-polymer solution and the photo-polymer in a plastic tube and we

vortexed for several minutes until the solution becomes completely homogeneous. Finally, we transferred the solution to an opaque (black) syringe barrel, to avoid exposure to any ambient light, and kept it at room temperature until use. We avoided putting the solution containing the pre-polymer and the photo-polymer in the fridge, as the photo-polymer has to be stored in a dry place at temperatures between 15 °C and 30 °C. Storage of the photo-polymer at temperatures close to 0 °C may result in a phase separation, an unstable state in which the photo-polymer splits into its components that have different composition as compared to the initial photo-polymer [27]. Although this process is reversible and can be corrected after heating the photo-polymer for 24 hours at 50 °C this action is not recommended as it may result in the degradation of the pre-polymer solution.

Finally, we tested the performance of the devices, via different designs, that contain the hydrogel using two different dyes namely a red chemical and a rhodamine as trial sample fluids both acquired from Sigma-Aldrich and diluted in DI water to have a concentration of 0.5 mg/mL. We also performed two diagnostic assays for the detection of CRP and the COVID-19 virus. For the CRP assay we used a conjugate pad (glass fibre) to pre-deposit and dry the detection antibody. The glass fibre was pre-treated with a blocking solution following sequential steps as follows: first the conjugate pad was soaked in a 0.05% Tween20 in PBS for 30 seconds and left to dry at 40 °C for 60 minutes. The conjugate pad was then soaked in a mixture of 0.25 g borate, 62.5 µL Triton X-100, 0.25 g sucrose and 0.75 g BSA in 25 mL of PBS for another 30 seconds. The pad was again dried for 60 minutes at 40 °C and then stored in a desiccated environment with $<$20% humidity until assembly of the final device. The CRP analyte was used in a concentration of 10 ng/mL and the conjugate was the same one that we used and described in the materials section of chapter 3. In the channels of the LFAs we dispensed and immobilized at the test line CRP capture antibodies with stock concentration of 1 mg/mL and at the control line a mouse IgG antibody with stock concentration of 500 µg/mL. For the COVID-19 assay we used the COVID-19 biomarker in a concentration of 100 ng/mL of 1% Triton X-100 in PBS and for the reagents we used 2 µL COVID-19 specific antibodies tagged with Au NPs. In the LFAs we dispensed and immobilized at the test line COVID-19 capture antibodies.

6.2.2 Characterization of different pre-polymer solutions containing NIPAM and MBIS for the creation of hydrogels

In this subsection we report and characterize different pre-polymer solutions based on their ability to form hydrogels following the exposure to the laser light source operating at a wavelength of 405 nm. After the photo-polymerization process, the hydrogels were placed in DI water to allow for swelling, and afterwards they were exposed to a blue LED light source operating at a wavelength of 470 nm in order to shrink. The aim of

this chapter is to trigger/activate the hydrogels after their exposure to light at certain wavelength and also measure the degree of their swelling and shrinking following the illumination process.

In this set of experiments, all the synthesized pre-polymer solutions (see appendix E.1 for the chemical structure) consist of the following main ingredients in different proportions for each case: NIPAM used as the water soluble monomer, acrylic acid used as the proton donor, MBIS used as a cross-linker, spiropyran 1 used as the photo-responsive element and irgacure used as the photo-initiator. Table 6.1 shows the four different pre-polymer solutions that we prepared and each one of them was mixed with 1 mL of 2:1 dioxane in DI water to completely dissolve all the components and make a homogeneous mixture. After the synthesis, we pipetted a droplet of 10 µL from each of the pre-polymer solutions on a glass slide, and immediately after we exposed them to the 405 nm light source with a fluence of $10.8\,J/cm^2$. In figure 6.2A we see photos of the polymerized pre-polymer solutions that led to the formation of hydrogels after the exposure to light. Although in this first experiment we did not make a parametric study of the light exposure conditions that lead to the formation of a hydrogel, we are sure that the formed materials are indeed hydrogels due to the fact that after the exposure to the light with the given fluence of $10.8\,J/cm^2$, they are no longer liquid but instead they have all transformed to semi-solid elastic (gel) materials.

After the polymerization process, we removed the hydrogels from the glass slide and rinsed them first with ethanol and then with DI water to remove any unpolymerized monomers that might remain inside the structure of the hydrogel. This washing step is essential as we believe that the unpolymerized monomers can interfere with the process of swelling thus preventing the hydrogel from its full activation after the water incubation.

In the next step, we placed the hydrogels inside the water and we kept them for 3 hours to ensure their full swelling. In photos 1 of cycle 1 in figure 6.2B we present images of the hydrogels at the state in which they are fully swollen and as we can clearly see this is associated with a colour change as compared with their colour in the initial state (figure 6.2A). This colour transition from light yellow (after polymerization with 405 nm) to dark yellow (after water incubation) is an indication of the activation of the spiropyran, which results in an increase in the volume of the hydrogel (swelling). Afterwards, we removed the hydrogels from water and we placed them on top of a paper tissue to remove the excess amount of water and then we exposed the hydrogels to the blue LED light source (470 nm) with energy per area of $132.5\,J/cm^2$ in order to induce their shrinking. Photos of the hydrogels at the stage when they are shrunk are illustrated in images 2 of figure 6.2B and again there is a colour transition from dark yellow to light yellow. Similar to our previous observation, this colour change is an indication that light with a wavelength of (470 nm) triggers the spiropyran resulting in the shrinking of the hydrogel.

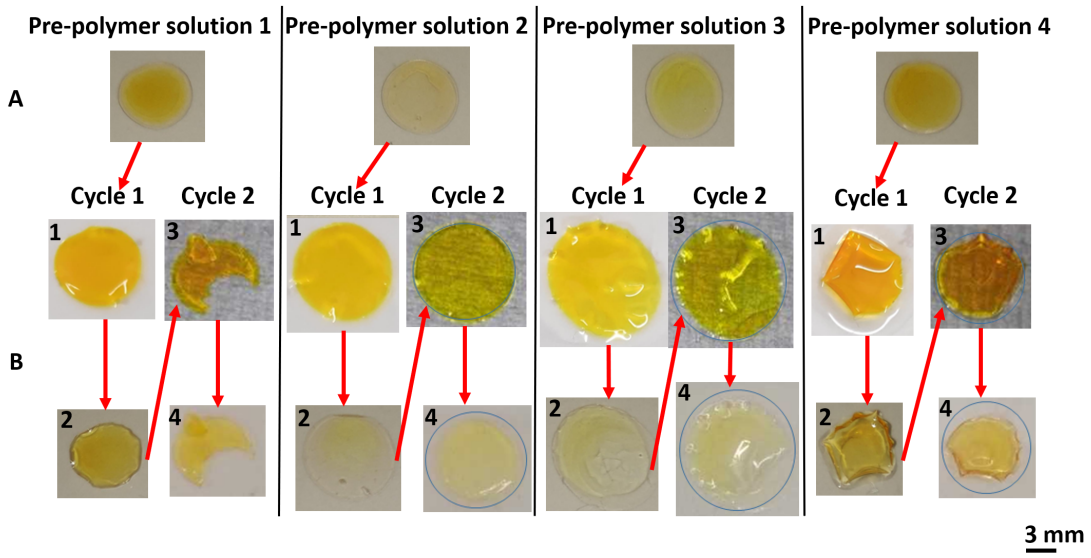

FIGURE 6.2: (A) Photos of the four pre-polymer solutions after their exposure to laser light at a wavelength of 405 nm to become hydrogels. (B) Following their exposure to 405 nm, the hydrogels, in cycle 1, were first incubated in water until they fully swell (photo 1) and then they were exposed to light at a wavelength of 470 nm to induce their shrinkage (photo 2). In cycle 2, we repeated the process as the same hydrogels were again incubated in water (photo 3) and then exposed to the 470 nm light source (photo 4).

In table 6.4 we present the results after measuring the volume change of the four different hydrogels in both cases after the water incubation and the exposure to the blue LED light source. In order to calculate the volume change we took photos of the hydrogels, as presented in figure 6.2, and then we used the RGB channel in the histogram function of the Adobe photoshop program to count the number of pixels in the cases after the exposure to 405 nm (figure 6.2A), in their swollen state after the incubation to water (photos 1 of figure 6.2B) and in their shrunk state after exposure to 470 nm (photos 2 of figure 6.2B). Then we used equation 6.1 to measure the percentage volume change.

$$\text{Volume change (\%)} = \left(1 - \frac{\text{Number of pixels after 405 nm exposure}}{\text{Number of pixels in swollen/shrunk state}}\right) \times 100 \quad (6.1)$$

It is well known that the hydrogels exhibit a reversible behaviour upon exposure to light of certain wavelength and that means that the hydrogel can transition from the shrunk state back to the swollen state multiple times. The purpose of the next experiment is to test the reversible behaviour of the four synthesized hydrogels and measure again the volume change in each of their states. For that we used the same hydrogels that we previously discussed and after their exposure to the 470 nm light source, we placed them back in water for another 3 hours in order to fully swell. After that, the hydrogels were removed from the water and we placed them on a paper tissue to remove the excess amount of water and then we took pictures as presented in photos

TABLE 6.4: Percentage volume change of the four hydrogels after the incubation to water (results in swelling) and the exposure to light at a wavelength of 470 nm (results in shrinking). The process of swelling and shrinking of the hydrogels was repeated two times.

Pre-polymer solution	After water Incubation	After exposure to 470 nm	After water Incubation	After exposure to 470 nm
1	+26.7%	-34%	-	-
2	+40%	-18%	+26.8%	-40%
3	+47.5%	-32.9%	+31%	-21.5%
4	+35%	-25%	+22%	-30%

3 of figure 6.2B (cycle 2). Afterwards, the hydrogels were again exposed to the blue LED light source (470 nm) for 10 minutes in order to shrink and photos of them are illustrated in images 4 of figure 6.2B. Despite the fact that only the hydrogel synthesized from the pre-polymer solution 1 was brittle and after removing from water it broke into pieces, we can see that there is an increase in their volume after the second incubation to water, whereas the volume of the hydrogels decreased upon their second expose to

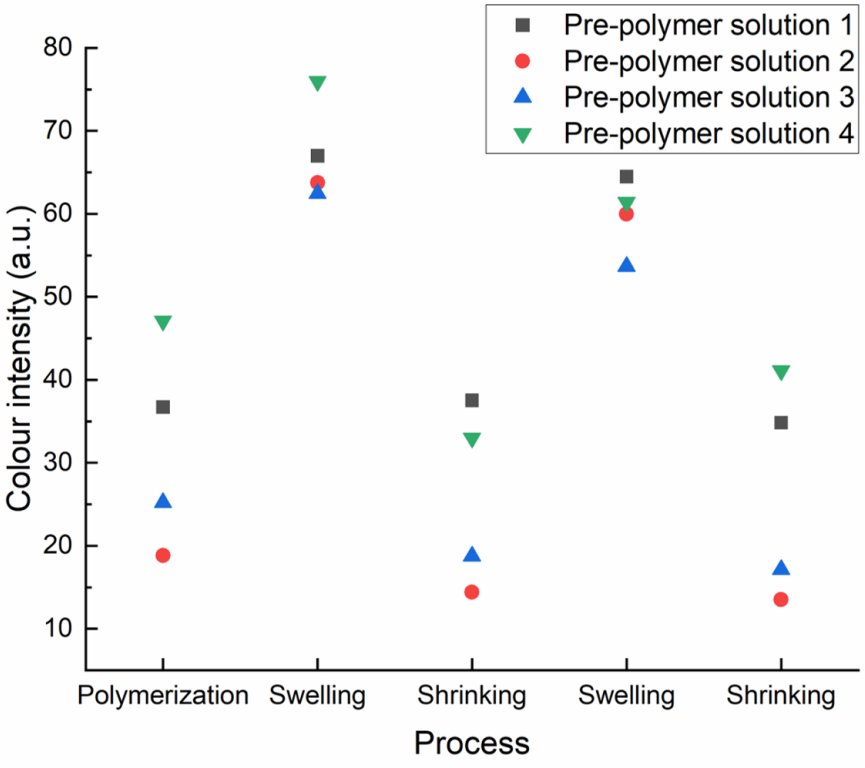

FIGURE 6.3: Colour intensity of the four pre-polymer solutions after each process namely: polymerization with 405 nm laser light source, incubation to water (swelling) and exposure to the 470 nm light source (shrinking). The colour intensity of all the hydrogels was measured in both cycle 1 and cycle 2.

light at 470 nm (table 6.4). As previously mentioned, the volume change of the hydrogels is associated with their colour change and in figure 6.3 we present a graph showing the colour intensity of the four pre-polymer solutions after each process namely: polymerization with the 405 nm laser light source, incubation to water to allow for swelling and finally exposure to 470 nm light source to allow for shrinking. As we can clearly see, for all the different hydrogels after their first and second exposure to the 470 nm light source (shrinking) their colour intensity is similar to the colour intensity of the hydrogel in the initial state (after the polymerization with the 405 nm). Furthermore, when the hydrogels are incubated in water (swelling) in cycle 1 and cycle 2 they exhibit similar colour intensity. These results show that the synthesized hydrogels exhibit a good reversible response when they are incubated in water as well as after their optical stimulation with the blue light source. In order to measure the colour intensity of the hydrogels, we used again the Adobe photoshop program, but this time we measured the mean intensity value of the pixels for each of the photos of the hydrogels presented in figure 6.2.

The reversible behaviour of the previously described hydrogels opens the path for their use as optical switches for the control of the sample flow. To test that, in the next experiment we used the local photo-polymer deposition method to fabricate channels on cellulose paper with the design as presented in figure 6.4A. Next, we pipetted different volumes of the hydrogel in the range between 2–4 µL in the centre of the fluidic channel

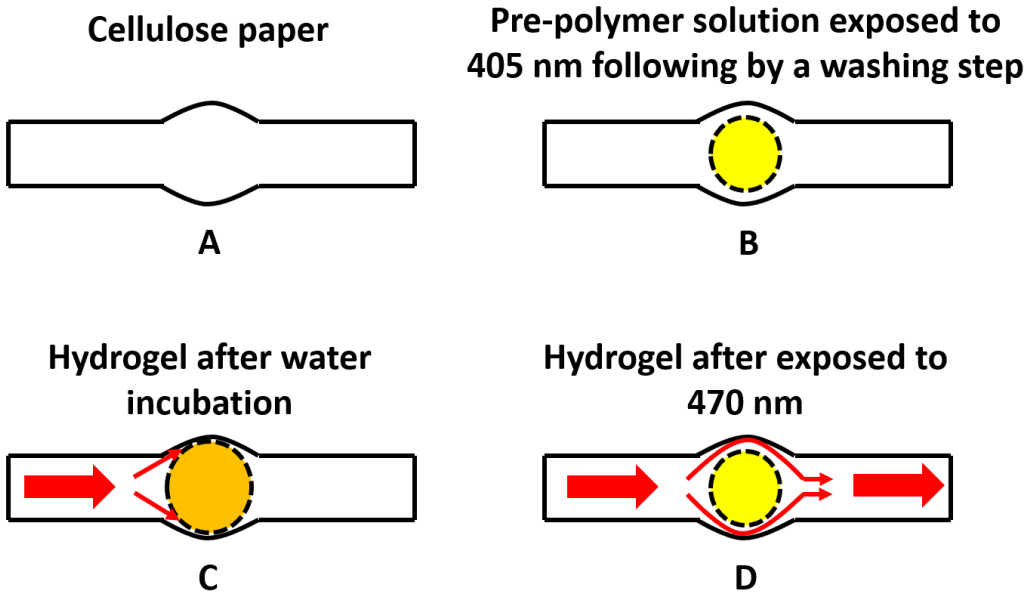

FIGURE 6.4: (A) Patterning of cellulose paper to create a channel able to guide the flow of liquids. (B) Pipetting the pre-polymer solution on the paper and polymerize with the 405 nm light source to make a hydrogel. (C) Incubation of the hydrogel in water to swell and block the sample flow. (D) Exposure of the hydrogel to 470 nm light source to shrink and enable the sample flow. The red arrow shows the direction of the sample flow on the fluidic channel.

as shown in figure 6.4B and immediately after we exposed to the 405 nm light source with a fluence of 10.8 J/cm^2. Due to the small viscosity of the hydrogel, it only took a few seconds to spread throughout the entire thickness of the cellulose paper and for that we set the time delay between the hydrogel deposition and the laser exposure to 10 seconds. Afterwards, we rinsed the hydrogel first with ethanol and then with DI water to remove any unpolymerized monomers and later we incubated in water for 3 hours to allow for swelling (figure 6.4C). After the water incubation step the paper device was left to dry for 30 minutes at room temperature before flowing 10 µL of a red dye to test whether the sample is able to flow around the hydrogel and towards the end of the fluidic channel. Finally, using the same device we exposed the hydrogel to the blue light source at 470 nm with energy per area of 132.5 J/cm^2 in order to allow for shrinking and we tested whether in that case a larger volume of the red dye is able to flow beyond the position of the hydrogel following the direction of the sample flow (figure 6.4D).

In figure 6.5A we illustrate an image of the cellulose paper device that we used for this experiment. Also, in figure 6.5B we present the results after pipetting different

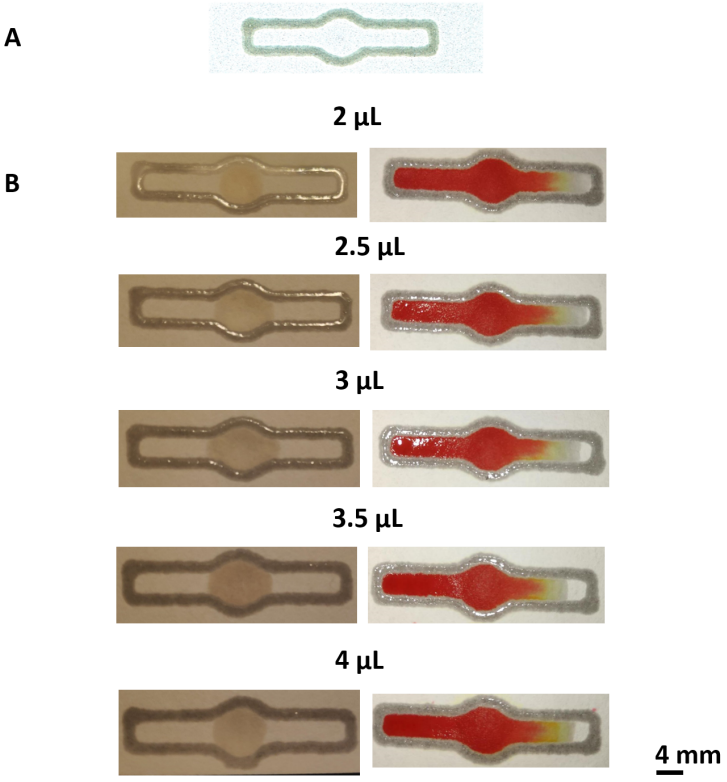

FIGURE 6.5: (A) Image of the paper device made on cellulose paper and designed for the optical control of a sample. (B) Left image: Devices in which we deposited the pre-polymer solution 1 in different volumes in the range between 2–4 µL and then exposed to the laser light at a wavelength of 405 nm with fluence at 10.8 J/cm^2 to make hydrogels. Right image: The same devices were incubated in water for 3 hours to allow for the hydrogel swelling before testing 10 µL of a red dye.

volumes, between 2–4 µL, of pre-polymer solution 1 in the centre of the paper device, following by a photo-polymerization using the 405 nm light source (left image) and then testing 10 µL of a red dye after the water incubation step and when the hydrogel is swollen (right image). Our choice to use the pre-polymer solution 1 in this first demonstration, stems from the fact that this pre-polymer leads to the formation of a hydrogel which exhibits the biggest volume change (-34%) upon exposure to the 470 nm light source (shrinking) according to the results in table 6.4. We believed that using pre-polymer solution 1, we would be able to allow a large volume of sample to flow around the hydrogel after the exposure to the blue light source. Unlike what we expected to observe, in figure 6.5B we see that when the hydrogel is in its swollen state and despite the volume we deposited, it was unable to block the flow of the red dye which immediately penetrated through it and towards the end of the fluidic channel. We believe that this is the result of the low viscosity of the pre-polymer solution 1 and the fact that after it was deposited it spreads within the cellulose and is unable to block the pores of the paper even when it is swollen.

In the last demonstration of this method, we repeated the same experiment but this time we used pre-polymer solution 3 which according to the results shown in table 6.4 exhibits the largest volume change (+47.5%) after the water incubation. We believe that using pre-polymer solution 3 and after incubating in water, we would be able to

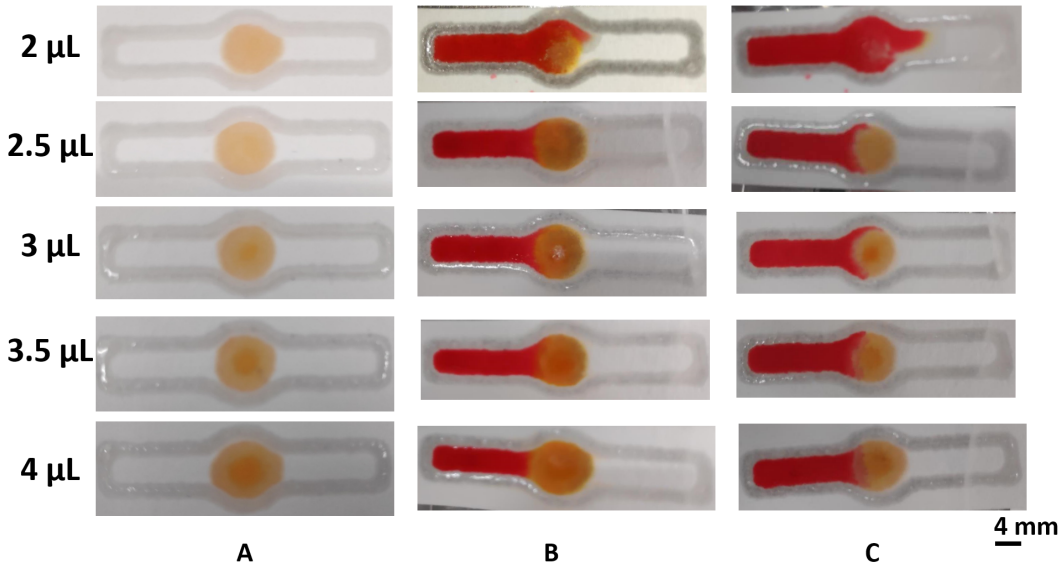

FIGURE 6.6: (A) Fluidic channels with different volumes of the pre-polymer solution 3 between 2–4 µL and after the exposure to the 405 nm light source to make hydrogels. (B) Photos of the devices after incubation to water for 3 hours to allow for the hydrogel to swell and then tested with 10 µL of a red dye. (C) Photos of the same fluidic devices after the hydorgels were exposed to the 470 nm blue light source with energy per area of 132.5 J/cm^2 in order to shrink.

block the flow of the sample and potentially allow its flow after the exposure to the blue light source. Furthermore, in order to make the pre-polymer solution we reduced the amount of solvent we used and specifically we diluted all its components in 300 µL of 2:1 dioxane in DI water to increase the viscosity of the pre-polymer solution and avoid its wide spreading on the paper. Figure 6.6A presents the results after pipetting different volumes of the pre-polymer solution 3 in the range between 2–4 µL, followed by the polymerization and cross-linking using the 405 nm (fluence at 10.8 J/cm^2) laser source to create hydrogels. Afterwards, the devices were washed following the protocol previously described and incubated in water for 3 hours. In figure 6.6B we depict the fluidic devices after the water incubation step and at the moment that the red dye (10 µL) reaches the position of the hydrogel. As can be clearly seen, only for the case that the pre-polymer solution was deposited at a volume of 2 µL the red dye can barely flow around the hydrogel whereas, for larger pre-polymer solution volumes (2.5–4 µL) the formed hydrogel is able to block the flow of the sample. However, after the exposure of the same hydrogels to the 470 nm light source with energy per area of 132.5 J/cm^2 (figure 6.6C), we observe that the red dye has indeed flowed more around the hydrogel, but is unable to reach the end of the fluidic channel despite the fact that there was a decrease in the volume of the pre-polymer solution 3 by 32.9% (table 6.4) when tested on a glass slide.

From the previously described results, we conclude that the four synthesized pre-polymer solutions, listed in table 6.1, were successful for the creation of light activated hydrogels when polymerized with the 405 nm laser light source, and they were also able to change their volume either by increasing their size after incubation in water or decreasing their size after exposed to the 470 nm blue light source. However, these hydrogels were not successful when tested on a paper device for the control of the flow of a sample and this arose primarily from their low viscosity and the fact that they spread widely on cellulose paper and this therefore put a limitation for the design of the device. Despite that, the main issue with these pre-polymer solutions, that prevented us from further exploration, is that they are too smelly because of the use of the acrylic acid and they cannot be used outside of the chemical fume hood. The factor of the odour is not only detrimental for the use of such a device for POC testing but can also be harmful for individuals during the device fabrication process. Another disadvantage of these pre-polymer solutions is the use of MBIS and igracure which are not water soluble and for that we need to dilute the pre-polymer solutions in dioxane and this adds an undesired additional step in the device fabrication process.

6.2.3 Characterization of different pre-polymer solutions containing $OEGMA_{300}$ and EGDMA for the creation of hydrogels

In order to solve the problems of the previously described pre-polymer solutions, in our next experiments we replaced NIPAM and MBIS with $OEGMA_{300}$ and EGDMA respectively. $OEGMA_{300}$ and EGDMA are both liquids and can dissolve the solid irgacure and spiropyran monomer without the addition of a solvent therefore, their use simplifies the process of synthesis of the pre-polymer solutions. Additionally, to prevent the strong smell of the pre-polymer solutions we replaced the acrylic acid with methacrylic acid and this allowed us to use the pre-polymer solutions outside of the chemical fume hood, thus making easier and most importantly safer the device fabrication process. In table 6.2 we present the list and the amount of the ingredients used for the synthesis of different pre-polymer solutions containing $OEGMA_{300}$ which is used as the water soluble monomer, methacrylic acid used as the proton donor, EGDMA used as a cross-linker, spiropyran 1 used as the photo-responsive element and irgacure used as the photo-initiator.

In the first experiment we used pre-polymer solution 5 (see appendix E.2 for the chemical structure) and we pipetted 2 µL in the middle of the paper device (cellulose) which has the same design as the one previously reported. Then we polymerized with the 405 nm laser light source using the same fluence as before, hence $10.8\,J/cm^2$ to form a hydrogel and a photo of the device is presented in figure 6.7A. Although, we do not present images here, we tested the pre-polymer solution 5 as well as the pre-polymer solution 6 (see appendix E.2 for the chemical structure) on a glass slide and we observed that the fluence of $10.8\,J/cm^2$ is sufficient for the creation of a hydrogel. Following the exposure and cross-linking of the pre-polymer solution 5, it was then washed with ethanol and DI water to remove any unpolymerized monomers and then incubated in water for 20 minutes to allow the hydrogel to swell. Afterwards, the paper device was tested with 10 µL of rhodamine dye and a photo of it after the testing process is illustrated in figure 6.7B. As we can see, the hydrogel, even in its swollen state, is unable to prevent the flow of the dye which immediately penetrates through it. We had similar results when using the pre-polymer solution 6 which was deposited in different volumes in the range between 2–4 µL on the paper device and tested with the same volume of the rhodamine dye (the polymerization with 405 nm, the washing and the water incubation steps remained unaltered). The respective photos are shown in figure 6.7C-F.

From these two sets of experiments we conclude that although we prepared pre-polymer solutions that removed the problem of smell, both of these pre-polymer solutions have low viscosity and hence they spread widely on the paper. This makes them unsuitable for use to control the flow of samples hence, pre-polymer solutions 5 and 6 were not studied further. Moreover, one of the main issues still remaining is

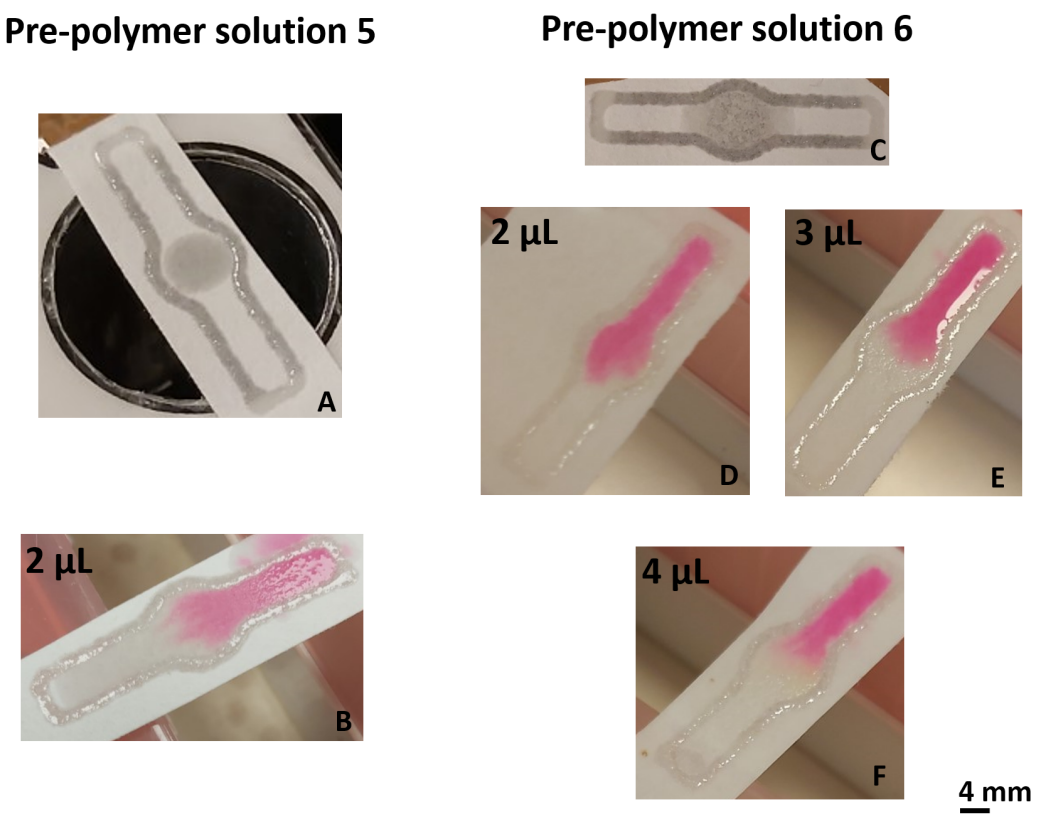

FIGURE 6.7: (A) 2 µL of pre-polymer solution 5 deposited on cellulose paper and polymerized with the 405 nm laser light source.(B) After the water incubation step the same device was tested with 10 µL of rhodamine dye. (C) 4 µL of pre-polymer solution 6 deposited on cellulose paper and polymerized with the 405 nm laser light source. (D)-(F) Different volumes of pre-polymer solution 6 between 2–4 µL deposited on cellulose paper and after the water incubation step each of the devices was tested with 10 µL of rhodamine dye.

the need for incubation of the hydrogel in water following the cross-linking in order to allow for swelling. The water incubation step is a limiting factor for the device fabrication not only because a paper-based device requiring such a preparation step can not be used for POC testing due to the fact that it requires a long waiting time but also, the wetting of the paper can alter its flow properties and make it incompatible for the dispensing and immobilization of antibodies.

In our next approach we synthesized a different pre-polymer solution that addresses the previously described problems. The pre-polymer solution 7 (see appendix E.2 for the chemical structure) had higher viscosity compared with the previous pre-polymer solutions, thus it spreads over a smaller area on the paper. This is due to the fact that we added $OEGMA_{900}$ into the pre-polymer solution in a way that the $OEGMA_{300}$ to $OEGMA_{900}$ mole ratio was kept to 4:1. The main difference between $OEGMA_{300}$ and $OEGMA_{900}$ is that the latter has a longer polymer chain and is solid at room temperature. However, a very small amount of water (a few hundred microliters) can dissolve it

and its addition to the pre-polymer solution can drastically increase the viscosity. The detailed list of the other components which are mixed in 200 µL of water to synthesize the pre-polymer solution 7 is shown in table 6.2. Apart from the use of $OEGMA_{900}$ in the pre-polymer 7 to increase the viscosity of the solution, the other key difference is that in this approach the hydrogel is not activated after water incubation, instead the swelling of the hydrogel happens by its exposure to a UV light source operating at 365 nm. This approach represents a big advancement over the previous methods as the water needed for the activation of the hydrogel already exists in the pre-polymer solution (i.e. is used as a solvent) and by making the hydorgel hydrophilic (attracts water) after exposing to the UV light source we allow for its swelling.

Our next aim was to be able to use our developed local photo-polymer deposition method to dispense the pre-polymer solution 7 onto porous substrates such as cellulose paper and NC membrane. The use of this method is highly desired as it will give us the flexibility to pattern the porous substrates by creating different designs for a more efficient control of the flow of samples. Despite the fact that we added $OEGMA_{900}$, the pre-polymer solution 7 is still not viscous enough in order to use it with the dispensing system and for that we mixed it with the Desolite photo-polymer in different proportions between 10–60 % in order to further increase the viscosity of the solution. In order to check whether the mixed solution (pre-polymer 7 + Desolite photo-polymer) is able to form uniform lines when deposited with the dispensing system, we printed lines with length of 8 cm on an NC membrane and then polymerized with the 405 nm laser light source with a fluence of $0.35\,J/cm^2$. A critical parameter in that experiment is the temperature at which the mixed solution is heated, as this dictates the resultant viscosity, hence the uniformity of the lines. For the purpose of this experiment, we heated the mixed solution to reach a temperature in the range between 50–70 °C and we deposited lines with various speeds in the range between 30–90 mm/s. The results are depicted in figure 6.8 where the mixed solutions consists of 10% of pre-polymer solution 7 in Desolite and although photos are not provided here, the results were the same when we tested pre-polymer solution 7 with a concentration of up to 40% in Desolite. For higher amounts of pre-polymer solution 7 (>40%) in Desolite the viscosity of the mixed solution is low, therefore the deposited lines are not uniform. From the results we see that when the mixed solution is heated to reach a temperature of 65 °C it provides the most uniform lines and for that reason the parameter of temperature is fixed to that value for the rest of the experimental process.

After establishing the parameter of temperature, the next step is to define the parameter of the time delay between the deposition and the laser scanning and the minimum fluence required for the hydrogel to activate. For that purpose, we designed a square wall with the same geometry as the one previously described ($5 \times 5\,mm^2$), and after testing with a red dye we visually observed whether the hydrogel swells enough to retain the sample inside the square wall. First, we deposited the mixed solution of 10% of

hydrogel in Desolite on cellulose paper with a deposition speed of 15 mm/s and using different time delays between 30–180 s we polymerized with the 405 nm laser light source with fluence of 0.35 J/cm^2 to create a solid structure. For each of the different cases we fabricated six square walls and tested each one of them with 10 µL of a red dye. In figure 6.9A we show one representative photo of a tested device for each of the

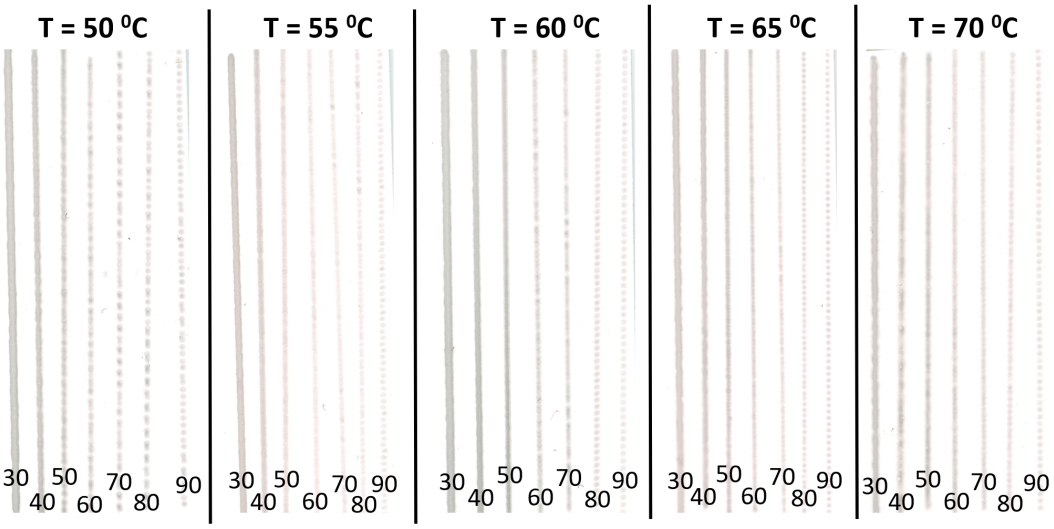

FIGURE 6.8: Lines of 10% of pre-polymer 7 in Desolite are printed on NC membrane at different deposition speeds in the range between 30–90 mm/s. In each of the different cases the solution was heated at different temperatures between 50–70 °C in order to be deposited as a uniform line with length of 8 cm.

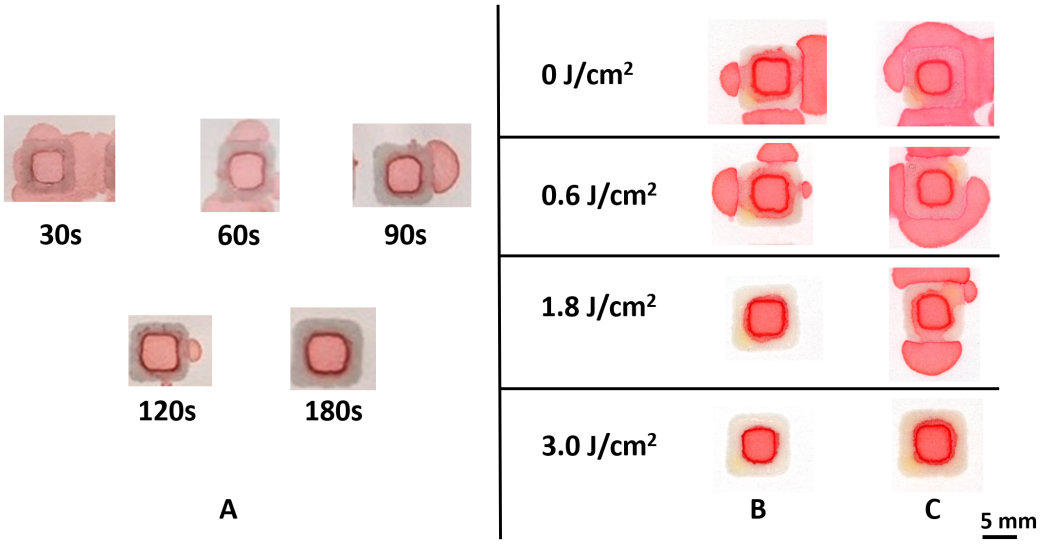

FIGURE 6.9: (A) Squares fabricated with the same deposition speed of 15 mm/s using a mixed solution of 10% of pre-polymer 7 in Desolite. The time delay between the deposition and the 405 nm laser scanning varies between 30–180 s. Squares fabricated with a mixed solution with 10% (B) and 20% (C) of pre-polymer 7 in Desolite and exposed to 365 nm with different energies per area between 0–3.0 J/cm^2. All the squares were tested with 10 µL of a red dye.

different cases and we can see that only for the case that the time delay was set at 180 s did the red dye not leak. From this experiment we conclude that the minimum time delay between the deposition of the mixed solution and the laser exposure has to be 180 s and this value did not change during the experimental process. Afterwards, we printed the mixed solution of 10% (figure 6.9B) and 20% (figure 6.9C) of pre-polymer 7 in Desolite and each of the squares was tested with 10 µL of a red dye. All the square walls were fabricated with the same deposition speed of 30 mm/s and we only changed the energy per area exposure of the 365 nm light source from 0 J/cm^2 to 3.0 J/cm^2. From the results of figure 6.9B,C we observe that the chosen deposition speed and without exposure to the UV light (0 J/cm^2) leads to the creation of porous squares in which the red dye cannot be contained. However, in the case of using the mixed solution with 10% of pre-polymer 7 in Desolite, an exposure of the lines to the 365 nm with 1.8 J/cm^2 is able to activate the hydrogel which swells enough to block the leakage of the red dye outside of the square wall. On the other hand, the mixed solution of 20% of pre-polymer 7 in Desolite requires a minimum energy per area of at least 3.0 J/cm^2 in order for the hydrogel to activate and prevent the leakage of the red dye. We believe that the difference in the minimum energy per area required for the activation of the hydrogel between the 10% and the 20% of pre-polymer 7 in Desolite stems from the fact that in the latter case the amount of spiropyran contained in the mixed solution is higher, therefore is needs a higher energy per area for it to allow for activation.

After successfully finding the parameters of the temperature, the time delay and the minimum fluence required for the activation of the hydrogel, in the next experiment we used these values and we printed fluidic channels on cellulose paper with an incorporated in-line barrier positioned at 90° to the direction of the sample flow (figure 6.10A). The solid boundary walls of the channel are made using the Desolite photo-polymer which is deposited at a line-speed of 20 mm/s whereas, the optically triggered in-line barrier is made with the mixed solution of 20% of pre-polymer 7 in Desolite which is deposited at line-speeds in the range between 30–50 mm/s and exposed to the 365 nm light source with different energies per area between 0–18.3 J/cm^2. After the deposition both the boundary walls and the in-line barrier were exposed to the 405 nm laser light source (fluence of 0.35 J/cm^2) to cross-link. The aim of this experiment is to fabricate porous in-line barriers which after their exposure to the 365 nm light source become impermeable to the flow of the sample (figure 6.10B) and only allow the flow of the sample after being exposed to the 470 nm light source (figure 6.10C). Each of the devices was tested with 15 µL of a red dye and from the results in figure 6.11A, where we have fabricated a fluidic channel without an in-line barrier, we can see that this volume of sample is sufficient to flow across the whole channel. In that figure we observe that an in-line barrier that has not been exposed to the 365 nm light source (0 J/cm^2), is porous to the flow of the red dye only when deposited at line-speeds above 35 mm/s. Given that, we will not test devices with in-line barriers fabricated with deposition speeds

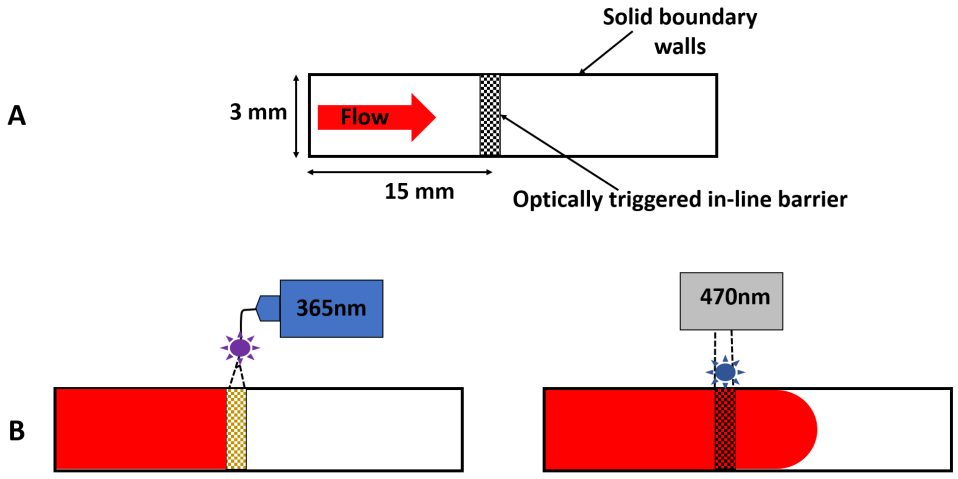

FIGURE 6.10: (A) Fluidic channel on cellulose paper with an incorporated in-line barrier positioned at 90° to the direction of the sample flow. The solid boundary walls are fabricated using the Desolite photo-polymer whereas, for the fabrication of the optically triggered in-line barrier we used the mixed solution of 20% of pre-polymer 7 in Desolite. When the in-line barrier is exposed to the 365 nm light source it becomes impermeable to the flow of the sample (B) however, the sample penetrates through the in-line barrier after its exposure to the blue light source at 470 nm.

below this threshold point, as this will make the use of the UV light unnecessary and therefore negate the purpose of this experiment.

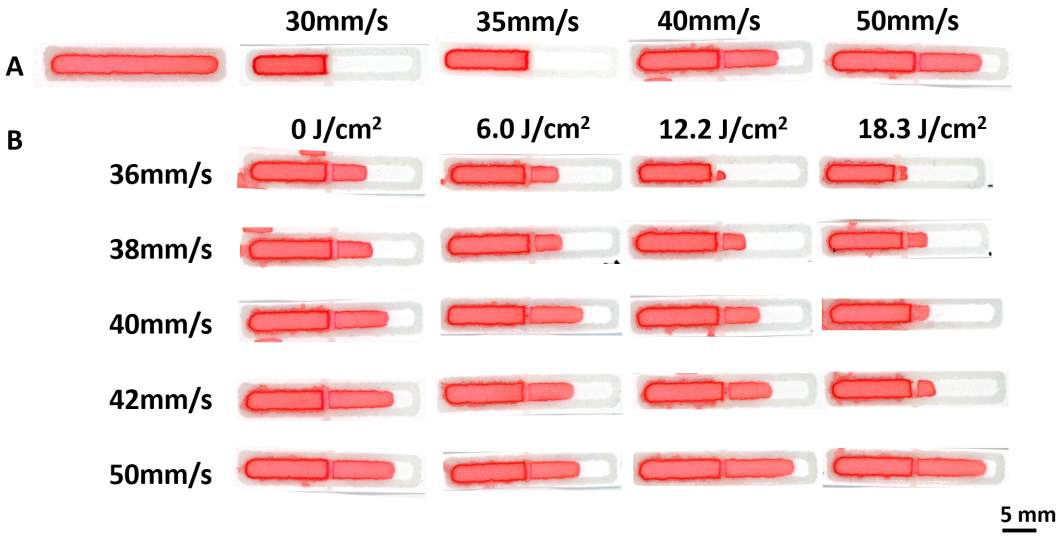

FIGURE 6.11: (A) Fluidic channel on cellulose paper fabricated with no in-line barrier and with in-line barriers at deposition speeds between 30–50 mm/s. (B) Fluidic channels with in-line barriers fabricated with deposition speeds between 36–50 mm/s and exposed to the 365 nm light source with different energies per area and in the range between 0–18.3 J/cm^2. Each of the devices was tested with 15 µL of a red dye.

In figure 6.11B we present the results of fluidic devices fabricated with an in-line barrier at deposition speeds in the range between 36–50 mm/s which were later exposed to the 365 nm light source with varying energies per area between 0–18.3 J/cm^2. We observe that for the very porous in-line barriers (e.g. 50 mm/s) an increase in the energy per area of the UV light does not result in any change in the flow of the red dye and we believe that this is due to the small amount of the hydrogel (higher speed is associated with lower deposited volume) contained inside the barrier. Additionally, an in-line barrier fabricated at 36 mm/s can significantly delay the flow of the red dye when exposed to 12.2 J/cm^2 whereas more porous barriers fabricated with deposition line-speeds between 38–42 mm s require an energy per area of at least 18.3 J/cm^2 in order to observe a significant delay in the flow of the sample. In none of the cases were the in-line barriers were able to completely block the flow of the red dye after their exposure to the 365 nm light source and for that reason we did not expose the barriers to the 470 nm light source to make them more porous.

In order to estimate the effect that the UV light has in the delay of the sample flow, we measured the time required for the sample to travel 5 mm beyond the position of the barrier and towards the end of the fluidic channel. For this measurement, we set as a

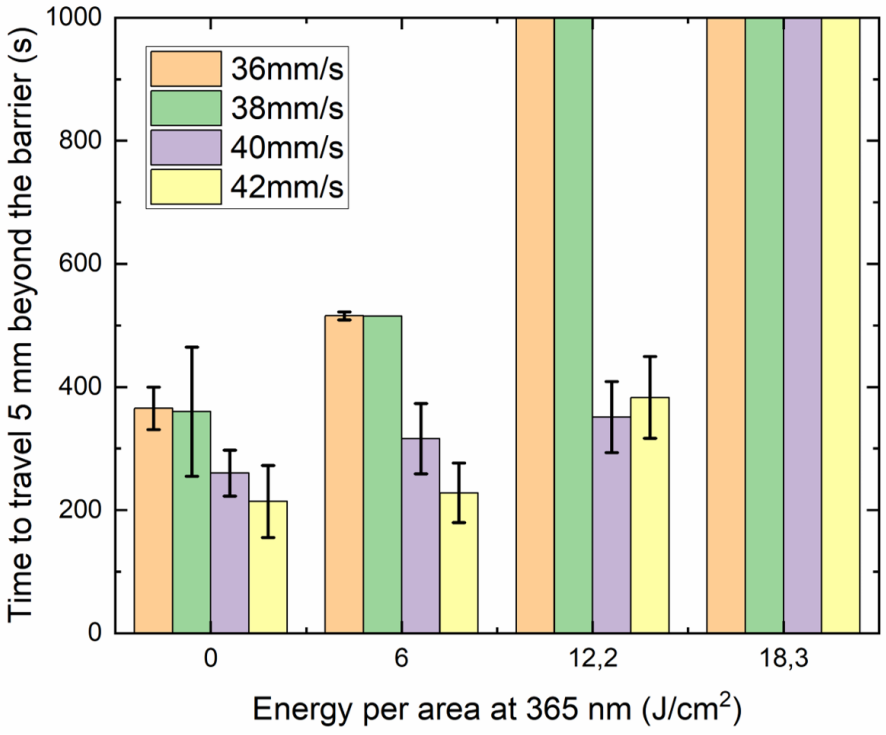

FIGURE 6.12: Graph presenting the time that the sample requires to travel 5 mm beyond the position of barriers fabricated with deposition speeds between 36–42 mm/s and exposed to the 365 nm light source with energy per area in the range between 0–18.3 J/cm^2.

starting point (t=0) the time that the sample is first introduced to the fluidic channel. The choice of the value of 5 mm was arbitrary and does not have any physical significance but instead, it is used as a measure to evaluate the performance of the in-line barriers after their exposure to the UV light. In figure 6.12 we present a graph showing the time required for the red dye to travel 5 mm beyond the position of barriers fabricated with line-speeds between 36–42 mm/s and exposed to the 365 nm light source with energy per area in the range between 0–18.3 J/cm^2. As previously stated, lower porosity barriers such as the ones fabricated at 36 mm/s and 38 mm/s are more efficient for the delay in the flow of the sample as they require a lower energy per area for that purpose. Despite this, in all the tested devices we observe that the sample is leaking outside of the boundary walls and this arises primarily from the inner structure of the cellulose which makes it difficult to guide the flow of liquids. Furthermore, another disadvantage of using cellulose paper is its low antibody binding capability to its surface, and this makes it unsuitable for implementation of diagnostic assays.

In our last demonstration we used pre-polymer 7 and we fabricated devices with the same geometry as the ones previously reported but this time on an NC membrane. The purpose of this experiment was not only to make devices able to control the flow of samples, but also to study the effect that different porous substrates have in the activation of the hydrogel after its exposure to the UV light. For the fabrication of fluidic channels we followed the same procedure as the one previously described, however

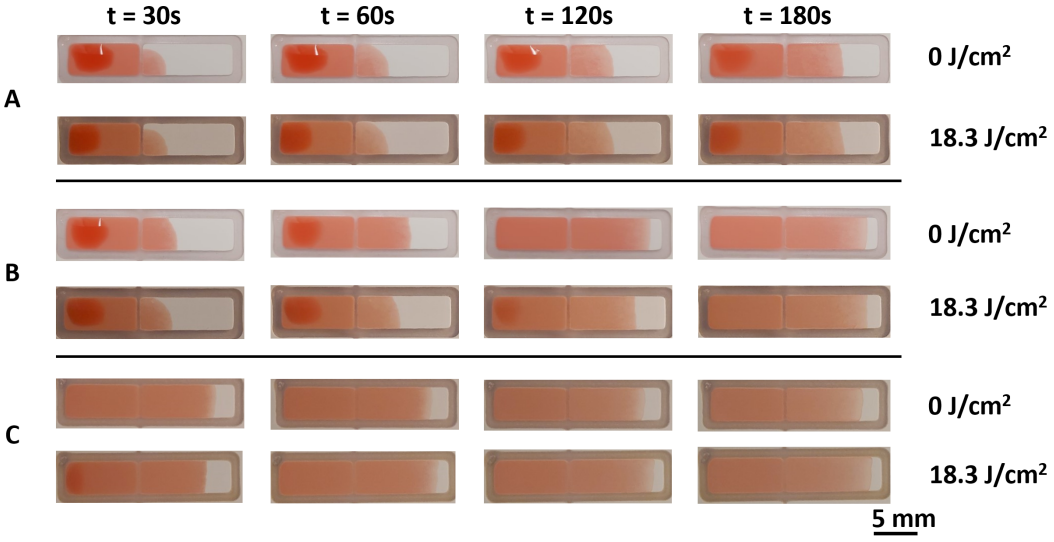

FIGURE 6.13: Fluidic channels on an NC membrane with an in-line barrier fabricated at deposition speeds of (A) 60 mm/s, (B) 65 mm/s and (C) 70 mm/s. In each of the cases the in-line barriers were exposed to the 365 nm light source with energy per area of 18.3 J/cm^2 and with 0 J/cm^2 (control). All the devices were tested with 15 µL of red dye and photos were taken at different times between 30–180 s after depositing the sample on the channel.

the mixed solution used for the fabrication of the in-line barrier contained 40% of pre-polymer solution 7 in Desolite. We used a higher concentration of the pre-polymer solution 7 in order to increase the degree of the hydrogel activation (swelling). Furthermore, we fabricated more porous in-line barriers, compared with the previous experiment, at higher deposition speeds namely 60 mm/s (figure 6.13A), 65 mm/s (figure 6.13B) and 70 mm/s (figure 6.13C) in order to increase the amount of sample flowing through the barrier after the exposure to the blue light source. The in-line barriers were exposed to the 365 nm light source with energy per area of 18.3 J/cm^2 and as a reference we tested devices where the barrier was not exposed to the UV light (0 J/cm^2). Each one of the devices was tested with 15 µL of red dye and photos of them were taken at different times between 30–180 s to visualize the progression of the sample flow along the channel. Similar to our previous measurement of time, we set as a starting point the moment that the sample is introduced to the channel. The results after the testing process are depicted in figure 6.13 and as we can see for the different porosities the sample is flowing through the barrier and towards the end of the channel. Given the fact that the barriers were unable to block the flow of the red dye after their expose to the UV light, we did not illuminate them with the 470 nm light source. Unlike what we expected to see and despite the fact that we used a higher concentration of pre-polymer 7, this approach can not be used for the control of the flow of samples and pre-polymer 7 will not be studied further for that purpose. It is also worth mentioning here that throughout the whole experimental process using pre-polymer 7, we did not observe any colour change of the hydrogel after the exposure to the 365 nm light source. Although we are not sure about that reason, one explanation could be the low degree of swelling of that hydrogel or the fact that the surface of some substrates such as the one of the NC membrane is chemically treated (e.g. for antibodies attachment) and this might limit or prevents the activation of the hydrogel.

6.2.4 Study of different designs on porous substrates to control the flow of samples.

Following the study of different hydrogels to control the flow of samples, in this section we focused on the use of the pre-polymer solution 8 (see appendix E.3 for the chemical structure) which contains a new formulation of the photo-responsive element namely spiropyran 2. The complete list of the ingredients used for the creation of the pre-polymer solution 8 and mixed in 200 µL of water is shown in table 6.3. Similar to the previously synthesized pre-polymer solutions, the pre-polymer solution 8 is not viscous enough to be deposited with our dispensing system and for that we mixed it with the Desolite photo-polymer in different proportions in the range between 10–40 %.

In order to characterize the response of the pre-polymer solution 8 after the exposure to light of different wavelengths, we pipetted a 1 µL droplet onto different porous

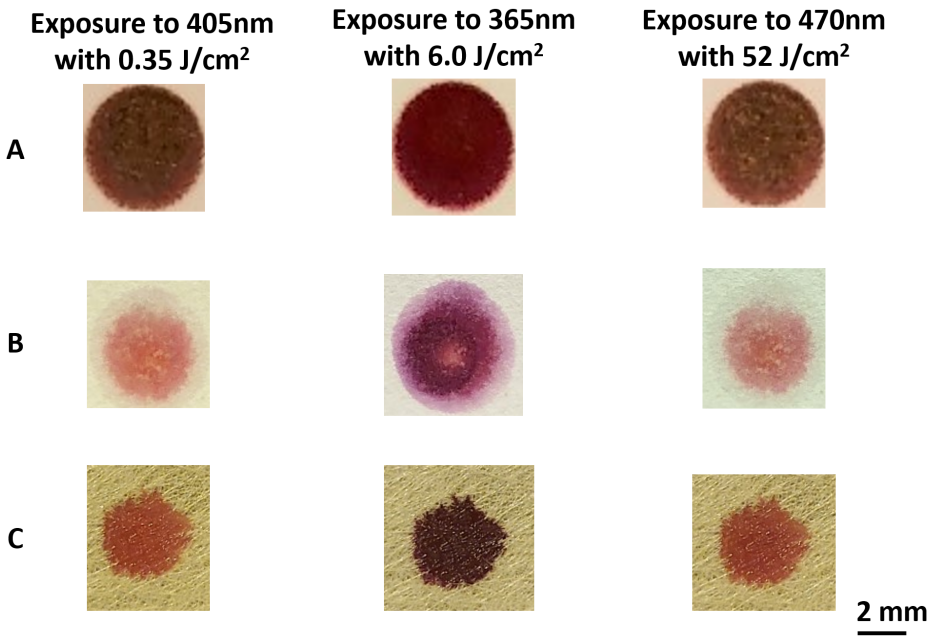

FIGURE 6.14: Image showing the results after a 1 µL droplet of pre-polymer solution 8 was deposited on different porous substrates namely (A) NC membrane, (B) cellulose paper and (C) microglass fibre and cross-linked after exposing to the 405 nm laser light source. The hydrogels were later exposed to the 365 nm and 470 nm light sources in order to allow for swelling or shrinking respectively.

substrates namely NC membrane (figure 6.14A), cellulose paper (figure 6.14B) and microglass fibre (figure 6.14C). The droplets were polymerized with the 405 nm laser light source with a fluence of 0.35 J/cm^2 (initial state) and after cross-linking, the hydrogel was exposed to the 365 nm light source with energy per area of 6.0 J/cm^2. Finally, the droplets of hydrogel were exposed to the 470 nm blue light source with energy per area of 52 J/cm^2 and photos of them after their exposure to different wavelengths are shown in figure 6.14. This process was repeated twice and for each we measured the number of pixels of the area that the hydrogel had spread on the porous substrate using the Adobe photoshop program. From the results shown in table 6.5 we observe that for the case in which the pre-polymer solution 8 was deposited on the NC membrane, there is a small colour change of the hydrogel after its exposure to the UV light with a difference (before and after the exposure to the 365 nm) in the colour intensity at 26.9 a.u. and this is associated with a small volume increase of 2%. However, in the cases that the pre-polymer solution 8 was deposited on the cellulose paper and the microglass fibre, we observe a bigger colour change after exposure to the 365 nm light source with differences in the colour intensities at 56.9 a.u. and 46.3 a.u. respectively. Additionally, there was an increase in the volume of 17% and 9.3% for the cellulose paper and the microglass fibre respectively. The pre-polymer solution 8 also exhibits a reversible behaviour and this is evident by the fact that in all the three different cases both the colour intensity and the volume of the hydrogel change become similar to the ones of

TABLE 6.5: Table presenting the percentage increase and decrease in the volume of the hydrogel when exposed to light at different wavelengths. To measure the volume change, a 1 µL droplet deposited onto different porous substrates namely NC membrane, cellulose paper and microglass fibre before exposure to the 405 nm laser light source.

Porous substrate	After exposure to 365 nm	After exposure to 470 nm
NC membrane	+2%	-2%
Cellulose paper	+17%	-17%
Microglass fibre	+9.3%	-10.1%

the initial state after the exposure to the 470 nm blue light source.

After the characterization of the pre-polymer solution 8, we used it with our dispensing system and for that we mixed it with the Desolite photo-polymer to make a mixed solution of 40% of pre-polymer 8 in Desolite. In our first demonstration we used the mixed solution to fabricate devices on a NC membrane with the same design and geometry as the one presented in the schematic of figure 6.10A. In this experiment we used the same mixed solution to fabricate both the solid boundary walls at a deposition speed of 20 mm/s and the in line-barriers at deposition speeds of 60 mm/s (figure 6.15A) and 65 mm/s (figure 6.15B). After polymerizing with the 405 nm light source with fluence of 0.35 J/cm^2, each device was tested with 15 µL of a red dye. In photos 1 we can see the fluidic devices without exposing the in-line barrier to the 365 nm light source and these

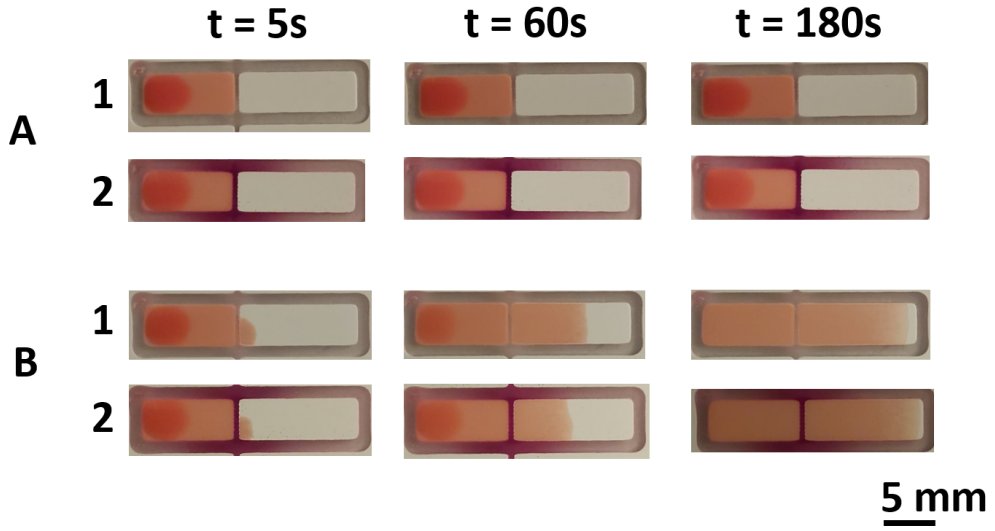

FIGURE 6.15: Fluidic devices with an incorporated in-line barrier fabricated with deposition speeds at (A) 60 mm/s and (B) 65 mm/s. Each of the devices was tested with 15 µL of a red dye in the cases of (1) no exposure and (2) exposure to the 365 nm light source with energy per area of 6.0 J/cm^2. Photos of the same device were taken at different times between 5–180 s after the deposition of the sample.

used as a reference, whereas in photos 2 we can see devices fabricated with the same patterning conditions as the previous ones but where the in-line barrier was exposed to the UV light with energy per area of 6.0 J/cm^2. Photos of the devices were taken at different times between 5–180 s after the sample deposition, and as we can see an in-line barrier fabricated at a line-speed of 60 mm/s is not porous enough to allow the flow of the sample as presented in figure 6.15 A1. On the other hand, an in-line barrier fabricated at a line-speed of 65 mm/s is porous both before (figure 6.15 B1) and after the exposure to the UV light (figure 6.15 B2) we do not observe any difference in the flow of the sample between these two cases. We believe that this is the result of the low degree of the hydrogel swelling on the NC membrane (2%) and due to that, this substrate will not be used any more for deposition and activation of the light responsive material.

In our next experiment we used again the mixed solution with 40% of pre-polymer 8 in Desolite and we fabricated in-line barriers on a fluidic channel made on cellulose paper. Similar to our previous method, we used again the same mixed solution to make both the solid boundary walls with deposition speed of 20 mm/s and the in-line barriers with deposition speeds of 70 mm/s (figure 6.16A,C) and 80 mm/s (figure 6.16B). After polymerizing with the 405 nm light source with the same fluence as before, each of

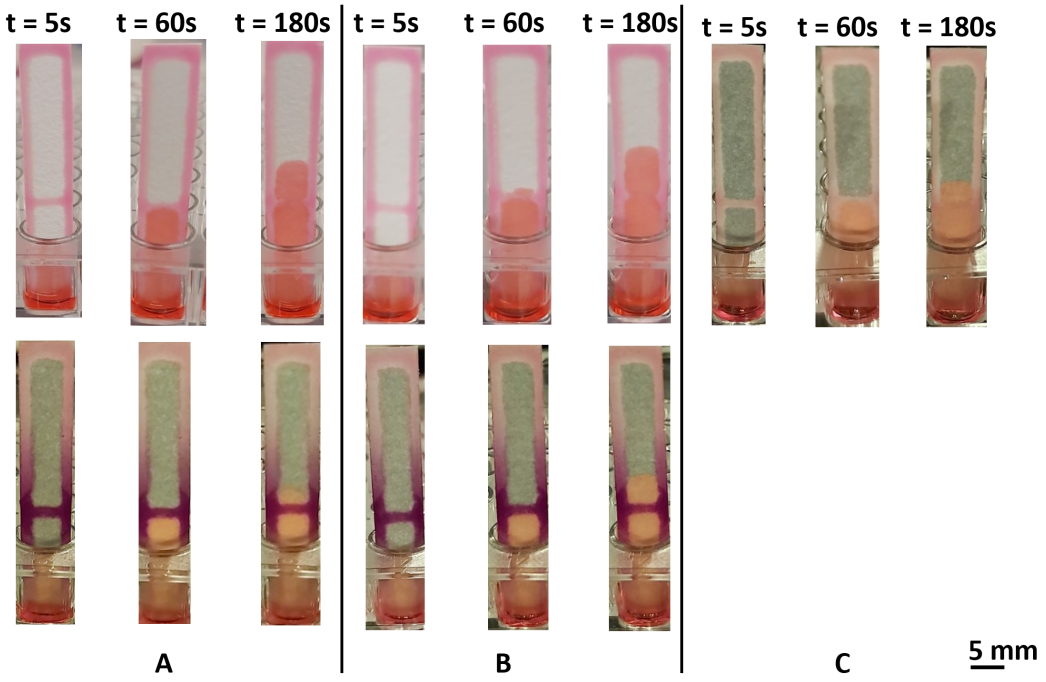

FIGURE 6.16: Fluidic devices on cellulose paper with an in-line barrier fabricated at deposition speeds of (A) 70 mm/s and (B) 80 mm/s. The devices were tested for the cases of non exposure and exposure of the barrier to the 365 nm light source with energy per area of 6.0 J/cm^2. (C) Devices in which the in-line barrier was fabricated at a deposition speed of 70 mm/s, then exposed to the 365 nm light source with energy per area of 6.0 J/cm^2 and finally to the 470 nm blue light source with energy per area of 130 J/cm^2. All the devices were dipped into 15 µL of a red dye during the testing process.

the devices was dipped into 15 µL of a red dye and photos of the same device were taken at different times between 5–180 s. In figures 6.16A,B we observe that the in-line barriers which are not exposed to the UV light (top devices) are porous to the flow of the red dye, however after their exposure to the 365 nm light source (bottom devices) with energy per area of 6.0 J/cm^2 the barriers become less porous and therefore the amount of the sample flowing through the barriers is reduced. In order to measure the effect that the UV light has in controlling the flow of the sample, we took photos of the devices at different times and in each case we measured the distance that the red dye has travelled above the position of the barrier in both the cases of non exposure and exposure of the in-line barriers to the 365 nm light source. In figure 6.17 we present graphs from the results after testing the devices with barriers fabricated at (A) 70 mm/s and (B) 80 mm/s and we observe that the biggest change (delay) in the flow of sample

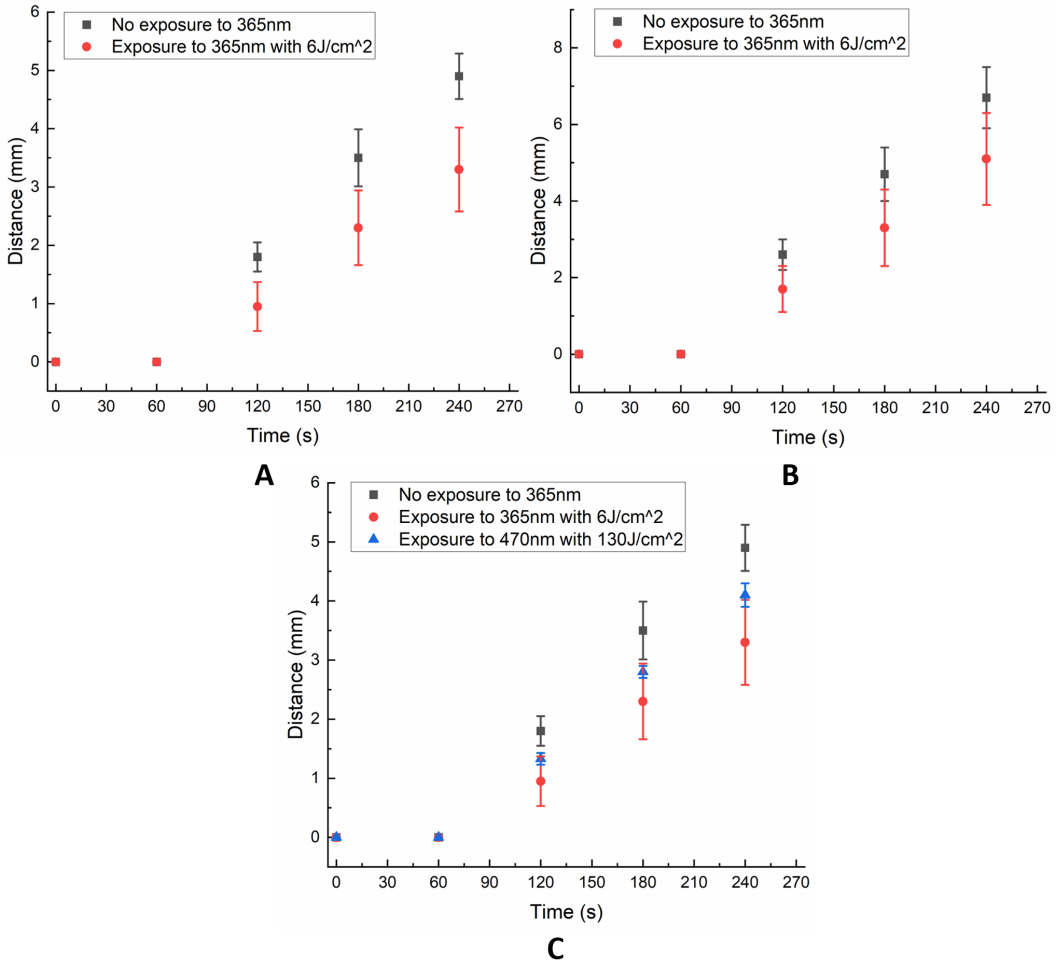

FIGURE 6.17: Distance that the red dye has flowed beyond the position of the barrier at different times when fabricated at (A) 70 mm/s and (B) 80 mm/s in the cases of non exposure and exposure to the 365 nm light source. (C) Distance that the red dye has flowed above a barrier fabricated at 70 mm/s which was exposed to the 365 nm and then to the 470 nm light source.

TABLE 6.6: Percentage delay in the flow of sample at different times after the exposure of barriers fabricated with different line-speeds to the UV light.

Barrier line-speed (mm/s)	**60 s**	**120 s**	**180 s**	**240 s**
70	0%	47%	35%	32%
80	0%	34%	29%	23%

happens for the barriers fabricated at 70 mm/s after their exposure to the UV light.

In order to measure the percentage in the flow delay of the sample after the exposure of the barriers to the UV light, we used equation 6.2 to produce the results depicted in table 6.6. Using that method we were able to measure the efficiency of the barriers for delaying the flow of the sample at different times between 60–240 s when exposed to the UV light and from the results we can see that the maximum flow delay (47%) happens 2 minutes after depositing the sample in a channel with a barrier fabricated at 70 mm/s.

$$\text{Flow delay (\%)} = \left(1 - \frac{\text{Distance after exposure to 365 nm}}{\text{Distance with no exposure to 365 nm}}\right) \times 100 \tag{6.2}$$

Afterwards, and in order to check the reversible process of the hydrogel, we fabricated again an in-line barrier with a deposition speed of 70 mm/s and we exposed it to the 365 nm after the polymerization with 405 nm. The fabrication parameters remained the same as the ones previously reported but in that experiment and before testing the devices we illuminate the in-line barrier with the 470 nm blue light source with energy per area of 130 J/cm^2 in order to allow for the hydrogel to shrink, hence increase the porosity of the barrier. The results during the testing process are illustrated in figure 6.16C and the respective graph is presented in figure 6.17C where the lines in the cases of non exposure and exposure to the 365 nm are also plotted for comparison. As we can see when the in-line barrier is exposed to the 470 nm light source, the porosity increases and this is evident by the fact that the sample can travel a longer distance in the fluidic channel as compared with the case when the barrier was exposed to 365 nm. Despite the success of this method for the optical control of the sample flow, the disadvantage of this method arises from the non repeatability of the results. Specifically, during the testing process we experienced a lot of inconsistency in the results and we believe that this is due to the inner structure of the paper and the small variations from batch to batch. As a matter of fact, we believe that the local photo-polymer deposition method is not ideal for use on a cellulose paper to control the flow of samples.

In our last demonstration using the mixed solution with the local photo-polymer deposition method, we patterned microglass fibre to make a constriction on a fluidic channel able to block or enable the flow of a sample upon exposure to light of wavelength of 365 nm or 470 nm respectively. For the purpose of this experiment we used again the

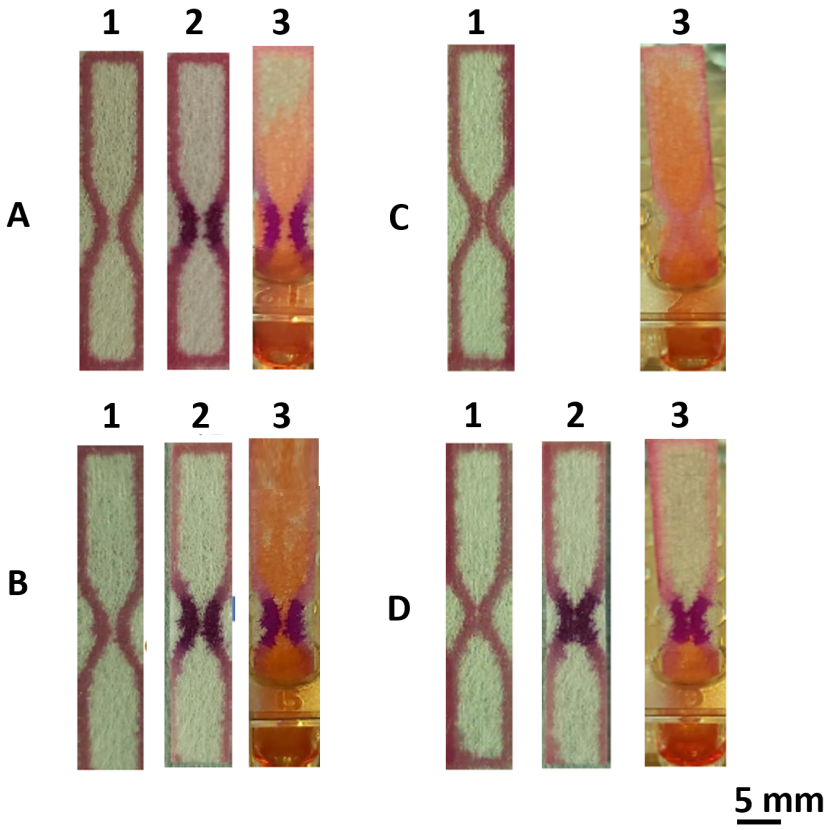

FIGURE 6.18: Images showing fluidic devices on a microglass fibre with a constriction of different widths namely (A) 1 mm, (B) 0.5 mm and (C,D) 0.2 mm. Photos 1 show the devices after the polymerization with the 405 nm, photos 2 show the same devices after the constriction was exposed to the 365 nm light source with energy per area of 6.0 J/cm^2 and finally photos 3 show the devices tested with 15 µL of a red dye.

mixed solution of 40% of pre-polymer 8 in Desolite and we created constricted channels of varying widths namely 1 mm (figure 6.18A), 0.5 mm (figure 6.18B) and 0.2 mm (figure 6.18C,D). In photos 1 of figure 6.18 we show the channels after the polymerization with the 405 nm laser light source, in photos 2 we present the same channels after the constriction exposed to the 365 nm light source with energy per area of 6.0 J/cm^2 and finally in photos 3 the same channels were tested with 15 µL of a red dye. From the results we observe that a channel fabricated with a constriction width of 1 mm and 0.5 mm is unable to block the flow of the sample even after its exposure to the UV light (figures 6.18A,B). However, a channel with a constriction width of 0.2 mm although it is porous and allows the flow of the sample (figure 6.18C), after exposure of the constriction to the 365 nm light source it is able to completely block the flow of the red dye (figure 6.18D). Although the method of patterning a constricted channel on a microglass fibre is successful to block the flow of the sample after exposure to the UV light, we observe that the constrictions are not uniform between identical devices. Specifically, in photos 1 of figures 6.18C and 6.18D although we used the same patterning conditions such as deposition speed, laser scanning speed and time delay, we observe that the polymer

lines at the point of the constriction are not completely uniform and this can clearly affect the repeatability of our results.

In our last demonstration of using the pre-polymer solution 8 we use an alternative approach which includes the use of an optically triggered pad to control the flow of samples. Unlike the previous reported methods, in this approach we do not make use of the local photo-polymer deposition technique but instead, we are using a more simple approach which involves the impregnation of a porous substrate on the mixed solution contained pre-polymer solution 8 in Desolite (step 1). Next, we removed the excess monomer from the porous substrate and we exposed it to the 405 nm laser light source in order to create an optically triggered pad (step 2). Afterwards, the pad was placed on an LFA and after its exposure to the 365 nm laser light source it becomes impermeable to the flow of sample (step 4). Finally, the optically triggered pad was exposed to the 470 nm blue light source in order to allow for the hydrogel to shrink, and therefore enable the flow of the sample through the pad and towards the end of

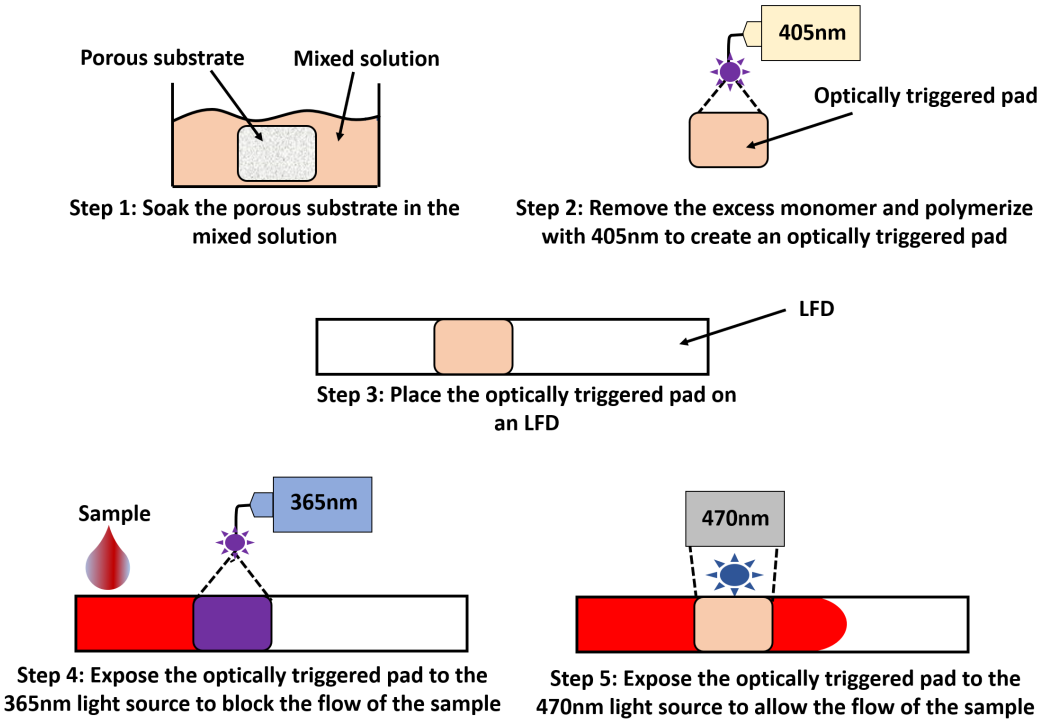

FIGURE 6.19: Schematic showing the various steps requiring for the optical flow control of a sample on an LFA. First the porous substrate is impregnated on a mixed solution containing pre-polymer 8 in Desolite (step 1) and then after removing the excessive monomers from the substrate we expose it to the 405 nm laser light source to polymerize and create an optically triggered pad (step 2). Next the optically triggered pad is placed on an LFA (step 3) and is exposed to the 365 nm laser light source to activate the hydrogel and block the flow of the sample (step 4). Finally, the pad is exposed to the 470 nm blue light source to allow the flow of the sample towards the end of the LFA(step 5).

the LFA. The various steps involved for the fabrication of the optically triggered pad are depicted in figure 6.19.

In our first demonstration of using the previously described method, we used micro-glass fibre as a material to make the optically triggered pad and we soaked it (for 1 minute) in a mixed solution containing 10% of pre-polymer 8 in Desolite. Next, we removed the excessive amount of monomer and exposed it to the 405 nm laser light source with a fluence of 0.35 J/cm^2 to create the optically triggered pad. This pad was later placed on an LFA between the fluidic channel(NC membrane) and the sample pad (cellulose paper). We decided to use this configuration of the materials to mimic the design of a standard LFA in which we have replaced the conjugate pad with the optically triggered pad in order to be able to control the flow of samples. The device was tested with 10 µL of a red dye and the results are depicted in figure 6.20A where photos of the same device are taken at different times between 60–180 s. As we can see the optically triggered pad is porous, thus the red dye is flowing in the channel 180 s after its deposition on the sample pad. However, when the optically triggered pad is exposed to the 365 nm light source with energy per area of 6.0 J/cm^2, then the hydro-gel contained in it swells and therefore there is a delay in the flow of the red dye in

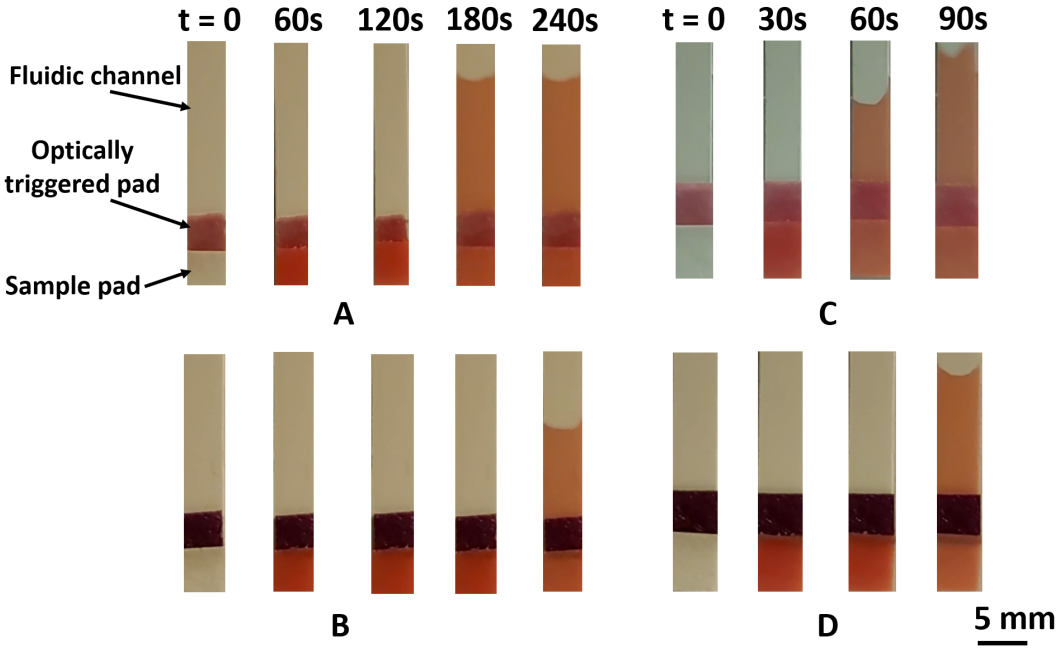

FIGURE 6.20: LFAs with an optically triggered pad to control the flow of sample. The optically triggered pad contains the mixed solution of 10% of pre-polymer 8 in Desolite and the devices were tested with 10 µL of a red dye in both the cases of (A) non exposure and (B) exposure of the pad to the 365 nm laser light source. Images of LFAs in which the optically triggered pad is made of the mixed solution of 20% of pre-polymer 8 in Desolite and tested with the same volume of the red dye again in the cases of (C) no exposure and (D) exposure to the UV light. Photos of the LFAs were taken at different times.

the channel (figure 6.20B). Since the optically triggered pad was not able to completely block the flow of the sample to the fluidic channel, we did not expose it to the 470 nm light source.

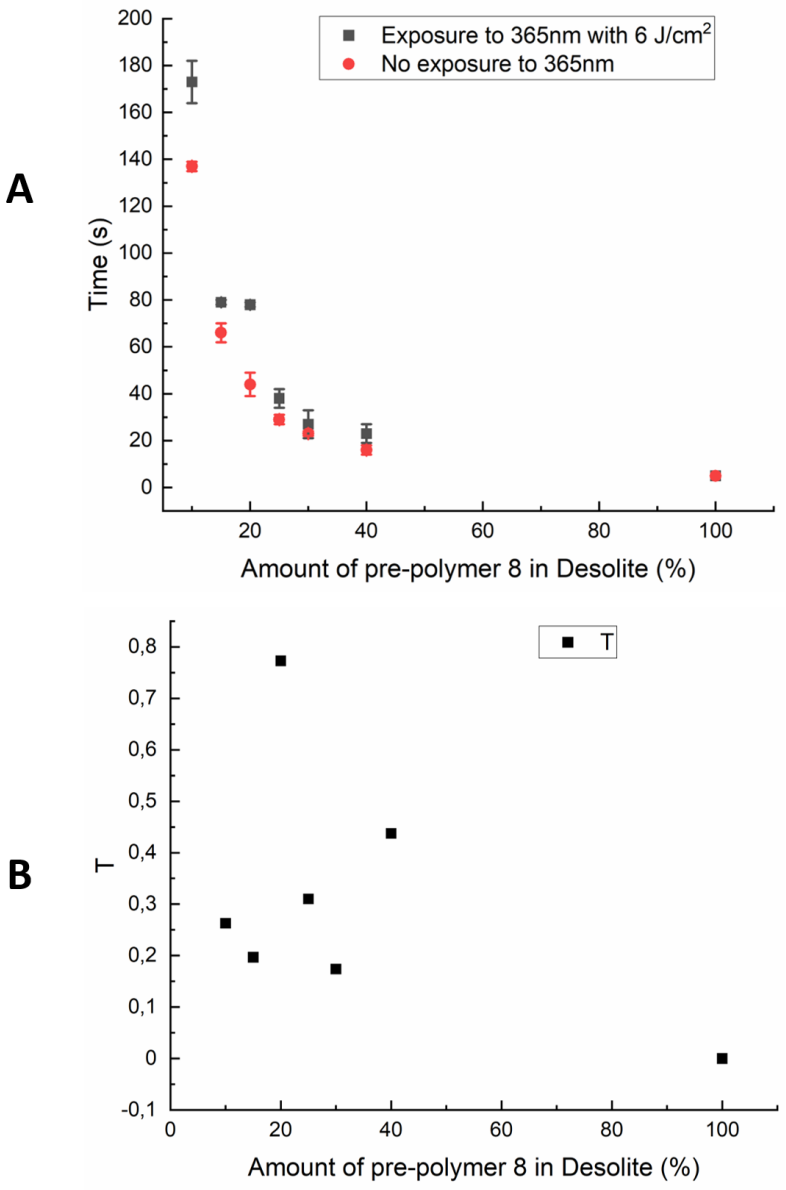

FIGURE 6.21: (A) Time that the sample takes to flow from the sample pad to the fluidic channel in the cases of no exposure and exposure of the optically triggered pad to the 365 nm light source. This experiment was repeated for mixed solutions of varying proportions of pre-polymer 8 in Desolite in the range between 10–100 %. (B) Plot showing the difference (T) between the time that the sample takes to flow from the optically triggered pad to the fluidic channel when the pad is exposed and without being exposed to the UV light.

Next, we studied the effect that different mixed solutions have in the delay of the flow of the sample, and for that we prepared different mixed solutions with pre-polymer 8 between 20–100 % in Desolite. We then repeated the same experiment as before using the same volume of the red dye as well as the same light exposure parameters for polymerization and activation of the hydrogel, and the results after testing the mixed solution of 20% of pre-polymer 8 in Desolite are depicted in figures 6.20C (before exposure to 365 nm) and 6.20D (after exposure to 365 nm). Additionally, in figure 6.21A we present a graph with all the results for the cases of non exposure and exposure of the optically triggered pad to the 365 nm light source. In each of the different cases we measured the time that the red dye takes to flow from the sample pad to the fluidic channel. As we can see, for the solution that contains only pre-polymer 8 (or 100% of pre-polymer 8 in Desolite) we were not able to see any delay in the flow of the sample after exposing the optically triggered pad to the 365 nm light source. In fact for both the cases of non exposure and exposure of the pad to the UV light, the red dye flows instantly to the fluidic channel and we believe that this is the result of the poor adhesion of the hydrogel on the cellulose paper after the polymerization process and this therefore results in the hydrogel being washed away from the sample. On the other hand, for the rest of the cases that we used the mixed solution between 10–40 %, we repeated each measurement three times and we observe a delay in the flow of the sample after the exposure to the UV light. In order to find out which one of the mixed solutions produces the maximum flow delay of the sample, in figure 6.21B we plotted the difference (T) between the time that the sample takes to flow from the optically triggered pad to the fluidic channel when the pad is exposed and without being exposed to the UV light. For this we used equation 6.3 where $T_{exposure}$ refers to the time that the red dye takes to flow from the sample pad to the fluidic channel for the case that the optically triggered pad is exposed to the 365 nm light source, whereas $T_{no\ exposure}$ refers to the same case however, the optically triggered pad in not exposed to the UV light. From the results we see that using a mixed solution of 20% of pre-polymer 8 in Desolite and after exposing the light activated pad filled with this mixed solution to the UV light we produce the maximum flow delay of the sample. This method proved successful for the delay in the flow of a sample and will be later used in an assay to enhance the signal in the detection of an analyte.

$$T = \left(\frac{T_{exposure} - T_{no\ exposure}}{T_{no\ exposure}} \right) \tag{6.3}$$

Next, we tested another method to optically control the flow of samples in which we used as an optically triggered component a square flow-through pad with dimensions of 25 mm^2 located at the front end of an LFA. This approach is the same as the flow-through filtration process that we reported in chapter 7.3 with the only difference being that we deposited the mixed solution of pre-polymer 8 in Desolite inside the solid

boundary walls of the square pad instead of the Desolite diluted in IPA that we previously used for the creation of the porous flow-through filters.

For the fabrication of the flow-through optically triggered pad we started with the local photo-polymer deposition method to deposit the Desolite photo-polymer on cellulose paper (deposition speed 20 mm/s) and after exposing to the 405 nm laser light source we created the solid boundary walls which are able to contain the flow of liquids. Next, we followed the same device fabrication process as the one described in the schematic 6.19 and we soaked the flow-through pad in the mixed solution of 20% of pre-polymer 8 in Desolite. After removing the excess monomer from the pad, we exposed it to the 405 nm laser light source with a fluence of 0.35 J/cm^2 in order to polymerize. Afterwards, the flow-through optically triggered pad was placed at the front-end of an LFA (NC membrane) and it was either exposed to the 365 nm laser light source to block or

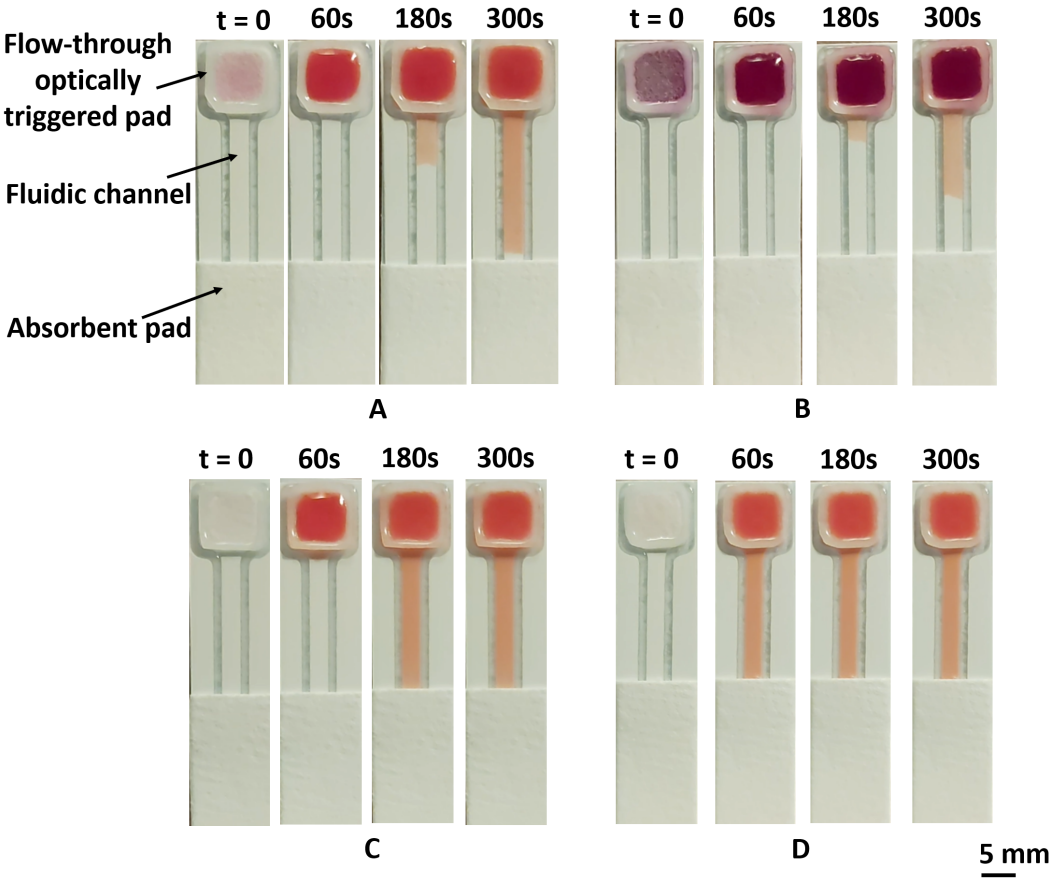

FIGURE 6.22: (A) A flow-through optically triggered pad after the polymerization with the 405 nm laser light source is placed at the front-end of an LFA and tested with 10 µL of a red dye. (B) The optically triggered pad is later exposed to the 365 nm light source and tested with the same volume of sample. Finally the pad is exposed to the 470 nm blue light source following the polymerization with energy per area of (C) with 130 J/cm^2 and (D) with 260 J/cm^{2}s and tested with the same volume of the red dye. Photos of the tested devices were taken at different times between 60–300 s after the deposition of the sample.

delay the flow of sample, or to the 470 nm blue light source in order to enable its flow. Each one of the flow-through pads was tested with 10 µL of red dye and photos of the same device were taken at different times between 60–300 s after the deposition of the sample. At the end of the LFAs we have placed an absorbent pad to remove the excess amount of sample that reaches the end of the fluidic channel.

In figure 6.22A we present the results when we tested a flow-through optically triggered pad after its polymerization with the 405 nm laser light source (control device) and as we can see, the red dye is flowing in the fluidic channel 180 s after the sample deposition. However, when we expose the optically triggered pad to the 365 nm light source with energy per area of 6.0 J/cm^2, then the pad is again porous but with a delay in the flow of the sample as compared with the previous case (figure 6.22B). Furthermore, in figures 6.22C and 6.22D we depict the results after exposing the flow-through optically triggered pads to the 470 nm blue light source with energy per area of 130 J/cm^2 and 260 J/cm^2 respectively following the polymerization with the 405 nm laser light source. From these results, we observe that an exposure with 130 J/cm^2 of the pad to the blue light results in an increase in its porosity, hence the red dye is flowing along the whole channel 180 s after the sample deposition. Additionally, an exposure of the pad to the blue light with 260 J/cm^2 results in a further increase

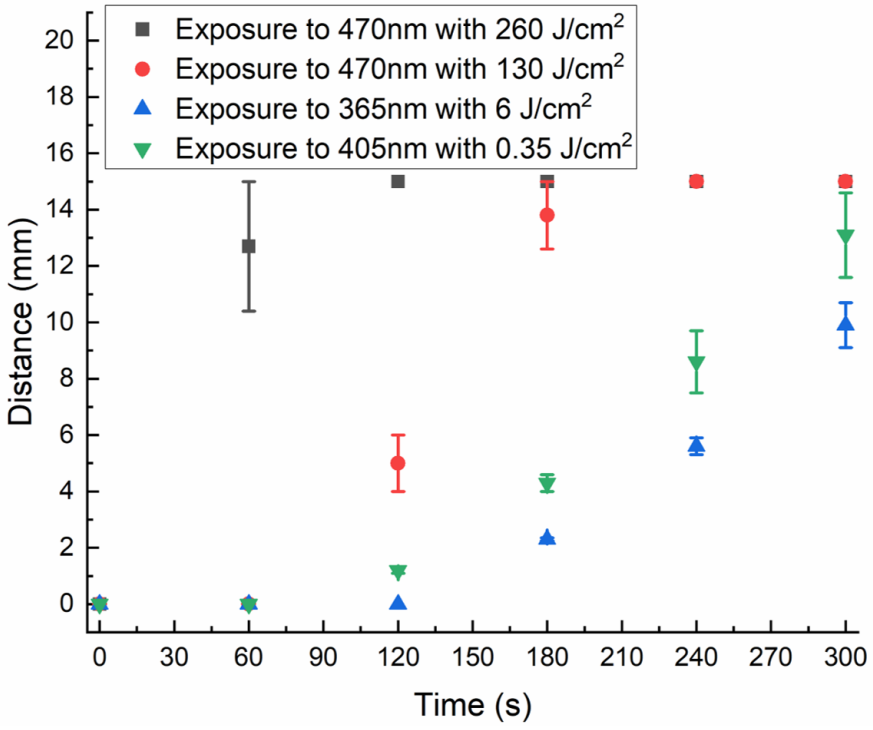

FIGURE 6.23: Graph presenting the distance that the red dye has travelled in the fluidic channel at different times between 60–300 s for the cases in which the flow-through optically triggered pad exposed to the 405 nm, 365 nm and 470 nm light sources.

in its porosity and in that case the red dye can flow along the fluidic channel within 60 s. This experiment was repeated three times for each of the different cases, and in figure 6.23 we present a graph in which we have measured the distance that the red dye has travelled in the fluidic channel at different times between 60–300 s following the deposition of the sample.

Similar to the previously reported method, the use of a flow-through optically triggered pad proved to be successful for the delay in the flow of a sample and this approach will be later used in an assay to increase the signal intensity for the detection of a pre-determined analyte.

6.2.5 Application of the optically control fluid flow of samples in assays.

In the last section of this chapter, we use the optically controlled fluid flow to increase the sensitivity of an assay designed for the detection of a pre-determined analyte. The aim of this experiment is to use the methods that we previously reported and successfully resulted in a delay in the flow of a sample upon exposure to the UV light, in order to increase the incubation time of the sample therefore, enhance the signal intensity on the test line of the assay. This can be achieved with two methods either by delaying the flow of the sample at the point of the test line to increase the incubation time between the detection and the capture antibodies, or by delaying the flow of the sample in the conjugate pad in order to increase the incubation time between the sample and the detection antibodies. Both of these methods will be studied in two different assays to increase the sensitivity for the detection of the COVID-19 virus and the common inflammation marker CRP. The approach that we will use to delay the flow of the sample is the one that was previously described and involves the use of an optically triggered pad which is soaked in the mixed solution of pre-polymer 8 in Desolite and then positioned in an LFA.

In our first demonstration, we used the optically triggered pad of 20% of pre-polymer 8 in Desolite to increase the sensitivity for the detection of the COVID-19 virus. For this assay we pre-deposited and dried in the microglass fibre 2 µL of COVID-19 specific antibodies tagged with Au NPs (used as the reagent) and also flowed 100 µL of the COVID-19 antigen (used as a sample) in a concentration of 100 ng/mL. In the test line of the fluidic channel (width at 5 mm) we have dispensed and immobilized COVID-19 capture antibodies and at the end of the LFA we have an absorbent pad which removes the excess sample. In figure 6.24A we present the results of a standard LFA (control device) that is designed for the detection of the COVID-19 virus and this produces a signal on the test line with an intensity of 7.2 a.u. Next, we used an optically triggered pad which is polymerized and cross-linked with the 405 nm laser light source (fluence of 0.35 J/cm^2) and placed between the microglass fibre and the fluidic channel as presented in figure 6.24B. We chose to place the pad at this position as we believe

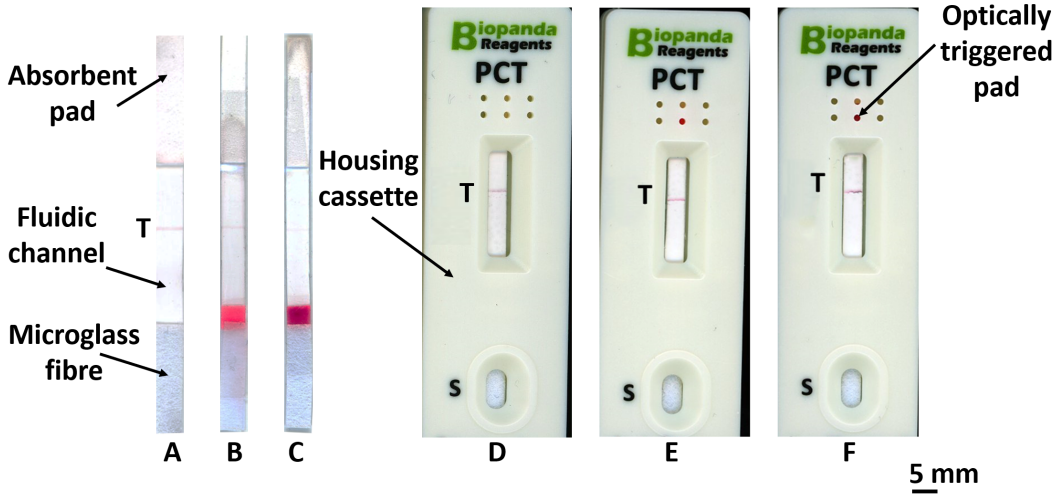

FIGURE 6.24: (A) Control LFA used for the detection of COVID-19 virus. (B) We placed in the LFA an optically triggered pad between the microglass fibre and the fluidic channel (C) which later was exposed to the 365 nm light source in order to test the increase in the sensitivity of the assay. (D-F) We repeated the same experiment however, this time the optically triggered pad was placed at the end of the fluidic channel and also the LFAs were enclosed in a housing cassette.

that this will assist in an increase in the incubation time between the sample and the reagents, thus increase the intensity of the signal on the test line. Unlike what we expected, from the test results we observe that the signal intensity decreased to a mean value (from the total of the three tested devices) of 4.4 a.u. Furthermore, in figure 6.24C we depict the results after exposing the optically triggered pad to the 365 nm light source with a fluence of $6.0\,J/cm^2$ and we see a further decease in the signal intensity which in that case has a mean value of 1.5 a.u. We believe that the decrease in the intensity of the signal is due to the position of the optically triggered pad and its pore size, which is possibly smaller than the size of COVID-19 antigen (50–140 nm) therefore, the analyte tagged with the detection antibodies is getting blocked from the pad and only a small amount of it reaches the test line.

In the next experiment, we used again an optically triggered pad with 20% of prepolymer 8 in Desolite, but this time we position it at the end of the fluidic channel. Compared with the previous experiment, in this approach we do not aim to increase the incubation time between the sample and the reagents, instead we intend to delay the flow of the sample at the position of the test line thus, increase the incubation time between the sample and the capture antibodies. The tested LFAs are the same as the ones presented in figures 6.24A-C with a fluidic channel designed to have a width at 4 mm and in order to ensure proper contact between the layers we enclosed the LFAs in a cassette housing. The reagents for the assay (2 µL) were again pre-deposited and dried in the microglass fibre and each of the devices was tested with 100 µL of sample which was introduced from the opening with the indication ”S” on the cassette. In

figure 6.24D we illustrate the results after testing a device with no optically triggered pad (control) and this results in a mean colour intensity, from the total of three tested devices, of the test line at 18.8 a.u. However, when we repeated the same experiment and we added an optically triggered pad, after its polymerization with the 405 nm laser light source, at the end of the LFA this resulted in a mean colour intensity of the test line at 32.1 a.u (figure 6.24E). We observe here that by positioning the optically triggered pad at the end of the fluidic channel, there is an increase in the colour intensity of the test line by 41.2%. Afterwards, we repeated the previous experiment but we exposed the optically triggered pad to the 365 nm light source with a fluence of $6.0\,J/cm^2$, and from the photo shown in figure 6.24F we observe that this resulted in an appearance of a test line with mean color intensity of 40.1 a.u. From these results and following equation 3.4, we conclude that by putting the optically triggered pad at the end of the fluidic channel and exposing it to the UV light, we successfully improved the sensitivity of the assay by 1.1-fold.

In our second demonstration, we used the flow-through optically triggered pads with 20% of pre-polymer 8 in Desolite and as reported in the previous subsection we placed them at the front end of an LFA. The applicability of this method was tested to increase the sensitivity for the detection of a CRP biomarker, which is used on this assay at a concentration of 10 ng/mL. The reagents for this assay were pre-deposited (8 µL) and dried on a microglass fibre, which is treated with a blocking solution to effectively release the reagents and is placed on the top of the flow-through optically triggered pad during the testing process. The aim of this experiment is to increase the incubation time between the sample and the reagents, resulting in an increase of the capture of the CRP analyte by the detection antibodies. We believe that this will result to an increase in the colour intensity of the test line. In the fluidic channel of the LFAs we have dispensed and immobilized antibodies that capture the CRP analyte (test line) and the detection antibodies (control line). Each of the devices was tested with 20 µL of sample, containing the analyte, and at the end of the LFAs we have placed an absorbent pad to remove the excess amount of liquid that passes the control line.

In figure 6.25A we depict an image of the control device used for this experiment which only has the microglass fibre that is placed at the front end of the LFA. The testing of the sample resulted in the appearance of a test line with a colour intensity of 36 a.u. Next, we used a flow-through optically triggered pad which was polymerized with the 405 nm light source, with a fluence of $0.35\,J/cm^2$, and placed on the top of the front end of the LFA (figure 6.25B). After putting the microglass fibre on top of the pad and tested with the sample, this resulted in a delay in its flow and consequently the colour intensity of the test line was measured at 38.5 a.u. Finally, in our last experiment we exposed the flow-through optically triggered pad to the 365 nm light source with a fluence of $6.0\,J/cm^2$ (figure 6.25C) and then we placed the microglass fibre on top of it before testing the sample. This resulted in a further delay in the flow of the sample,

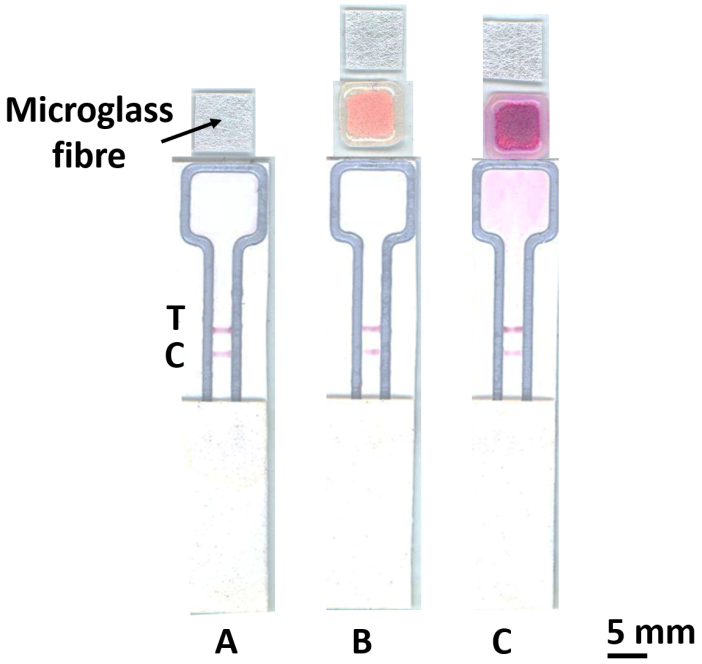

FIGURE 6.25: (A) A control device where the microglass fibre, containing the dry reagents for the CRP assay, is placed on the top of the front end of an LFA and tested with 20 µL of sample. The same experiment was repeated but this time the microglass fibre was placed on top of the flow-through optically triggered pad and the LFA was tested with the same volume of sample in the cases that the pad (B) polymerized with the 405 nm and (C) exposed to the 365 nm light source after polymerization.

therefore the colour intensity of the test line was measured at 40.6 a.u. From the results, we conclude that this method was successful in improving the sensitivity for the detection of CRP, as the signal on the test line was increased by 0.1-fold. It is important to note here that after testing the flow-through light activated pad that was exposed to the UV light, we observed a pink colour residual which is stuck at the front end of the LFA. We believe that this is the result of the poor adhesion of the hydrogel on the flow-through pad after the polymerization process, and this resulted in a small part of it to get washed away after flowing the sample. Despite that fact, we do not have any indication that the hydrogel which is washed away from the sample interferes with the analyte and compromises the detection of CRP.

For the previously mentioned experiments, we measured the colour intensity on the test line using the RGB channel in the histogram function of the Adobe photoshop and equation 3.3.

6.3 Summary

In this chapter we report the use of different pre-polymer solutions (1-4) which after their exposure to the 405 nm laser light source they form hydrogels. These hydrogels

were deposited in paper-based devices, with different designs, and used for the optical control of the flow of a sample. In our first demonstration, we report the use of four pre-polymer solutions each one contained: NIPAM (used as a water soluble monomer), acrylic acid (used as the proton donor), MBIS (used as a cross-linker), spiropyran 1 (used as the photo-responsive element) and Irgacure (used as the photo-initiator) in different proportions. We were able to successfully polymerize all the pre-polymer solutions and create hydrogels, which after their incubation in water they increased their volume (swelling). Later, the same hydrogels were exposed to the 470 nm blue light source, and this resulted in a decrease in their volume (shrinkage) and additionally, this process was shown to be repeatable. Despite that, this method was not successful for the optical control in the flow of a red dye on a cellulose paper device, and also these solutions produced a smell which makes them unsuitable for use.

Next, we tested different pre-polymer solutions (5-7) in which we replaced NIPAM and MBIS with OEGMA and EGDMA respectively, and instead of incubating the hydrogels in water for activation, we exposed them to the 365 nm light source for that purpose. We were able to use these pre-polymer solutions with our local photo-polymer deposition method, and after conducting a detailed study, we proved that they can lead to the formation of hydrogels after their polymerization with the 405 nm laser light source, and they can also activate upon exposure to the 365 nm. We tested these pre-polymer solutions to control the flow of a sample, by fabricating a fluidic channel with an optically triggered in-line barrier. Although this method resulted in a flow delay of the sample on cellulose paper, it was not successful when tested on an NC membrane which is the substrate of choice for the implementation of diagnostic assays.

Last but not least, we tested another pre-polymer solution (8) containing a different formulation of the photo-responsive element (spiropyran 2), which was again used with our local photo-polymer deposition method. Although we deposited the hydrogel in different designs such as an in-line filter on cellulose paper and NC membrane and as a constriction on a fluidic channel on microglass fibre, these methods were either not able to delay the flow of the sample or they resulted in inconsistent measurements. A method that successfully resulted in a delay in the flow of a sample, included the use of an optically triggered pad either in the form of a microglass fibre pad or as a flow-through pad (cellulose paper) which after soaking in a mixed solution of pre-polymer 8 and Desolite, was placed on an LFA to control the flow of the sample. Although with this method we were not able to completely block the flow of a sample, it was successful for the delay of its flow after exposure of the optically triggered pad to the 365 nm light source. The methods of using the optically triggered, microgalss fibre, pad and the flow-through pad were applied on assays to increase the sensitivity in the detection of the COVID-19 virus and the CRP respectively. Both of these methods were successful, as in the first case we were able to increase the signal intensity on the test

line by 1.1-fold, whereas in the latter case we observed a signal enhancement on the test line by 0.1-fold.

Chapter 7

Conclusions and future work

7.1 Conclusions

This chapter is a summary of the work presented in this thesis which is focused on the use of a LDW technique for enabling newer functionalities in paper-based devices in order to improve their performance and allow their use as POC diagnostic sensors on a wider scale.

7.1.1 In-line filtration process in paper-based devices

In chapter 7.3 we used the LDW technique of the local photo-polymer deposition to create in-line filters in paper-based devices. As a primary substrate for the experiments we used a NC membrane, which was later patterned to make both a channel with solid polymer walls that are able to guide the flow of liquids and an in-line filter, used as a barrier, and positioned at 90° to the direction of the sample flow. From the results we show that adjustment of the photo-polymer deposition parameters determined the porosity of the in-line barriers, which when carefully designed and integrated within a fluidic channel, can act as filters that enable either complete blocking, selective flow or controlled separation of particles of different sizes. We have successfully identified the fabrication parameters for the creation of in-line barriers that allow the filtration of two different types of particles, Au NPs with sizes of 40 nm, 100 nm and 200 nm and latex microbeads with sizes of 200 nm and 1000 nm. Furthermore, we presented the results of using a porous in-line barrier for selective separation of 40 nm Au NPs from 1000 nm latex microbeads, thereby showing the usefulness of this method for enabling the filtration of different-sized particles when flowing within the same channel of a paper-based device.

The use of this method and the in-line filters created in a fluidic channel is not only limited to separation of the various constituents of a complex sample, but can also be

used to delay the flow of the sample, therefore increasing the sensitivity for the detection of a pre-determined analyte. After conducting a series of experiments we found the optimum porosity and the position of the in-line barriers in the fluidic channel that result in a maximum signal increase (4.6-fold) in the detection of CRP.

7.1.2 Flow-through filtration process for analyte detection

In chapter 7.3 we presented another functionality of the local photo-polymer deposition method, namely the creation of porous flow-through filters. Unlike the filtration method that we presented in chapter 7.3, in this approach the flow-through filters are created in cellulose paper. After dilution, in IPA, the photo-polymer is deposited inside a solid polymeric wall and followed by exposure to a laser light source. By changing the concentration of the photo-polymer in IPA we were able to create flow-through filters of different porosities. We presented the results for successfully defining the parameters of the photo-polymer concentration to create porous flow-through filters that were able to completely block or enable the flow of latex microbeads of different sizes namely 200 nm, 500 nm, 1000 nm and 3000 nm.

When the flow-through filters are located on top of the front end of an LFA they provide an alternative method for the detection of CRP. The novelty of this analyte detection method stems from the fact that although we are using materials that are commonly used in standard LFAs, we do not make use of a sample pad and a conjugate pad, therefore simplifying the design of the LFA and the fabrication protocol. Additionally, with this detection method we were able to counter the Hook effect which is a limiting factor in many LFAs and we were able to detect CRP over a broad concentration range between 10–50.000 ng/mL. Compared with the previously reported method of the in-line filtration, this approach provided a successful pathway for the separation of plasma from red blood cells within blood treated with Anti-D solution, and we achieved a maximum extraction efficiency of 50.6%. Lastly, we presented the results of the flow-through filtration method for another application which included the purification of a water-based sample which contained the bacteria, E. coli.

Overall, in this chapter we presented a simple method for the fabrication of flow-through filters which are multi-functional and can be used for different applications, and therefore have the potential to enable the use of paper-based devices on a wider scale.

7.1.3 Development of 3D multilayer paper-based devices

The LDW technique of the local photo-polymer deposition is not only limited to the fabrication of two dimensional paper-based devices as presented in the previous chapters,

but can also be extended to the development of 3D multilayer paper platforms. In chapter 7.3 we present of the method that we used to pattern and stack multiple layers of cellulose paper to create multilayer paper-based devices. Unlike other methods, are approach is simple and it does not require any alignment between the layers, hence simplifying the device fabrication process. Additionally, it eliminates the use of external equipment during the assembly of the device as the photo-polymer that is deposited assists with the bonding of each layer. We highlighted the use of our developed four-layered 3D paper-based device for the simultaneous detection of three analytes namely BSA, glucose and nitrite, in artificial urine, as well as the pH of the tested urine sample. This paper patterning method can be further extended to add more layers (greater than four) of porous materials and create multiple flow paths within the 3D structure for the detection of additional analytes.

7.1.4 Optically control fluid flow in paper-based devices

In order to improve the performance of paper-based devices, in chapter 7.3 we used the LDW technique to deposit light-responsive materials (hydrogels) in order to control the flow of a sample within a paper-based device. We tested different pre-polymer solutions which after being exposed to laser light at 405 nm formed hydrogels that have the ability to change their volume. Firstly, we tested hydrogels that were able to swell after being incubated in water for several hours. However, this step adds a constraint to the use of such material for the development of POC diagnostic devices. In order to solve this problem, we next used hydrogels that increased their volume after being exposed to a 365 nm light source, and subsequently were able to shrink when they were illuminated with a 470 nm light source.

After identifying the light exposure parameters that resulted in a maximum volume change of the hydrogels, we patterned various porous substrates in different designs in order to to control the flow of a liquid sample. From the results presented in this chapter we conclude that we were successful in making paper-based devices that were able to delay the flow of a sample when hydrogels were exposed to the 365 nm light source. Additionally, we observed that a sample flowed faster when the same hydrogels were exposed to the 470 nm light source. This method of optical control of the sample flow was later used in two different assays to increase the sensitivity in the detection of analytes including CRP and the COVID-19 virus. This was achieved by either increasing the incubation time between the sample and the capture antibodies located on the test line of the LFA or by increasing the incubation time between the analyte and the conjugate. In both cases we observed an increase in the signal intensity of the test line which was one of the main objectives we had set for this work.

7.2 Limitations

Despite the fact that we achieved most of the targets that we set for this thesis, some of them were not fulfilled, and that is due to some limitations we recognised during the course of this work. These can be categorized as follows:

7.2.1 Local photo-polymer deposition method

One of the disadvantages of the local photo-polymer deposition method as compared with other device fabrication techniques, is the large feature size (width of polymer line approximately 1 mm) of our developed paper-based devices. This is due to the fact that the width of the polymer lines depends on the spreading of the photo-polymer on the porous substrate, which are unable to control and therefore produce paper-based devices with smaller size. Another disadvantage of the local photo-polymer deposition method concerns the uniformity of the polymerized structures fabricated in certain porous substrates such as microglass fibre. As previously mentioned, lack of precise control of the spreading of the photo-polymer affects the reproducibility of the patterned polymer lines. This was obvious from the results presented in chapter 7.3 and illustrated in figure 6.18 in which we were unable to produce identical polymer lines (see for example at the point of the constriction), although we used the same patterning conditions during fabrication.

7.2.2 Designs of paper-based devices

Another limitation that we encountered is associated with the designs of the paper devices that we used for some of the applications reported in this research thesis. Specifically, one of the objectives that we set for this research work was to separate the plasma from the RBCs when blood is untreated with the Anti-D solution. Although we used different methods to achieve that goal such as the design of in-line filters on an NC membrane as well as the design of porous flow-through filters on cellulose paper (reported in the subsections 3.3.5 and 4.3.4 respectively) we were unable to separate the plasma from the RBCs. This can be thought of as a constraint of our designed porous filters as pores were getting blocked from the various constituents of a complex liquid sample.

7.2.3 Materials used

The last limitation that we identified in this thesis arises from the use of the hydrogels as a light-responsive material to control the flow of samples in paper-based devices.

Despite the fact that we successfully reported the use of hydrogels to increase the sensitivity for the detection of two different analytes namely CRP and the COVID-19 virus, the main objective was to completely block and then enable the flow of samples, when the hydrogels were exposed to the 365 nm and 470 nm respectively, which was never achieved. In fact from the results reported throughout chapter 7.3 we can see that we only managed to delay the flow of samples after exposure of the hydrogels to the 365 nm light source instead of completely blocking their flow which would have resulted in a further increase in the sensitivity of the assays. We believe that this is a limitation of the synthesized hydrogels which are either not swelling enough in order to completely block the pores of the paper or their adhesion to the paper is poor resulting in some parts of the hydrogel being washed away from the sample.

7.3 Future work

We believe that the LDW technique described in this thesis has great potential and can further improve the performance of paper-based devices to enable their widespread use as a commercial product for POC diagnostics. Despite the fact that we have done an extensive study of the LDW approach to enable newer functionalities in paper-based devices, there is still room to improve and evolve the methods that we have already reported through this project as well as open new areas of exploitation.

Firstly, as reported in the subsection 7.2.2 one of the biggest limitations of the LDW technique is the lack of the ability to separate plasma from RBCs. However, the flexibility of our developed local photo-polymer deposition method enable the study and patterning of a variety of porous materials with different properties (e.g. thickness, porosity, pore size etc.) to either create filters (in-line and/or flow-through) or different designs and structures for the efficient extraction of plasma from whole blood. We intend to include the aforementioned study as part of our future work and potentially add this new functionality to the existing paper-based devices which will open a new route to the use of such low-cost devices at the POC.

Secondly, the use of the porous flow-through filters can be further exploited in different applications. Apart from the detection of analytes, they can also be used as a tool to remove particles which otherwise can be captured in the test line producing false negative results. This application has the potential to improve the performance as well as the LOD of the LFAs and this will be part of our future studies. Additionally, in the subsection 4.3.5 we showed that the porous flow-through filters can be successfully used for the purification of a water-based solution containing the bacteria E. coli. Our next aim is to adopt this filtration method for more complex systems where separation

and identification of different types of bacteria contained in the same water-based solution is required. This can pave the road for the use of the porous flow-through filters for different application such as the detection of food-borne pathogens.

Thirdly, the local photo-polymer deposition method is not only limited to pattern and stack layers from the same porous material but it can also be extended to pattern and stack different types of porous materials. As part of our future work, we intend to further explore this idea to make 3D-µPADs where each layer is made from a different material (e.g. first layer is cellulose paper, second layer is microglass fibre and third layer is NC membrane). This will allow us to overcome the limitation of only being able to perform single step assays, as the use of such 3D-µPADs will enable the implementation of more complex assays (e.g. ELISA), where mixing of different compounds is needed.

Finally, the main objective of our future work is to focus on the study and application on our paper-based devices of new light-responsive materials that will serve the purpose of completely blocking and then enabling the flow of samples upon light stimulation. Our first approach towards that direction will be the use of newly synthesized hydrogels with more reactive formulation that have better adhesion on the paper. Using our local photo-polymer deposition method, we will study the patterning of porous substrates with different designs and structures in order to create light-activated gates able to control the flow of samples. Additionally, we will study the use of photo-responsive materials that are based on different light-induced reactions such as photocleavage, in order to test their efficacy on creating light-activated gates. Apart from the application of the hydrogels to increase the incubation time of a sample, that was reported in this thesis, we aim to use them for different applications to improve the performance of paper-based devices. These include the creation of on/off gating which will allow the repeated dispensing of a desired volume of sample to the test line, and this will make µPADs suitable for semi-quantitative detection of analytes. Also, a paper-based device can be designed to have multiple flow channels within the same strip. The addition of light-activated gates to such a device could enable the flow of selected reagents to multiple test sites enabling sophisticated multiplexed testing. We believe that the incorporation of light-responsive materials on paper-based devices will greatly improve their performance and have a tremendous impact of the use of this platform for clinical diagnostics at the POC.

Appendix A

Operation of BioDot dispensing system

In this appendix, we will describe the operation of the BioDot, which is the dispensing system that we use to deposit the antibodies onto the porous substrates.

The BioJet Plus^{TM} technology is a hydraulically driven system designed for high speed dispensing of liquids that involves the combination of a high speed micro valve with a high resolution syringe pump as well as the synchronization of the dispense system with the movements of the stage. This attributes allow for fast and non-contact dispensing of liquids of volumes as low as 4 nL per dispensed drop. The BioDot dispensing system consists of a syringe pump that is connected to a dispense micro valve. For continuous dispensing, the reagent or solvent is pulled from a reservoir into the syringe and then dispensed through the micro valve.

Using the BioDot system we can deposit liquids in two different ways namely continuously and with aspiration/dispensing. With continuous dispensing the reagents are pulled from the reservoir and then dispensed through the micro valve. On the other hand, with aspirate/dispense the system is first filled with a backing fluid and then the tip of the valve is dipped into the sample. The next step involves withdrawing of the syringe to aspirate the sample and finally we dispense the aspirated sample. For dispensing the antibodies, that described in this thesis, we chose to use the second mode of aspirate/dispensing due to the smaller volume required.

As previously mentioned, the BioDot system is hydraulically driven and for that it requires a fluid medium to be present from the syringe to the micro valve. The dispensing process starts with the syringe which is displaced a given amount. Next, the micro valve opens for a short time (milliseconds) and then the fluid is released from the valve and travels to the tip. Afterwards, the fluid increase its linear velocity as it passes

through the tip orifice and then ejects as drop. Finally, it is important to mention that one valve actuation results in one drop.

The key aspect of the BioDot system that ensures proper volume dispensing is the steady-state pressure (SSP). This pressure has several important characteristics such as the fact that it is achieved by the displacement of fluid by the syringe pump and is proportional to the displacement (drop size). Additionally, the SSP is determined by the system compliance, which is dominated by entrapped air bubbles. Once the SSP is established, the amount of fluid displaced by the syringe pump will equal the amount dispensed.

The main procedures that influence the SSP and therefore the dispensed volume are: priming, aspiration, pre-pressurization and pre-dispensing. Starting with the priming, it is used to initialize and fill the syringe pumps with fluid from the reservoir. The reservoir fluid can be either system fluid for an aspirate/dispense step of the reagent or sample fluid for continuous dispensing. During priming step, several hundred micro litres of fluid are dispensed as a stream. The resistance to flow caused by the valve and tip orifice causes the pressure within the system to become higher than desired for SSP. In order to achieve SSP, we must first vent the valve, which involves opening the valves without displacing the fluid. This brings the system to ambient pressure and from this point the SSP can be achieved.

Following the priming is the aspiration step in which the sample is collected from the reservoir (micro-well plate) into the tip of the dispenser. During the aspiration process, a negative pressure is produced which is relieved by performing a vent, which opens the micro valve without displacing any fluid. When the sample is aspirated, the syringe pump draws fluid through the tip orifice. The resistance to flow from the tip and valve creates a negative pressure, which must be overcome to achieve a SSP. As with priming, venting can bring the system to ambient pressure from which SSP can be applied.

Lastly, pre-pressurization and pre-dispensing steps are required in order to bring the pressure of the system from the ambient back to the SSP, which then allows accurate dispensing of the programmed volume of the reagents. During pre-pressurization step, the syringe pump is displaced without opening the micro valve, which raises the pressure of the system to approximately the desired SSP. Afterwards, several pre-dispenses at the programmed volume should be performed for fine-tuning the SSP that brings the brings the pressure to the appropriate level for the programmed volume. Finally, the dispensing happens under the SSP, where the syringe pump moves and the micro valve opens resulting to dispense a series of micro-droplets of the programmed volume.

Appendix B

Calculation of the volume of the photo-polymer per volume of paper

For the calculation of the volume of the photo-polymer per volume of paper, we dispensed polymeric lines on an NC membrane with the same length of 70 mm and with varying deposition speeds in the range between 30–90 mm/s (figure B.1). During the fabrication of these lines, the frequency at which the valve dispenses the photo-polymer is set at 104.6 Hz and from this value we can simply calculate the amount of time between deposition of each droplet which is 9.56 ms. We also calculated that the Nordson dispensing system deposits droplets of a volume of 100 nL each, therefore for the different photo-polymer deposition speeds we can now calculate the volume of the photo-polymer that we deposit per 70 mm line. We will show the calculations for the case that we deposit a line with a speed of 30 mm/s, however we can follow the same steps to calculate the volume of the photo-polymer for different speeds.

In order to calculate the time required to dispense a polymeric line we use equation B.1 and for the case of dispensing a line with length of 70 mm at a deposition speed of 30 mm/s this value is 2.3 s. Since the time between deposition of each droplet is 9.56 ms,

FIGURE B.1: Polymeric lines deposited on an NC membrane with different speeds in the range between 30–90 mm/s.

as previously stated, and the volume of each droplet is 100 nL then the volume of the photo-polymer ($V_{polymer}$) that we deposit is given by equation B.2 and has a value of 24.3 µL.

$$\text{t [s]} = \frac{\text{Distance [mm]}}{\text{Photo-polymer deposition speed [mm/s]}} \tag{B.1}$$

$$\text{V}_{\text{polymer}}\ \text{[uL]} = \frac{\text{t [s]} \times \text{volume of each droplet [uL]}}{\text{Time between deposition of each droplet [s]}} \tag{B.2}$$

However, in our previous calculation we did not account the volume of the first droplet that we deposited, hence the total volume of the photo-polymer that we deposit per 70 mm line is $V_{polymer}$ + 0.1 µL and for the case of a line deposited at a speed of 30 mm/s the volume is equal to 24.4 µL.

In order to calculate the area (A) over which the photo-polymer is deposited we used equation B.3. Assuming that the width of the polymeric line is roughly 1 mm when deposited with a speed of 30 mm/s and given the fact that the length of the line is 70 mm, the area has a value of 70 mm^2. Additionally, if we consider that the thickness of the NC membrane has a mean value of 150 µm and the porosity is 70%, we can calculate the volume of the paper following equation B.4 and this gives a value of 7.3 mm^3.

$$\text{A [mm}^2\text{]} = \text{Width [mm]} \times \text{Length [mm]} \tag{B.3}$$

$$\text{V}_{\text{Paper}}\ \text{[mm}^3\text{]} = \text{A [mm}^2\text{]} \times \text{Thickness [mm]} \times \text{Porosity} \tag{B.4}$$

Lastly, for the case of the polymeric line deposited with a speed of 30 mm/s we can calculate the volume of the photo-polymer per volume of the paper (D) following equation B.5 and this gives a value of 3.3 µL/mm^3.

$$\text{D [uL/mm}^3\text{]} = \frac{V_{\text{polymer}}[uL]}{V_{\text{Paper}}[mm^3]} \tag{B.5}$$

In table B.1 we present the results after the calculation of the volume of the photo-polymer, the volume of the paper over which the photo-polymer is deposited as well as the volume of the photo-polymer per volume of the paper substrate for the different deposition speeds in the range between 30–90 mm/s. In figure B.2 we depict the graph based on the results from table B.1.

TABLE B.1: Parameters used to calculate the volume of the photo-polymer per volume of the paper substrate for the different deposition speeds.

Photo-polymer line-speed(mm/s)	Volume polymer (uL)	Volume paper (mm^3)	D (uL/mm^3)
30	24.4	7.3	3.3
40	18.4	5.9	3.1
50	14.7	5.1	2.8
60	12.2	4.4	2.7
70	10.5	3.9	2.6
80	9.0	3.4	2.6
90	8.2	3.1	2.6

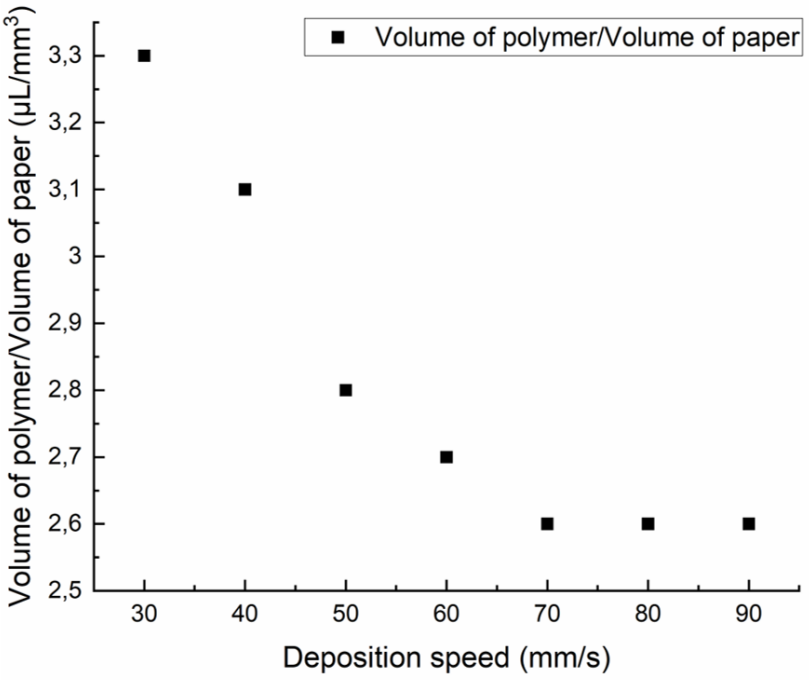

FIGURE B.2: Volume of the photo-polymer per volume of the paper substrate for the different deposition speeds in the range between 30–90 mm/s.

Appendix C

Calculation of the laser fluence

Laser fluence is an important parameter that we use throughout the experimental work. In optics, the fluence of a laser pulse is defined as the optical energy delivered per unit area and is measured in units of [J/cm^2]. Equation C.1 describes the formula used to calculate the laser fluence of a laser pulse:

$$\text{Fluence}\left[\frac{Joules}{cm^2}\right] = \frac{\text{Laser pulse energy}[J]}{\text{Exposure area}[cm^2]} \tag{C.1}$$

However, in order to polymerize the light-curable materials, we use a CW laser and in that case the laser fluence is defined by optical power rather than pulsed energy. By definition, the optical power (or power) is the energy of light per unit of time, as it is delivered to the material by a laser beam. It is described by equation C.2

$$\text{Laser power}[W] = \frac{\text{Energy of light}[J]}{\text{Scan time}[s]} \tag{C.2}$$

However, for out LDW method, the focused laser beam scans along the polymeric lines on the porous substrate, therefore the exposure area can be approximated as a rectangular area with length that of the scanned distance and width that of the laser spot. The length of the scanned distance can be simply calculated from the laser scanning speed as well as the scan time. We make the assumption here that the exposure area has a rectangular shape that neglects the start and the end of the scanned area, which should be semi-circular because the beam itself is circular. These areas of the two semi-circles at the start and end of the scan are negligible compared with the total exposure area. Therefore equation C.3 is used to describe the exposure area:

$$\begin{aligned} \text{Exposure area}[cm^2] &= \text{Laser spot diameter}[cm] \times \text{Scanned distance}[cm] \\ &= \text{Laser spot diameter}[cm] \times \text{Laser scanning speed}[cm/s] \times \text{Scan time}[s] \end{aligned} \tag{C.3}$$

Substituting equations C.2 and C.3 into equation C.1 and considering that the laser pulsed energy is in fact the energy of light in the case of a CW laser, then the laser fluence of a CW laser is described by equation C.4:

$$\text{Fluence}\left[\frac{Joules}{cm^2}\right] = \frac{\text{Energy of light}[J]}{\text{Exposure area}[cm^2]}$$

$$= \frac{\text{Laser power}[W] \times \text{Scan time}[s]}{\text{Laser spot diameter}[cm] \times \text{Laser scanning speed}[cm/s] \times \text{Scan time}[s]}$$

$$= \frac{\text{Laser power}[W]}{\text{Laser spot diameter}[cm] \times \text{Laser scanning speed}[cm/s]} \tag{C.4}$$

Appendix D

Assay protocols

D.1 Assay for the detection of BSA

1. Add 49.2 mg/ml of citrate buffer at 1.8 pH and allow glass fibre to dry for at least 1 hour.
2. Add 2.2 mg/ml of TBPB in 95% of ethanol solution and allow glass fibre to dry for at least 1 hour.
3. Add the artificial urine sample containing various concentrations of BSA.
4. Capture photos of the detection zones to determine the concentration of BSA.

D.2 Assay for glucose detection

1. Dissolve o-Dianisidine reagent to 1 mL of DI water and add 0.8 mL to the bottle containing glucose oxidase.
2. Add the glucose oxidase/peroxidase solution (5:1 ratio and 15 units of protein per mL of solution) on the glass fibre and allow to dry for at least 1 hour.
3. Add the artificial urine sample containing various concentrations of D-(+)-glucose.
4. Capture photos of the detection zones to determine the concentration of D-(+)-glucose.

D.3 Assay for nitrite detection

1. Prepare Griess reagent by dissolving in DI water 8.63 mg/ml sulfanilamide, 63.3 mg/ml citric acid and 2.56 mg/ml of N-(1-naphthyl) ethylenediamine dihydrochloride.
2. Add Griess reagent on the glass fibre and allow to dry for at least 1 hour.
3. Add the artificial urine sample containing various concentrations of sodium nitrite.
4. Capture photos of the detection zones to determine the concentration of sodium nitrite.

D.4 Assay for the measurement of the pH

1. Add bromothymol blue on the glass fibre and allow to dry for at least 1 hour.
2. Add the artificial urine sample.
3. Capture photos of the detection zones to measure the pH of the sample.

Appendix E

Chemical structures of pre-polymers

Below we list the chemical structures of the various pre-polymer solutions that we used during the experimental work presented in chapter 7.3.

E.1 Pre-polymer solutions 1-4

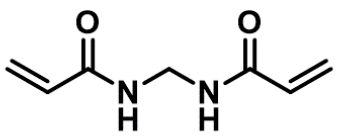

MBIS

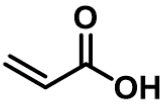

Acrylic acid

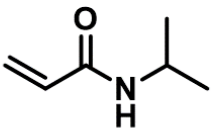

NIPAM

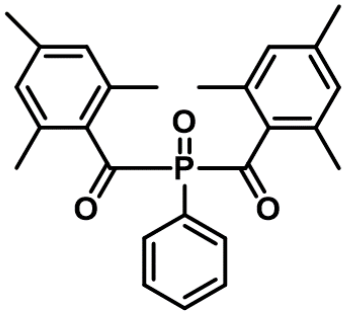

Irgacure

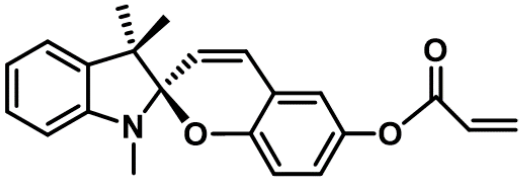

Spiropyran 1

E.2 Pre-polymer solutions 5-7

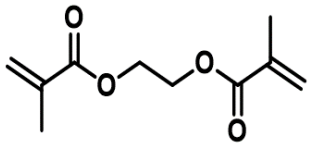

EGDMA

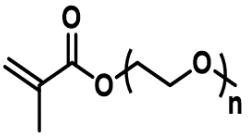

$OEGMA_{300}$
or
$OEGMA_{900} + OEGMA_{300}$

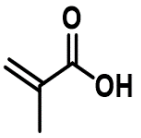

Methacrylic acid

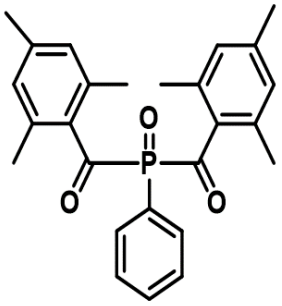

Irgacure

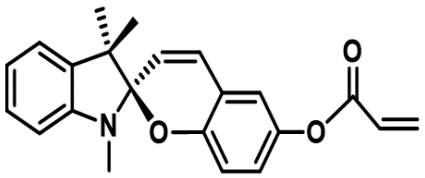

Spiropyran 1

E.3 Pre-polymer solution 8

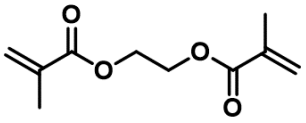

EGDMA

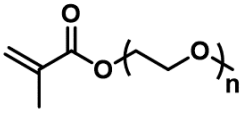

$OEGMA_{900} + OEGMA_{300}$

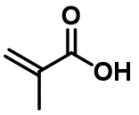

Methacrylic acid

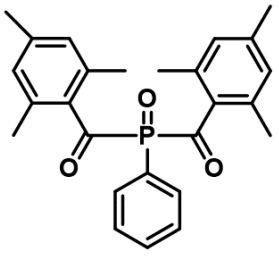

Irgacure

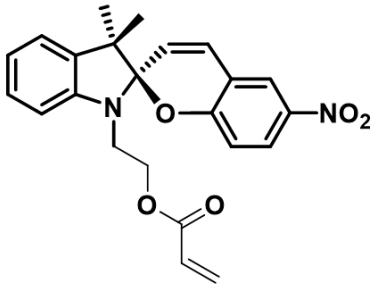

Spiropyran 2

Bibliography

Bibliography for Chapter 1

[1] G. J. Fermann and J. Suyama, "Point of care testing in the emergency department," *The Journal of Emergency Medicine*, vol. 22, no. 4, pp. 393–404, 2002.

[2] P. Von Lode, "Point-of-care immunotesting: approaching the analytical performance of central laboratory methods," *Clinical Biochemistry*, vol. 38, no. 7, pp. 591–606, 2005.

[3] T. R. Kozel and A. R. Burnham-Marusich, "Point-of-care testing for infectious diseases: past, present, and future," *Journal of Clinical Microbiology*, vol. 55, no. 8, pp. 2313–2320, 2017.

[4] S. Smith, J. G. Korvink, D. Mager, and K. Land, "The potential of paper-based diagnostics to meet the ASSURED criteria," *RSC Advances*, vol. 8, no. 59, pp. 34 012–34 034, 2018.

[5] A. W. Martinez, S. T. Phillips, M. J. Butte, and G. M. Whitesides, "Patterned paper as a platform for inexpensive, low-volume, portable bioassays," *Angewandte Chemie*, vol. 119, no. 8, pp. 1340–1342, 2007.

[6] A. W. Martinez, S. T. Phillips, and G. M. Whitesides, "Three-dimensional microfluidic devices fabricated in layered paper and tape," *Proceedings of the National Academy of Sciences*, vol. 105, no. 50, pp. 19 606–19 611, 2008.

Bibliography for Chapter 2

[1] A. W. Martinez, S. T. Phillips, G. M. Whitesides, and E. Carrilho, "Diagnostics for the developing world: Microfluidic paper-based analytical devices," *Analytical Chemistry*, vol. 82, no. 1, pp. 3–10, 2010.

[2] A. W. Martinez, S. T. Phillips, M. J. Butte, and G. M. Whitesides, "Patterned paper as a platform for inexpensive, low-volume, portable bioassays," *Angewandte Chemie*, vol. 119, no. 8, pp. 1340–1342, 2007.

[3] A. W. Martinez, S. T. Phillips, and G. M. Whitesides, "Three-dimensional microfluidic devices fabricated in layered paper and tape," *Proceedings of the National Academy of Sciences*, vol. 105, no. 50, pp. 19 606–19 611, 2008.

[4] M. Toner and D. Irimia, "Blood-on-a-chip," *Annual Review of Biomedical Engineering*, vol. 7, pp. 77–103, 2005.

[5] G. M. Whitesides, "Cool, or simple and cheap? Why not both?" *Lab on a Chip*, vol. 13, no. 1, pp. 11–13, 2013.

[6] K. M. Koczula and A. Gallotta, "Lateral flow assays," *Essays in Biochemistry*, vol. 60, no. 1, pp. 111–120, 2016.

[7] M. de Lourdes Moreno, Á. Cebolla, A. Muñoz-Suano, C. Carrillo-Carrion, I. Comino, Á. Pizarro, F. León, A. Rodríguez-Herrera, and C. Sousa, "Detection of gluten immunogenic peptides in the urine of patients with coeliac disease reveals transgressions in the gluten-free diet and incomplete mucosal healing," *Gut*, vol. 66, no. 2, pp. 250–257, 2017.

[8] E. C. Schramm, N. R. Staten, Z. Zhang, S. S. Bruce, C. Kellner, J. P. Atkinson, V. C. Kyttaris, G. C. Tsokos, M. Petri, E. S. Connolly *et al.*, "A quantitative lateral flow assay to detect complement activation in blood," *Analytical Biochemistry*, vol. 477, pp. 78–85, 2015.

[9] A. Carrio, C. Sampedro, J. L. Sanchez-Lopez, M. Pimienta, and P. Campoy, "Automated low-cost smartphone-based lateral flow saliva test reader for drugs-of-abuse detection," *Sensors*, vol. 15, no. 11, pp. 29 569–29 593, 2015.

[10] S. A. Klasner, A. K. Price, K. W. Hoeman, R. S. Wilson, K. J. Bell, and C. T. Culbertson, "Based microfluidic devices for analysis of clinically relevant analytes present in urine and saliva," *Analytical and Bioanalytical Chemistry*, vol. 397, no. 5, pp. 1821–1829, 2010.

[11] E. Carrilho, A. W. Martinez, and G. M. Whitesides, "Understanding wax printing: a simple micropatterning process for paper-based microfluidics," *Analytical Chemistry*, vol. 81, no. 16, pp. 7091–7095, 2009.

[12] X. Li, J. Tian, G. Garnier, and W. Shen, "Fabrication of paper-based microfluidic sensors by printing," *Colloids and Surfaces B: Biointerfaces*, vol. 76, no. 2, pp. 564–570, 2010.

[13] Y.-Y. Lin, J. Wang, G. Liu, H. Wu, C. M. Wai, and Y. Lin, "A nanoparticle label/immunochromatographic electrochemical biosensor for rapid and sensitive

detection of prostate-specific antigen," *Biosensors and Bioelectronics*, vol. 23, no. 11, pp. 1659–1665, 2008.

[14] H.-A. Joung, Y. K. Oh, and M.-G. Kim, "An automatic enzyme immunoassay based on a chemiluminescent lateral flow immunosensor," *Biosensors and Bioelectronics*, vol. 53, pp. 330–335, 2014.

[15] L.-W. Song, Y.-B. Wang, L.-L. Fang, Y. Wu, L. Yang, J.-Y. Chen, S.-X. Ge, J. Zhang, Y.-Z. Xiong, X.-M. Deng *et al.*, "Rapid fluorescent lateral-flow immunoassay for hepatitis B virus genotyping," *Analytical Chemistry*, vol. 87, no. 10, pp. 5173–5180, 2015.

[16] Y. He, X. Zhang, S. Zhang, M. K. L. Kris, F. C. Man, A.-N. Kawde, and G. Liu, "Visual detection of single-base mismatches in DNA using hairpin oligonucleotide with double-target DNA binding sequences and gold nanoparticles," *Biosensors and Bioelectronics*, vol. 34, no. 1, pp. 37–43, 2012.

[17] T. Ngo and H. Lenhoff, "Enzymes as versatile labels and signal amplifiers for monitoring immunochemical reactions," *Molecular and Cellular Biochemistry*, vol. 44, no. 1, pp. 3–12, 1982.

[18] M. Ren, H. Xu, X. Huang, M. Kuang, Y. Xiong, H. Xu, Y. Xu, H. Chen, and A. Wang, "Immunochromatographic assay for ultrasensitive detection of aflatoxin b1 in maize by highly luminescent quantum dot beads," *ACS Applied Materials & Interfaces*, vol. 6, no. 16, pp. 14 215–14 222, 2014.

[19] K. Hon, L. Li, and I. Hutchings, "Direct writing technology—Advances and developments," *CIRP Annals*, vol. 57, no. 2, pp. 601–620, 2008.

[20] D. B. Chrisey, "The power of direct writing," *Science*, vol. 289, no. 5481, pp. 879–881, 2000.

[21] A. Alasadi, F. Claeyssens, and D. Allwood, "Laser direct writing (LDW) of magnetic structures," *AIP Advances*, vol. 8, no. 5, p. 056322, 2018.

[22] C. B. Arnold, P. Serra, and A. Piqué, "Laser direct-write techniques for printing of complex materials," *MRS Bulletin*, vol. 32, no. 1, pp. 23–31, 2007.

[23] G. Kopitkovas, T. Lippert, C. David, A. Wokaun, and J. Gobrecht, "Fabrication of micro-optical elements in quartz by laser induced backside wet etching," *Microelectronic Engineering*, vol. 67, pp. 438–444, 2003.

[24] M. A. Mahmud, E. J. Blondeel, M. Kaddoura, and B. D. MacDonald, "Creating compact and microscale features in paper-based devices by laser cutting," *Analyst*, vol. 141, no. 23, pp. 6449–6454, 2016.

[25] P. Spicar-Mihalic, B. Toley, J. Houghtaling, T. Liang, P. Yager, and E. Fu, "CO2 laser cutting and ablative etching for the fabrication of paper-based devices," *Journal of Micromechanics and Microengineering*, vol. 23, no. 6, p. 067003, 2013.

[26] D. Chrisey, A. Pique, J. Fitz-Gerald, R. Auyeung, R. McGill, H. Wu, and M. Duignan, "New approach to laser direct writing active and passive mesoscopic circuit elements," *Applied Surface Science*, vol. 154, pp. 593–600, 2000.

[27] M. Kaur and A. Srivastava, "Photopolymerization: A review," *Journal of Macromolecular Science, Part C: Polymer Reviews*, vol. 42, no. 4, pp. 481–512, 2002.

[28] E. Andrzejewska, "Photopolymerization kinetics of multifunctional monomers," *Progress in Polymer Science*, vol. 26, no. 4, pp. 605–665, 2001.

[29] J. Shao, Y. Huang, and Q. Fan, "Visible light initiating systems for photopolymerization: status, development and challenges," *Polymer Chemistry*, vol. 5, no. 14, pp. 4195–4210, 2014.

[30] Y. Yamaguchi, B. J. Palmer, C. Kutal, T. Wakamatsu, and D. B. Yang, "Ferrocenes as anionic photoinitiators," *Macromolecules*, vol. 31, no. 15, pp. 5155–5157, 1998.

[31] C. Decker, "Photoinitiated crosslinking polymerisation," *Progress in Polymer Science*, vol. 21, no. 4, pp. 593–650, 1996.

[32] P. Kramer and R. Jones, "Control of free-radical reactivity in photopolymerization of acrylates," in *2012 UV & EB Technical Conference Proceedings*, no. 4, 2012, pp. 33–41.

[33] J. Kloosterboer and G. M. Lijten, "Deuterium isotope and oxygen effects on the rate of photopolymerization of a diacrylate," *Polymer Communications (Guildford)*, vol. 28, no. 1, pp. 2–5, 1987.

[34] A. J. Magenau, N. C. Strandwitz, A. Gennaro, and K. Matyjaszewski, "Electrochemically mediated atom transfer radical polymerization," *Science*, vol. 332, no. 6025, pp. 81–84, 2011.

[35] M. M. Caruso, D. A. Davis, Q. Shen, S. A. Odom, N. R. Sottos, S. R. White, and J. S. Moore, "Mechanically-induced chemical changes in polymeric materials," *Chemical Reviews*, vol. 109, no. 11, pp. 5755–5798, 2009.

[36] M. V. Humbert, L. E. Costa, I. Katis, F. Fonseca Ramos, A. Sanchéz Machado, C. Sones, E. A. Ferraz Coelho, and M. Christodoulides, "A rapid diagnostic test for human visceral leishmaniasis using novel leishmania antigens in a laser direct-write lateral flow device," *Emerging Microbes & Infections*, vol. 8, no. 1, pp. 1178–1185, 2019.

[37] P. J. He, I. N. Katis, R. W. Eason, and C. L. Sones, "Rapid multiplexed detection on lateral-flow devices using a laser direct-write technique," *Biosensors*, vol. 8, no. 4, p. 97, 2018.

[38] P. J. He, I. N. Katis, A. J. Kumar, C. A. Bryant, C. W. Keevil, B. K. Somani, N. Mahobia, R. W. Eason, and C. L. Sones, "Laser-patterned paper-based sensors for rapid point-of-care detection and antibiotic-resistance testing of bacterial infections," *Biosensors and Bioelectronics*, vol. 152, p. 112008, 2020.

[39] J. Kopeček, "Hydrogel biomaterials: a smart future?" *Biomaterials*, vol. 28, no. 34, pp. 5185–5192, 2007.

[40] A. S. Hoffman, "Hydrogels for biomedical applications," *Advanced Drug Delivery Reviews*, vol. 64, pp. 18–23, 2012.

[41] M. F. Akhtar, M. Hanif, and N. M. Ranjha, "Methods of synthesis of hydrogels… a review," *Saudi Pharmaceutical Journal*, vol. 24, no. 5, pp. 554–559, 2016.

[42] C. L. Bell and N. A. Peppas, "Modulation of drug permeation through interpolymer complexed hydrogels for drug delivery applications," *Journal of Controlled Release*, vol. 39, no. 2-3, pp. 201–207, 1996.

[43] F. Yokoyama, I. Masada, K. Shimamura, T. Ikawa, and K. Monobe, "Morphology and structure of highly elastic poly (vinyl alcohol) hydrogel prepared by repeated freezing-and-melting," *Colloid and Polymer Science*, vol. 264, no. 7, pp. 595–601, 1986.

[44] P. Gacesa, "Alginates," *Carbohydrate Polymers*, vol. 8, no. 3, pp. 161–182, 1988.

[45] T. Miyata, N. Asami, and T. Uragami, "Preparation of an antigen-sensitive hydrogel using antigen-antibody bindings," *Macromolecules*, vol. 32, no. 6, pp. 2082–2084, 1999.

[46] Y. Zu, Y. Zhang, X. Zhao, C. Shan, S. Zu, K. Wang, Y. Li, and Y. Ge, "Preparation and characterization of chitosan–polyvinyl alcohol blend hydrogels for the controlled release of nano-insulin," *International Journal of Biological Macromolecules*, vol. 50, no. 1, pp. 82–87, 2012.

[47] S. G. Abd Alla, M. Sen, and A. W. M. El-Naggar, "Swelling and mechanical properties of superabsorbent hydrogels based on tara gum/acrylic acid synthesized by gamma radiation," *Carbohydrate Polymers*, vol. 89, no. 2, pp. 478–485, 2012.

[48] M. C. I. M. Amin, N. Ahmad, N. Halib, and I. Ahmad, "Synthesis and characterization of thermo-and ph-responsive bacterial cellulose/acrylic acid hydrogels for drug delivery," *Carbohydrate Polymers*, vol. 88, no. 2, pp. 465–473, 2012.

[49] J. J. Sperinde and L. G. Griffith, "Synthesis and characterization of enzymatically-cross-linked poly (ethylene glycol) hydrogels," *Macromolecules*, vol. 30, no. 18, pp. 5255–5264, 1997.

[50] X. Li, Q. Sun, Q. Li, N. Kawazoe, and G. Chen, "Functional hydrogels with tunable structures and properties for tissue engineering applications," *Frontiers in Chemistry*, vol. 6, p. 499, 2018.

[51] H. Holback, Y. Yeo, and K. Park, "Hydrogel swelling behavior and its biomedical applications," in *Biomedical Hydrogels*. Elsevier, 2011, pp. 3–24.

[52] N. Peppas, P. Bures, W. Leobandung, and H. Ichikawa, "Hydrogels in pharmaceutical formulations," *European Journal of Pharmaceutics and Biopharmaceutics*, vol. 50, no. 1, pp. 27–46, 2000.

[53] I. Tomatsu, K. Peng, and A. Kros, "Photoresponsive hydrogels for biomedical applications," *Advanced Drug Delivery Reviews*, vol. 63, no. 14-15, pp. 1257–1266, 2011.

[54] K. Peng, I. Tomatsu, and A. Kros, "Light controlled protein release from a supramolecular hydrogel," *Chemical Communications*, vol. 46, no. 23, pp. 4094–4096, 2010.

[55] T. Muraoka, C.-Y. Koh, H. Cui, and S. I. Stupp, "Light-triggered bioactivity in three dimensions," *Angewandte Chemie*, vol. 121, no. 32, pp. 6060–6063, 2009.

[56] Y. Chujo, Y. Yoshifuji, K. Sada, and T. Saegusa, "A novel nonionic hydrogel from 2-methyl-2-oxazoline," *Macromolecules*, vol. 22, no. 3, pp. 1074–1077, 1989.

[57] K. G. Yager and C. J. Barrett, "Novel photo-switching using azobenzene functional materials," *Journal of Photochemistry and Photobiology A: Chemistry*, vol. 182, no. 3, pp. 250–261, 2006.

[58] H. Meier, "The photochemistry of stilbenoid compounds and their role in materials technology," *Angewandte Chemie International Edition in English*, vol. 31, no. 11, pp. 1399–1420, 1992.

[59] Č. Koňák, R. C. Rathi, P. Kopecková, and J. Kopecek, "Photoregulated association of water-soluble copolymers with spirobenzopyran-containing side chains," *Macromolecules*, vol. 30, no. 18, pp. 5553–5556, 1997.

[60] C. L. Fleming, S. Li, M. Grøtli, and J. Andreasson, "Shining new light on the spiropyran photoswitch: a photocage decides between cis–trans or spiro-merocyanine isomerization," *Journal of the American Chemical Society*, vol. 140, no. 43, pp. 14 069–14 072, 2018.

[61] L. Kortekaas and W. R. Browne, "The evolution of spiropyran: fundamentals and progress of an extraordinarily versatile photochrome," *Chemical Society Reviews*, vol. 48, no. 12, pp. 3406–3424, 2019.

[62] Y. Hirshberg and E. Fischer, "Photochromism and reversible multiple internal transitions in some spiro pyrans at low temperatures. part i," *Journal of the Chemical Society (Resumed)*, pp. 297–303, 1954.

[63] R. Klajn, "Spiropyran-based dynamic materials," *Chemical Society Reviews*, vol. 43, no. 1, pp. 148–184, 2014.

[64] K. Sumaru, K. Ohi, T. Takagi, T. Kanamori, and T. Shinbo, "Photoresponsive properties of poly (n-isopropylacrylamide) hydrogel partly modified with spirobenzopyran," *Langmuir*, vol. 22, no. 9, pp. 4353–4356, 2006.

[65] T. Satoh, K. Sumaru, T. Takagi, and T. Kanamori, "Fast-reversible light-driven hydrogels consisting of spirobenzopyran-functionalized poly (n-isopropylacrylamide)," *Soft Matter*, vol. 7, no. 18, pp. 8030–8034, 2011.

[66] A. Szilágyi, K. Sumaru, S. Sugiura, T. Takagi, T. Shinbo, M. Zrínyi, and T. Kanamori, "Rewritable microrelief formation on photoresponsive hydrogel layers," *Chemistry of Materials*, vol. 19, no. 11, pp. 2730–2732, 2007.

[67] S. Sugiura, K. Sumaru, K. Ohi, K. Hiroki, T. Takagi, and T. Kanamori, "Photoresponsive polymer gel microvalves controlled by local light irradiation," *Sensors and Actuators A: Physical*, vol. 140, no. 2, pp. 176–184, 2007.

[68] B. Ziółkowski, L. Florea, J. Theobald, F. Benito-Lopez, and D. Diamond, "Self-protonating spiropyran-co-nipam-co-acrylic acid hydrogel photoactuators," *Soft Matter*, vol. 9, no. 36, pp. 8754–8760, 2013.

[69] J. Ter Schiphorst, J. Saez, D. Diamond, F. Benito-Lopez, and A. P. Schenning, "Light-responsive polymers for microfluidic applications," *Lab on a Chip*, vol. 18, no. 5, pp. 699–709, 2018.

[70] J. Ter Schiphorst, S. Coleman, J. E. Stumpel, A. Ben Azouz, D. Diamond, and A. P. Schenning, "Molecular design of light-responsive hydrogels, for in situ generation of fast and reversible valves for microfluidic applications," *Chemistry of Materials*, vol. 27, no. 17, pp. 5925–5931, 2015.

[71] F. Benito-Lopez, R. Byrne, A. M. Răduţă, N. E. Vrana, G. McGuinness, and D. Diamond, "Ionogel-based light-actuated valves for controlling liquid flow in micro-fluidic manifolds," *Lab on a Chip*, vol. 10, no. 2, pp. 195–201, 2010.

[72] W. Francis, A. Dunne, C. Delaney, L. Florea, and D. Diamond, "Spiropyran based hydrogels actuators—walking in the light," *Sensors and Actuators B: Chemical*, vol. 250, pp. 608–616, 2017.

Bibliography for Chapter 3

[1] B. Kowalczyk, I. Lagzi, and B. A. Grzybowski, "Nanoseparations: Strategies for size and/or shape-selective purification of nanoparticles," *Current Opinion in Colloid & Interface Science*, vol. 16, no. 2, pp. 135–148, 2011.

[2] G. Chen, Y. Wang, L. H. Tan, M. Yang, L. S. Tan, Y. Chen, and H. Chen, "High-purity separation of gold nanoparticle dimers and trimers," *Journal of the American Chemical Society*, vol. 131, no. 12, pp. 4218–4219, 2009.

[3] G. DanieláLilly *et al.*, "Free flow electrophoresis for the separation of cdte nanoparticles," *Journal of Materials Chemistry*, vol. 19, no. 10, pp. 1390–1394, 2009.

[4] A. H. Latham, R. S. Freitas, P. Schiffer, and M. E. Williams, "Capillary magnetic field flow fractionation and analysis of magnetic nanoparticles," *Analytical Chemistry*, vol. 77, no. 15, pp. 5055–5062, 2005.

[5] X. Sun, S. M. Tabakman, W.-S. Seo, L. Zhang, G. Zhang, S. Sherlock, L. Bai, and H. Dai, "Separation of nanoparticles in a density gradient: FeCo@C and gold nanocrystals," *Angewandte Chemie*, vol. 121, no. 5, pp. 957–960, 2009.

[6] M. Hanauer, S. Pierrat, I. Zins, A. Lotz, and C. Sönnichsen, "Separation of nanoparticles by gel electrophoresis according to size and shape," *Nano Letters*, vol. 7, no. 9, pp. 2881–2885, 2007.

[7] J. H. Jung, K. H. Lee, K. S. Lee, B. H. Ha, Y. S. Oh, and H. J. Sung, "Optical separation of droplets on a microfluidic platform," *Microfluidics and Nanofluidics*, vol. 16, no. 4, pp. 635–644, 2014.

[8] M. Hejazian and N.-T. Nguyen, "Negative magnetophoresis in diluted ferrofluid flow," *Lab on a Chip*, vol. 15, no. 14, pp. 2998–3005, 2015.

[9] P. Li, Z. Mao, Z. Peng, L. Zhou, Y. Chen, P.-H. Huang, C. I. Truica, J. J. Drabick, W. S. El-Deiry, M. Dao *et al.*, "Acoustic separation of circulating tumor cells," *Proceedings of the National Academy of Sciences*, vol. 112, no. 16, pp. 4970–4975, 2015.

[10] J. A. Davis, D. W. Inglis, K. J. Morton, D. A. Lawrence, L. R. Huang, S. Y. Chou, J. C. Sturm, and R. H. Austin, "Deterministic hydrodynamics: taking blood apart," *Proceedings of the National Academy of Sciences*, vol. 103, no. 40, pp. 14 779–14 784, 2006.

[11] S. Ranjan, K. K. Zeming, R. Jureen, D. Fisher, and Y. Zhang, "DLD pillar shape design for efficient separation of spherical and non-spherical bioparticles," *Lab on a Chip*, vol. 14, no. 21, pp. 4250–4262, 2014.

[12] R. T. Davies, J. Kim, S. C. Jang, E.-J. Choi, Y. S. Gho, and J. Park, "Microfluidic filtration system to isolate extracellular vesicles from blood," *Lab on a Chip*, vol. 12, no. 24, pp. 5202–5210, 2012.

[13] L. Amato, Y. Gu, N. Bellini, S. M. Eaton, G. Cerullo, and R. Osellame, "Integrated three-dimensional filter separates nanoscale from microscale elements in a microfluidic chip," *Lab on a Chip*, vol. 12, no. 6, pp. 1135–1142, 2012.

[14] G. Cheng, "Circulating miRNAs: roles in cancer diagnosis, prognosis and therapy," *Advanced Drug Delivery Reviews*, vol. 81, pp. 75–93, 2015.

[15] B. Olsson, R. Lautner, U. Andreasson, A. Öhrfelt, E. Portelius, M. Bjerke, M. Hölttä, C. Rosén, C. Olsson, G. Strobel *et al.*, "CSF and blood biomarkers for the diagnosis of Alzheimer's disease: a systematic review and meta-analysis," *The Lancet Neurology*, vol. 15, no. 7, pp. 673–684, 2016.

[16] S. Neugebauer, E. J. Giamarellos-Bourboulis, A. Pelekanou, A. Marioli, F. Baziaka, I. Tsangaris, M. Bauer, and M. Kiehntopf, "Metabolite profiles in sepsis: developing prognostic tools based on the type of infection," *Critical Care Medicine*, vol. 44, no. 9, pp. 1649–1662, 2016.

[17] W. S. Mielczarek, E. Obaje, T. Bachmann, and M. Kersaudy-Kerhoas, "Microfluidic blood plasma separation for medical diagnostics: is it worth it?" *Lab on a Chip*, vol. 16, no. 18, pp. 3441–3448, 2016.

[18] J. Noiphung, T. Songjaroen, W. Dungchai, C. S. Henry, O. Chailapakul, and W. Laiwattanapaisal, "Electrochemical detection of glucose from whole blood using paper-based microfluidic devices," *Analytica Chimica Acta*, vol. 788, pp. 39–45, 2013.

[19] B. Kim and S. Choi, "Smart pipette and microfluidic pipette tip for blood plasma separation," *Small*, vol. 12, no. 2, pp. 190–197, 2016.

[20] L. Anfossi, F. Di Nardo, C. Giovannoli, C. Passini, and C. Baggiani, "Increased sensitivity of lateral flow immunoassay for ochratoxin a through silver enhancement," *Analytical and Bioanalytical Chemistry*, vol. 405, no. 30, pp. 9859–9867, 2013.

[21] D. Tang, J. Sauceda, Z. Lin, S. Ott, E. Basova, I. Goryacheva, S. Biselli, J. Lin, R. Niessner, and D. Knopp, "Magnetic nanogold microspheres-based lateral-flow immunodipstick for rapid detection of aflatoxin B2 in food," *Biosensors and Bioelectronics*, vol. 25, no. 2, pp. 514–518, 2009.

[22] C. Parolo, M. Medina-Sánchez, A. De La Escosura-Muñiz, and A. Merkoçi, "Simple paper architecture modifications lead to enhanced sensitivity in nanoparticle based lateral flow immunoassays," *Lab on a Chip*, vol. 13, no. 3, pp. 386–390, 2013.

[23] I. N. Katis, P. J. He, R. W. Eason, and C. L. Sones, "Improved sensitivity and limit-of-detection of lateral flow devices using spatial constrictions of the flow-path," *Biosensors and Bioelectronics*, vol. 113, pp. 95–100, 2018.

[24] L. Rivas, M. Medina-Sánchez, A. De La Escosura-Muñiz, and A. Merkoçi, "Improving sensitivity of gold nanoparticle-based lateral flow assays by using wax-printed pillars as delay barriers of microfluidics," *Lab on a Chip*, vol. 14, no. 22, pp. 4406–4414, 2014.

[25] K. Lachin, N. Le Sauze, N. D. M. Raimondi, J. Aubin, C. Gourdon, and M. Cabassud, "Aggregation and breakup of acrylic latex particles inside millimetric scale reactors," *Chemical Engineering and Processing: Process Intensification*, vol. 113, pp. 65–73, 2017.

[26] V. Oles, "Shear-induced aggregation and breakup of polystyrene latex particles," *Journal of Colloid and Interface Science*, vol. 154, no. 2, pp. 351–358, 1992.

[27] C.-F. Lee, "Effects of surfactants on the morphology of composite polymer particles produced by two-stage seeded emulsion polymerization," *Journal of Polymer Science Part A: Polymer Chemistry*, vol. 43, no. 11, pp. 2224–2236, 2005.

[28] A. Bransky, N. Korin, Y. Nemirovski, and U. Dinnar, "Correlation between erythrocytes deformability and size: a study using a microchannel based cell analyzer," *Microvascular Research*, vol. 73, no. 1, pp. 7–13, 2007.

[29] D. Brinc and A. H. Lazarus, "Mechanisms of anti-D action in the prevention of hemolytic disease of the fetus and newborn," *ASH Education Program Book*, vol. 2009, no. 1, pp. 185–191, 2009.

[30] M. Stucki, J. Schnorf, H. Hustinx, H. Gerber, P. Lerch, A. Halabi, C. Kleinbloesem, and A. Morell, "Anti-D immunoglobulin in Rh (D) negative volunteers: clearance of Rh (D) positive red cells and kinetics of serum anti-D levels," *Transfusion Clinique et Biologique*, vol. 5, no. 3, pp. 180–188, 1998.

[31] R. Lemieux, S. Verrette, H. Broly, and S. Perron, "Direct Agglutination of Weak D Red Cells by Tetramolecular Complexes Containing Monoclonal IgG Anti-D," *Vox Sanguinis*, vol. 65, no. 2, pp. 141–145, 1993.

Bibliography for Chapter 4

[1] A. St John and C. P. Price, "Existing and emerging technologies for point-of-care testing," *The Clinical Biochemist Reviews*, vol. 35, no. 3, p. 155, 2014.

[2] B. O'Farrell, "Lateral flow technology for field-based applications–basics and advanced developments," *Topics in Companion Animal Medicine*, vol. 30, no. 4, p. 139, 2015.

[3] G. Aragay, F. Pino, and A. Merkoçi, "Nanomaterials for sensing and destroying pesticides," *Chemical Reviews*, vol. 112, no. 10, pp. 5317–5338, 2012.

[4] H. de Puig, I. Bosch, L. Gehrke, and K. Hamad-Schifferli, "Challenges of the nano–bio interface in lateral flow and dipstick immunoassays," *Trends in Biotechnology*, vol. 35, no. 12, pp. 1169–1180, 2017.

[5] P. Yager, G. J. Domingo, and J. Gerdes, "Point-of-care diagnostics for global health," *Annual Review of Biomedical Engineering*, vol. 10, 2008.

[6] Y. Zhao, H. Wang, P. Zhang, C. Sun, X. Wang, X. Wang, R. Yang, C. Wang, and L. Zhou, "Rapid multiplex detection of 10 foodborne pathogens with an up-converting phosphor technology-based 10-channel lateral flow assay," *Scientific Reports*, vol. 6, no. 1, pp. 1–8, 2016.

[7] M. de Lourdes Moreno, Á. Cebolla, A. Muñoz-Suano, C. Carrillo-Carrion, I. Comino, Á. Pizarro, F. León, A. Rodríguez-Herrera, and C. Sousa, "Detection of gluten immunogenic peptides in the urine of patients with coeliac disease reveals transgressions in the gluten-free diet and incomplete mucosal healing," *Gut*, vol. 66, no. 2, pp. 250–257, 2017.

[8] E. C. Schramm, N. R. Staten, Z. Zhang, S. S. Bruce, C. Kellner, J. P. Atkinson, V. C. Kyttaris, G. C. Tsokos, M. Petri, E. S. Connolly *et al.*, "A quantitative lateral flow assay to detect complement activation in blood," *Analytical Biochemistry*, vol. 477, pp. 78–85, 2015.

[9] A. Carrio, C. Sampedro, J. L. Sanchez-Lopez, M. Pimienta, and P. Campoy, "Automated low-cost smartphone-based lateral flow saliva test reader for drugs-of-abuse detection," *Sensors*, vol. 15, no. 11, pp. 29 569–29 593, 2015.

[10] K. M. Koczula and A. Gallotta, "Lateral flow assays," *Essays in Biochemistry*, vol. 60, no. 1, pp. 111–120, 2016.

[11] G. A. Posthuma-Trumpie, J. Korf, and A. van Amerongen, "Lateral flow (immuno) assay: its strengths, weaknesses, opportunities and threats. a literature survey," *Analytical and Bioanalytical Chemistry*, vol. 393, no. 2, pp. 569–582, 2009.

[12] M. Sajid, A.-N. Kawde, and M. Daud, "Designs, formats and applications of lateral flow assay: A literature review," *Journal of Saudi Chemical Society*, vol. 19, no. 6, pp. 689–705, 2015.

[13] J.-H. Cho and S.-H. Paek, "Semiquantitative, bar code version of immunochromatographic assay system for human serum albumin as model analyte," *Biotechnology and Bioengineering*, vol. 75, no. 6, pp. 725–732, 2001.

[14] E. G. Rey, D. O'Dell, S. Mehta, and D. Erickson, "Mitigating the hook effect in lateral flow sandwich immunoassays using real-time reaction kinetics," *Analytical Chemistry*, vol. 89, no. 9, pp. 5095–5100, 2017.

[15] G. M. Ross, D. Filippini, M. W. Nielen, and G. I. Salentijn, "Unraveling the hook effect: A comprehensive study of high antigen concentration effects in sandwich lateral flow immunoassays," *Analytical Chemistry*, vol. 92, no. 23, pp. 15 587–15 595, 2020.

[16] Y. K. Oh, H.-A. Joung, H. S. Han, H.-J. Suk, and M.-G. Kim, "A three-line lateral flow assay strip for the measurement of C-reactive protein covering a broad physiological concentration range in human sera," *Biosensors and Bioelectronics*, vol. 61, pp. 285–289, 2014.

[17] J. Hu, J. R. Choi, S. Wang, Y. Gong, S. Feng, B. Pingguan-Murphy, T. J. Lu, and F. Xu, "Multiple test zones for improved detection performance in lateral flow assays," *Sensors and Actuators B: Chemical*, vol. 243, pp. 484–488, 2017.

[18] R. D. Ramamoorthy, V. Nallasamy, R. Reddy, N. Esther, and Y. Maruthappan, "A review of C-reactive protein: A diagnostic indicator in periodontal medicine," *Journal of Pharmacy & Bioallied Sciences*, vol. 4, no. Suppl 2, p. S422, 2012.

[19] Y.-y. Luan and Y.-m. Yao, "The clinical significance and potential role of c-reactive protein in chronic inflammatory and neurodegenerative diseases," *Frontiers in Immunology*, vol. 9, p. 1302, 2018.

[20] M. M. Ragy and N. N. Kamal, "Linking senile dementia to type 2 diabetes: role of oxidative stress markers, C-reactive protein and tumor necrosis factor-α," *Neurological Research*, vol. 39, no. 7, pp. 587–595, 2017.

[21] P. M. Ridker, "Clinical application of c-reactive protein for cardiovascular disease detection and prevention," *Circulation*, vol. 107, no. 3, pp. 363–369, 2003.

[22] L. S. A. Busa, S. Mohammadi, M. Maeki, A. Ishida, H. Tani, and M. Tokeshi, "Advances in microfluidic paper-based analytical devices for food and water analysis," *Micromachines*, vol. 7, no. 5, p. 86, 2016.

[23] Y. Liu and Y. Li, "Detection of Escherichia coli O157: H7 using immunomagnetic separation and absorbance measurement," *Journal of Microbiological Methods*, vol. 51, no. 3, pp. 369–377, 2002.

[24] Ç. Dilek and H. A. Öktem, "Optimizations needed for lateral flow assay for rapid detection of pathogenic E. coli," *Turkish Journal of Biology*, vol. 41, no. 6, pp. 954–968, 2017.

[25] S. Ma, Y. Tang, J. Liu, and J. Wu, "Visible paper chip immunoassay for rapid determination of bacteria in water distribution system," *Talanta*, vol. 120, pp. 135–140, 2014.

[26] S. Burnham, J. Hu, H. Anany, L. Brovko, F. Deiss, R. Derda, and M. W. Griffiths, "Towards rapid on-site phage-mediated detection of generic Escherichia coli in water using luminescent and visual readout," *Analytical and Bioanalytical Chemistry*, vol. 406, no. 23, pp. 5685–5693, 2014.

[27] Y. K. Oh, H.-A. Joung, S. Kim, and M.-G. Kim, "Vertical flow immunoassay (VFA) biosensor for a rapid one-step immunoassay," *Lab on a Chip*, vol. 13, no. 5, pp. 768–772, 2013.

[28] J. Park and J.-K. Park, "Pressed region integrated 3D paper-based microfluidic device that enables vertical flow multistep assays for the detection of C-reactive protein based on programmed reagent loading," *Sensors and Actuators B: Chemical*, vol. 246, pp. 1049–1055, 2017.

[29] M. Khosravi, "Shifting the "hook effect" in one-step immunometric assays," *Clinical Chemistry*, vol. 36, no. 1, pp. 169–170, 1990.

[30] A. Bransky, N. Korin, Y. Nemirovski, and U. Dinnar, "Correlation between erythrocytes deformability and size: a study using a microchannel based cell analyzer," *Microvascular Research*, vol. 73, no. 1, pp. 7–13, 2007.

[31] O. K. Baskurt and H. J. Meiselman, "RBC aggregation: more important than RBC adhesion to endothelial cells as a determinant of in vivo blood flow in health and disease," *Microcirculation*, vol. 15, no. 7, pp. 585–590, 2008.

[32] Z. Lu, E. Rey, S. Vemulapati, B. Srinivasan, S. Mehta, and D. Erickson, "High-yield paper-based quantitative blood separation system," *Lab on a Chip*, vol. 18, no. 24, pp. 3865–3871, 2018.

[33] X. Su, J. Zhang, D. Zhang, Y. Wang, M. Chen, Z. Weng, J. Wang, J. Zeng, Y. Zhang, S. Zhang *et al.*, "High-efficiency plasma separator based on immunocapture and filtration," *Micromachines*, vol. 11, no. 4, p. 352, 2020.

Bibliography for Chapter 5

[1] A. W. Martinez, S. T. Phillips, and G. M. Whitesides, "Three-dimensional microfluidic devices fabricated in layered paper and tape," *Proceedings of the National Academy of Sciences*, vol. 105, no. 50, pp. 19 606–19 611, 2008.

[2] T. Akyazi, L. Basabe-Desmonts, and F. Benito-Lopez, "Review on microfluidic paper-based analytical devices towards commercialisation," *Analytica Chimica Acta*, vol. 1001, pp. 1–17, 2018.

[3] R. A. de Oliveira, F. Camargo, N. C. Pesquero, and R. C. Faria, "A simple method to produce 2D and 3D microfluidic paper-based analytical devices for clinical analysis," *Analytica Chimica Acta*, vol. 957, pp. 40–46, 2017.

[4] E. Fu and C. Downs, "Progress in the development and integration of fluid flow control tools in paper microfluidics," *Lab on a Chip*, vol. 17, no. 4, pp. 614–628, 2017.

[5] S.-G. Jeong, J. Kim, S. H. Jin, K.-S. Park, and C.-S. Lee, "Flow control in paper-based microfluidic device for automatic multistep assays: A focused minireview," *Korean Journal of Chemical Engineering*, vol. 33, no. 10, pp. 2761–2770, 2016.

[6] P. Lisowski and P. K. Zarzycki, "Microfluidic paper-based analytical devices (μPADs) and micro total analysis systems (μTAS): Development, applications and future trends," *Chromatographia*, vol. 76, no. 19, pp. 1201–1214, 2013.

[7] X. Li, J. Tian, T. Nguyen, and W. Shen, "Based microfluidic devices by plasma treatment," *Analytical Chemistry*, vol. 80, no. 23, pp. 9131–9134, 2008.

[8] E. Fu, T. Liang, P. Spicar-Mihalic, J. Houghtaling, S. Ramachandran, and P. Yager, "Two-dimensional paper network format that enables simple multistep assays for use in low-resource settings in the context of malaria antigen detection," *Analytical Chemistry*, vol. 84, no. 10, pp. 4574–4579, 2012.

[9] M. S. Verma, M.-N. Tsaloglou, T. Sisley, D. Christodouleas, A. Chen, J. Milette, and G. M. Whitesides, "Sliding-strip microfluidic device enables ELISA on paper," *Biosensors and Bioelectronics*, vol. 99, pp. 77–84, 2018.

[10] K. M. Schilling, A. L. Lepore, J. A. Kurian, and A. W. Martinez, "Fully enclosed microfluidic paper-based analytical devices," *Analytical Chemistry*, vol. 84, no. 3, pp. 1579–1585, 2012.

[11] C. K. Camplisson, K. M. Schilling, W. L. Pedrotti, H. A. Stone, and A. W. Martinez, "Two-ply channels for faster wicking in paper-based microfluidic devices," *Lab on a Chip*, vol. 15, no. 23, pp. 4461–4466, 2015.

[12] J. Jeon, C. Park, D. V. Ponnuvelu, and S. Park, "Enhanced sensing behavior of three-dimensional microfluidic paper-based analytical devices (3D-μPADs) with evaporation-free enclosed channels for point-of-care testing," *Diagnostics*, vol. 11, no. 6, p. 977, 2021.

[13] L. Ge, S. Wang, X. Song, S. Ge, and J. Yu, "3D origami-based multifunction-integrated immunodevice: Low-cost and multiplexed sandwich chemiluminescence immunoassay on microfluidic paper-based analytical device," *Lab on a Chip*, vol. 12, no. 17, pp. 3150–3158, 2012.

[14] C.-A. Chen, W.-S. Yeh, T.-T. Tsai, C.-F. Chen *et al.*, "Three-dimensional origami paper-based device for portable immunoassay applications," *Lab on a Chip*, vol. 19, no. 4, pp. 598–607, 2019.

[15] R. Derda, S. K. Tang, A. Laromaine, B. Mosadegh, E. Hong, M. Mwangi, A. Mammoto, D. E. Ingber, and G. M. Whitesides, "Multizone paper platform for 3D cell cultures," *PLOS ONE*, vol. 6, no. 5, p. e18940, 2011.

[16] G. G. Lewis, M. J. DiTucci, M. S. Baker, and S. T. Phillips, "High throughput method for prototyping three-dimensional, paper-based microfluidic devices," *Lab on a Chip*, vol. 12, no. 15, pp. 2630–2633, 2012.

[17] R. B. Channon, M. P. Nguyen, A. G. Scorzelli, E. M. Henry, J. Volckens, D. S. Dandy, and C. S. Henry, "Rapid flow in multilayer microfluidic paper-based analytical devices," *Lab on a Chip*, vol. 18, no. 5, pp. 793–802, 2018.

[18] B. Kalish and H. Tsutsui, "Patterned adhesive enables construction of nonplanar three-dimensional paper microfluidic circuits," *Lab on a Chip*, vol. 14, no. 22, pp. 4354–4361, 2014.

[19] H. Liu and R. M. Crooks, "Three-dimensional paper microfluidic devices assembled using the principles of origami," *Journal of the American Chemical Society*, vol. 133, no. 44, pp. 17 564–17 566, 2011.

[20] S. Choi, S.-K. Kim, G.-J. Lee, and H.-K. Park, "Based 3D microfluidic device for multiple bioassays," *Sensors and Actuators B: Chemical*, vol. 219, pp. 245–250, 2015.

[21] C. Renault, J. Koehne, A. J. Ricco, and R. M. Crooks, "Three-dimensional wax patterning of paper fluidic devices," *Langmuir*, vol. 30, no. 23, pp. 7030–7036, 2014.

[22] P. He, I. Katis, R. Eason, and C. Sones, "Laser direct-write for fabrication of three-dimensional paper-based devices," *Lab on a Chip*, vol. 16, no. 17, pp. 3296–3303, 2016.

[23] E. Lepowsky, F. Ghaderinezhad, S. Knowlton, and S. Tasoglu, "Based assays for urine analysis," *Biomicrofluidics*, vol. 11, no. 5, p. 051501, 2017.

[24] S. Aitekenov, A. Gaipov, and R. Bukasov, "Detection and quantification of proteins in human urine," *Talanta*, p. 121718, 2020.

[25] E. Gelamo, C. Silva, H. Imasato, and M. Tabak, "Interaction of bovine (BSA) and human (HSA) serum albumins with ionic surfactants: spectroscopy and modelling," *Biochimica et Biophysica Acta (BBA)-Protein Structure and Molecular Enzymology*, vol. 1594, no. 1, pp. 84–99, 2002.

[26] V. Gounden and I. Jialal, *Hypoalbuminemia*. StatPearls Publishing, Treasure Island (FL), 2018.

[27] M. Mohammadifar, M. Tahernia, and S. Choi, "An equipment-free, paper-based electrochemical sensor for visual monitoring of glucose levels in urine," *SLAS technology*, vol. 24, no. 5, pp. 499–505, 2019.

[28] P. King, I. Peacock, and R. Donnelly, "The UK prospective diabetes study (UKPDS): clinical and therapeutic implications for type 2 diabetes," *British Journal of Clinical Pharmacology*, vol. 48, no. 5, p. 643, 1999.

[29] C. Honrado and T. Dong, "A capacitive touch screen sensor for detection of urinary tract infections in portable biomedical devices," *Sensors*, vol. 14, no. 8, pp. 13 851–13 862, 2014.

[30] J. Lundberg, S. Carlsson, L. Engstrand, E. Morcos, N. Wiklund, and E. Weitzberg, "Urinary nitrite: More than a marker of infection," *Urology*, vol. 50, no. 2, pp. 189–191, 1997.

[31] C. Chen and T. Dong, "Microfluidic paper-based analytical devices for colorimetric detection of urinary tract infection biomarkers on adult diapers," in *2015 37th Annual International Conference of the IEEE Engineering in Medicine and Biology Society (EMBC)*. IEEE, 2015, pp. 5892–5895.

[32] J. Noiphung and W. Laiwattanapaisal, "Multifunctional paper-based analytical device for in situ cultivation and screening of Escherichia coli infections," *Scientific Reports*, vol. 9, no. 1, pp. 1–10, 2019.

[33] W. Wang, W.-Y. Wu, and J.-J. Zhu, "Tree-shaped paper strip for semiquantitative colorimetric detection of protein with self-calibration," *Journal of Chromatography A*, vol. 1217, no. 24, pp. 3896–3899, 2010.

[34] D. Tsikas, "Analysis of nitrite and nitrate in biological fluids by assays based on the Griess reaction: appraisal of the Griess reaction in the L-arginine/nitric oxide area of research," *Journal of Chromatography B*, vol. 851, no. 1-2, pp. 51–70, 2007.

[35] B. V. McCleary, L. M. Charmier, and V. A. McKie, "Measurement of starch: critical evaluation of current methodology," *Starch-Stärke*, vol. 71, no. 1-2, p. 1800146, 2019.

Bibliography for Chapter 6

[1] H. Lim, A. T. Jafry, and J. Lee, "Fabrication, flow control, and applications of microfluidic paper-based analytical devices," *Molecules*, vol. 24, no. 16, p. 2869, 2019.

[2] T. H. Kim, Y. K. Hahn, and M. S. Kim, "Recent advances of fluid manipulation technologies in microfluidic paper-based analytical devices (μPADs) toward multi-step assays," *Micromachines*, vol. 11, no. 3, p. 269, 2020.

[3] E. Fu, B. Lutz, P. Kauffman, and P. Yager, "Controlled reagent transport in disposable 2D paper networks," *Lab on a Chip*, vol. 10, no. 7, pp. 918–920, 2010.

[4] R. B. Channon, M. P. Nguyen, A. G. Scorzelli, E. M. Henry, J. Volckens, D. S. Dandy, and C. S. Henry, "Rapid flow in multilayer microfluidic paper-based analytical devices," *Lab on a Chip*, vol. 18, no. 5, pp. 793–802, 2018.

[5] B. J. Toley, B. McKenzie, T. Liang, J. R. Buser, P. Yager, and E. Fu, "Tunable-delay shunts for paper microfluidic devices," *Analytical Chemistry*, vol. 85, no. 23, pp. 11 545–11 552, 2013.

[6] B. Lutz, T. Liang, E. Fu, S. Ramachandran, P. Kauffman, and P. Yager, "Dissolvable fluidic time delays for programming multi-step assays in instrument-free paper diagnostics," *Lab on a Chip*, vol. 13, no. 14, pp. 2840–2847, 2013.

[7] H. Noh and S. T. Phillips, "Metering the capillary-driven flow of fluids in paper-based microfluidic devices," *Analytical Chemistry*, vol. 82, no. 10, pp. 4181–4187, 2010.

[8] E. A. Phillips, R. Shen, S. Zhao, and J. C. Linnes, "Thermally actuated wax valves for paper-fluidic diagnostics," *Lab on a Chip*, vol. 16, no. 21, pp. 4230–4236, 2016.

[9] J. H. Shin and J.-K. Park, "Functional packaging of lateral flow strip allows simple delivery of multiple reagents for multistep assays," *Analytical Chemistry*, vol. 88, no. 21, pp. 10 374–10 378, 2016.

[10] P. Theato, B. S. Sumerlin, R. K. O'Reilly, and T. H. Epps III, "Stimuli responsive materials," *Chemical Society Reviews*, vol. 42, no. 17, pp. 7055–7056, 2013.

[11] E. M. Ahmed, "Hydrogel: Preparation, characterization, and applications: A review," *Journal of Advanced Research*, vol. 6, no. 2, pp. 105–121, 2015.

[12] M. C. Koetting, J. T. Peters, S. D. Steichen, and N. A. Peppas, "Stimulus-responsive hydrogels: Theory, modern advances, and applications," *Materials Science and Engineering: R: Reports*, vol. 93, pp. 1–49, 2015.

[13] C. Echeverria, S. N. Fernandes, M. H. Godinho, J. P. Borges, and P. I. Soares, "Functional stimuli-responsive gels: Hydrogels and microgels," *Gels*, vol. 4, no. 2, p. 54, 2018.

[14] P. Gupta, K. Vermani, and S. Garg, "Hydrogels: from controlled release to pH-responsive drug delivery," *Drug Discovery Today*, vol. 7, no. 10, pp. 569–579, 2002.

[15] L. A. Sharpe, A. M. Daily, S. D. Horava, and N. A. Peppas, "Therapeutic applications of hydrogels in oral drug delivery," *Expert Opinion on Drug Delivery*, vol. 11, no. 6, pp. 901–915, 2014.

[16] L. Klouda and A. G. Mikos, "Thermoresponsive hydrogels in biomedical applications," *European Journal of Pharmaceutics and Biopharmaceutics*, vol. 68, no. 1, pp. 34–45, 2008.

[17] S. Purushotham and R. Ramanujan, "Thermoresponsive magnetic composite nanomaterials for multimodal cancer therapy," *Acta Biomaterialia*, vol. 6, no. 2, pp. 502–510, 2010.

[18] T. Miyata, A. Jikihara, K. Nakamae, T. Uragami, A. S. Hoffman, K. Kinomura, and M. Okumura, "Preparation of glucose-sensitive hydrogels by entrapment or copolymerization of concanavalin a in a glucosyloxyethyl methacrylate hydrogel," in *Advanced Biomaterials in Biomedical Engineering and Drug Delivery Systems*. Springer, 1996, pp. 237–238.

[19] J.-F. Gohy and Y. Zhao, "Photo-responsive block copolymer micelles: design and behavior," *Chemical Society Reviews*, vol. 42, no. 17, pp. 7117–7129, 2013.

[20] K. Unger, P. Salzmann, C. Masciullo, M. Cecchini, G. Koller, and A. M. Coclite, "Novel light-responsive biocompatible hydrogels produced by initiated chemical vapor deposition," *ACS Applied Materials & Interfaces*, vol. 9, no. 20, pp. 17 408–17 416, 2017.

[21] I. Tomatsu, K. Peng, and A. Kros, "Photoresponsive hydrogels for biomedical applications," *Advanced Drug Delivery Reviews*, vol. 63, no. 14-15, pp. 1257–1266, 2011.

[22] S. Sugiura, A. Szilágyi, K. Sumaru, K. Hattori, T. Takagi, G. Filipcsei, M. Zrínyi, and T. Kanamori, "On-demand microfluidic control by micropatterned light irradiation of a photoresponsive hydrogel sheet," *Lab on a Chip*, vol. 9, no. 2, pp. 196–198, 2009.

[23] J. Ter Schiphorst, S. Coleman, J. E. Stumpel, A. Ben Azouz, D. Diamond, and A. P. Schenning, "Molecular design of light-responsive hydrogels, for in situ generation of fast and reversible valves for microfluidic applications," *Chemistry of Materials*, vol. 27, no. 17, pp. 5925–5931, 2015.

[24] T. Akyazi, A. Tudor, D. Diamond, L. Basabe-Desmonts, L. Florea, and F. Benito-Lopez, "Driving flows in microfluidic paper-based analytical devices with a cholinium based poly (ionic liquid) hydrogel," *Sensors and Actuators B: Chemical*, vol. 261, pp. 372–378, 2018.

[25] R. R. Niedl and C. Beta, "Hydrogel-driven paper-based microfluidics," *Lab on a Chip*, vol. 15, no. 11, pp. 2452–2459, 2015.

[26] X. Wei, T. Tian, S. Jia, Z. Zhu, Y. Ma, J. Sun, Z. Lin, and C. J. Yang, "Target-responsive DNA hydrogel mediated "stop-flow" microfluidic paper-based analytic device for rapid, portable and visual detection of multiple targets," *Analytical Chemistry*, vol. 87, no. 8, pp. 4275–4282, 2015.

[27] Y. Ochi, R. Kawakubo, D.-T. Van-Pham, Y. Kitamura, H. Nakanishi, T. Norisuye, and Q. Tran-Cong-Miyata, "Phase separation of polymer mixtures induced by light and heat: a comparative study by light scattering," *Advances in Natural Sciences: Nanoscience and Nanotechnology*, vol. 6, no. 4, p. 045002, 2015.

Reprints of published papers

Laser-direct-writing to enable filtration in paper-based devices

Panagiotis P. Galanis, Peijun J. W. He, Ioannis N. Katis, Michael R. Thomas, Yunlei Xianyu, et al.

Panagiotis P. Galanis, Peijun J. W. He, Ioannis N. Katis, Michael R. Thomas, Yunlei Xianyu, Molly M. Stevens, Robert W. Eason, Collin L. Sones, "Laser-direct-writing to enable filtration in paper-based devices," Proc. SPIE 10875, Microfluidics, BioMEMS, and Medical Microsystems XVII, 108750P (4 March 2019); doi: 10.1117/12.2508753

SPIE.

Event: SPIE BiOS, 2019, San Francisco, California, United States

Laser direct-writing to enable filtration in paper-based devices

Panagiotis P. Galanis[a], Peijun J. W. He[a], Ioannis N. Katis[a], Michael R. Thomas[b], Yunlei Xianyu[b], Molly M. Stevens[b], Robert W. Eason[a] and Collin L. Sones[*a]

[a]Optoelectronics Research Centre, University of Southampton, Highfield, Southampton, SO17 1BJ, U.K.; [b]Department of Materials, Department of Bioengineering and Institute of Biomedical Engineering, Imperial College London, London SW7 2BP, U.K. Electronic supplementary information (ESI) available. See DOI: 10.5258/SOTON/D0471.

ABSTRACT

We report the use of a laser-based direct-write (LDW) technique that allows the fabrication of porous barriers, which enable in-line filtration within a paper-based microfluidic device. The barriers were produced within porous substrates, namely nitrocellulose membranes, *via* local deposition of a photo-polymer that was subsequently polymerised by exposure from a laser source. Adjustment of the photo-polymer deposition parameters determines the porosity of the barriers, which, when carefully designed and integrated within a fluidic channel, can act as filters that enable either complete blocking, selective flow or controlled separation of particles of different sizes within a fluid travelling through the channel. We have successfully identified the fabrication parameters for the creation of barriers that allow the filtration of two different types of particles, Au-nanoparticles with sizes of 40, 100 and 200 nm and latex microbeads with sizes of 200 nm and 1 μm, dispersed within an aqueous solution. We also report the use of a variable-porosity barrier for selective separation of latex microbeads from Au-nanoparticles, thereby showing the usefulness of this technique for enabling in-line filtration in such paper-based microfluidic devices.

Keywords: Paper-based devices, Microfluidics, Laser-direct write, Filtration, Porous barriers, Photo-polymerisation.

1. INTRODUCTION

The demand for low-cost diagnostic devices that are user-friendly and deliver results rapidly is a universally accepted goal that has led to extensive development of paper-based microfluidic devices, a concept which was first proposed by the Whitesides' group in 2007 [1, 2]. The use of paper for such microfluidic devices stems from its many inherent advantages such as being biocompatible, chemically modifiable, disposable *via* incineration, and of course its low cost that can lead to mass produced diagnostic devices [3].

Apart from these advantages that are clearly useful for the creation of paper-based microfluidic devices, some important requirements have also been identified, which if addressed, would allow for implementation of paper as a platform for diagnostic devices on a wider scale. Paper has certain limitations that arise from its random, fibrous internal structure, which result in the paper substrate not being uniform in cross-section even across a single sheet, potentially affecting the fluid wicking rate which makes the control of fluid flow difficult. Furthermore, ambient conditions and especially humidity play a critical role with use of paper-based devices as this can also affect the fluid wicking rate [4]. Despite such limitations and drawbacks, over the last decade there has been an extensive research effort directed towards the use of paper for creating microfluidic devices for point-of-care (POC) clinical diagnostics and other testing applications [3]. However, for improved performances and use as standalone in-field tools such simplistic paper-based POC devices need to be enabled with different additional

Microfluidics, BioMEMS, and Medical Microsystems XVII, edited by Bonnie L. Gray, Holger Becker, Proc. of SPIE Vol. 10875, 108750P · © 2019 SPIE · CCC code: 1605-7422/19/$18 · doi: 10.1117/12.2508753

functionalities such as filtration for complex sample processing and analysis [5]. The use of filtration in microfluidic devices has been reported not only for the filtration of micro and nano-scale particles suspended in solution [6, 7], but also for identification and analysis of specific particles [8-10]. The process of filtration is interesting because it allows the segregation and analysis of a complex liquid sample through separation based on particle size. A variety of applications incorporating filtration in their process include membrane chromatography [11], protein digestion [12], liquid-liquid extraction [13] and separation of plasma from red blood cells [14-18]. The latter application is of significant importance for clinical testing that often requires cell-free samples, such as serum or plasma, as cell inclusion and lysis affect reproducibility and can interfere with readouts for colorimetric assays[19].

Several techniques that enable a filtration process within microfluidic devices have been described in the literature including centrifuging [20], on-chip separation according to size using comb-like [21], wire-like [22] or mesh-like filtering [23], and external active methods using forces such as electric or magnetic field interactions and acoustic waves [24-26]. However, all of these methods are performed externally to the device, and add an additional, undesirable sample preparation step.

In this report, we focus on the use of a laser-based technique that enables in-line filtration within a flow-path of a paper-based microfluidic device. To the best of our knowledge, this is the first report of the implementation of an integrated fluid-filtration process within a low-cost paper-based microfluidic device. In our earlier publications, we have reported on the use of our laser direct-write (LDW) technique not only for the creation of fluidic devices in paper [27, 28], but also for enabling control over the flow within such devices by demonstrating a flow-delay mechanism [29]. In this report we present the use of the LDW technique to implement our mechanism of flow-filtration, thereby presenting another pathway for making paper-based devices with newer functionalities.

2. EXPERIMENTAL SECTION

2.1 Experimental setup and materials

The laser used for the LDW patterning procedure was a fibre- coupled 405 nm continuous wave (c.w.) diode-laser (Cobolt MLD, Cobolt AB, Sweden, P/N 00069911871) with a maximum output power of 60 mw and a spot size of 2 mm at a distance of 2.5 cm. The dispenser platform (P/N 7362707) used for the local deposition of the photopolymer onto the various substrates was a PICO® Pμlse™ dispensing system from Nordson EFD, UK. The substrate material used was a UniSart CN 95 nitrocellulose membrane (P/N 500537435) from Sartorius Stedim Biotech GmbH, Germany, and the photopolymer chosen for these experiments was DeSolite® 3471-3-14 from DSM Desotech, Inc., USA. The thickness of the nitrocellulose membrane is 140-170 μm with a pore size of roughly 15 μm and a capillary flow speed of 90-135 s/40 mm. A coloured dye solution and water-based suspensions of Au-nanoparticles and latex microbeads were used to characterise the fluid flow and filtration properties of the laser-patterned devices. The dye solution was made by dissolving Fast Green FCF chemical dye (P/N F7252) from Sigma Aldrich in de-ionised water at a concentration of 0.5 mg/ml. The Au-nanoparticles (P/N (P/N 021195) used for validating the filtration capabilities of the laser-patterned variable-porosity barriers were obtained from BBI Solutions, UK and had sizes of 40, 100 and 200 nm. The latex microbeads (P/N 24287) with sizes of 200 nm and 1 μm were acquired from Polysciences, Inc., USA.

2.2 Methods and Procedure

The fluidic devices were created within porous nitrocellulose substrates via the local deposition of the photo-polymer and its subsequent curing via exposure from the laser irradiation. The photo-polymerised structures that form the walls extend through the thickness of the porous substrate and thereby demarcate the boundaries of a fluidic channel and hence the complete fluidic device. Beyond forming the impermeable boundary walls of the fluidic channels, the same technique was used to pattern the variable-porosity barriers that enabled in-line filtration and were positioned within the fluidic channel at 90 degrees to the direction of fluid flow. The schematic of the LDW setup used to create the devices is shown in Figure 1.

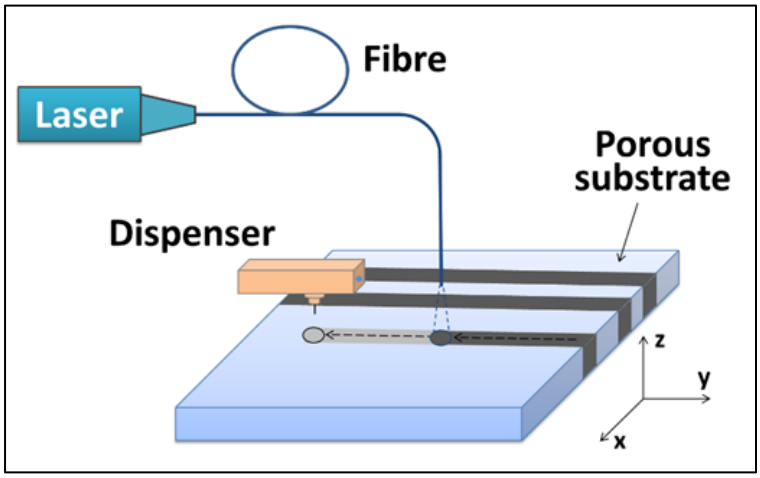

Figure 1. Schematic of the laser-based direct-write setup showing the local deposition of photo-polymer that is illuminated by exposure from a c.w. laser operating at 405 nm. Creating fluidic pathways and in-line filters.

A photo-polymer was first locally deposited onto the paper substrate with a deposition nozzle at locations pre-defined by the device design. A laser beam that follows the deposition head illuminated the entire polymer pattern 30 s after the deposition, and induced photo-polymerisation of all the dispensed polymer. The wait time of 30 s prior to illumination was sufficient for the polymer to spread throughout the thickness of the nitrocellulose membrane. This is evidenced by the fact that (as can be seen in Fig.3-Fig.7) for this wait period the polymer walls of the flow channels have spread to have a width of ~1 mm, which is larger than the thickness of (~180 µm) the nitrocellulose substrate. In addition to the above, the fact that the fluids did no leak out of the channels further confirms that the polymeric wall structures were formed throughout the thickness of the nitrocellulose. The wait time was similar for the barriers too and therefore ensured that they also extended throughout the thickness of the substrate. The use of a different photopolymer with a different viscosity and chemical properties would require adjustment of the time needed for penetration throughout the substrate, however, this can be easily evaluated.

The spatial resolution and the achievable feature size in this approach is defined by the polymer spreading through the porous membrane. This spreading is determined by the viscosity of the polymer and also the pore-size and the porosity of the membrane and all of these therefore influence the minimum producible feature dimension. In addition, the achievable feature dimension is also influenced by the time to exposure after deposition, and critically the incident laser fluence. The minimum feature size i.e. line widths of the polymerised wall structures we have been able to produce is in the range of 200µm.

Using our LDW procedure, we were able to fabricate variable porosity barriers by controlling the local deposition speed of the photo-polymer, which translates into a controllable volume of the photo-polymer that is deposited onto the substrate, and hence a programmable concentration of polymer within a given barrier. Importantly, this

level of control means that it is possible to create polymerised structures that have a variable level of permeability, between completely impermeable – i.e. a wall - or partially permeable – a barrier - to any fluid flow. Following the writing of the walls of the fluidic channel, experiments were performed to identify the range of deposition speeds that create partially permeable barriers that also extend throughout the thickness of the substrate to be used for in-line filtration of a fluid travelling through the channel.

For these less dense, permeable barriers, the polymerised material does not completely fill the pores of the nitrocellulose matrix. Instead, these barriers act as a porous mesh with a pore size smaller than that of the nitrocellulose membrane and therefore act as filters for the fluid passing through it. The porosity of this 3D-mesh can be tailored *via* precise control of the deposition speed. As illustrated schematically in Figure 2, using a barrier with a pre-selected porosity provides a route for creating devices to filter or block particles with sizes above a defined threshold. It can therefore also provide a pathway for selective differentiation/separation between particles of different sizes within a fluid.

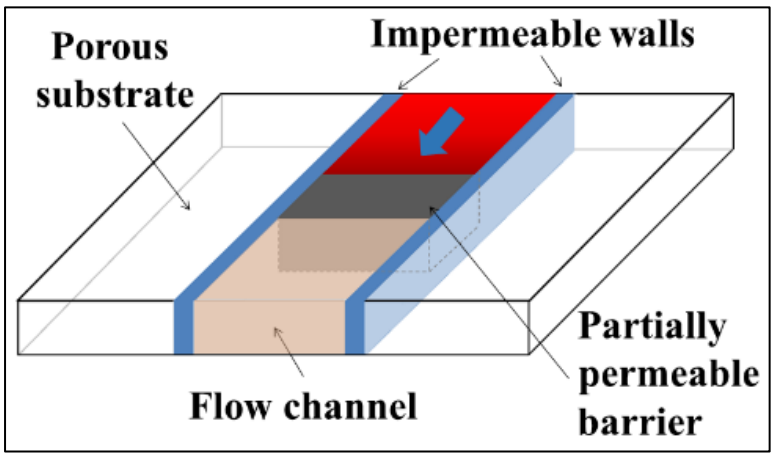

Figure 2. Schematic representation of the cross-section of a fluidic channel with an incorporated variable-porosity barrier within the channel to act as a filter.

3. RESULTS AND DISCUSSION

We have characterised the filtration performance of these porous in-line barriers by wicking through the channel a water-based suspension of either Au-nanoparticles or latex microbeads of differing sizes to highlight the ability of the barriers to discriminate objects by size.

This discrimination was then used to effectively separate a mixture of Au-nanoparticles and latex microbeads of different sizes. We initially aimed to establish the parameters for creating porous barriers using colloids typically employed in lateral-flow assays: Au-nanoparticles and latex microbeads. Their extensive use in microfluidics-based lateral flow diagnostic devices originates from strong absorbance of light when used as coloured-labels that tag detection-antibodies to the test-lines of a lateral flow device. Since both the fluidic channel walls and filtering barriers can be patterned using the same LDW process, this technique should have immediate appeal to manufacturers wishing to develop such paper-based devices on a large scale where roll-to-roll production can be envisaged and where production speed and cost are two of the main considerations.

Laser-patterned fluidic devices were prepared with a simple straight-flow channel geometry as shown in Figure 3, using an optimised LDW process as previously described [30, 31]. The performance of porous polymer barrier for liquid-based size exclusion was explored as a function of the size of coloured suspensions of dyes or nanoparticles.

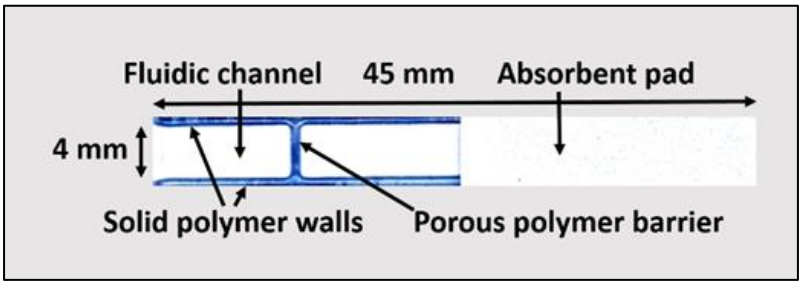

Figure 3. Image showing an example device that we used to study the filtering capabilities of a laser-patterned barrier.

The width and length of the fluidic channel was set to 4 mm and 25 mm respectively. The channel walls were defined *via* local deposition of the photo-polymer at a line-speed of 20 mm/s, followed by laser curing at a scan-speed of 27 mm/s. We then patterned the variable-porosity barriers across the channel using the same procedure but with a higher photo-polymer deposition speed that ranged from 30 mm/s to 60 mm/s.

Above a certain threshold deposition speed, the structures that were created were always found to be porous. It is important to note that the distance between the fibre tip and the substrate (2.5 cm), the laser scanning speed and the laser power were unaltered for all of the device fabrication work. Any change in the values of these parameters leads to an alteration of the incident laser-fluence that governs the photo-polymerisation process and consequently a variation in the porosity of the barriers. In all cases however, the incident laser-fluence was always sufficient to polymerise all of the deposited photo-polymer.

3.1 Characteristic study of barriers in nitrocellulose membrane

Prior to characterising the filtration properties of the barriers with solutions consisting of particles of predetermined sizes, it was important to investigate the exact deposition condition that would allow the barrier to change from being completely impermeable to partially permeable. We therefore fabricated a set of identical devices each of which had a single barrier created at a different deposition speed, and then introduced a coloured dye at their inlet (Figure 4, bottom-end in the images). The coloured dye provided an aid that not only helped visualise the progression of the aqueous solvent along the channel but also allowed to identify whether a barrier was porous or not.

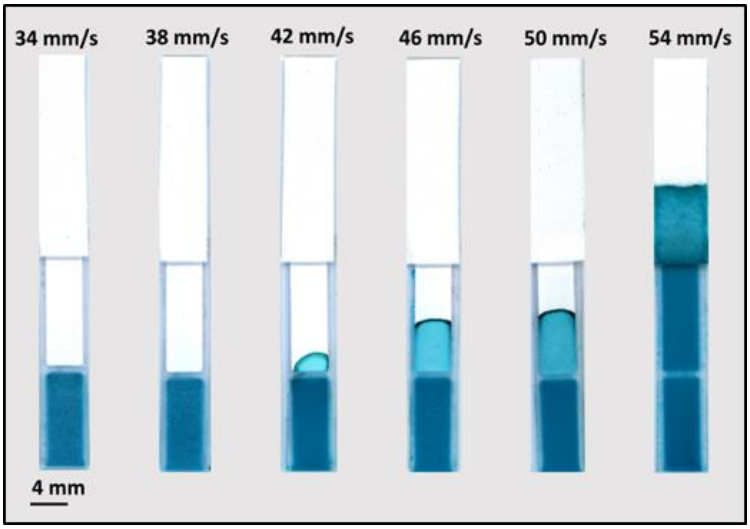

Figure 4. Images showing the flow of a green dye solution through a channel with barriers created with deposition speeds of 34, 38, 42, 46, 50 and 54 mm/s respectively.

In the subsequent section, Au-nanoparticles and latex microbeads, with minimal variations in their sizes were used as a means to characterise the porosity of the barriers. The variation in size was defined by the maximum value of the coefficient of variance which is defined as the ratio of the standard deviation over the diameter of the particle, multiplied by 100 (8% for the Au-nanoparticles, 5% for latex microbeads of size 200 nm and 3% for latex microbeads of size 1000 nm).

As seen in Figure 4, the barriers, written at speeds of 38 mm/s and less were impermeable, however, for a writing speed of 42 mm/s and greater, they were porous and allowed the green dye to pass through them. The time taken for the coloured dye to reach the top end of the device is determined by the porosity of the barriers. Alternatively, this can also provide a mechanism to introduce a delay in the flow of liquids.

3.2 Filtering of Au-nanoparticles with different sizes

Once the threshold deposition speed that allows for the creation of partially permeable barriers was defined, we then used this as a starting-point for exploring the deposition conditions that would produce barriers that block Au-nanoparticles of a specific size namely 40, 100 and 200 nm. In each case, the bottom end of the devices was dipped in 20 µL Au-nanoparticle suspension for 15 minutes. The stock concentrations of the Au-nanoparticles in the suspension were 9×10^{10} particles/ml for 40 nm Au-nanoparticles, 5.6×10^{9} particles/ml for 100 nm Au-nanoparticles and 7×10^{8} particles/ml for 200 nm Au-nanoparticles. The images in Figure 5 show representative examples of tests performed with the 40 nm Au-nanoparticle suspensions. As shown in Table 1, the 40 nm Au-nanoparticles were able to pass through barriers created with deposition speeds that were at least 36 mm/s, and below this speed, the nanoparticles concentrated at the lower side of the barrier. For barriers produced with speeds at or greater than 36 mm/s, the particles flowed through and accumulated towards the top end of the device. For a comparative analysis of the collected data, we have chosen to define a 'threshold' speed that permits the flow-through of a particle of a specific size. Table 1 shows our results for all of the differently sized Au-particles and were obtained from five repeated measurements where the images in Figure 5 are representative of a threshold speed below which these solutions did not flow through.

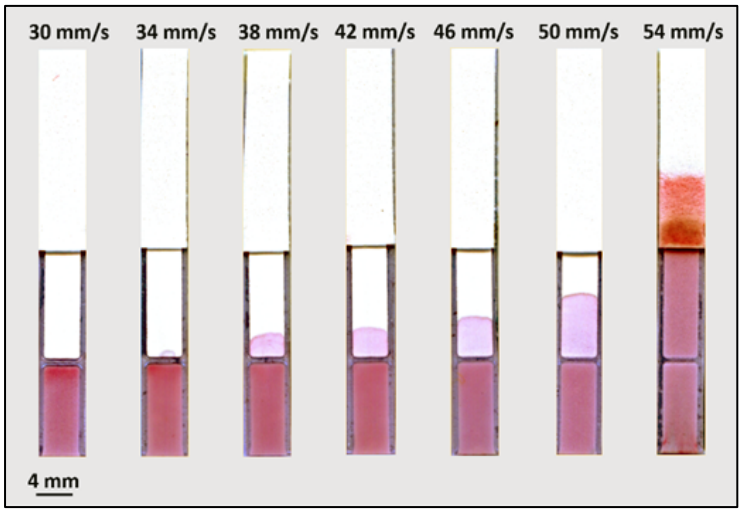

Figure 5. Images showing the flow of the 40 nm Au-nanoparticles through identical devices each of which had a single barrier that was fabricated with a different deposition speed that ranged from 30-54 mm/s respectively.

There is a deposition speed range (~ few mm/s, and marked with a red box in Table 1 and similary in Table 3) for which the barriers transition from being impermeable to being partially and then consistently permeable. This transitional range could be the result of either of the following: minor variability in the nitrocellulose pore size in different regions of nitrocellulose membranes and between batches, variation in the composition of the membrane (surfactant coverage for example) or humidity influencing the penetration and wetting of the photopolymer, or the variability in the photopolymer deposition. Taking this transitional range into account, we defined the threshold as the deposition speed at which more than 60% of the devices have permeable barriers. Despite the overlapping transitional ranges between 40 nm and 100 nm Au-nanoparticles, we observe that the deposition speed threshold increases with particle size (Table 2), with the latex microbeads following the same trend (Table 3). This effect is understood to occur because faster deposition speeds result in less deposited photopolymer volume per unit of length, consequently creating a permeable barrier with larger unfilled voids.

We envisage the use of the porous barriers as in-line filters within a lateral flow device and therefore our device design and its operation was configured to mimic that of a lateral flowdevice. Hence, the devices seen in Figures 3-6, have an absorbent pad at the end.

Made of cellulose paper, the abosrbent pad also serves as a drain-pump for the fluidic sample passing along a lateral flow device. On completion of the test, the residual fluid accumulates in this absorbent pad, and as seen in the last device of Figure 5 and in last two in Figure 6, the Au-nanoparticles have collected there and changed the colour of the absorbent pad from white to red. The pore-size, the porosity of the porous nitrocellulose and its uniformity are all critical parameters influencing the threshold as they determine the way the photopolymer wicks and creates the barrier. Also, the nature of the porous material is important where the wicking of the polymer will be affected by the internal structure. Our choice of the nitrocellulose membrane and its type (CN95) was because of its wide use in the construction of lateral flow devices such as those constructed herein. Such nitrocellulose membranes exhibit porous sponge-like structures whereas materials such as cellulose paper exhibit more fibrous internal structures and this structure would require different deposition times. Both the porous substrate characteristics/nature and the structure are expected to be important factors influencing the threshold deposition line-speed either to higher or lower values. Also, if there is a variation in the porous material from batch to batch this would indeed also be reflected in the threshold values.

Table 1. Number of devices in which Au-nanoparticles passed through the barrier written at different line-speeds.

Line-speed (mm/s)	40 nm	100 nm	200 nm
30	0/5	0/5	0/5
32	0/5	0/5	0/5
34	3/5	2/5	0/5
36	5/5	5/5	0/5
38	5/5	5/5	2/5
40	5/5	5/5	0/5
42	5/5	5/5	5/5
44	5/5	5/5	5/5
46	5/5	5/5	5/5
48	5/5	5/5	5/5
50	5/5	5/5	5/5
52	5/5	5/5	5/5
54	5/5	5/5	5/5
56	5/5	5/5	5/5
60	5/5	5/5	5/5

Table 2. Threshold deposition speeds for creating barriers that block each of the different Au-nanoparticle sizes.

Au-Nanoparticle size (nm)	Flow-through threshold speed (mm/s)
40	34
100	36
200	42

3.3 Filtering of latex microbeads with different sizes

To further test the capabilities of the variable-porosity barriers for larger colloids, we tested 200 and 1000 nm latex microbeads. The images in Figure 6 show the results for suspensions of latex microbeads of size 1000 nm. The bottom ends of the devices were dipped for 15 minutes in 20 µL of an aqueous latex bead suspension with particle concentration of 5.68×10^{11} and 4.55×10^{9} particles/ml for the 200 nm and 1000 nm particles, respectively. As can be clearly seen in the images, for speeds below a threshold of 52 mm/s, the barrier was impermeable to the 1000 nm latex microbeads. Table 3 shows the results for the devices tested for each of the different barrier line-speeds for the two different latex microbeads sizes, and Table 4 shows the threshold speed values for the same.

The thresholds for 200 nm latex microbeads and similarly sized, 200 nm Au-nanoparticles should be identical for size-dependent barriers such as those used in our experiments. However, we believe this difference in the thresholds could be as a result of the nature i.e. surface properties of the particles and more specifically their flow properties.

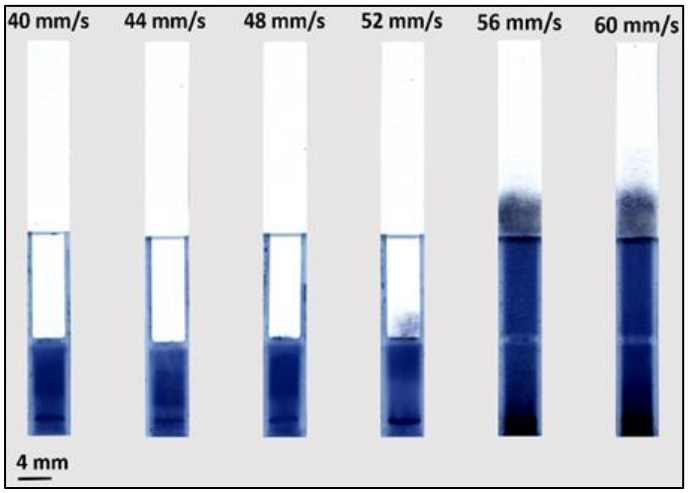

Figure 6. Images showing the flow of the 1000 nm latex microbeads through identical devices each of which had a single barrier that was fabricated with a different deposition speed that ranges from 40-60 mm/s.

Table 3. Number of devices in which latex microbeads passed through the barrier written at different line-speeds.

Line-speed (mm/s)	200 nm	1000 nm
30	0/5	0/5
32	0/5	0/5
34	0/5	0/5
36	0/5	0/5
38	0/5	0/5
40	0/5	0/5
42	0/5	0/5
44	0/5	0/5
46	0/5	0/5
48	3/5	0/5
50	5/5	0/5
52	5/5	5/5
54	5/5	5/5
56	5/5	5/5
60	5/5	5/5

Table 4. Threshold deposition speeds for creating barriers that block each of the different latex microbead sizes.

Latex bead size (nm)	Flow-through threshold speed (mm/s)
200	48
1000	52

3.4 Simultaneous filtering of different sized particles in the same flow channel

Lastly, to explore the possibility of using such porous barriers for a selective differentiation between two differently sized particles, we tested a device that can allow for separation of 40 nm Au- nanoparticles from 1 μm latex microbeads. We used an aqueous dispersion of 40 nm Au-nanoparticles (9×10^{10} particles/ml) and 1 μm (9.1×10^{8} particles/ml) latex microbeads. We fabricated a device with a deposition speed of 46 mm/s to create a barrier that would block the latex microbeads but be permeable to the Au-nanoparticles. Figure 7 shows a device for which the barrier was fabricated with a deposition speed of 46 mm/s, a speed that we know would serve to block the latex microbeads, but would allow the Au-nanoparticles to travel through. As shown in Figure 7, the Au-nanoparticles transit through the barrier while the latex microbeads are unable to flow through and accumulate in the channel just before the barrier.

Such a method of producing porous barriers for filtration could be exploited in a number of ways. One example could be to develop systems composed of successive barriers with decreasing sized pores to facilitate the separation of complex samples where there is a sizeable fraction of larger structures such as red blood cells.

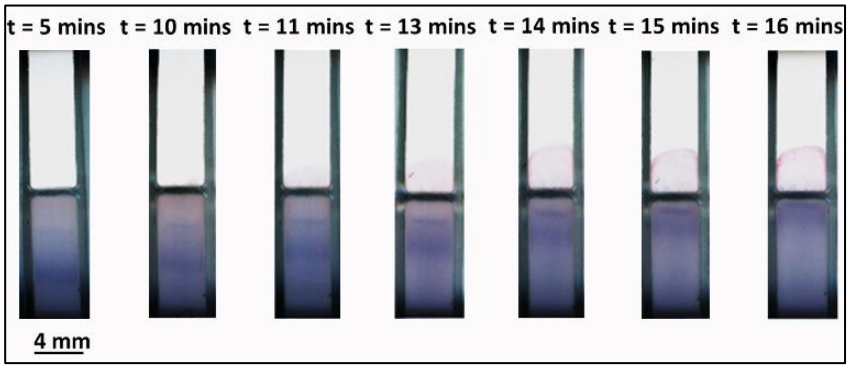

Figure 7. Images showing the result of filtering 1 μm latex beads from 40 nm Au-nanoparticles at different times.

4. CONCLUSIONS

To our knowledge, this is the first example of a relatively simple approach that allows in-line filtration of various constituents of a liquid analyte, and should enable scalable paper-based lateral flow device manufacture with more advanced device performance. We believe that for such devices this in-line filtration functionality provides a promising potential route to avoid or minimise sample-preparation, which is currently a critical impediment to the use of such low-cost devices at the point-of-care by unskilled patients.

ACKNOWLEDGEMENTS

The authors acknowledge the funding received *via* the Engineering and Physical Sciences Research Council (EPSRC) *via* Grant Nos. EP/N004388/1, EP/M027260/1, EP/N00468X/1 and EP/P025757/1, and the funding received *via* a Knowledge Mobilisation Fellowship for Dr. Collin Sones from the Institute for Life Sciences and the Faculty of Health Sciences of the University of Southampton. The underpinning RDM data for this paper can be found at 10.5258/SOTON/D0471.

REFERENCES

[1] Martinez, A. W., Phillips, S. T., Butte, M. J. and Whitesides, G. M., "Patterned paper as a platform for inexpensive, low-volume, portable bioassays", Angew. Chem.-Int. Edit., 46(8), 1318-1320 (2007).

[2] Martinez, A. W., Phillips, S. T. and Whitesides, G. M., "Three-dimensional microfluidic devices fabricated in layered paper and tape", Proc. Natl. Acad. Sci. U. S. A., 105(50), 19606-19611 (2008).

[3] Yang, Y., Noviana, E., Nguyen, M. P., Geiss, B. J., Dandy, D. S. and Henry, C. S., "Paper-Based Microfluidic Devices: Emerging Themes and Applications", Anal. Chem., 89(1), 71-91 (2016).

[4] Martinez, A. W., "Microfluidic paper-based analytical devices: from POCKET to paper-based ELISA", Bioanalysis, 3(23), 2589-2592 (2011).

[5] Tang, R. H., Yang, H., Choi, J. R., Gong, Y., Feng, S. S., Pingguan-Murphy, B., Huang, Q. S., Shi, J. L., Mei, Q. B. and Xu, F., "Advances in paper-based sample pretreatment for point-of-care testing", Critical reviews in biotechnology, 37(4), 411-428 (2017).

[6] Solomon, B., Castino, F., Lysaght, M., Colton, C. and Friedman, L., "CONTINUOUS FLOW MEMBRANE FILTRATION OF PLASMA FROM WHOLE BLOOD", ASAIO Journal, 24(1), 21-26(1978).

[7] Crowley, T. A. and Pizziconi, V., "Isolation of plasma from whole blood using planar microfilters for lab-on-a-chip applications", Lab Chip, 5(9), 922-929 (2005).

[8] Desitter, I., Guerrouahen, B. S., Benali-Furet, N., Wechsler, J., Jänne, P. A., Kuang, Y., Yanagita, M., Wang, L., Berkowitz, J. A. and Distel, R. J., "A new device for rapid isolation by size and characterization of rare circulating tumor cells", Anticancer research, 31(2), 427-441 (2011).

[9] Hayes, D. F., Cristofanilli, M., Budd, G. T., Ellis, M. J., Stopeck, A., Miller, M. C., Matera, J., Allard, W. J., Doyle, G. V. and Terstappen, L. W., "Circulating tumor cells at each follow-up time point during therapy of metastatic breast cancer patients predict progression-free and overall survival", Clinical Cancer Research, 12(14), 4218-4224 (2006).

[10] Hua, M., Zhang, S., Pan, B., Zhang, W., Lv, L. and Zhang, Q., "Heavy metal removal from water/wastewater by nanosized metal oxides: A review", Journal of Hazardous Materials 211, 317-331 (2012).

[11] Jiang, Y. and Lee, C. S., "On-line coupling of micro-enzyme reactor with micro-membrane chromatography for protein digestion, peptide separation, and protein identification using electrospray ionization mass spectrometry", Journal of Chromatography *A*, 924(1-2), 315-322 (2001).

[12] Gao, J., Xu, J., Locascio, L. E. and Lee, C. S., "Integrated Microfluidic System Enabling Protein Digestion, Peptide Separation, and Protein Identification", Anal. Chem., 73(11), 2648-2655 (2001).

[13] Cai, Z.-X., Fang, Q., Chen, H.-W. and Fang, Z.-L., "A microfluidic chip based liquid-liquid extraction system with microporous membrane", Anal. Chim. Acta, 556(1), 151-156 (2006).

[14] Ge, L., Wang, S., Song, X., Ge, S. and Yu, J., "3D origami-based multifunction-integrated immunodevice: low-cost and multiplexed sandwich chemiluminescence immunoassay on microfluidic paper-based analytical device", Lab Chip, 12(17), 3150-3158 (2012).

[15] Nilghaz, A. and Shen, W., "Low-cost blood plasma separation method using salt functionalized paper", Rsc Advance*s*, 5(66), 53172-53179 (2015).

[16] Songjaroen, T., Dungchai, W., Chailapakul, O., Henry, C. S. and Laiwattanapaisal, W., "Blood separation on microfluidic paper-based analytical devices", Lab Chip, 12(18), 3392-3398 (2012).

[17] Khan, M. S., Thouas, G., Shen, W., Whyte, G. and Garnier, G., "Paper diagnostic for instantaneous blood typing", Anal. Chem., 82(10), 4158-4164 (2010).

[18] Yang, X., Forouzan, O., Brown, T. P. and Shevkoplyas, S. S., "Integrated separation of blood plasma from whole blood for microfluidic paper-based analytical devices", Lab Chip, 12(2), 274-280 (2012).

[19] Thorslund, S., Klett, O., Nikolajeff, F., Markides, K. and Bergquist, J., "A hybrid poly(dimethylsiloxane) microsystem for on-chip whole blood filtration optimized for steroid screening", Biomedical microdevices, 8(1), 73-79 (2006).

[20] Hardwick, J., "Blood processing", ISBT Science Series 3, 148-176 (2008).

[21] Andersson, H., van der Wijngaart, W., Enoksson, P. and Stemme, G., "Micromachined flow-through filter-chamber for chemical reactions on beads", Sensors and Actuators B: Chemical, 67(1-2), 203-208 (2000).

[22] Broyles, B. S., Jacobson, S. C. and Ramsey, J. M., "Sample Filtration, Concentration, and Separation Integrated on Microfluidic Devices", Anal. Chem., 75(11), 2761-2767 (2003).

[23] Moorthy, J. and Beebe, D. J., "In situ fabricated porous filters for microsystems", Lab Chip, 3(2), 62-66 (2003).
[24] Choi, S. and Kyun-Park, J., "Microfluidic system for dielectrophoretic separation based on a trapezoidal electrode array", Lab Chip, 5(10), 1161-1167 (2005).
[25] Fong, E. J., Johnston, A. C., Notton, T., Jung, S.-Y., Rose, K. A., Weinberger, L. S. and Shusteff, M., "Acoustic focusing with engineered node locations for high-performance microfluidic particle separation", Analyst, 139(5), 1192-1200 (2014).
[26] Pamme, N., Eijkel, J. C. and Manz, A., "On-chip free-flow magnetophoresis: Separation and detection of mixtures of magnetic particles in continuous flow", Journal of Magnetism and Magnetic Materials, 307(2), 237-244 (2006).
[27] Sones, C. L., Katis, I. N., He, P. J. W., Mills, B., Namiq, M. F., Shardlow, P., Ibsen, M. and Eason, R. W., "Laser-induced photo-polymerisation for creation of paper-based fluidic devices", Lab Chip, 14(23), 4567-4574 (2014).
[28] He, P. J., Katis, I. N., Eason, R. W. and Sones, C. L., "Laser-based patterning for fluidic devices in nitrocellulose", Biomicrofluidics, 9(2), 026503-026510 (2015).
[29] He, P. J. W., Katis, I. N., Eason, R. W. and Sones, C. L., "Engineering fluidic delays in paper-based devices using laser direct-writing", Lab Chip, 15(20), 4054-4061 (2015).
[30] Sones, C. L. and Eason, R. W., *US Patent App. 15/572,190*, 2018.
[31] Katis, I. N., He, P. J., Eason, R. W. and Sones, C. L., "Improved sensitivity and limit-of-detection of lateral flow devices using spatial constrictions of the flow-path", Biosensors and Bioelectronics 113, 95-100 (2018).

Sensors & Actuators: B. Chemical 322 (2020) 128574

Contents lists available at ScienceDirect

Sensors and Actuators B: Chemical

journal homepage: www.elsevier.com/locate/snb

Local photo-polymer deposition-assisted fabrication of multilayer paper-based devices

P.P. Galanis*, P.J.W. He, I.N. Katis, A.H. Iles, A.J.U. Kumar, R.W. Eason, C.L. Sones

Optoelectronics Research Centre, University of Southampton, Highfield, Southampton, SO17 1BJ, UK

ARTICLE INFO

Keywords:
3D Multilayer device
Multiplexed detection
Photo-polymer
Laser patterning method
Diagnostics
Paper-based device

ABSTRACT

In this paper, we report on the use of a local acrylate-based negative photo-polymer deposition technique for the fabrication of 3D microfluidic paper-based analytical devices (3D-μPADs) where the sample flows in both the lateral and vertical directions through multiple stacked layers of porous materials. A simple and inexpensive manufacturing method was used, which is based on the local deposition of a photo-polymer (deposition speed 30 mm/s) on a porous cellulose paper substrate followed by the subsequent exposure (scanning speed 30 mm/s) to a laser source (fibre coupled continuous wave at 405 nm with maximum power of 60 mW), to stack four layers of cellulose paper and make 3D multilayer μPADs. With this technique, we provide a pathway to eliminate the limitations that other reported methods have during the fabrication of μPADs such as the need for multiple sophisticated alignments between adjoining layers and the use of additional tools to ensure adequate contact between the layers. In this study, we demonstrate the usefulness of our four-layer 3D-μPAD for simultaneous detection of three analytes, namely BSA, glucose, nitrite spiked in artificial urine and also the pH of the tested sample, through single step colorimetric assays with the limit of detection found at 0.4 mg/mL for BSA, 14.5 μg/mL for glucose and 2.5 μg/mL for nitrite. Our 3D-μPAD fabrication methodology can also be adapted in more complex analytical assays where multiple steps are needed for applications in point-of-care diagnostics.

1. Introduction

Public health is of universal importance and to that end, there is a constant research effort to create novel diagnostic tools world-wide [1,2]. According to the World Health Organization, a diagnostic sensor designed for use at the point-of-care in under resourced settings has to be affordable, sensitive, specific, user-friendly, rapid and robust, equipment-free and deliverable to those who need it [3]. Among the different substrates, such as silicon, polymer or glass, which have been used to manufacture diagnostic devices, paper is a promising alternative due to its inherent characteristics. Paper is a cost-effective material composed of a network of hydrophilic cellulose fibres and has a porous structure that allows the passive transport of liquids via capillary action [4]. Furthermore, paper is lightweight, can be found in different forms and properties, and is biocompatible and disposable via incineration [5]. The concept of paper-based analytical devices (μPADs) was first proposed from the Whiteside's group back in 2007 and has been developed for a range of analytical assays such as the detection of proteins [6], heavy metals [7,8], pesticides [9] and food-borne pathogens [10]. Such devices have the capability to obtain, control and process small volumes of complex fluids with efficiency and speed and the miniaturization of the device further reduces the detection times and the volumes of the reagents that are used [11].

In the last few years, a variety of methods to develop 2D-μPADs have been widely reported. Some of these include laser treatment [12], photolithography [13], wax printing [14] and inkjet printing [15] and have been shown to be used for various applications such as detection of biomarkers i.e. lactate, glutamate, uric acid and nitrite using different colour indicators in each case. Compared with 2D-μPADs, three-dimensional (3D) μPADs have also been widely studied due to some unique advantages they offer for certain applications, e.g. multiplexed assay and assays involve multiple steps. Firstly, in 2D-μPADs, the spatial distribution of samples is limited when compared with 3D-μPADs where the flow and delivery of fluids is enabled in all three dimensions. As a result, for 3D-μPADs the device footprint is reduced and also additional fluidic channels can be incorporated for enabling multiplexed testing of a large number of analytes with the same device footprint of a 2D device [16]. All of this leads to a reduced detection time and a reduced sample volume [17]. Despite the progress in the development of fluid flow control using different methods for more efficient performance of μPADs [18], it has been reported that 3D-μPADs exhibit better analytical performance when compared to lateral flow devices with sample

* Corresponding author.
E-mail address: pg1n15@soton.ac.uk (P.P. Galanis).

https://doi.org/10.1016/j.snb.2020.128574
Received 3 March 2020; Received in revised form 7 July 2020; Accepted 8 July 2020
Available online 11 July 2020

flow limited in one direction [19]. In the case of 3D-μPADs, reagents can be stored within the middle layers of the device and furthermore as fluids transport within these layers the evaporation is minimized [20]. Additionally, using 3D-μPADs we can overcome the limitation of only being able to implement single step assays, as one can perform complex assays where mixing of different compounds is needed (e.g. ELISA) [21]. Furthermore, 3D-μPADs can eliminate any contamination of the sample as it can be largely transported within the in-between paper layers by creating appropriate fluidic pathways. Finally, it also helps prevent any cross-contamination between multiple samples thus enabling simultaneous testing of different assays independently within the same device.

3D-μPADs have therefore gained much attention of the research community in the last few years and many groups are working towards the development of these platforms. Reported fabrication methods include the development of 3D origami devices, which involve folding of the paper [22,23] and the use of a stack of pre-patterned papers [24]. The origami-based methods, while ingenious, require sequential steps for assembly and alignment of the layers of paper, which might be difficult or incorrectly performed by untrained individuals. The most important requirement during the fabrication of 3D-μPADs is the need for sufficient contact between the multiple layers of the device. In order to assemble the pre-patterned paper layers and create a 3D-μPAD, a double-sided tape [25] or spray adhesive [26] is often used. Additional processes to ensure contact between the layers include the use of clamps [22,27] or even holding the device between the thumb and index fingers [28]. An alternative method reports the formation of 3D structures directly on the paper layer, a method that sorts out any contact issues but lacks simplicity as it requires double-sided wax printing and an extra aligning step during the fabrication process [29]. As described, each of these aforementioned techniques require external/additional equipment (e.g. clamps, tapes) and further fabrication steps, two factors that increase the complexity of the design. Additionally, the method of stacking the individual pre-patterned layers of paper requires an extra aligning step, which is a critical parameter for the performance of the final device.

In our previous reported method we used a laser direct writing technique to create 3D-μPADs [30]. That method not only involved additional fabrication steps such as polymer soaking and solvent-based developing of the paper device but was also limited in terms of the maximum number of layers which can be bonded together. In contrast, this paper reports the use of a simpler and faster fabrication technique, which enables the stacking of several layers of porous materials to create 3D-μPADs and exceeds the maximum number of the three layers that our previous method had.

We then demonstrate the use of this technique to produce a 3D-μPAD for implementation of single step colorimetric assays for the detection of three analytes, namely BSA, glucose and nitrite and the pH of the tested artificial urine sample. The choice of the model analytes was made because of the following - these analytes are commonly used in diagnostics (e.g. urine reagent strip testing) for monitoring or screening for kidney function, acid-base balance and urinary tract functions. BSA is the model protein for human albumin in urine and is studied extensively because it has similar composition [31] (e.g. molecular weight ~66 kDa) to the human protein. Elevated levels of albumin in urine corresponds to very low levels in blood and this is an indication of kidney damage (hypoalbuminemia). Elevated levels of glucose in urine is also an indication of underlying health conditions. In the case of people having diabetes [32] they can develop chronic complications such as kidney problems, which can lead to the excretion of glucose into the urine (glycosuria). Apart from the measurement of albumin and glucose levels in urine, the measurement of nitrite is equally important and very common in urinalysis. The presence of nitrites in urine can be an indication of bacterial infection (most commonly Escherichia coli) in the urinary tract [33], which if left untreated can lead to kidney failure or even sepsis. Finally yet importantly, pH measures how acidic or alkaline a person's urine is. Abnormal levels are associated with medical conditions such as kidney stones or urinary tract infections.

2. Experimental section

2.1. Experimental setup and materials

The laser used for the polymerization of the photo-polymer was a fibre-coupled continuous wave (c.w.) diode laser (Cobolt MLD, Cobolt AB Sweden) operating at 405 nm with a maximum output power of 60 mW. As previously mentioned, the photo-polymer is locally deposited onto the paper substrate using a PICO® Pμlse™ dispenser platform from Nordson EFD, UK, which deposits micro-droplets through a tip with diameter 100 μm with volumes as small as 0.5 nL at a frequency at 100 Hz. The porous paper used to make the multilayer 3D-μPADs is Whatman™ grade 1 qualitative filter paper (cellulose) with nominal thickness 180 μm and pore size 11 μm from GE Healthcare. The substrate where the reagents for the assay are pre-deposited is glass fiber with 355 μm in thickness from GE Healthcare. The acrylate-based negative photo-polymer that we used in the device fabrication work was DeSolite® 3471 − 3-14 from DSM Desotech, Inc., USA. The performance of our paper-based 3D-μPADs was tested with single step colorimetric assays for the detection of BSA, glucose, nitrite and pH. For the BSA assay the reagents used were 49.2 mg/mL citrate buffer at 1.8 pH and 2.2 mg/mL tetrabromophenol blue (TBPB) in 95 % ethanol solution (Sigma-Aldrich, 199311). The BSA protein (Sigma-Aldrich, A3059) which was used as the analyte for the BSA assay was prepared at a concentration of 50 mg/mL. The reagents used for the glucose assay were glucose oxidase/peroxidase solution (Sigma-Aldrich, G3660) in 5:1 ratio and 15 units of protein per ml in deionized water and o-Dianisidine dihydrochloride (Sigma-Aldrich, D2679) with a concentration of 5 mg/mL in deionized water. D-(+)-glucose solution was used as the analyte for the glucose assay with a concentration of 1 mg/mL in 0.1 % benzoic acid (Sigma-Aldrich, G3285). For the detection of nitrite, we prepared Griess reagent by dissolving in deionized water 8.63 mg/mL sulfanilamide (Sigma-Aldrich, S9251), 63.3 mg/mL citric acid (Sigma-Aldrich, 251275) and 2.56 mg/ml of N-(1-naphthyl) ethylenediamine dihydrochloride (Sigma-Aldrich, 222488). We prepared sodium nitrite (Sigma-Aldrich, 237213) at a concentration of 0.68 mg/mL as the analyte for testing of this assay. Finally, for the pH testing we used bromothymol blue (Sigma-Aldrich, 114413) as an indicator and a red chemical dye (Allura Red AC, Sigma Aldrich) diluted in deionized water at a concentration of 0.5 mg/mL, to visualize the progression of the sample throughout the layers of the multilayer devices.

2.2. Methods and procedure

Our patterning method used in creating polymeric structures within the porous paper substrates and for the creation of the 3D-μPADs is based on the local deposition of an acrylate-based negative photo-polymer at locations pre-defined by the device design. The schematic in Fig. 1 illustrates the setup used for the manufacture of our 3D-μPADs.

First, a dispensing system delivers the photo-polymer on top of a porous substrate at locations user-defined by a computer. Next, a laser source (spot size ~5 mm and fluence 40 mJ/cm^2) controlled by the same design program follows the same pattern and, illuminates the polymer inducing photo-polymerization leading to the creation of solid polymeric structures extending throughout the thickness of the substrate. A delay of 3 min between the deposition and photo-polymerisation steps was introduced to ensure that the photo-polymer had penetrated throughout the thickness of the paper (~ 180 μm). After this time delay, the photo-polymer had spread laterally to a width of ~2 mm, which defined the minimum width of the polymeric line that we can create with our patterning method for this specific substrate. The time required to make a single 3D-μPAD depends on the time required (3 min) for the photo-polymer to penetrate throughout a paper

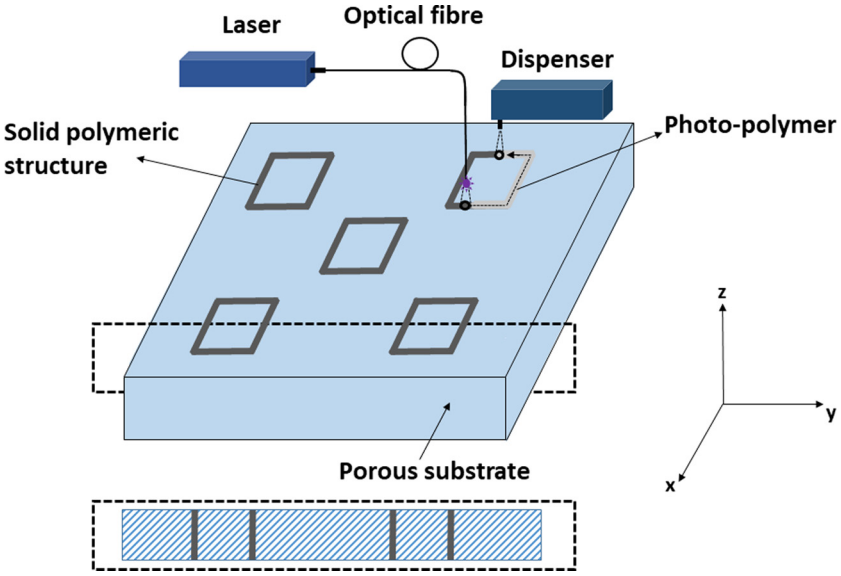

Fig. 1. Schematic of the local photo-polymer deposition setup. The photo-polymer is locally deposited on top of a porous substrate and subsequently exposed to a c.w. laser source operating at 405 nm to create solid polymeric structures. In the dashed line box, we represent a cross-sectional image of the porous substrate in which the polymerized photo-polymer has extended throughout its thickness.

substrate. However, one of the advantages of the local photo-polymer deposition method is that we could fabricate six 3D-μPADs in a single cellulose paper A4 sheet within a period of 3 min. Considering that it required 12 min to pattern and stack the six, four-layer devices, we deduced that the time required to make a single four-layer 3D-μPAD does not exceed 2 min.

The photo-polymerization process is affected by the scanning speed of the laser and therefore the laser fluence. The fabrication conditions of the photo-polymer deposition speed, the laser scanning speed and the time delay between these two steps that we have used for the device processing are sufficient to fully polymerize the photo-polymer and create solid polymeric walls that define the boundaries of the flow paths within our devices. Any residual un-polymerized material that remains within these walls would result in sideways leakage of the fluids through them, and this is not the case as we see in either of the Figs. 4–6. Use of these fabrication conditions lead to the formation of fully solidified walls required to guide the flow of liquids without any leakage that would be detrimental to the performance of the device.

This patterning method was also used to stack several layers of the same (grade 1) porous material and create our multilayer 3D-μPADs. Fig. 2 depicts the various steps involved in the fabrication of a two-layer 3D-μPAD. First, a photo-polymer pattern as required by the device geometry is locally deposited on top of a porous substrate. The photo-polymer is allowed to spread throughout its thickness (step 1) before exposure to the laser source (step 2). Next, the photo-polymer is deposited again (step 3) over the same pattern and a second paper substrate is placed (step 4) over the top. In order to facilitate complete contact between the two adjacent layers and therefore ensure proper flow of the sample between the layers, a contact pad of the same cellulose material is added between the two paper layers only at the intersection points where the sample flows happens, from one layer into the other. The photo-polymer pattern is added again on top of the second layer (step 5), followed by exposure from the laser source to assist with the bonding of the two layers (step 6). This paper patterning technique can easily be extended to stack several layers of porous materials and create a multilayer device where the fluids are able to

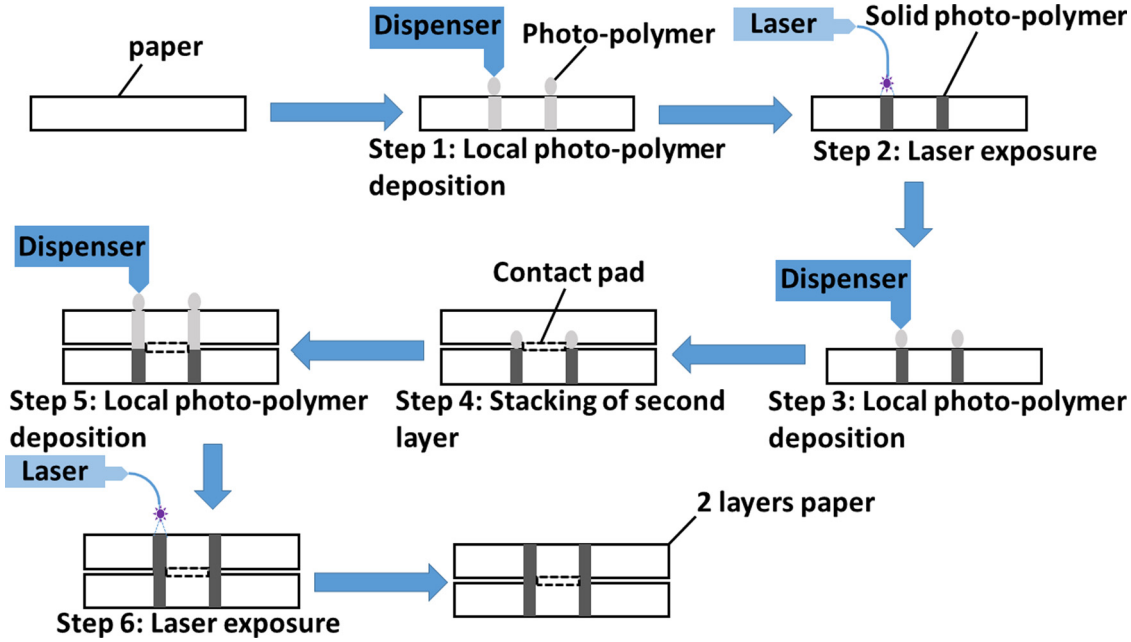

Fig. 2. Schematic of the fabrication process that is used to stack two layers of paper.

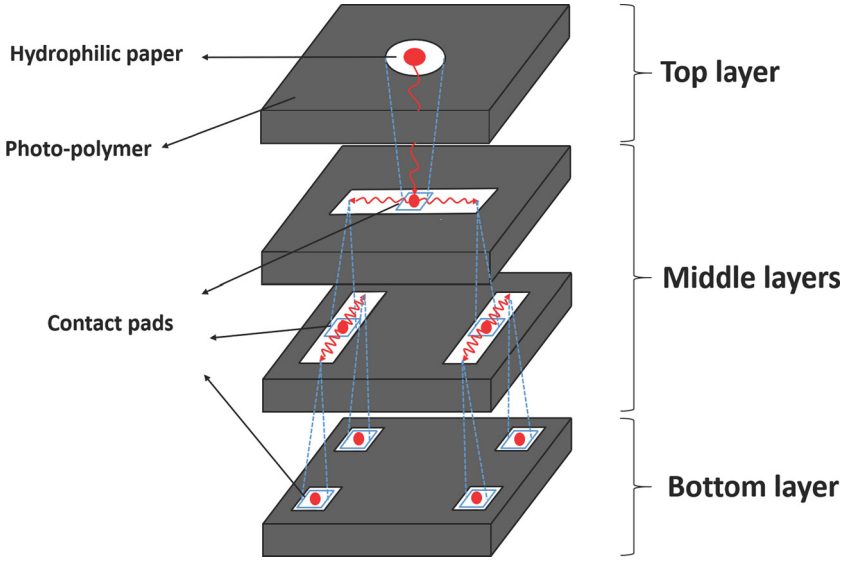

Fig. 3. Schematic of the 3D device used to make the single step colorimetric assays.

flow within the multiple layers of the user-designed device.

In order to create 3D-μPADs where the samples travel in lateral and vertical directions and through multiple, stacked layers, as suggested above, we then used the described patterning technique to produce a multilayer device that implements four independent single-step colorimetric assays. Fig. 3 shows the schematic of such a multilayer device that was fabricated to allow for single-step colorimetric assay-based detection of BSA, glucose, nitrite and the pH. It consists of four different layers patterned and stacked using our method described via Figs. 1 and 2. In each layer, the sample can only flow in the hydrophilic areas, which are demarcated by the photo-polymer patterns preventing the flow into undesired locations. The top layer has an inlet port for introduction of the sample and the bottom layer has four rectangular readout zones designed to visualize the outcome of the colorimetric assays. The two middle layers allow distribution of the sample homogeneously into the four detection areas. To assist with the flow of the sample throughout the device, from the top layer all through to the bottom layer, contact pads (represented as a blue square in Fig. 3) of a hydrophilic material were placed at the intersection of the channels between the adjoining layers. Cellulose paper was used for contacting the top three layers, whereas, glass fibre was used as the hydrophilic contact pad material between the third and the bottom layer containing the four detection zones. The glass fibre not only allowed proper flow of the sample between the third and the bottom layer, but also served as pads for storage of reagents required for each of the different assays. The reagents were deposited (and dried at room temperature) on the glass fibre pads prior to their addition between the two final layers of our device. The choice of glass fibre was due to its known attribute of effective release of the reagents on rehydration from an incoming flow of a liquid sample. As shown in Fig. 3 red coloured lines indicate the direction of the flow of the sample from the top into the middle layers and then into the bottom layer where the outcome of the assays would be visualized.

3. Results and discussion

3.1. Stacking method for the fabrication of multilayer devices

In order to evaluate the performance of our local deposition-assisted paper-stacking method, we next tested our devices using a red chemical dye that allowed us to visualise the fluid flow through the different layers. The results for an example are as shown in Fig. 4. The dimensions of the squares (shown in Fig. 4) were designed to be $5 \times 5\,mm^2$ and the photo-polymer walls that defined those squares had a width of ~2 mm (the corresponding photo-polymer deposition speed was 30 mm/s). The laser exposure of the photo-polymer was at the same speed of 30 mm/s. To ensure the creation of solid photo-polymer structures that guide and hold the liquid sample the same protocol for deposition, time delay, and photo-polymerization was used to create the structures within each of the paper layers. The laser power was set at 60 mW and had a spot size at 5 mm, which is larger than the width of the photo-polymer line and these ensured the complete curing of the photo-polymer. Fig. 4 presents the results of different multilayer paper devices where we have successfully stacked two, three, four and five layers of paper following the same procedure each time and tested the flow within them with 20 μL of red dye. We followed the same process to produce six devices for each of the four different multilayer cases and Fig. 4 shows images of these four different multilayer devices with 2–5 layers respectively. The results were consistent for each one of them. As can be clearly seen the red dye which is deposited from the top face of the device, flows through the successive layers of paper and ends up at the bottom face of the device. In order to visualize that the red dye flown through each of the different layers of our stack, a cross-sectional image was taken, which shows that in each case the red dye has successfully travelled through all the layers.

3.2. 3D Paper-based device

In these sections, we explore the capability of our patterning method to create 3D multilayer devices that can detect multiple analytes with a liquid sample – artificial urine. The fabrication parameters (photo-polymer deposition speed, time delay, scanning speed of the laser and the laser fluence) remained unaltered for fabrication of these devices. Fig. 5 shows one such 3D device designed according to the schematic of Fig. 3 where four layers of cellulose paper are patterned and stacked together to form a $20 \times 20\ mm^2$ square device. The dimensions of the channels in each layer are as listed in Table 1. The performance of the 3D device was similarly evaluated using the same red dye; 35 μL of the dye was pipetted into the inlet point and the result was observed by viewing the bottom face of the device. The red dye provided an aid to visualize the progression of fluids through the multiple layers of this design and the volume of 35 μL is the least sample volume that is needed in order for it to flow through the successive layers, soak completely the middle paper layers, and end up at the bottom face of the device (Fig. 5).

We next evaluated the usefulness of our methodology by fabricating

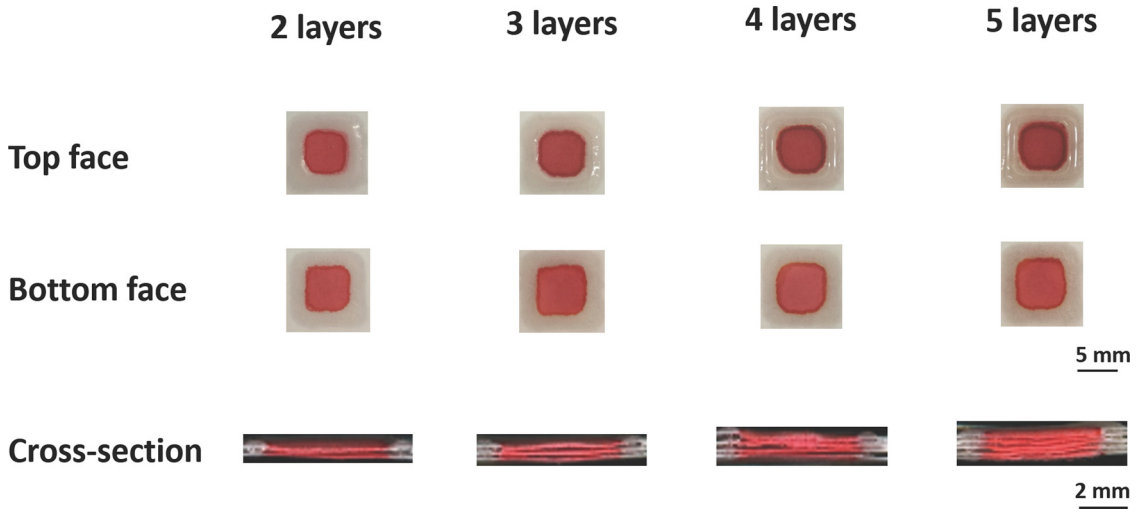

Fig. 4. Multilayer paper device tested with a red chemical dye. (For interpretation of the references to colour in this figure legend, the reader is referred to the web version of this article).

and testing the performance of devices with geometries (shown in Fig. 3) identical to those above (four layers with two middle layers) for detection of three common analytes presented in urine. For this testing, artificial urine samples spiked with the three chosen biomarkers, BSA, glucose and nitrite were used, and the detection of each of these was through a colour development in individual detection zones within the bottom layer of the device. The intensity of the colour produced is also an indication of the concentration of the biomarker in the artificial urine sample and was therefore use to further not just detect, but also quantify the levels of the different markers in our samples. For the BSA the colour change within the detection zone should be from yellow to blue-green, for glucose the change should be from brown to pink, and for nitrite, the change should be from light pink to a darker reddish colour. In case of pH the colour changes from yellow (6.0) to green (7.6) for the corresponding pH values. As described earlier, the different reagents were pre-deposited and dried on the glass fibre pad that was placed between the bottom two layers of the device. The reagents that were pre-deposited in the devices for the different assays were as follows: For the BSA assay we used 1 μL of TBPB, for the glucose assay we used 2 μL of glucose oxidase/peroxidase solution, for the nitrite assay we used 1 μL of the Griess reagent and for the pH measurement we used 2 μL of bromothymol blue.

Table 1
Dimensions of the channels within each layer of the 3D multilayer device.

Layer	Length (mm)	Width (mm)
Top layer	3	3
Middle with one channel	16	3
Middle with two channels	3	19
Bottom layer	3	4.5

Fig. 6 shows the bottom face of our 3D-μPADs at different times

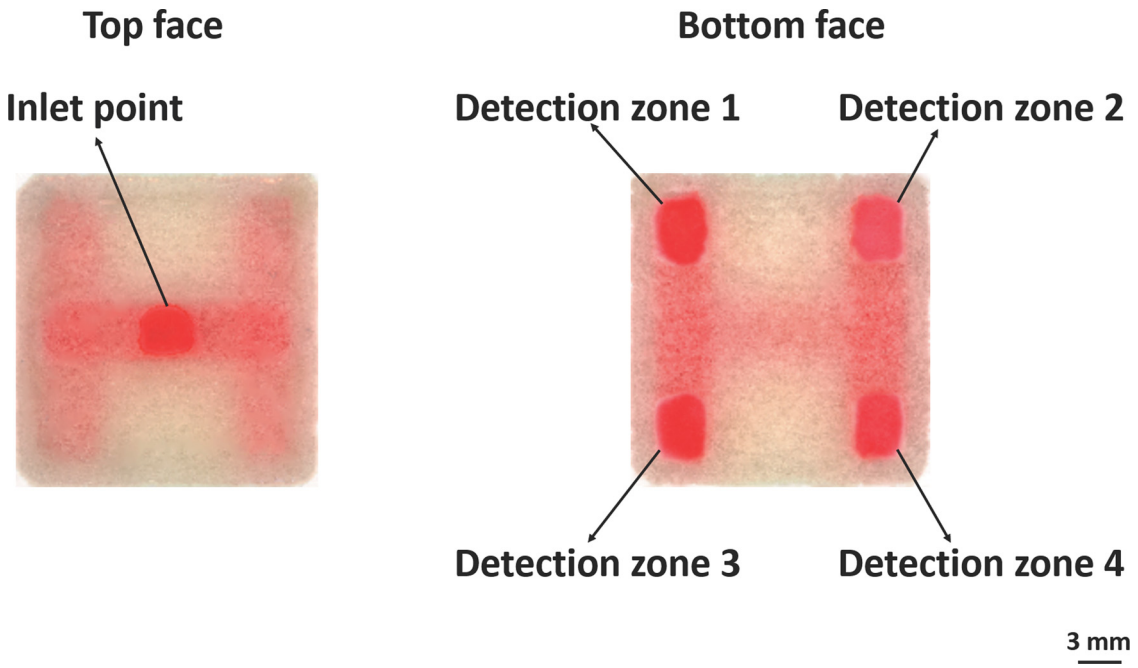

Fig. 5. 3D multilayer paper-based device tested with a red dye. Left image: Top face of the device where the red dye is introduced. Right image: Bottom face of the device where we visualize the outcome of the testing process. (For interpretation of the references to colour in this figure legend, the reader is referred to the web version of this article).

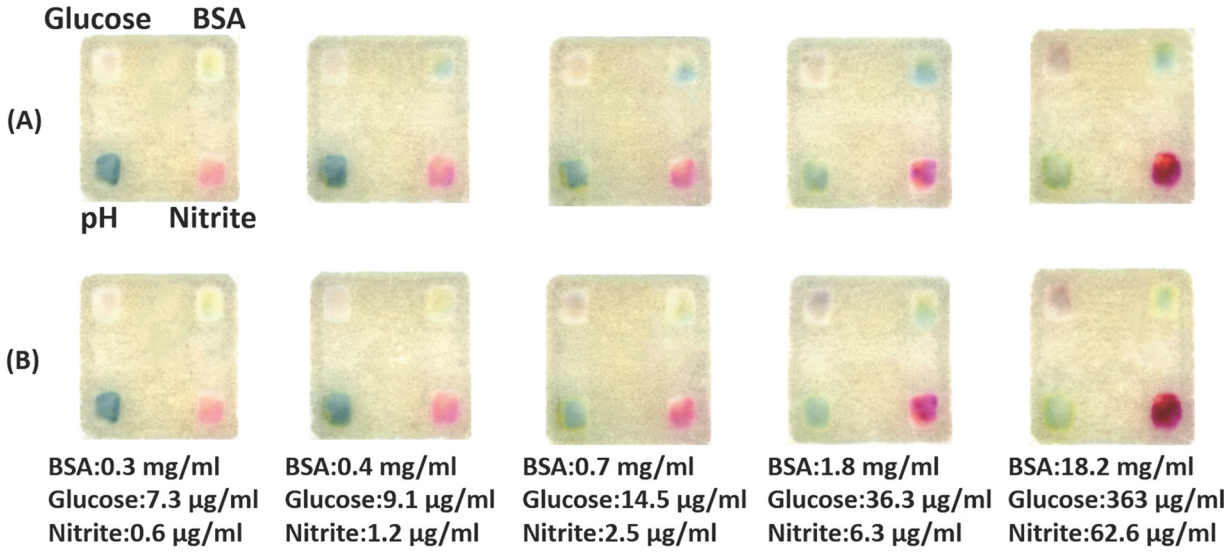

Fig. 6. Images of the bottom face of the four-layer 3D µPADs used to detect three analytes in artificial urine- BSA, glucose and nitrite, and measure of sample's pH. Images in (A) are for different concentrations of the analytes 1 min after the assay. Images in (B) are for the different concentrations of the analytes 10 min after the assay.

after 50 µL of the artificial urine sample was introduced from the top face of each device. The purpose of increasing the sample volume from 35 µL to 50 µL for actual tests, is for the acquisition of a better sensitivity during the measurement of the tested analytes. From the results presented in Fig. 6, we know that the volume of 50 µL is sufficient for the sample to travel through all the layers of the 3D-µPAD without overloading the device and producing any sideways leakage of the sample. Once the sample rehydrates and reacts with the reagents stored in the in-between glass fibre pads it then carriers on to the detection zones to produce a corresponding colour change within the different detection zones. We performed a detailed study testing several devices with known samples concentration across a range of 0.3 mg/mL to 18.2 mg/mL for BSA, 7.3 µg/mL to 363 µg/mL for glucose and a range of 0.6 µg/mL to 62.6 µg/mL for nitrite. As can be clearly seen in Fig. 6 there is a gradient colour change of the intensity for each of the analytes as their concentrations change from a lower to a higher value. The higher the concentration of the analyte in the sample, the more increased is the colour intensity in the detection zone.

For our 3D paper devices, the limit of detection (LOD) for the three analytes we chose to measure were found to be 0.4 mg/mL for BSA, 14.5 µg/mL for glucose and 2.5 µg/mL for nitrite. For the calculation of these values we used the following equations:

$$LOD = LOB + 3 \times SD_{Lowest\ concentration\ sample}$$

$$LOB = \langle Blank \rangle + 1.645 \times SDBlank$$

LOB refers to the limit of the blank, blank refers to the devices tested with a sample containing no analyte and SD is the standard deviation.

In the case of BSA, as the value of the limit of detection of our 3D µPADs is 0.4 mg/mL, this allows the use of such a device for the detection of nephrotic syndrome (protein > 2.32 mg/mL), subnephrotic range proteinuria (0.66 < protein < 2.32 mg/mL,) and tubular proteinuria (protein < 0.66 mg/mL). Additionally, the LOD of 14.5 µg/mL for glucose suggest its usefulness for the practical application of detecting elevated levels of glucose in urine (glucose levels greater than 250 µg/mL is an indication of diabetes). Last but not least, our reported device is capable of detecting nitrites in urine as their presence is an indication of a urinary tract infection.

The colour intensities on the test zones for each device were analysed using Adobe Photoshop. After using a scanner to take photos of the tested devices, the RGB channel in the histogram function in Adobe Photoshop was used to measure the mean intensity value of the pixels for each one of the four detection zones. The colour intensity values of the control device (no analyte) was subtracted from the values for the devices tested with the analytes in order to obtain the actual signal intensity. For BSA and nitrite, we measured the signal 1 min after the assay (Fig. 6a). However, as the glucose assay requires a longer time to complete, ~10 min, the colour was allowed to develop over this period of time, and intensity measured thereafter (Fig. 6b). Calibration curves based on the actual colour intensities is shown in Fig. 7 and as can be clearly seen, for each of the three analytes, as the concentration of the

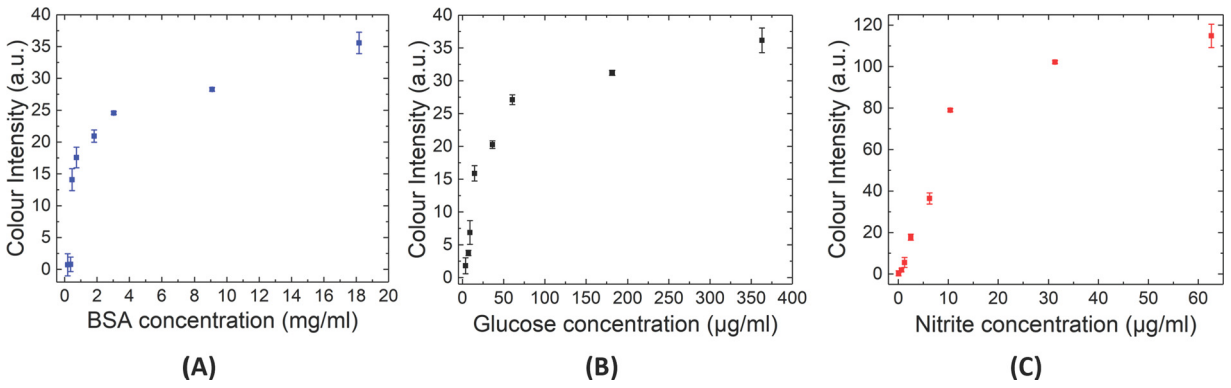

Fig. 7. Calibration curves showing the colour intensity of (A) BSA, (B) glucose and (C) nitrite for their different concentrations in the artificial urine samples.

analyte increases, the corresponding intensity of the colour produced also increases. Each measurement was repeated three times to estimate the error.

4. Conclusion

In this paper, we report the use of a simple, fast and inexpensive method to create 3D-μPADs using porous paper substrates. This technique is based on the local deposition of an acrylate-based negative photo-polymer followed by its exposure to a laser source to make multilayer paper devices. Unlike other reported methods, our patterning technique eliminates the need for any sophisticated alignment that may be required between the layers further also does not mandate the need for the use of external or additional equipment during the assembly of the device. The performance of our method was tested by stacking several layers of paper and making multilayer 3D paper-based devices, which were tested with a red dye that visualize that the sample flowed through the layers without blockage or leakage. Finally, we used the 3D-μPADs (with reagents, dried and stored within) to perform simple one-step colorimetric assays for the detection of BSA, glucose, nitrite and pH using artificial urine samples. Based on the results we observed a colour change for each one of the biomarkers relative to the concentration that we used in our sample. Additionally, the devices were shown to be used for a quantitative detection of the tested analytes. We believe that our paper patterning method that allows for the fabrication of 3D-μPADs is promising and presents important advantages when compared with other reported methods and can be further explored for use in more complex assays, where multiple sequential steps are needed.

Declaration of Competing Interest

There are no conflicts of interest to declare.

Acknowledgements

The authors acknowledge the funding received via the Engineering and Physical Sciences Research Council (EPSRC) via Grant Nos. EP/P025757/1, EP/N004388/1, EP/M027260/1 and EP/S003398/1. The underpinning RDM data for this paper can be found at 10.5258/SOTON/D1178

References

[1] P. Yager, T. Edwards, E. Fu, K. Helton, K. Nelson, M.R. Tam, B.H. Weigl, Microfluidic diagnostic technologies for global public health, Nature 442 (2006) 412–418, https://doi.org/10.1038/nature05064.
[2] M.M. Gong, D. Sinton, Turning the page: advancing paper-based microfluidics for broad diagnostic application, Chem. Rev. 117 (2017) 8447–8480, https://doi.org/10.1021/acs.chemrev.7b00024.
[3] A.K. Yetisen, M.S. Akram, C.R. Lowe, Paper-based microfluidic point-of-care diagnostic devices, Lab Chip 13 (2013) 2210–2251, https://doi.org/10.1039/c3lc50169h.
[4] A.W. Martinez, S.T. Phillips, G.M. Whitesides, E. Carrilho, Diagnostics for the developing world: microfluidic paper-based analytical devices, Anal. Chem. 82 (2010) 3–10, https://doi.org/10.1021/ac9013989.
[5] C.L. Sones, I.N. Katis, P.J.W. He, B. Mills, M.F. Namiq, P. Shardlow, M. Ibsen, R.W. Eason, Laser-induced photo-polymerisation for creation of paper-based fluidic devices, Lab Chip 14 (2014) 4567–4574, https://doi.org/10.1039/c4lc00850b.
[6] A.W. Martinez, S.T. Phillips, M.J. Butte, G.M. Whitesides, Patterned paper as a platform for inexpensive, low-volume, portable bioassays, Angew. Chem. Int. Ed. 46 (2007) 1318–1320, https://doi.org/10.1002/anie.200603817.
[7] J.J. Shi, F. Tang, H.L. Xing, H.X. Zheng, L.H. Bi, W. Wang, Electrochemical detection of Pb and Cd in paper-based microfluidic devices, J. Braz. Chem. Soc. 23 (2012) 1124–1130, https://doi.org/10.1590/s0103-50532012000600018.
[8] P. Rattanarat, W. Dungchai, D. Cate, J. Volckens, O. Chailapakul, C.S. Henry, Multilayer paper-based device for colorimetric and electrochemical quantification of metals, Anal. Chem. 86 (2014) 3555–3562.
[9] W. Liu, J. Kou, H.Z. Xing, B.X. Li, Paper-based chromatographic chemiluminescence chip for the detection of dichlorvos in vegetables, Biosens. Bioelectron. 52 (2014) 76–81, https://doi.org/10.1016/j.bios.2013.08.024.
[10] V. Mani, K. Kadimisetty, S. Malla, A.A. Joshi, J.F. Rusling, Paper-based electrochemiluminescent screening for genotoxic activity in the environment, Environ. Sci. Technol. 47 (2013) 1937–1944, https://doi.org/10.1021/es304426j.
[11] G.M. Whitesides, Cool, or simple and cheap? Why not both? Lab Chip 13 (2013) 11–13, https://doi.org/10.1039/c2lc90109a.
[12] E. Evans, E.F.M. Gabriel, T.E. Benavidez, W.K.T. Coltro, C.D. Garcia, Modification of microfluidic paper-based devices with silica nanoparticles, Analyst 139 (2014) 5560–5567, https://doi.org/10.1039/c4an01147c.
[13] W. Dungchai, O. Chailapakul, C.S. Henry, Use of multiple colorimetric indicators for paper-based microfluidic devices, Anal. Chim. Acta 674 (2010) 227–233, https://doi.org/10.1016/j.aca.2010.06.019.
[14] W. Dungchai, O. Chailapakul, C.S. Henry, A low-cost, simple, and rapid fabrication method for paper-based microfluidics using wax screen-printing, Analyst 136 (2011) 77–82, https://doi.org/10.1039/C0AN00406E.
[15] X. Li, J.F. Tian, W. Shen, Progress in patterned paper sizing for fabrication of paper-based microfluidic sensors, Cellulose 17 (2010) 649–659, https://doi.org/10.1007/s10570-010-9401-2.
[16] A.W. Martinez, S.T. Phillips, G.M. Whitesides, Three-dimensional microfluidic devices fabricated in layered paper and tape, Proc. Natl. Acad. Sci. U.S.A. 105 (2008) 19606–19611, https://doi.org/10.1073/pnas.0810903105.
[17] T. Akyazi, L. Basabe-Desmonts, F. Benito-Lopez, Review on microfluidic paper-based analytical devices towards commercialisation, Anal. Chim. Acta 1001 (2018) 1–17, https://doi.org/10.1016/j.aca.2017.11.010.
[18] E. Fu, C. Downs, Progress in the development and integration of fluid flow control tools in paper microfluidics, Lab Chip 17 (2017) 614–628, https://doi.org/10.1039/c6lc01451h.
[19] R.A.G. de Oliveira, F. Camargo, N.C. Pesquero, R.C. Faria, A simple method to produce 2D and 3D microfluidic paper-based analytical devices for clinical analysis, Anal. Chim. Acta 957 (2017) 40–46, https://doi.org/10.1016/j.aca.2017.01.002.
[20] K.M. Schilling, A.L. Lepore, J.A. Kurian, A.W. Martinez, Fully enclosed microfluidic paper-based analytical devices, Anal. Chem. 84 (2012) 1579–1585, https://doi.org/10.1021/ac202837s.
[21] M.S. Verma, M.N. Tsaloglou, T. Sisley, D. Chrisfodouleas, A. Chen, J. Milette, G.M. Whitesides, Sliding-strip microfluidic device enables ELISA on paper, Biosens. Bioelectron. 99 (2018) 77–84, https://doi.org/10.1016/j.bios.2017.07.034.
[22] L. Ge, S.M. Wang, X.R. Song, S.G. Ge, J.H. Yu, 3D Origami-based multifunction-integrated immunodevice: low-cost and multiplexed sandwich chemiluminescence immunoassay on microfluidic paper-based analytical device, Lab Chip 12 (2012) 3150–3158, https://doi.org/10.1039/c2lc40325k.
[23] C.A. Chen, W.S. Yeh, T.T. Tsai, Y.D. Li, C.F. Chen, Three-dimensional origami paper-based device for portable immunoassay applications, Lab Chip 19 (2019) 598–607, https://doi.org/10.1039/c8lc01255e.
[24] G.G. Lewis, M.J. DiTucci, M.S. Baker, S.T. Phillips, High throughput method for prototyping three-dimensional, paper-based microfluidic devices, Lab Chip 12 (2012) 2630–2633, https://doi.org/10.1039/c2lc40331e.
[25] R.B. Channon, M.P. Nguyen, A.G. Scorzelli, E.M. Henry, J. Volckens, D.S. Dandy, C.S. Henry, Rapid flow in multilayer microfluidic paper-based analytical devices, Lab Chip 18 (2018) 793–802, https://doi.org/10.1039/c7lc01300k.
[26] B. Kalish, H. Tsutsui, Patterned adhesive enables construction of nonplanar three-dimensional paper microfluidic circuits, Lab Chip 14 (2014) 4354–4361, https://doi.org/10.1039/c4lc00730a.
[27] H. Liu, R.M. Crooks, Three-dimensional paper microfluidic devices assembled using the principles of origami, J. Am. Chem. Soc. 133 (2011) 17564–17566, https://doi.org/10.1021/ja2071779.
[28] S. Choi, S.K. Kim, G.J. Lee, H.K. Park, Paper-based 3D microfluidic device for multiple bioassays, Sen. Actuators B Chem. 219 (2015) 245–250, https://doi.org/10.1016/j.snb.2015.05.035.
[29] C. Renault, J. Koehne, A.J. Ricco, R.M. Crooks, Three-dimensional wax patterning of paper fluidic devices, Langmuir 30 (2014) 7030–7036, https://doi.org/10.1021/la501212b.
[30] P.J.W. He, I.N. Katis, R.W. Eason, C.L. Sones, Laser direct-write for fabrication of three-dimensional paper-based devices, Lab Chip 16 (2016) 3296–3303, https://doi.org/10.1039/c6lc00789a.
[31] E.L. Gelamo, C. Silva, H. Imasato, M. Tabak, Interaction of bovine (BSA) and human (HSA) serum albumins with ionic surfactants: spectroscopy and modelling, Biochim. Et Biophys. Acta Protein Struct. Mol. Enzymol 1594 (2002) 84–99, https://doi.org/10.1016/s0167-4838(01)00287-4.
[32] P. King, I. Peacock, R. Donnelly, The UK Prospective Diabetes Study (UKPDS): clinical and therapeutic implications for type 2 diabetes, Br. J. Clin. Pharmacol. 48 (1999) 643–648, https://doi.org/10.1046/j.1365-2125.1999.00092.x.
[33] J.O.N. Lundberg, S. Carlsson, L. Engstrand, E. Morcos, N.P. Wiklund, E. Weitzberg, Urinary nitrite: more than a marker of infection, Urology 50 (1997) 189–191, https://doi.org/10.1016/s0090-4295(97)00257-4.

Talanta 238 (2022) 123056

Contents lists available at ScienceDirect

Talanta

journal homepage: www.elsevier.com/locate/talanta

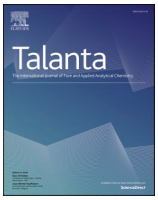

Laser-patterned paper-based flow-through filters and lateral flow immunoassays to enable the detection of C-reactive protein

P.P. Galanis *, I.N. Katis, P.J.W. He, A.H. Iles, A.J.U. Kumar, R.W. Eason, C.L. Sones

Optoelectronics Research Centre, University of Southampton, Highfield, Southampton, SO17 1BJ, UK

ARTICLE INFO

Keywords:
Paper-based device
Pre-polymer
Laser patterning
Porous flow-through filter
CRP detection
Hook effect

ABSTRACT

We report the use of a laser-based fabrication process in the creation of paper-based flow-through filters that when combined with a traditional lateral flow immunoassay provide an alternative pathway for the detection of a pre-determined analyte over a wide concentration range. The laser-patterned approach was used to create polymeric structures that alter the porosity of the paper to produce porous flow-through filters, with controllable levels of porosity. When located on the top of the front end of a lateral flow immunoassay the flow-through filters were shown to block particles (of known sizes of 200 nm, 500 nm, 1000 nm and 3000 nm) that exceed the effective pore size of the filter while allowing smaller particles to flow through onto a lateral flow immunoassay. The analyte detection is based on the use of a size-exclusive filter that retains a complex (~3 μm in size) formed by the binding of the target analyte with two antibodies each of which is tagged with different-sized labels (40 nm Au-nanoparticles and 3 μm latex beads), and which is larger than the effective pore size of the filter. This method was tested for the detection of C-reactive protein in a broad concentration range from 10 ng/ml to 100,000 ng/ml with a limit-of-detection found at 13 ng/ml and unlike other reported methods used for analyte detection, with this technique we are able to counter the Hook effect which is a limiting factor in many lateral flow immunoassays.

1. Introduction

Point-of-care (POC) tests have been widely developed for more than a decade and are intended for near patient diagnostic testing for detection of various conditions and diseases [1]. These diagnostic tests, which can be of vital importance especially in resource-limited settings, are simple to use and can be easily performed by untrained personnel giving results within 30 min [2,3]. Any POC diagnostic sensor designed for use in resource-limited settings would need to comply with the criteria set by the World Health Organization (WHO) which address the need to be affordable, sensitive and specific for analyte detection, user friendly, robust and provide the results rapidly to the patients and be equipment-free and deliverable to those who need it [4]. Paper has been shown to be an attractive platform for the development of POC sensors [5] that would comply with all these WHO-specified requirements. Due to its inherent characteristics (e.g. cost-effectiveness, biocompatibility, wicking of fluids through capillary action etc.), paper has been used extensively, for more than a decade, for the detection of pathogens and it has been established as a material for commercial products in the market [6,7].

Lateral flow immunoassays (LFIAs) are a specific category of POC sensors that have been used for the detection and quantification of analytes within biological fluids such as urine [8], blood [9] and saliva [10]. LFIAs are made up of four constituents: the sample pad, conjugate pad, detection pad and absorbent pad and the principle of operation of an LFIA is based on the interaction (binding) of the target analyte with antibodies. The sample, which contains the analyte, is introduced via the sample pad and after travelling laterally in the porous paper, it first encounters the conjugate pad where immobilized antibodies (detection antibodies) tagged with a coloured label such as Au-nanoparticles bind with the analyte. The sample then flows to the detection pad where antibodies (capture antibodies) specific to the analyte are immobilized at the test line and capture the target analyte thus producing a visual signal. The sample continues flowing past the control line where the detection antibodies are captured (by a different capture antibody specific to the detection antibody) regardless of the presence of the analyte thus producing a visual signal at the control line, showing that the test has performed properly. The excess liquid is finally absorbed in a pad at

Abbreviations: POC, Point-of-care; WHO, World Health Organization; LFIAs, Lateral flow immunoassays; CRP, C-reactive protein; c.w, continuous wave.

* Corresponding author.
E-mail address: pg1n15@soton.ac.uk (P.P. Galanis).

https://doi.org/10.1016/j.talanta.2021.123056
Received 12 July 2021; Received in revised form 13 October 2021; Accepted 7 November 2021
Available online 9 November 2021

the end of the LFIA [11].

LFIAs have some unique advantages over other diagnostics, one of the most important being that these devices do not need to be stored in a refrigerator following manufacture, which makes them ideal for use in remote settings and developing countries [12]. Furthermore, the test procedure is relatively simple and produces results which can then be interpreted visually by the patients [13]. Despite their advantages, LFIAs have some drawbacks arising primarily from the detection methods (i.e. chemistries/immunoassays) that are used, and this can limit the range of concentrations in which the analytes can be detected. Secondly, for semi-quantitative analysis, visual evaluation may not be reliable or definitive and therefore readers, cameras or even use of multiple lines as capture sites in the detection pad are reported [14].

For the case where the tested sample contains high analyte concentrations, and of direct relevance to our work here, the detection is limited as a consequence of the Hook effect [15]. This is a result of the increased number of unlabelled analytes which bind to the test line of the LFIA preventing the capture of labelled analytes on the same line. Above a certain concentration, as a result of the Hook effect the colour intensity of the test line decreases with increasing concentration of the analyte, consequently leading to a false interpretation of the results. In order to overcome this problem and increase the dynamic range across which the analyte can be detected, methods have been reported that either use an additional line formed of the antigen and positioned between the test line and the control line [16] or use of multiple test lines in the detection pad [17]. These methods can successfully increase the dynamic range in which the analyte can be detected, however they require the use of a conjugate pad and subsequently the incubation and drying of the detection antibodies for several minutes, a step that increases the time for the device fabrication.

Unlike our previously reported method that applied laser-patterned constrictions within the channel of an LFIA [18] for improving the limit-of-detection of a common inflammation marker namely C-reactive protein (CRP) [19], in this paper we report a novel filter-based method used for the detection of the same marker over a broad concentration range. The detection of CRP is clinically significant [20], and it is important for it to be measured over a wide concentration range. Although CRP is present in our body, elevated levels are associated with diseases such as chronic inflammation as well as type 2 diabetes mellitus [21]. Common methods used for the detection of CRP [22] include the use of ELISA tests [23] and LFIAs [24]. However, due to the limiting factor of the Hook effect, there is a limitation in the concentration range across which this analyte can be detected. This limitation can be detrimental in the case of CRP detection as it is reported [25] that the levels of this protein are associated with different risk levels for cardiovascular disease ranging widely from $<$1000 ng/ml for low risk to $>$3000 ng/ml for high risk.

To address the aforementioned challenge, it is important to have a device capable of detecting CRP over a broad range spanning from a few ng/ml to values greater than 3000 ng/ml. Here we employ a combination of a laser-patterned flow-through filter, and an LFIA to demonstrate such a detection strategy. The flow-through filter was designed to block particles larger than a specific size while allowing smaller particles to flow through the filter and get captured in the test line of a standard LFIA. Both the filters and the LFIAs are made using the principle of light-induced polymerization of an acrylate-based negative pre-polymer which is locally deposited across an LFIA to create user-defined flow paths. We have previously reported the use of such laser-patterned LFIAs for the detection of a single analyte such as the Leishmaniasis antigen [26] but also in multiplexed detection of analytes [27] as well as bacterial infection testing [28]. In this method, the pre-polymer is deposited on a cellulose paper and after penetration throughout the paper thickness it is polymerised using laser light to form solid polymeric structures of controllable porosity.

The detection strategy is based on the interaction and binding of the target analyte with two antibodies, each tagged with a differently sized label namely 40 nm Au-nanoparticles and 3 μm latex beads. The presence of the analyte in the sample leads to the formation of a complex formed of the analyte and the two antibodies tagged with the small and large particles. This complex is blocked by the flow-through filter, as its total size is larger than the effective pore size of the filter. In the case of a (i) positive sample with a high analyte concentration, the Au-nanoparticles bind to form the complex which cannot flow through the filter and hence the Au-nanoparticles cannot be captured by the test line on the LFIA, therefore no signal is produced at the test line (similar to a competitive immunoassay). When the analyte is (ii) not present in the sample, i.e. the sample is negative, the complex is not formed and therefore the Au-nanoparticles are free to flow through the filter onto the LFIA and get captured at the test line. So, in the case of a negative sample, a strong coloured red line will appear at the test line (again similar to a competitive immunoassay). For samples of (iii) different analyte concentrations, some of the Au-nanoparticles will be captured to form the complex and only the unbound ones will flow through the filter and get captured at the test line. In that case a coloured signal of variable intensity will be produced in the test line, indicating the presence of the analyte in the sample.

Our proposed method is simple and uses the same materials that are used in standard LFIAs. However, unlike the case for standard LFIA operation and other methods reported for improving the dynamic range, we do not make use of the sample pad and the conjugate pad thereby simplifying further the device design and fabrication protocol. Instead, we are using a porous filter which is able to retain particles of a specific size while allowing smaller particles to flow through. We tested this method and were able to measure the presence of CRP over a broad concentration range from 10 ng/ml to 50,000 ng/ml with a limit-of-detection found at 13 ng/ml.

Several studies in the literature [16,29–31] report observing the Hook effect in LFIAs for CRP at concentrations higher than a threshold value of 500 ng/ml. We do not present herein a measurement of this threshold for a direct comparison of our flow-through filter-based detection immunoassay with a traditional LFIA, because we cannot use the same detection and capture antibodies for a direct comparison. However, since the three repeats (for each of the different analyte concentration) produce the same answer, our proposed method is able to operate accurately and detect CRP over a broad concentration range from 10 ng/ml to 50,000 ng/ml which is beyond the previously mentioned threshold value for the Hook effect.

2. Experimental section

2.1. Experimental setup and materials

The porous paper used for the fabrication of the flow-through filters is Whatman™ grade 1 qualitative filter paper (cellulose) with a thickness of 180 μm and pore size of 11 μm from GE Healthcare. The part of the sample that flows through the filter ends up in an LFIA and the material of choice for that is an UniSart CN 95 (nitrocellulose) membrane from Sartorius Stedim Biotech GmbH, Germany with thickness of 140–170 μm and pore size of 15 μm. The sample that flows over the test line accumulates in an absorbent pad (Whatman™ CF4) which is acquired from GE Healthcare and has thickness of 482 μm. In order to change the porosity of the paper and make the flow-through filters, we used an acrylate-based negative pre-polymer (DeSolite® 3471-3-14) from DSM Desotech, Inc., USA which is deposited using a PICO® Pμlse™ dispenser platform from Nordson EFD, UK. The dispensing system, which delivers the pre-polymer, deposits micro-droplets with a volume of 0.5 nL through an orifice with diameter 100 μm at a frequency of 100 Hz. The light source that is used to cure the pre-polymer is a fibre-coupled continuous wave (c.w.) diode laser (Cobolt MLD, Cobolt AB Sweden) operating at a wavelength of 405 nm and output power of 60 mW.

In order to create flow-through filters with different levels of

porosity, we deposited a solution of the pre-polymer that was diluted with isopropyl alcohol (IPA) (Sigma-Aldrich) in different concentrations. For the characterization of the different porosity filters we used solutions of black dyed polystyrene microspheres (Polysciences, Inc.) of different sizes: 200 nm (5.68×10^{12} particles/ml, product number 24290-15), 500 nm (3.64×10^{11} particles/ml, product number 24291-15), 1000 nm (4.55×10^{10} particles/ml, product number 24287-15) and 3000 nm (1.68×10^{9} particles/ml, product number 24292-15) suspended in deionized water with a concentration of 25 mg/ml. In order to demonstrate the detection mechanism of this filtration method, we used an immunoassay with mouse biotinylated IgG (R&D systems with stock concentration of 500 μg/ml, product number IC002B) as the analyte, anti-mouse antibody (R&D systems with stock concentration of 500 μg/ml, product number G-202-C) labelled with 40 nm Au-nanoparticles (acquired from Abcam with an optical density 20, product number ab269932) as the detection antibody and 3 μm latex beads (white dyed) labelled with streptavidin as the filtration antibody (acquired from Spherotech Inc. with stock concentration of 500 μg/ml, product number SVP-30-5). The mouse IgG (R&D systems with stock concentration of 500 μg/ml, product number AF007) was dispensed and immobilized as a capture antibody for the test line on the LFIA. We tested the performance of the flow-through filters with an immunoassay for the detection of CRP. For this we used (as the analyte) human CRP (Sigma-Aldrich with stock concentration of 1 mg/ml, product number C1617), mouse anti-human CRP (acquired from R&D systems with stock concentration of 500 μg/ml, product number MAB17071) labelled with 40 nm Au-nanoparticles (as the detection antibody) and mouse anti-human CRP biotinylated IgG antibody (R&D systems with stock concentration of 50 μg/ml, product number BAM17072) tagged with 3 μm latex beads (white dyed) labelled with streptavidin as the filtration antibody. Goat anti-mouse IgG (R&D systems with stock concentration of 500 μg/ml, product number G-202-C) was used at the test line to capture the detection antibody. At the end of the testing process the LFIAs were washed with 10 μL of phosphate-buffered saline to ensure that all the sample had reached the position of the test line. The antibodies were immobilized on the test line of the LFIA using a XYZ3210 platform with a Biojet HR solenoid dispenser from Biodot.

2.2. Methods and procedure

The method for the fabrication of solid polymeric walls in both cellulose paper-based flow-through filter and nitrocellulose membrane of the LFIA, involves the use of an acrylate-based negative pre-polymer, which is locally deposited on top of these porous substrates before the exposure to a laser light source. The schematic in Fig. 1 illustrates the setup used to pattern the porous substrates and create the paper-based devices i.e. the flow-through filter and the LFIA. First, the pre-polymer is locally deposited by a dispenser on top of a porous substrate at locations pre-defined by a computer design to demarcate the boundaries of the device. The pre-polymer is then allowed to soak for a sufficient time (typically between 1 and 3 min depending on the substrate of choice) throughout the entire thickness of the substrate before exposure to the laser light source to induce photo-polymerization. The laser traces exactly the same pre-polymer pattern previously deposited and the photo-polymerization creates a solid polymeric structure able to contain the flow of liquids. The precise time delay, defined as the difference in time between the pre-polymer deposition and the laser scanning (exposure) depends on the properties of the porous substrate on which the pre-polymer is deposited.

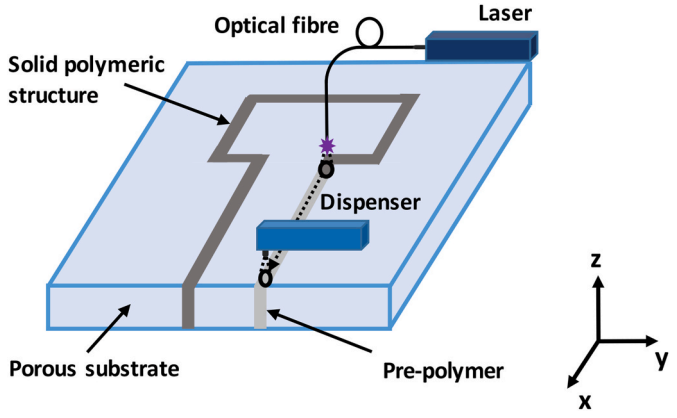

Fig. 1. Schematic representation of the local pre-polymer deposition setup. In this image, the pre-polymer is locally deposited onto a porous substrate (nitrocellulose membrane) followed by the subsequent exposure to a fiber-coupled c.w. laser source to create solid polymeric structures/walls that define the fluid-flow path of a lateral flow device.

Fig. 2 illustrates (A) a schematic showing the different stages of the fabrication of a porous flow-through filter as well as (B) a three-dimensional schematic of the same filter positioned on the top of the front end of an LFIA. For the fabrication of a square-shaped frame that forms the impregnable polymeric wall of our filter, the pre-polymer is first deposited as a square-frame (stage 1) on the cellulose paper with a speed of 20 mm/s. After a time delay of 180 s, which was sufficient for the pre-polymer to penetrate throughout the entire thickness of the paper, the pre-polymer along with the square frame was exposed to the laser irradiation with the same scanning speed of 20 mm/s (laser spot size of 2 mm with a laser fluence of 0.15 J/cm^2). During this time delay, the pre-polymer spreads laterally to create an impregnable square frame with a width of ~1 mm and this therefore defines the minimum width of the solid polymer wall created in the cellulose paper. It is important to note here that the laser follows the same pattern as the pre-polymer that was previously deposited and that is because the set values of the laser spot size and the laser fluence are sufficient to fully polymerize the pre-polymer. Any increase in the laser spot size or change in the laser scanning pattern will result in a decrease of the laser fluence and consequently it would take longer to polymerize any given area or structure which would be detrimental to the overall manufacturing process as it would introduce a potential uncertainty to the post-deposition polymerization step.

In order to make the porous flow-through filters with controllable levels of porosity, we used the same pre-polymer but this time diluted in IPA in different concentrations. The porosity of the flow-through filters is defined by the volume concentration of the deposited pre-polymer solution in IPA and by changing the v/v% concentration, we were able to create filters with different porosities. The fabrication process involves pipetting 10 μL of the diluted pre-polymer inside the solid polymeric structure (stage 2) and exposing the filter after a time delay of 60 s to laser light (stage 3) with the same fluence as before (with a laser spot size of 7 mm) to induce photo-polymerization and create the porous flow-through filter. The time delay of 60 s is sufficient for the diluted pre-polymer to extend throughout its whole thickness. As can be seen, the time delay of 60 s is smaller than the time delay of 180 s that we used to make the solid square polymeric structure on the same substrate. This difference stems from the fact that the pre-polymer that we used to make the porous filter is diluted in IPA and as a result it has lower viscosity and penetrates faster throughout the paper. Pipetting the pre-polymer in different concentrations on cellulose paper and exposing to laser light will result in the creation of porous filters with correspondingly different levels of permeability for subsequent liquid sample flow. Flow-through filters made with higher pre-polymer concentrations will be less porous compared with flow-through filters made with lower pre-polymer concentrations as the concentration of the pre-polymer in each case dictates the resultant porosity of the filters.

Finally, using the same acrylate-based pre-polymer we patterned the LFIA on the nitrocellulose membrane. The patterning conditions remained unaltered during the device fabrication work (pre-polymer deposition speed 20 mm/s and laser scanning speed 20 mm/s).

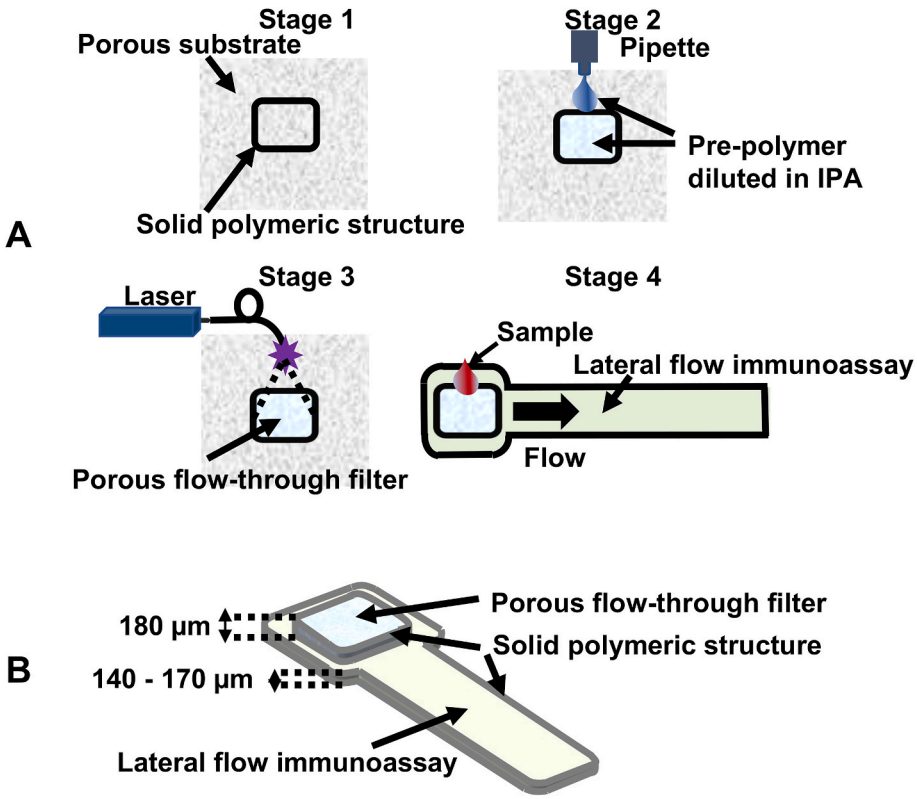

Fig. 2. (A) Schematic showing the various steps involved in the fabrication and use of the porous filter with an LFIA: the creation of a solid polymeric structure on a porous substrate (stage 1), pipetting of 10 μL of the diluted pre-polymer inside the solid polymeric structure (stage 2), laser light exposure of the diluted pre-polymer to create the flow-through filter (stage 3) and finally the position of this filter on the top of the front end of an LFIA (stage 4). (B) Three-dimensional schematic showing both the porous flow-through filter and the LFIA.

However, due to the different porosity, thickness and internal structure of the nitrocellulose membrane, which has a porous sponge-like internal structure compared with the fibrous internal structure of the cellulose paper the time delay is different and after extended studies [32] was set to be 30 s for the nitrocellulose membrane.

After the fabrication, the flow-through filter is cut around its solid boundary walls and then positioned on the top of the front end of an LFIA (stage 4) before a sample is deposited onto the flow-through filter. The key point to note is that the porosity of the flow-through filter is controllable and can be designed to retain particles larger than a user-defined size and allow smaller particles to flow through and into the LFIA.

3. Results and discussion

3.1. Characteristic study of the filtration properties of the porous flow-through filters

Images of the fabricated devices are depicted in Fig. 3. The porous flow-through filters are designed to have an area of ~25 mm^2 whereas the front end of the LFIA was designed to have a square shape as well but with an area of 49 mm^2 and a channel with length of 20 mm and width of 3 mm. As can be clearly seen, the square front end of the LFIA was deliberately designed to have an area bigger than that of the flow-through filter so that the porous filter will totally fit inside enabling intimate contact between the two substrates.

To study the filtration properties of the porous flow-through filters, we fabricated identical LFIAs and filters with different porosities. Fig. 4 shows an example of porous flow-through filters tested with 10 μL of black dyed polystyrene microspheres with a size of 1000 nm. Each of the filters has a different level of porosity starting from a very porous (5.8% of pre-polymer in IPA) to a less porous filter (11.1% of pre-polymer in IPA) and each one was replicated and tested three times. As a reference, we provide the results of a blank filter (no pre-polymer added) which proved incapable of retaining the 1000 nm polystyrene microspheres

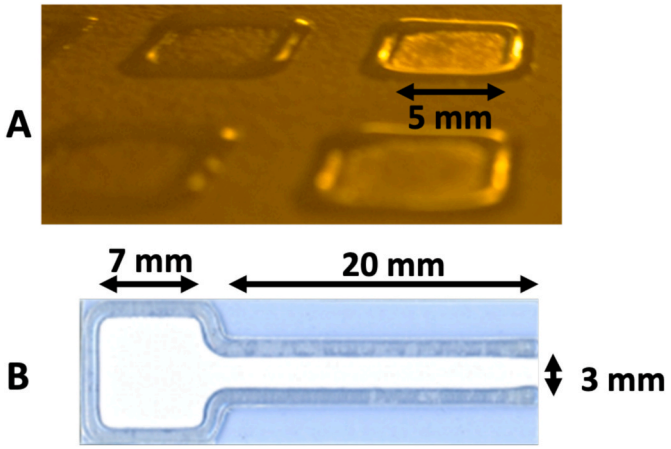

Fig. 3. Images of (A) a flow-through porous filter and (B) an LFIA with their respective dimensions. A porous filter is able to retain particles larger than a specific size while allowing smaller particles to flow through and into the LFIA.

and consequently allowed them to flow through the filter and into the LFIA. All the flow-through filters were positioned on the top of the front end of the LFIA during the testing process as shown in Fig. 2B and only removed after the end of the experiment to capture photos as presented in Fig. 4A.

In Fig. 4A, we observe that a low porosity filter made with pre-polymer concentration at 11.1% is able to fully retain the polystyrene microspheres. However, using a higher porosity filter made with pre-polymer concentration between 9.1% and 7.7%, we are able to retain the microspheres in the porous filter and at the same time allow the deionized water, in which the microspheres are dispersed, to flow through the filter and end up in the LFIA. An even higher porosity filter made with pre-polymer concentration below 7.7%, is porous to 1000 nm

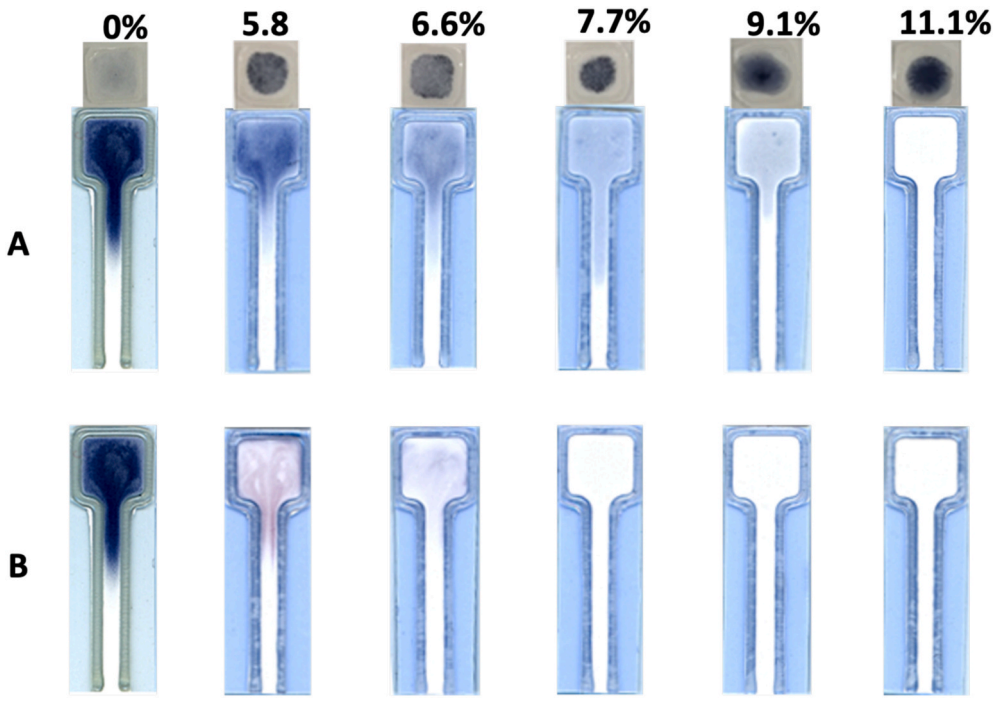

Fig. 4. Images showing flow-through filters tested with 10 μL of black dyed polystyrene microspheres of size 1000 nm. The LFIAs are all identical, but the flow-through filters are made with different pre-polymer concentrations ranging from 0% to 11.1% of pre-polymer in IPA. Images show (A) the flow-through filters and the LFIAs immediately after the testing process and (B) the same LFIAs after the evaporation of the deionized water.

polystyrene microspheres thus enabling the flow of this particle size through the filter. As we can see in Fig. 4A, we have the formation of a dark region on top of the filters after the completion of the filtration process. This is a result of the porous filters which delay the flow of the samples and due to interaction forces between the polystyrene particles, the microspheres aggregate to form a complex bigger than the porosity of the filter and are therefore unable to flow through. Since for the filters with pre-polymer concentration at 9.1% and below the deionized water flows through (Fig. 4A), it is difficult to visualize whether the polystyrene microspheres are retained by the filter or flowed into the LFIA. For that reason, photos of the same LFIAs were taken after the evaporation of the deionized water (Fig. 4B) in order to visually assess the ability of the porous flow-through filters to block particles larger than a specific size. Apart from testing with polystyrene microspheres with 1000 nm size, we also tested the flow-through filters with polystyrene microspheres of different sizes namely 200 nm, 500 nm and 3000 nm, all dispersed in deionized water. For each of the different particle sizes and filter porosities, we fabricated and tested three identical devices and the results after testing each one of the devices with 10 μL of the solution are all depicted in Table 1. Based on the ability of the porous flow-through filters to block particles of different sizes, we defined a transitional range for the concentration (indicated with a red box in Table 1) for which the porous filters transition from being completely impermeable to being permeable to polystyrene particles of a specific size. Looking at this transitional range we observe that there is an increasing trend in terms of the v/v% concentration of the pre-polymer and the ability of the filters to block particles decreasing in size.

In Fig. 5, we have plotted the particle filtration efficiency of flow-through filters with different porosities after testing with polystyrene microspheres of varying sizes. The particle filtration efficiency is a measure of the performance of a porous flow-through filter when filtering out particles of a specific size. In order to calculate the values for the particle filtration efficiency, we performed colour analysis using Adobe Photoshop. Specifically, we used the RGB channel in the histogram function and measured the mean intensity value of the pixels in both the filters (Fig. 4A) and the LFIAs (Fig. 4B).

Table 1
A range of flow-through filters with different porosities for which polystyrene microspheres of different sizes will pass through. For each polystyrene particle size, we have defined a transitional range of pre-polymer concentration (marked in red) in which the filters transition from being completely impermeable to being porous.

Concentration (v/v%)	200 (nm)	500 (nm)	1000 (nm)	3000 (nm)
33.3	0/3	-	-	-
20.0	0/3	0/3	-	-
14.3	3/3	0/3	-	-
11.1	3/3	0/3	0/3	-
9.1	3/3	0/3	0/3	-
7.7	3/3	3/3	0/3	-
6.6	-	3/3	3/3	-
5.8	-	-	3/3	0/3
5.3	-	-	-	1/3
4.8	-	-	-	3/3
3.8	-	-	-	3/3
3.3	-	-	-	3/3

We then used equation (1) to calculate the particle filtration efficiency (%) for the different filter porosities. A value of 255 corresponds to the pixel intensity for white, which is the background of both the flow-through filter and the LFIA before testing. We subtracted the mean colour intensities (for the total of three devices) of both the flow-through filters and the lateral flow-devices from this value in order to obtain the actual signal intensities.

Using this methodology, we can use such flow-through filters and the principle of size exclusive filtration as an immunoassay for the detection of an analyte, and this is described in the subsequent sections.

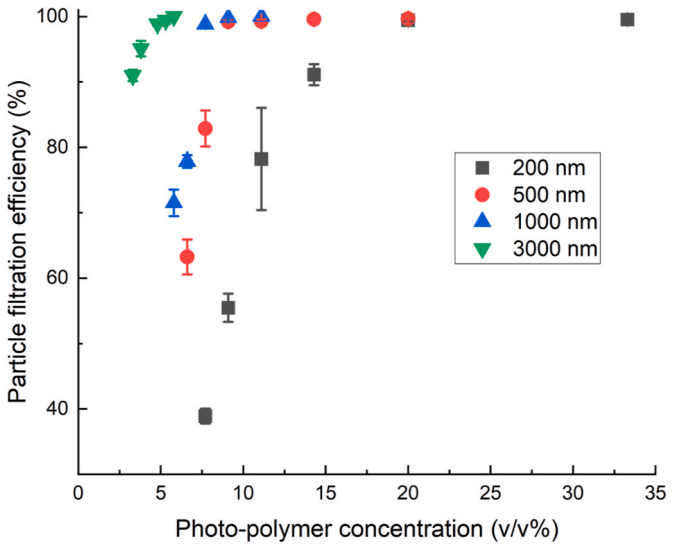

Fig. 5. Particle filtration efficiency of flow-through filters made with different pre-polymer concentrations and tested with polystyrene microspheres of varying sizes.

$$(1 - [(255 - \textit{colour intensity on device}) / (255 - \textit{colour intensity on filter})]) \times 100 \quad (1)$$

3.2. *Flow-through filtration for analyte detection*

These porous flow-through filters were then used with standard LFIAs for the detection of an analyte using an immunoassay which is based on particle size selection. For this we made the flow-through filter and the lateral flow devices with materials commonly used in LFIAs such as cellulose paper (sample pad), nitrocellulose membrane (detection pad) and absorption pad. Unlike a standard LFIA configuration, in this case we do not make use of the sample or conjugate pads. Instead, we use a porous flow-through filter, which is located on the top of the front end of an LFIA and by altering its porosity, we can design it to retain particles above a certain size. The analyte detection is based on the filtration of different-sized Au-nanoparticles (40 nm) and latex beads (3 μm) that both bind to the same target analyte via antibodies. In this immunoassay, the filters were designed to have a defined pore size bigger than the size of the Au-nanoparticles and thus the particles are able to flow through and reach the test line, whereas the latex beads which have size bigger than the effective pore size of the filters are blocked or retained in the filters. Both Au and latex particles are captured by the analyte and therefore if the analyte is present in the sample (positive sample) it will bind to both and form a complex (~3 μm in size), which is bigger than the pore size of the filter and as a result is unable to flow through and reach the test line. Only the unbound detection antibodies left in the sample will be able to flow through the filter and get captured at the test line of the LFIA producing a red-coloured line indicating the presence of the analyte in the sample. Similar to the principle of a competitive immunoassay, a test line displaying a clear signal means that the analyte is not present in the sample. For our filter-based immunoassay, an increase in the concentration of the analyte will result in a decrease of the number of unbound detection antibodies consequently captured at the test line, and this therefore will result in a decreased signal at the test line. In the schematic of Fig. 6 we describe the principle of operation of the filter-based immunoassay in the cases of no analyte, low and high analyte concentrations.

In our first demonstration of this filtration-based immunoassay, we tested a sample that contained a 1:1:1 ratio of anti-mouse antibody labelled with 40 nm Au-nanoparticles (diluted in phosphate-buffered saline to have a concentration at 100 μg/ml used as a detection antibody), 3 μm latex beads (labelled with streptavidin (stock concentration) used as a filtration antibody) and finally a mouse biotinylated IgG antibody as the target analyte (tested in different concentration from 0 μg/ml-500 μg/ml). In the channel of the LFIAs, we dispensed and immobilized mouse IgG antibody (stock concentration) as the test line (Figs. 6 and 7). There is no a-priori rationale for the choice of the use of the detection antibody, the filtration antibody, and the analyte on the tested sample in an equal ratio. However, we are well aware that any alteration of this ratio would change the interaction and binding of the target analyte with the detection and the filtration antibodies and therefore result in a change in the number of the complexes that are

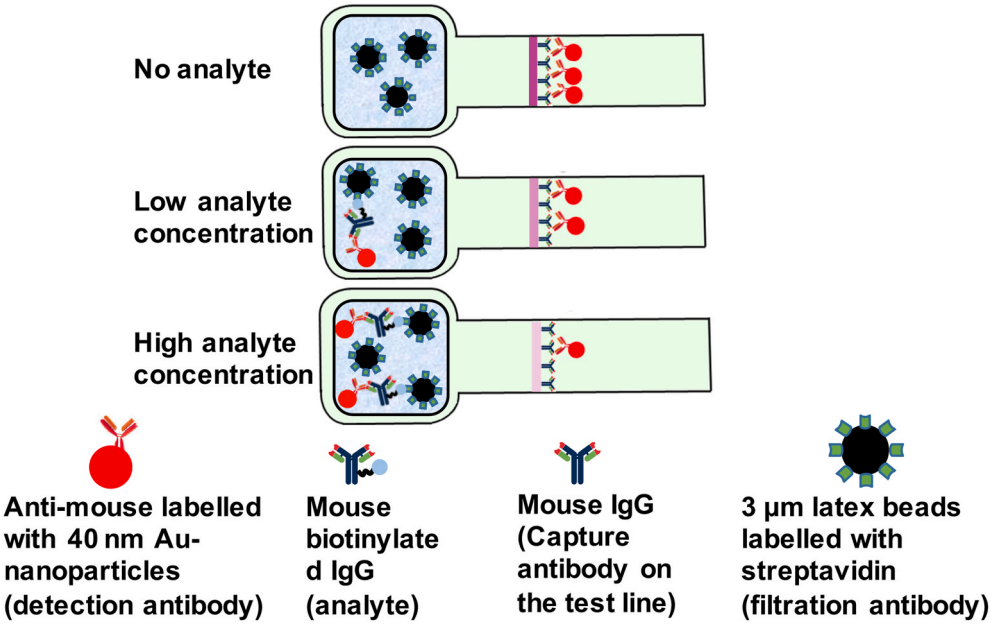

Fig. 6. Schematic representation of the method used for the detection of an analyte. For the case where the analyte in not present in the sample all the detection antibodies are captured at the test line producing a strong signal. However, as we increase the concentration of the analyte, the number of the unbound detection antibodies left in the sample decreases and this will result in a decrease of the signal at the test line.

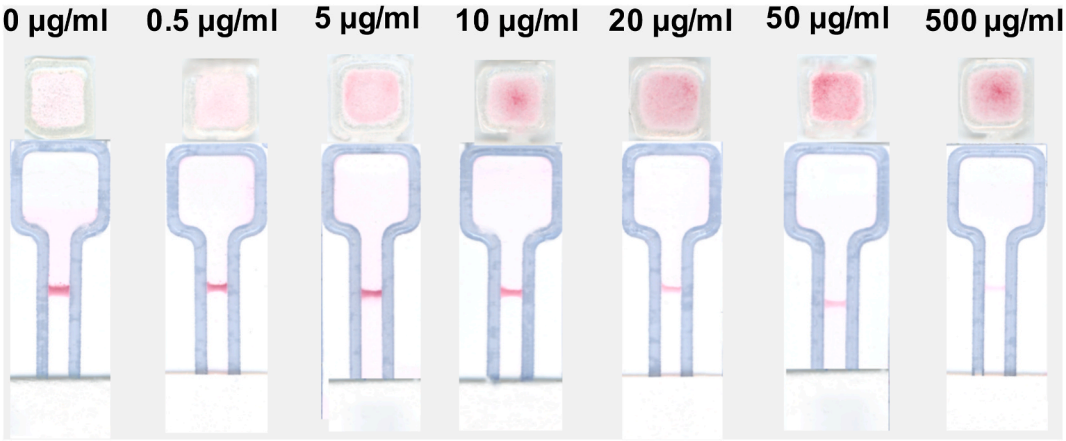

Fig. 7. Flow-through filter with pre-polymer concentration of 7.7% tested with 20 μL of a sample that contains anti-mouse antibody labelled with 40 nm Au-nanoparticles, 3 μm latex beads labelled with streptavidin and mouse biotinylated IgG antibody (analyte) at concentrations between 0 μg/ml and 500 μg/ml.

being formed. In that case, the number of the unbound detection antibodies left in the sample would change, and this would not only affect the colour intensity of the test line of the LFIA but also the concentration range in which the analyte can be detected.

For this immunoassay we fabricated and tested with a 20 μL sample a flow-through filter made with 7.7% pre-polymer concentration (Fig. 7). For this case we replicated and tested the devices three times. From the results in Fig. 7 we observe that on using a filter with 7.7% pre-polymer concentration that is capable of completely retaining particles with a size of 3 μm, we were able to detect the target analyte in a concentration ranging between 0.5 μg/ml and 500 μg/ml. In this case, we observe that an increase in the analyte concentration results in a decrease of the signal at the test line and Fig. 8 plots the colour intensity of the test line versus the analyte concentration. Each data point is the mean value from the total of three devices. As previously stated, the presence of the analyte in the sample will lead to the formation of the following complex: detection antibody, filtration antibody and mouse biotinylated IgG antibody and the increase in the concentration of the analyte will lead to an increase in the number of such complexes that are being formed. Testing the sample with a porous filter (7.7% pre-polymer concentration) the complex thus formed is completely retained in the filter and

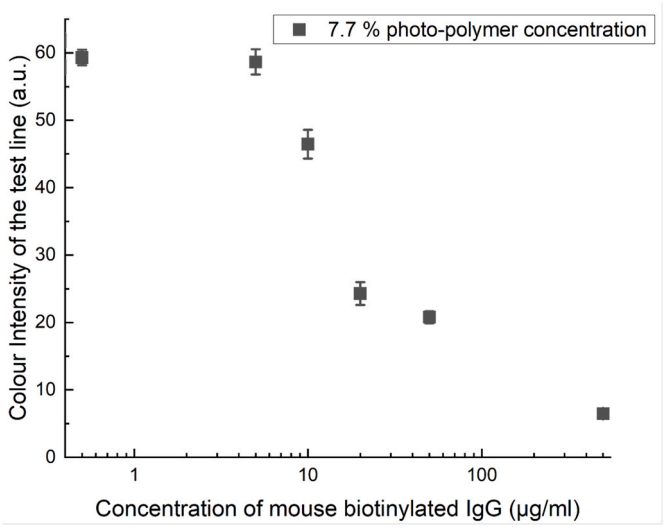

Fig. 8. Colour intensity on the test line of LFIAs for different mouse biotinylated IgG (analyte) concentrations in the range between 0.5 μg/ml and 500 μg/ml. The analyte was detected using a flow-through filter with 7.7% pre-polymer concentration.

only the unbound detection antibodies flow through and get captured at the test line indicating the presence of the analyte on the tested sample. The results presented in Figs. 4, Figs. 7 and Fig. 9 suggest that there is no associated non-specific binding of either the detection antibody or the filtration antibody with the porous filter. If that were the case, then the latex beads would not be able to flow through the porous filters unlike the case presented in Fig. 4. Additionally, in the cases illustrated in Figs. 7 and 9, some of the unbound detection antibodies would non-specifically bind to the porous filter and thus would not be able to flow through it and get captured by the capture antibodies at the test line of the LFIA. As a result, we would not be able to distinguish between a low and a high analyte concentration which has enabled us to detect the analyte over a broad concentration range. Lastly, we cannot be sure if the analytes can non-specifically bind to the polymeric structure of the flow-through filters, however this will have no effect to the immunoassay as the appearance of the test line depends only on the number of the unbound detection antibodies left in the sample.

3.3. *Filter-based immunoassay for CRP detection*

The performance of the flow-through filters was tested using an immunoassay for the detection of the common inflammation marker C-reactive protein (CRP). Similar to the previous immunoassay, we used a sample which contains the following constituents mixed in a 1:1:1 ratio: human CRP (analyte) in concentrations ranging from 10 ng/ml to 100,000 ng/ml, mouse anti-human CRP antibody labelled with 40 nm Au-nanoparticles (stock concentration) used as a detection antibody and mouse anti-human CRP biotinylated IgG antibody tagged with 3 μm latex beads labelled with streptavidin (stock concentration) used as a filtration antibody. The principle of operation of this immunoassay is the same as the one previously described. If the analyte, CRP, is present in the sample, it binds with both the detection antibody and the filtration antibody forming a complex with size bigger than the effective pore size of the filter. Hence this complex is unable to flow through and only the unbound detection antibodies left in the sample are able to flow through the filter and enter the LFIA where they are captured at the test-line (by the goat anti-mouse IgG antibodies) producing a red coloured line. The remaining part of the sample, which is not captured flows over the test line and accumulates in an absorbent pad located at the end of the LFIA (Fig. 9). The sample, which contains the analyte in different concentrations, was tested on a filter with 7.7% pre-polymer concentration. Our choice to use a flow-through filter with the given porosity stems from the fact that such a filter is capable of completely retaining particles with size bigger than 3 μm (see Table 1), and therefore is able to detect an analyte in a broad dynamic concentration range (Fig. 7).

In Fig. 9, we present the results when 20 μL of sample containing the

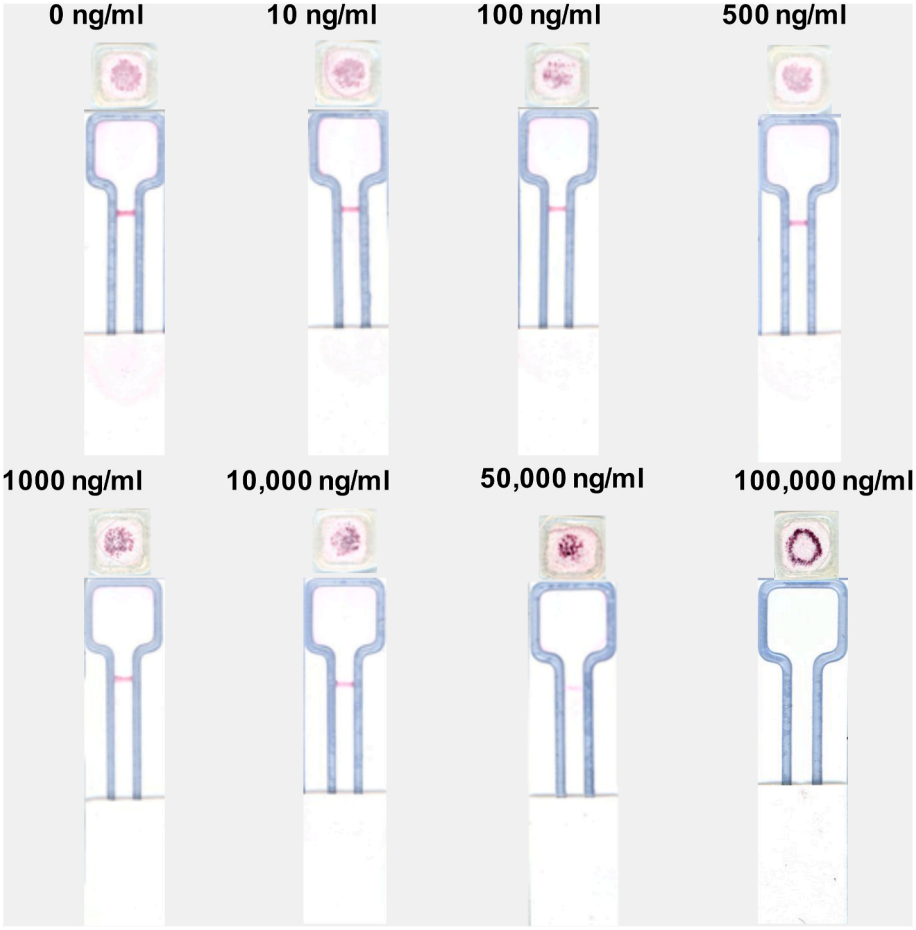

Fig. 9. Images of flow-through filters made with 7.7% pre-polymer concentration and tested with 20 μL of a sample containing varying CRP concentrations from 0 ng/ml to 100,000 ng/ml. Particles that flow through the filter end up in an LFIA where anti-mouse IgG antibodies have been dispensed and used as a test line.

CRP analyte in different concentrations (0–100,000 ng/ml) was tested on a porous flow-through filter and Fig. 10 depicts the respective colour intensity on the test line where the intensity of the control device (0 ng/ml) corresponds to a mean value (from the total of three devices) at 46.18 a.u. In this graph, each data point represents the mean value of three devices that were tested. As can be clearly seen, the colour of both the filter and the test line change according to the concentration of the analyte. Similar to our previous experiment, an increase in the CRP concentration will lead to an increase in the number of the complexes (CRP-detection antibody-filtration antibody) that are being formed thus leaving a smaller amount of unbound detection antibodies in the sample which flow through the filter and get captured on the test line of the LFIA. As a result, an increase in the concentration of the analyte will result in a decrease in the signal on the test line and using this filter-based method we are able to detect the CRP with a limit-of-detection found at 13 ng/ml.

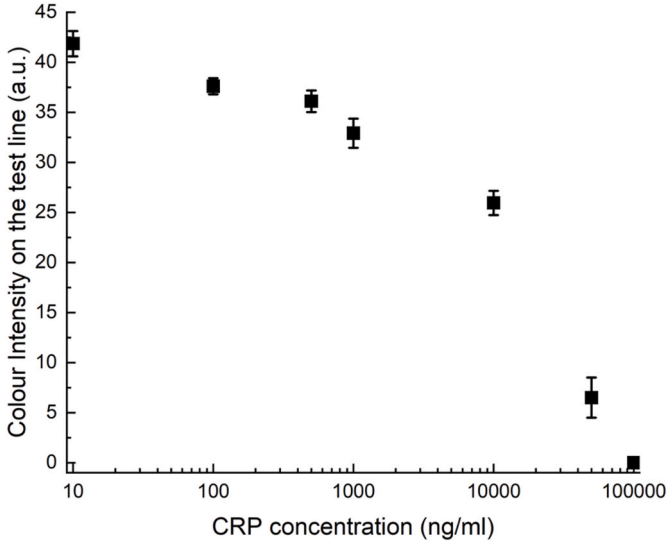

Fig. 10. Colour intensity on the test line of the LFIA for various CRP concentrations in the range between 10 ng/ml and 100,000 ng/ml.

In order to measure the colour intensity in the test line of the LFIAs (Figs. 7 and 9) we used again the RGB channel in the histogram function of Adobe Photoshop and we measured the mean intensity value (from the total of three devices) of the pixels of the test line. This value was subtracted from the value of 255 which is the intensity value of the pixels corresponding to the background of the LFIAs (white) in order to obtain the actual signal intensities. For the calculation of the limit-of-detection we used equation (2) [33]:

$$LOD = 3.3 \times (\sigma / s) \quad (2)$$

where LOD refers to the limit-of-detection, σ refers to the standard deviation of the regression line and s refers to the slope of the calibration curve. The values of σ and s were both measured from the graph depicted in Fig. 10 and calculated at 4.3 and 1.1 respectively.

4. Conclusion

We have reported a laser-based technique for the fabrication of porous flow-through filters, on a paper substrate, with different levels of porosity that are able to retain particles of a specific size while allowing smaller particles to flow through. The filtration properties and the particle retention efficiency of the flow-through filters were studied by testing polystyrene microspheres of different sizes and we have successfully found the parameters to make filters able to completely block or allow the flow of the different particle sizes. This filtration technique was later used as an analyte detection mechanism based on the binding of the target analyte with two antibodies, each one tagged with a differently-sized label namely 40 nm Au-nanoparticles and 3 μm latex beads. The antibody-antigen interaction leads to the formation of a complex, which is unable to flow through the filter of a certain porosity when the analyte is present in the sample. Only the unbound detection antibodies with a size smaller than the porosity of the filter can flow through and get captured at the test line of the LFIA indicating the presence or absence of the analyte in the sample. The flow-through filtration method provides an alternative pathway compared to standard LFIAs for the detection of analytes. Unlike other methods reported for the fabrication of standard LFIAs, our proposed technique uses a porous flow-through filter located on the top of the front end of an LFIA which is able to remove particles of a specific size. Using this method, we are able to detect analytes in a concentration range which is beyond the Hook effect threshold, thus avoiding this limiting factor that many analyte detection methods encounter. This method was tested for the detection of a CRP marker covering a broad concentration range between 10 ng/ml and 100,000 ng/ml, with a limit-of-detection of 13 ng/ml. We believe that this size-exclusive filtration method can be further studied for different applications. Apart from the detection of analytes the porous flow-through filters can also be used as a tool to remove particles which otherwise can be captured in the test line producing false negative results. This application has the potential to improve the performance as well as the limit-of-detection of the LFIAs and this will be part of our future work.

Declaration of competing interest

The authors declare that they have no known competing financial interests or personal relationships that could have appeared to influence the work reported in this paper.

Acknowledgements

The authors acknowledge the funding received via the Engineering and Physical Sciences Research Council (EPSRC) via Grant Nos. EP/P025757/1, EP/N004388/1, EP/M027260/1 and EP/S003398/1. The underpinning RDM data for this paper can be found at 10.5258/SOTON/D1758.

References

[1] G.J. Fermann, J. Suyama, Point of care testing in the emergency department, J. Emerg. Med. 22 (2002) 393–404, https://doi.org/10.1016/s0736-4679(02)00429-8.
[2] P. von Lode, Point-of-care immunotesting: approaching the analytical performance of central laboratory methods, Clin. Biochem. 38 (2005) 591–606, https://doi.org/10.1016/j.clinbiochem.2005.03.008.
[3] T.R. Kozel, A.R. Burnham-Marusich, Point-of-Care testing for infectious diseases: past, present, and future, J. Clin. Microbiol. 55 (2017) 2313–2320, https://doi.org/10.1128/jcm.00476-17.
[4] S. Smith, J.G. Korvink, D. Mager, K. Land, The potential of paper-based diagnostics to meet the ASSURED criteria, RSC Adv. 8 (2018) 34012–34034, https://doi.org/10.1039/c8ra06132g.
[5] A. Abdollahi-Aghdam, M.R. Majidi, Y. Omidi, Microfluidic paper-based analytical devices (μPADs) for fast and ultrasensitive sensing of biomarkers and monitoring of diseases, Bioimpacts: BI 8 (2018) 237.
[6] K. Yamada, H. Shibata, K. Suzuki, D. Citterio, Toward practical application of paper-based microfluidics for medical diagnostics: state-of-the-art and challenges, Lab Chip 17 (2017) 1206–1249, https://doi.org/10.1039/c6lc01577h.
[7] T. Akyazi, L. Basabe-Desmonts, F. Benito-Lopez, Review on microfluidic paper-based analytical devices towards commercialisation, Anal. Chim. Acta 1001 (2018) 1–17, https://doi.org/10.1016/j.aca.2017.11.010.
[8] M.D. Moreno, A. Cebolla, A. Munoz-Suano, C. Carrillo-Carrion, I. Comino, A. Pizarro, F. Leon, A. Rodriguez-Herrera, C. Sousa, Detection of gluten immunogenic peptides in the urine of patients with coeliac disease reveals transgressions in the gluten-free diet and incomplete mucosal healing, Gut 66 (2017) 250–257, https://doi.org/10.1136/gutjnl-2015-310148.
[9] E.C. Schramm, N.R. Staten, Z. Zhang, S.S. Bruce, C. Kellner, J.P. Atkinson, V. C. Kyttaris, G.C. Tsokos, M. Petri, E.S. Connolly, P.K. Olson, A quantitative lateral flow assay to detect complement activation in blood, Anal. Biochem. 477 (2015) 78–85, https://doi.org/10.1016/j.ab.2015.01.024.
[10] A. Carrio, C. Sampedro, J. Luis Sanchez-Lopez, M. Pimienta, P. Campoy, Automated low-cost smartphone-based lateral flow saliva test reader for drugs-of-abuse detection, Sensors 15 (2015) 29569–29593, https://doi.org/10.3390/s151129569.
[11] E.B. Bahadir, M.K. Sezginturk, Lateral flow assays: principles, designs and labels, Trac. Trends Anal. Chem. 82 (2016) 286–306, https://doi.org/10.1016/j.trac.2016.06.006.
[12] G.A. Posthuma-Trumpie, J. Korf, A. van Amerongen, Lateral flow (immuno) assay: its strengths, weaknesses, opportunities and threats. A literature survey, Anal. Bioanal. Chem. 393 (2009) 569–582, https://doi.org/10.1007/s00216-008-2287-2.
[13] K.M. Koczula, A. Gallotta, Lateral flow assays, in: P. Estrela (Ed.), BIOSENSOR TECHNOLOGIES FOR DETECTION OF BIOMOLECULES, PORTLAND PRESS LTD, 5TH FL, 90 HIGH HOLBORN, LONDON, WC1V 6LJ, ENGLAND, 2016, pp. 111–120, https://doi.org/10.1042/EBC20150012.
[14] J.H. Cho, S.H. Paek, Semiquantitative, bar code version of immunochromatographic assay system for human serum albumin as model analyte, Biotechnol. Bioeng. 75 (2001) 725–732, https://doi.org/10.1002/bit.10094.
[15] G.M.S. Ross, D. Filippini, M.W.F. Nielen, G.I.J. Salentijn, Unraveling the hook effect: a comprehensive study of high antigen concentration effects in sandwich lateral flow immunoassays, Anal. Chem. 92 (2020) 15587–15595.
[16] Y.K. Oh, H.A. Joung, H.S. Han, H.J. Suk, M.G. Kim, A three-line lateral flow assay strip for the measurement of C-reactive protein covering a broad physiological concentration range in human sera, Biosens. Bioelectron. 61 (2014) 285–289, https://doi.org/10.1016/j.bios.2014.04.032.
[17] J. Hu, J.R. Choi, S. Wang, Y. Gong, S. Feng, B. Pingguan-Murphy, T.J. Lu, F. Xu, Multiple test zones for improved detection performance in lateral flow assays, Sensor. Actuator. B Chem. 243 (2017) 484–488.
[18] I.N. Katis, P.J.W. He, R.W. Eason, C.L. Sones, Improved sensitivity and limit-of-detection of lateral flow devices using spatial constrictions of the flow-path, Biosens. Bioelectron. 113 (2018) 95–100, https://doi.org/10.1016/j.bios.2018.05.001.
[19] R. Ramamoorthy, V. Nallasamy, R. Reddy, N. Esther, Y. Maruthappan, A review of C-reactive protein: a diagnostic indicator in periodontal medicine, J. Pharm. BioAllied Sci. 4 (2012) 422, https://doi.org/10.4103/0975-7406.100318.
[20] Y. Luan, Y. Yao, The clinical significance and potential role of C-reactive protein in chronic inflammatory and neurodegenerative diseases, Front. Immunol. 9 (2018) 1302.
[21] M.M. Ragy, N.N. Kamal, Linking senile dementia to type 2 diabetes: role of oxidative stress markers, C-reactive protein and tumor necrosis factor-α, Neurol. Res. 39 (2017) 587–595.
[22] M. Algarra, D. Gomes, J.C.G.E. da Silva, Current analytical strategies for C-reactive protein quantification in blood, Clin. Chim. Acta 415 (2013) 1–9.
[23] C.M. McGeough, S. O'Driscoll, Camera phone-based quantitative analysis of C-reactive protein ELISA, IEEE Trans. Biomed. Circuits Sys. 7 (2013) 655–659.
[24] M. Dong, J. Wu, Z. Ma, H. Peretz-Soroka, M. Zhang, P. Komenda, N. Tangri, Y. Liu, C. Rigatto, F. Lin, Rapid and low-cost CRP measurement by integrating a paper-based microfluidic immunoassay with smartphone (CRP-Chip), Sensors 17 (2017) 684.
[25] P.M. Ridker, Clinical application of C-reactive protein for cardiovascular disease detection and prevention, Circulation 107 (2003) 363–369.
[26] M.V. Humbert, L.E. Costa, I. Katis, F. Fonseca Ramos, A. Sanchéz Machado, C. Sones, E.A. Ferraz Coelho, M. Christodoulides, A rapid diagnostic test for human visceral Leishmaniasis using novel Leishmania antigens in a laser direct-write lateral flow device, Emerg. Microb. Infect. 8 (2019) 1178–1185.
[27] P.J.W. He, I.N. Katis, R.W. Eason, C.L. Sones, Rapid multiplexed detection on lateral-flow devices using a laser direct-write technique, Biosensors-Basel. 8 (2018), https://doi.org/10.3390/bios8040097.
[28] P.J.W. He, I.N. Katis, A.J.U. Kumar, C.A. Bryant, C.W. Keevil, B.K. Somani, N. Mahobia, R.W. Eason, C.L. Sones, Laser-patterned paper-based sensors for rapid point-of-care detection and antibiotic-resistance testing of bacterial infections, Biosens. Bioelectron. 152 (2020) 112008.
[29] Y.K. Oh, H.-A. Joung, S. Kim, M.-G. Kim, Vertical flow immunoassay (VFA) biosensor for a rapid one-step immunoassay, Lab Chip 13 (2013) 768–772.
[30] J. Park, J.-K. Park, Pressed region integrated 3D paper-based microfluidic device that enables vertical flow multistep assays for the detection of C-reactive protein based on programmed reagent loading, Sensor. Actuator. B Chem. 246 (2017) 1049–1055.

[31] E.G. Rey, D. O'Dell, S. Mehta, D. Erickson, Mitigating the hook effect in lateral flow sandwich immunoassays using real-time reaction kinetics, Anal. Chem. 89 (2017) 5095–5100.

[32] P.P. Galanis, P.J.W. He, I.N. Katis, M.R. Thomas, Y.L. Xianyu, M.M. Stevens, R. W. Eason, C.L. Sones, Laser direct-writing to enable filtration in paper-based devices, in: B.L. Gray, H. Becker (Eds.), Microfluidics, Biomems, and Medical Microsystems Xvii, Spie-Int Soc Optical Engineering, Bellingham, 2019, https://doi.org/10.1117/12.2508753.

[33] S.B. Bagadane, P.B. Jadhav, Development and validation of RP-HPLC method for simultaneous estimation of metformin hydrochloride and glipizide in bulk and pharmaceutical dosage form, J. Drug Deliv. Therapeut. 9 (2019) 146–155.